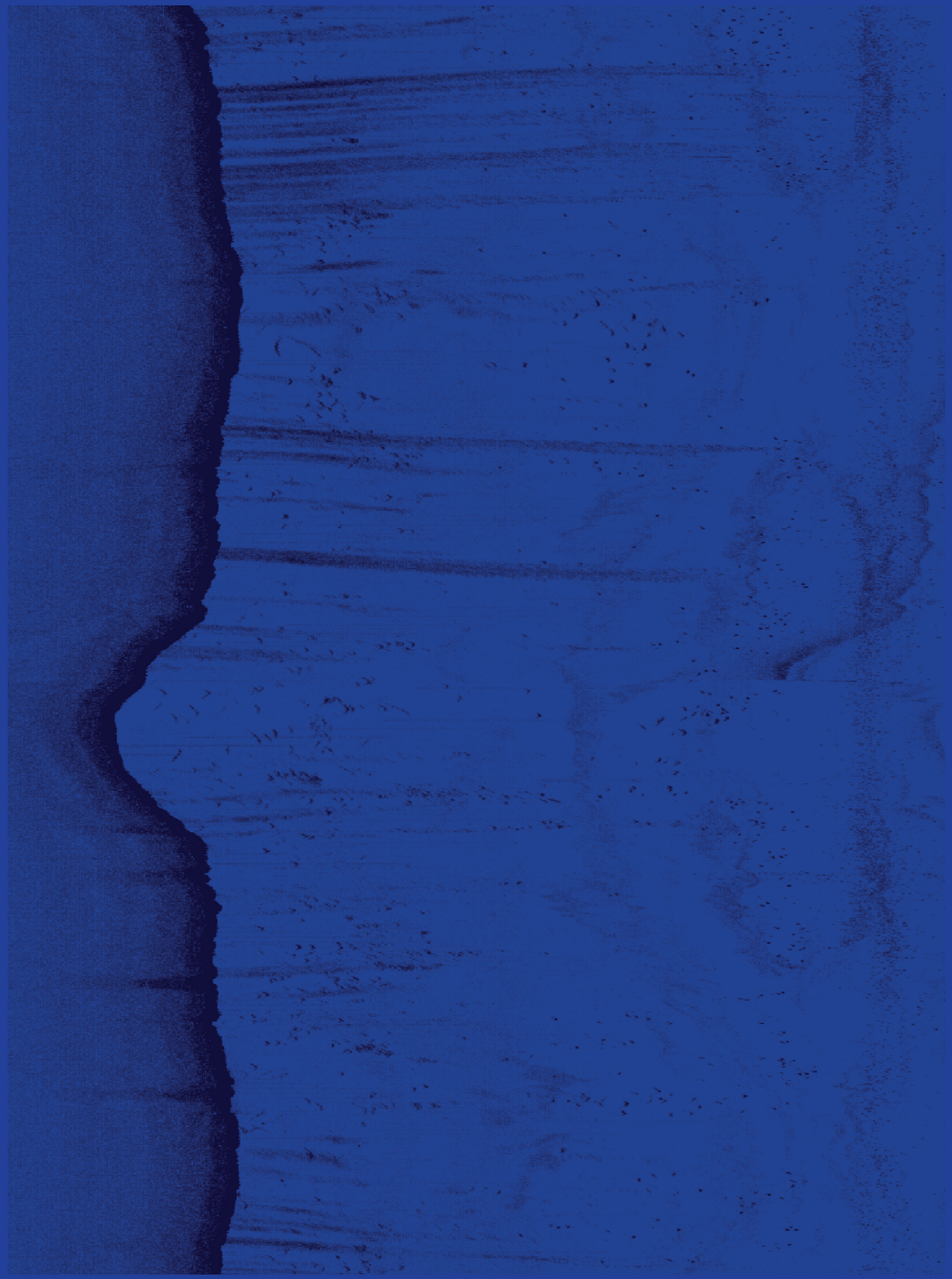

DETERMINING THE FLOW RATE OF FREE GAS IN THE WATER COLUMN USING HYDROACOUSTIC SYSTEMS

PROMOTER Prof. Dr. Marc De Batist
CO-PROMOTER Prof. Dr. Jens Greinert

—Faculty of Sciences
—Department of Geology
—Research unit Renard Centre of Marine Geology

Mario Enrique Veloso Alarcón

DETERMINING THE FLOW RATE OF FREE GAS IN THE WATER COLUMN USING HYDROACOUSTIC SYSTEMS

BEPALEN VAN DE STROOMSNELHEID VAN VRIJ GAS IN DE WATERKOLOM MET BEHULP VAN HYDRO-AKOESTISCHE SYSTEMEN

Thesis submitted in partial fulfilment of the requirements for the degree of Doctor in Sciences, Geology

Ghent University,
Academic Year 2015-2016

FACULTY OF SCIENCES
DEPARTMENT OF GEOLOGY

DETERMINING THE FLOW RATE OF FREE GAS IN THE WATER COLUMN USING HYDROACOUSTIC SYSTEMS

BEPALEN VAN DE STROOMSNELHEID VAN VRIJ GAS IN DE WATERKOLOM MET BEHULP VAN HYDRO-AKOESTISCHE SYSTEMEN

Mario Enrique Veloso Alarcón

Promoter: Prof. Dr. Marc De Batist
Co-Promoter: Prof. Dr. Jens Greinert

Faculty of Sciences
Department of Geology
Research unit Renard Centre of Marine Geology

Thesis submitted in partial fulfilment of the requirements for
the degree of Doctor in Sciences, Geology
Academic Year 2015-2016

To refer to this thesis:
Veloso-Alarcón M.E., 2016. Determining the flow rate of free gas in the water column using hydroacoustic systems, Ph.D. thesis, Ghent University, Ghent, Belgium.

Mario Veloso carried out the presented research as scientific personel of the Renard Centre of Marine Geology of Ghent University and at the Helmholtz Centre for Ocean Research Kiel, Geomar.

The author has been funded by the ERASMUS Mundus program of the EU (grant VECCEU) and the "Becas de doctorado en el extranjero, BECAS CHILE: CONICYT PAI/INDUSTRIA 79090016" program of the Chilean Government.

M. Veloso and J. Greinert both received support via COST Action ES0902 (PERGAMON) to join research cruises to acquire data.

Cover design: Lennart Van den Bossche

Members of the Examination Committee:

Prof. Dr. S. Louwye (Ghent University, Belgium): President

Prof. Dr. D. Van Rooij (Ghent University, Belgium): Secretary

Prof. Dr. J.P. Henriet (Ghent University, Belgium)

Dr. C. Sapart (Free University of Brussels, Belgium)

Prof. Dr. D. McGinnis (University of Geneva, Switzerland)

Prof. Dr. Marc De Batist (Ghent University, Belgium): Promoter

Prof. Dr. Jens Greinert (Geomar, Germany): Promoter

Acknowledgements

The work for this thesis was carried out at the Renard Centre of Marine Geology of Ghent University and the Helmholtz Centre for Ocean Research GEOMAR. The study was funded by the Erasmus Mundus scholarship of the EU (grant VECCEU), the "Becas de doctorado en el extranjero, BECAS CHILE: CONICYT PAI/INDUSTRIA 79090016" program of the Chilean Government and a full-time PhD position financed by GEOMAR during the last year. Additionally, financial support from COST Action ES0902 (PERGAMON) was awarded to join research cruises for data acquisition. I express my deepest gratitude for receiving this financial support.

Firstly, I would like to express my sincere gratitude to my supervisors Jens Greinert and Marc De Batist who believed in me, supported me and encouraged me to complete this project…many thanks to both of you, it has been a really good experience to learn from you and work together during these years. Additionally, I would like to thank Edna Hütten for always helping us with proof-reading the submitted manuscripts.

I want to thank the crew members of RV Helmer Hanssen with whom we shared many 'flarehunting' surveys. My gratitude is specially addressed to Iversen Steiner who was always willing to help and solve technical problems on board.

I want to express my gratitude to the researchers of the Centre for Arctic Gas Hydrate, Environment and Climate (CAGE), Jürgen Mienert and Tine Rassmussen who kindly let us participate in the Svalbard surveys on board RV Helmer Hanssen. Additionally, I want to thank the researchers from CAGE who I also consider good friends, Kamila Sztybor and Pär Jansson, thanks guys!!! It has been really nice to work with you.

I express my gratitude to the researchers from NOCS and Southamptom University who were willing to cooperate and exchange hydracoustic data used for the spatio/temporal analysis of submarine gas emissions at the study area. I would like to give special thanks to Tim Minshull.

I want to say thanks to my RCMG colleagues with whom I shared all the years while I was living in Ghent! ... thanks to Tist, Sebastien, Oscar, Mateu, Carmen, Stan, Wei Yao, Kainan, Hui, Thomas, Tuco, Willem, Katrien, Marc Faure, Kurt Blom, David G., Matthias, Maarten, Phillip, Jasper, Anita, Tine, David V.R., Koen, Jean Pierre, Sonia, Andres… it has been really nice meeting you and working with you guys! Dank u well!

I want to express my gratitude to the marine geology group of NIOZ who always greeted me warmly when I went to Texel! ... My special thanks go to Rineke, Henko and Henk! Additionally, I would like to thank the friends that I made there; it was always nice to share with you guys when I went to the island! Thanks Argiro, Claudia, Kevin, Andreas, Wouter, Santi, Jenny, Ivonne, Jurre, Anja, Michiel, Felix, Anasthasia, Anouk, Anna, Santiago Gonzalez, Irina, Colin, Elena, Niamh…. my apologies if I forgot someone.

I would like to thank my colleagues from the Deep Sea Monitoring at GEOMAR; it has been a nice experience to share knowledge together with good moments with you guys during this last year living in Kiel. Thanks Jens, Anne V., Anne J., Anne P., Cuiling, Tim, Kevin, Peter, Vagelis, Timm, Eva! Danke schön!

I want to thank the wave propagation group from FORTH Institute who warmly received me during my stay in Crete. My special thanks go to John Papadakis and Yiota Rigopoulou… Ευχαριστώ πάρα πολύ! I also want to thank my researcher friends from FORTH Eftixia Karasmani, Daniele Ancora, and Charalampos Mavidis with whom I have discussed some problems related to my research, thanks for your help guys!

My special thanks are directed to Sergei Muyakshin who kindly discussed his methodology with us during a visit at GEOMAR.

I would also like to use this opportunity to thank to the people who contributed in technical aspects of this thesis. My special thanks go to: Ira Leifer for kindly providing his Matlab routines for bubble rising speed calculations; Tim Weiss for helping me improving the FlareHunter GUI; Anne Jordt for the 'bubble image' used in the graphical abstract of chapter 5; Nore and Thomas for the 'last minute' translation to Dutch of the summary of this thesis; Lennart and Francois for helping me with the cover of the manuscript; Scarlett and Julie for kindly helping me with the proof-reading of the summary and conclusions.

I would like to express my gratitude to the members of the examination committee Dr. C. Sapart, Dr. S. Louwye, Dr. D. Van Rooij, Dr. J.P. Henriet and Dr. D. McGinnis who gave detailed insightful comments about my PhD research work. The comments have helped me greatly in preparing this final version of my thesis and at the same time have broadened my scientific knowledge.

My sincere thanks also goes to the friends I made during the evolution of my PhD at different places that I was, in special to Dimitris E., Liesbet, Maria, Argiro, François, Seb, Mieke, Sara, Emilio, Anita, Celestin, Maria del Mar, Daniel, 'Pescaito', Jaime, Erick, Leo, 'Tuco', Nele, Christoph, Danae, Tomas, Romina, Inés, Pedro, Oscar, Stan, Wei Yao, Cyrus, Lucia y Josefina, Paulina, Cote, Torben, Cindy, Lena, Stefanos, Dimitris A., Tim, Carola, Jaime, Cuiling, my apologies if I have forgotten someone.

Undoubtedly, I would like to deeply thank my family from Chile and the 'new one' from Greece, who 'strongly' supported me during the evolution of my studies! Muchas gracias familia! Ευχαριστώ πολύ οικογένειά μου! I specially want to thank my wife who has been day by day supporting me! Gracias Vicky por estar conmigo en todas las circunstancias y por darme la dicha de ser padre!

This thesis is dedicated to my little daughter Cristina, who was born at the same period that I was finishing this work and who is the most beautiful gift that I have ever received

August 2016, Athens

Summary

The interest in quantifying submarine sources of gas has increased since marine gas fluxes have been recognized as a potential source of atmospheric methane as well as a contributor to the 'greenhouse effect'. Estimates of the contribution of natural seabed gas to the atmospheric methane budget have been undertaken, but they are still poorly constrained and highly controversial. To a large extent, these estimates are based on extrapolations from spatially small data sets resulting in a broad range of uncertainty. Consequently, it is necessary to minimize this uncertainty for coming greenhouse gas flux estimates from the ocean. Additionally, methods for detecting and quantifying gas leakage from industrial gas and oil exploitation sites are in demand to control industrial processes and to assess marine pollution that occur during normal operation and blow-out scenarios.

Driven by this demand, several techniques have been developed to study gas emissions from the seabed. In general, these techniques can be divided into invasive and non-invasive methods. Examples of non-invasive methods include the inverted funnel technique, to capture bubbles in situ, and direct video observations at the seafloor. Both are used to physically describe bubble release and to quantify the amount of gas expelled. Both are highly precise methods, but they are less efficient in covering large areas in which seepages occur. Alternatively, hydroacoustic remote sensing techniques have become popular due to its non-invasive capability to detect, monitor and also quantify the emitted gas. Hydroacoustic systems can be divided in a) passive systems, which are able to 'listen' to the acoustic signature of bubbles when detached from a surface (e.g. sediments) and b) active systems, which send out an acoustic signal and record the sound backscattered from different targets within the water.

Passive systems are useful, as they allow detailed spectral analyses of the signal emitted by bubbles; but at the same time, they are limited to environments with high levels of background noise as these would mask/overprint the signal (e.g. oceans at strong weather conditions; ship noise, other artificial noise). To overcome this problem, passive devices are usually placed close to the sound source of interest, further limiting their ability to cover large seep areas.

Active hydroacoustic techniques presented in this thesis, are very efficient in detecting free gas (bubbles) in the water column because sound is strongly scattered when it hits bubbles due to the high impedance change at the gas-liquid interface. The emitted signal, although it provides less spectral information due to the narrow bandwidth of the signal, is easy to be detected because its waveform is known. Unlike passive hydroacoustic methods and invasive techniques, devices such as singlebeam and multibeam echosounder systems (SBES and MBES respectively) are able to cover larger seep areas than it is possible by e.g. ROV-based visual observations. In addition, active systems can be seen as a directional antenna (or a group of antennas in case of using MBES) rendering them useful in accurately positioning detected targets within a 3D space or, at least, providing valuable information about the depth in which targets are located in the water column.

The presented work attempts to reach two main objectives. The first is the development of a practical technique to evaluate gas flow rates of acoustically detected and mapped gas bubbles in the water column using SBES data. The second objective is the application of this method to the total methane emissions and the spatio/ temporal changes of a seep area located in the Arctic west of Spitzbergen. This study area has been chosen because it is considered a model area to eventually assess accelerated gas hydrate destabilization as a consequence of global warming induced by bottom water warming. Methane release at the study area has been hypothesized to be controlled by changes of the gas hydrate stability zone (GHSZ), which is vulnerable to changes of bottom-water temperature. Additionally, geochemical studies on methane-derived carbonates have shown that seepage is ongoing for at least 3000 years BP. In order to study seep activity changes, the seep area has been repeatedly hydroacoustically monitored since 2008. Hydroacoustic surveys in the seep area were carried out by different research groups (RCMG, GEOMAR, CAGE, NOCS and NIOZ) and the complete dataset presented in this thesis is the result of the cooperation between these groups.

With regard to the first objective of this thesis, the used approach applies the theoretical relationship between bubble sizes and the total acoustical scattering cross-section of a bubble cloud when it is insonified by a monochromatic acoustic plane wave. A scattering model for single bubbles based on the monopole bubble theory is tested as fundamental part of this method. It is assumed that the backscattering produced by the bubble cloud is the sum of the backscattering as it would be contributed by individual spherical bubbles with a specific size distribution. For flow calculations, bubble rising speeds are an essential input parameter. In the case that no bubble rising speed values have been measured, the developed method considers different bubble rising speed models to determine ascending speeds of bubbles in relation to their size. In the frame of this thesis, the above, briefly sketched method has been applied and despite that a validation of the method is still missing, the results obtained show realistic flow rates compared to visual or direct sampling techniques. Together with the description of the flow rate estimating method, a procedure for evaluating the total flow rate of large seep areas is described, which is based on the clustering of neighboring ‘acoustic flares’ (i.e. the name derives from the fact that multiple gas bubbles that are released from a seep location at the sea floor and rise through the water column are imaged on echograms with a typical ‘flare’ shape).

Because of the need to have an organized and rapid way to process hydroacoustic data, a software-package composed of FlareHunter and the FlareFlowModule has been developed during this PhD project and is now available to the general research community. The software, a user-friendly GUI for post-processing SBES data, is a valuable tool for standardizing gas flow rate estimates from SBES data. As the development of these two software tools was driven by the research needs, it is believed that others can make use of it and that additional use linked to more research questions will lead to new functionalities and general improvements.

With the quantitative method and the software-package in place it was possible to do comprehensive flow rate calculation of an entire large seep area based on complementary hydroacoustic dataset collected during 11 surveys (2008 - 2014). During these surveys 3145 acoustic flares were identified and the derived flow rates range from ~2500 to 4000 T CH4/yr when assuming continuous release and bubbles of 100 % methane. From these estimates, the determination of bubble size distributions (BSDs),

estimates of bubble rising speeds (BRS) using different models and interferences of unwanted acoustic signals (noise and reverberation) are recognized as the main sources of uncertainties to the results.

As part of the flow and flux investigations at the study area of Prins Karl Forland (PKF), the first attempt of identifying spatio/ temporal variations of methane release has been performed by using a complete hydroacoustic dataset available. Flux comparisons among surveys show no trend towards increased seepage for the time slots that the surveys were carried out. Results indicate that the important control mechanisms of methane emission namely the bottom water temperature and a possible migration of the top of the gas hydrate stability zone (TGHZ), pressure changes in the seabed due to tectonic stress or sea level change, did not change significantly. A moderate correlation between the sea bottom temperature and fluxes has been observed; it is believed that seabed temperature is the main mechanism that controls the free gas emissions at the study area. Furthermore, there are no indications that the free gas supplying reservoirs are depleted and that short-term events, such as earthquakes or smaller micro-seismic events that would open new gas migration pathways happened. A displacement of the TGHZ was not detectable when analyzing the flare positions in the SBES dataset. One explanation for this might be that the study area was only partially and differently insonified during each survey. On the other hand, because of the misalignment between the acoustic flare distribution and the TGHZ it is believed that the occurrence of seafloor gas release is mostly controlled by tectonic/geological pathways in the seabed. As such, a future gradual migration of the gas vents accompanied with a downward displacement of the TGHZ is unlikely. However, an eventual acceleration of gas hydrate dissociation due to anthropogenic induced climate change, which could be a long term process, cannot be discarded.

An alternation in flux magnitudes between two areas has been observed suggesting that both areas are connected and share a common gas source. Blocking and opening of gas conduits as a result of the formation and dissociation of shallow gas hydrates near the TGHZ is hypothesized as a possible explanation of this alternation.

To better prove and quantify gas flow fluctuations, stationary observatories such as side-looking sonars are recommended for long-term deployments to visualize flux changes on short and longer time scale. To advise on improving the data quality for spatio/temporal analysis of gas emissions, a set of recommendations are presented at the end of the thesis. As the spatio/temporal evaluation of the gas emissions using SBES is challenging and until now present high uncertainties, future efforts should be made in solving some of the identified problems like SBES resolution, the reproducible acoustic coverage at the seafloor and mapping of a total area to make hydroacoustic data more easily comparable.

Samenvatting

De wens om onderzeese gasbronnen te kwantificeren is toegenomen sedert bekend is geraakt dat mariene gasfluxen een mogelijke bron zijn van atmosferisch methaan en daardoor bijdragen aan het broeikaseffect. Schattingen van het aandeel van natuurlijk zeebodemgas in de atmosferische methaanvoorraad zijn reeds gemaakt, maar zijn nog steeds slecht onderbouwd en heel controversieel. Deze schattingen zijn voor een groot deel gebaseerd op extrapolaties van geografisch gezien kleine datasets en hebben dus een grote onzekerheid. Bijgevolg is het noodzakelijk deze onzekerheid aangaande broeikasgassen afkomstig van de oceanen te minimaliseren. Tevens zijn methodes voor de detectie en kwantificatie van gaslekken in industriële gas- en olie-exploitatiesites erg gegeerd, aangezien ze industriële processen beïnvloeden en mariene vervuiling, dat zowel tijdens normale operaties als tijdens een “blow-out” kan voorkomen, kunnen inschatten.

Gedreven door deze vraag zijn meerdere technieken ontwikkeld die gas-emissies van de zeebodem bestuderen. Algemeen kunnen deze technieken onderverdeeld worden in invasieve en niet-invasieve methodes. Voorbeelden van niet-invasieve methodes zijn “geïnverteerde funnel technieken” die gasbubbels in situ opvangen en rechtstreekse videowaarnemingen van de zeebodem verrichten. Beiden worden gebruikt om opborrelende bubbels fysisch te karakteriseren en om de hoeveelheid van het uitgestoten gas te kwantificeren. Dit zijn heel precieze methodes, maar ze zijn minder efficiënt in grotere gebieden waar gas vrijkomt. Anderzijds zijn hydroakoestische teledetectietechnieken heel populair geworden omdat ze niet-invasief het vrijgekomen gas kunnen detecteren, bestuderen en kwantificeren. Hydroakoestische systemen kunnen onderverdeeld worden in a) passieve systemen die naar het akoestisch signaal van bubbels kunnen “luisteren” wanneer deze van een oppervlak (bvb. sediment) vrijkomen en b) actieve systemen die een akoestisch signaal uitzenden en het teruggekaatste signaal van verschillen doelwitten in de waterkolom opvangen.

Passieve systemen zijn nuttig omdat ze toelaten om een gedetailleerde spectrale analyse van het signaal dat uitgezonden werd door de bubbels te maken. Maar tegelijkertijd zijn ze ook gelimiteerd aangezien ze niet kunnen gebruikt worden in gebieden met veel ruis want dit zou het signaal kunnen maskeren. Enkele voorbeelden van ruis zijn hevige weersomstandigheden, het geluid van het schip zelf of andere artificiële geluiden. Om dit probleem op te lossen worden passieve systemen meestal dicht tegen het studieobject geplaatst, wat hen tevens beperkt in geografische omvang.

Actieve hydroakoestische technieken worden in deze thesis besproken worden. Ze zijn heel efficiënt in het detecteren van vrij gas (bubbels) in de waterkolom omdat geluid sterk verstrooid wordt als het bubbels tegenkomt. Dit komt door de hoge impedantie-verandering op de grens tussen gas en vloeistof. Het uitgezonden signaal (dat weinig spectrale informatie oplevert door de nauwe bandbreedte van het signaal) is gemakkelijke te detecteren door de gekende vorm van de golf. In tegenstelling tot passieve hydroakoestische systemen en invasieve technieken zijn systemen zoals “singlebeam” en “multibeam echosounders” (SBES en MBES respectievelijk) in staat om grote gebieden te bedekken in vergelijking met bijvoorbeeld visuele observaties gebaseerd op ROV. Bovendien kunnen actieve systemen gezien worden als een directionele antenne (of een groep van antennes, zoals bij MBES). Dit maakt hen nuttig

in het precies positioneren van gedetecteerde doelwitten in de 3D ruimte. Op zijn minst geven ze precieze informatie over de diepte waarop de doelwitten voorkomen in de waterkolom.

Het gepresenteerde werk poogt twee grote doelen te bereiken. Het eerste doel is het ontwikkelen van een praktische techniek, gebaseerd op SBES data, die akoestisch gedetecteerde gasdebieten evalueert en gasbubbels ontdekt die zich in de waterkolom bevinden. Het tweede doel is de toepassing van deze methode op een Arctisch gebied, ten westen van Spitsbergen. In dit gebied zal de totale methaanemissie en zijn spatiale en temporele veranderingen gemeten worden. Dit gebied werd gekozen omdat het beschouwd wordt als een modelgebied dat toelaat om het mogelijks versneld vrijkomen van gedestabiliseerde gashydraten als gevolg van de wereldwijde opwarming van de aarde en bijgevolg de lokale bodemwatermassa, te bestuderen. Het vrijkomen van methaan in het studiegebied wordt geacht beïnvloed te zijn door veranderingen van de gashydraatstabiliteitszone die op zijn beurt gevoelig is voor temperatuursveranderingen van de bodemwatermassa. Tevens tonen geochemische studies van methaanafgeleide carbonaten aan dat sijpeling van methaan minstens 3000 jaar al gaande is. Om deze veranderingen te bestuderen, werd het studiegebied herhaaldelijk hydroakoestisch gemonitord sinds 2008. Hydroakoestische onderzoeken in het gebied werden uitgevoerd door verschillende onderzoeksgroepen (RCMG, GEOMAR, CAGE, NOCS en het NIOZ) en de volledige dataset die voorgesteld wordt in deze thesis, is het resultaat van de samenwerking tussen deze verschillende instituten.

Voor de eerste doelstelling werd de theoretische samenhang tussen de grootte van de bubbels en de totale akoestische verstrooiingsdoorsnede van een bubbelwolk bestudeerd, wanneer deze geïnsonifieerd wordt door een monochromatische akoestische golftrein. Een verstrooiingsmodel voor de individuele bubbels, gebaseerd op “de monopool bubbel theorie”, werd getest als een fundamenteel onderdeel van deze methode. Er wordt verondersteld dat de verstrooiing die veroorzaakt wordt door de wolk van bubbels, de optelsom is van de verstrooiing van de individuele sferische bubbels met een specifieke grootteverdeling. Stijgsnelheden van bubbels zijn een essentiële inputparameter van stromingsberekeningen. Indien geen stijgsnelheden van bubbels konden worden berekend, beschouwt de ontwikkelde methode verschillende modellen om deze, afhankelijk van de grootte, te berekenen. Voor deze thesis werd bovengenoemde methode toegepast en ondanks dat de methode nog gevalideerd moet worden, vertonen de resultaten realistische debieten wanneer deze vergeleken worden met de resultaten van visuele en directe waarnemingstechnieken. Samen met de beschrijving van de methode om het debiet te schatten, werd een procedure beschreven om het totale debiet van een groot gebied te evalueren . Deze is gebaseerd op het clusteren van naburige akoestische “flares” (deze naam is afkomstig van het feit dat de talrijke gasbubbels die vrijkomen van een sijpellocatie op de zeebodem en door de waterkolom stijgen, weergegeven worden op de echograms met een typische “flare” vorm).

Omwille van de noodzaak om op een georganiseerde en snelle manier hydroakoestische data te verwerken, werd een softwarepakket, bestaande uit FlareHunter en de FlareFlowModule, ontwikkeld gedurende dit doctoraat. Deze zijn nu vrij beschikbaar voor de onderzoeksgemeenschap. De software, een gebruikersvriendelijke GUI voor latere verwerking van SBES data, is een waardevol werktuig dat toelaat gasdebietschattingen, afgeleid van SBES data, te schatten. Aangezien de ontwikkeling van deze

twee programma's gedreven werd door wetenschappelijke noodzaak, geloven wij dat derden hiervan gebruik kunnen maken en dat bijkomende wetenschappelijke vraagstellingen zullen leiden tot nieuwe invoegtoepassingen en algemene verbeteringen.

Met de kwantitatieve methode en het softwarepakket is het mogelijk om uitgebreide debietberekeningen te maken van een groot sijpelgebied gebaseerd op hydroakoestische datasets die werden vergaard gedurende 11 campagnes (2008-2014). Gedurende deze campagnes werden 3145 akoestische "flares" geïdentificeerd en afgeleide debieten gaan van ~2500 tot 4000 T CH4/jaar, veronderstellend dat er continu gas (100 % methaan) wordt vrijgegeven. Uit deze schattingen kunnen grootteverdelingen van bubbels, stijgsnelheden van bubbels gebruikmakend van verschillende modellen en inmenging van ongewenste akoestische signalen (ruis en weerkaatsing) herkend worden als de belangrijkste bronnen van onzekerheid aangaande de resultaten.

Als een deel van de debiet- en fluxonderzoeken in het studiegebied Prins Karl Forland (PKF), werden initiële pogingen ondernomen om spatiale en temporele veranderingen van methaanemissie te identificeren door gebruik te maken van een complete hydroakoestische dataset. Het vergelijken van de flux van de verschillende campagnes toont geen trend van toenemende sijpeling gedurende de campagnes. De resultaten duiden wel aan dat de belangrijkste mechanismen van methaanemissie, zijnde bodemwatertemperaturen en de bijhorende mogelijke migratie van de TGHZ, drukveranderingen van de zeebodem door tektonische druk en zeespiegelveranderingen, niet significant veranderen. Een gemiddelde correlatie tussen zeebodemtemperaturen en debieten werd opgemerkt; er wordt aangenomen dat de zeebodemtemperatuur het belangrijkste mechanisme is dat beslist of vrij gas uitgestoten wordt in het studiegebied. Verder zijn er geen aanwijzingen dat vrij gas, dat de reservoirs bevoorraadt, uitgeput aan het raken is en dat gebeurtenissen zoals aardbevingen of kleinere micro-seismische gebeurtenissen die nieuwe gasmigratiewegen kunnen openen, hebben plaatsgevonden. Een verplaatsing van de TGHZ kon niet worden gedetecteerd bij de analyse van de "flare" posities in de SBES dataset. Een mogelijke verklaring hiervoor is dat het studiegebied slechts gedeeltelijk geïnsonifieerd werd gedurende elke campagne. Anderzijds, door de "misallignment" tussen de akoestische "flare" en de TGHZ denkt men dat het voorkomen van zeebodemgas vooral gecontroleerd wordt door tektonische/geologische processen in de zeebodem en dat de toekomstige graduele migratie van gas, samengaande met een neerwaartse verplaatsing van de TGHZ, onwaarschijnlijk is. Echter, een eventuele versnelling van de gashydraatdissociatie door een antropogeen-geïnduceerde klimaatsverandering (wat een langdurig proces kan voorstellen) , kan niet uitgesloten worden.

Een wisselwerking in debietmagnitudes tussen twee gebieden is geobserveerd, wat suggereert dat beide gebieden verbonden zijn en bovendien een gemeenschappelijke gasbron delen. Blokkering en opening van gasmigratiewegen als gevolg van de vorming en dissociatie van oppervlakkige gashydraten nabij de TGHZ, zou een mogelijke verklaring kunnen geven voor deze alternatie.

Om de gasstroomfluctuaties verder te bewijzen en beter te kwantificeren zijn stationaire waarnemingen, zoals zijwaarts gerichte sonars, aanbevolen gedurende langdurig gebruik. Deze kunnen debietveranderingen op zowel korte als lange termijn visualiseren. Een advies om de datakwaliteit van spatiale en temporele analyses van gasemissies te verbeteren, werd geformuleerd op het einde van de

thesis. Aangezien de spatiale en temporele beoordeling van gasemissies op basis van SBES uitdagend is en tot op heden grote onzekerheden met zich meebrengt, zouden pogingen moeten ondernomen worden om de geïdentificeerde problemen aan te pakken. Deze problemen bestaan uit de SBES resolutie, de reproduceerbaarheid van de akoestische bedekking van de zeebodem en het karteren van volledige gebieden die toelaten datasets te vergelijken.

Contents

List of Figures

List of Tables

Abbreviations

ADCP	:	ACOUSTIC DOPPLER CURRENT PROFILER
AOM	:	ANAEROBIC METHANE OXIDATION
AOEM	:	ARCTIC OCEAN ESONET MISSION
AW	:	ATLANTIC WATER
BRS	:	BUBBLE RISING SPEED
BRSM	:	BUBBLE RISING SPEED MODEL
BSD	:	BUBBLE SIZE DISTRIBUTION
CAGE	:	CENTER FOR ARCTIC GAS HYDRATES, ENVIRONMENT AND CLIMATE
CAC	:	COMMON AREA COMPARISON (METHOD)
CC	:	COASTAL CURRENT
CTD	:	CONDUCTIVITY, TEMPERATURE, AND DEPTH (SENSOR)
EK60	:	SPLIT-BEAM ECHOSOUNDER SYSTEM DEVELOPED BY KONGBERG
ESC	:	EAST SPITSBERGEN CURRENT
ESONET	:	EUROPEAN SEAFLOOR OBSERVATORY NETWORK OF EXCELLENCE
FFM	:	FLAREFLOWMODULE (GUI)
GGC	:	GRID BY GRID COMPARISON METHOD
GHSZ	:	GAS HYDRATE STABILITY ZONE
GMT	:	GENERIC MAPPING TOOLS
GPS	:	GLOBAL POSITIONING SYSTEM
GUI	:	GRAPHICAL USER INTERFACE
HMMV	:	HÅKON MOSBY MUD VOLCANO
IPCC	:	INTERNATIONAL PANEL OF CLIMATE CHANGE
LPTM	:	LATE PALEOCENE THERMAL MAXIMUM
MBES	:	MULTI-BEAM ECHOSOUNDER SYSTEM
M BSL	:	METERS BELOW THE SEA LEVEL
M1C	:	LEIFER BUBBLE RISING SPEED MODEL FOR CLEAN BUBBLES
M2C	:	MENDELSON BUBBLE RISING SPEED MODEL FOR CLEAN BUBBLES
M3C	:	LEIFER & PATRO BUBBLE RISING SPEED MODEL FOR CLEAN BUBBLES
M1D	:	LEIFER BUBBLE RISING SPEED MODEL FOR DIRTY BUBBLES
M2D	:	LEIFER & PATRO BUBBLE RISING SPEED MODEL FOR DIRTY BUBBLES
M3D	:	WOOLF93 BUBBLE RISING SPEED MODEL FOR DIRTY BUBBLES
M4D	:	THORPE 91 BUBBLE RISING SPEED MODEL FOR DIRTY BUBBLES
NAC	:	NORTH ATLANTIC CURRENT
NRCC	:	NATIONAL RESEARCH COUNCIL CANADA
PERGAMON	:	PERMAFROST AND GAS HYDRATE RELATED METHANE RELEASE IN THE ARCTIC AND IMPACT ON CLIMATE CHANGE (EUROPEAN COOPERATION FOR LONG-TERM MONITORING)
PKF	:	PRINS KARL FORLAND
RAC	;	RETURN ATLANTIC CURRENT
RF	:	REPRESENTATIVE FLUX
ROV	:	REMOTELY OPERATED VEHICLE
SB	:	SVALBARD BRANCH
SBES	:	SINGLE-BEAM ECHOSOUNDER SYSTEM
SPC	:	SPITSBERGEN POLAR CURRENT
STC	:	SPITSBERGEN TROUGH CURRENT
TAF	:	TOTAL AVERAGE FLUX (METHOD)
TAW	:	TRANSFORMED ATLANTIC WATER

TGHZ	:	TOP OF THE GAS HYDRATE STABILITY ZONE
UTM	:	UNIVERSAL TRANSVERSE MERCATOR (COORDINATE SYSTEM)
WSC	:	WEST SPITSBERGEN CURRENT
YB	:	YERMAK BRANCH

Nomenclature

A	:	Amplitude of incident plane wave
A_C	:	Cluster area [m^2]
A_H	:	Area with hydroacoustic data within the analyzed area [m^2]
A_i	:	Area of echosounder footprint of the source of an *i*-acoustic flare [m^2]
A_{iB}	:	Pressure amplitude inside the bubble
b	:	Function defined in Medwin (1977)
B	:	Amplitude of scattered spherical wave multiplied by distance from center of
b_r	:	Resistive component of this impedance evaluated at the bubble surface
c_W	:	Speed of sound in liquid [m/s]
C_1	:	Constant in Wildt (1946) related to viscous damping
D	:	Height of volume sample [m]
D_a	:	Thermal diffusivity [m^2/s]
D_P	:	Gas diffusivity
dp_i	:	Incremental inner bubble pressure
dV	:	Incremental bubble volume; $dV = 4\pi r^2 dr$
$\frac{d}{b}$	:	Function of X defined in Medwin (1977)
f_{echo}	:	Echosounder frequency [Hz]
$f(r)$	:	Probability density function of the bubble size distribution [1/m]
F_{ext}	:	External force over the bubble
F_m	:	Inertial force at the bubble surface
g	:	Acceleration of gravity [m/sec^2]
I_0	:	Incident intensity
I_S	:	Scattered intensity
k	:	Wave number $[2\pi f_{echo}/c]$
K	:	Constant of linear relationship between bubble flux and scattering defined by Muyakshin and Sauter (2010)
L_{th}	:	Thermal length
m	:	Bubble effective mass
n_j	:	Number of bubbles of radius r_j
n_P	:	Number of samples
N	:	Total number of bubbles
N_0	:	Total number of bubbles inside the sample volume *V*
N_{0C}	:	Bubble concentration

N_b : Bubble size distribution of water bubbly volume

N_{Cells} : Number of cells inside the cluster area

Ne : Number of cells with flux values, CAC method

N_i : Number of bubbles of *i*-size inside the sample volume *V*

$N(r)$: Distribution of bubbles in function of the radius size [1/m]

p : Number of acoustic flares that belong to the cluster

p_0 : Incident pressure

p_{EXT} : External pressure evaluated at the bubble surface $p_{EXT} = p_0 + p_S$

p_i : Bubble internal pressure

p_S : Scattered pressure

P_a : Static surrounding pressure

P_{int} : Inner bubble pressure

P_p : Root mean square pressure of the incident wave

P_{st} : Static pressure [Pa]

P_{st0} : Atmospheric pressure [Pa]

P_{0S} : Scattered pressure amplitude

$q_{i,j}$: Flux at the i, j grid

Q : Bubble flux

Q_C : Mean gas flux TAF method

Q_m : Bubble mass flux

Q_{RF} : Approximated representative flux (mean flux) of common area, CAC method

r : Bubble radius (m)

r_1, r_2 : Lower and upper limit of the bubble size distribution

r_0 : Bubble resonant radius at echosounder frequency and specific static pressure [m]

r_i : Bubble radius of i-size [m]

r_{av} : Most frequent bubble radius BSD [m]

$R_{Laplace}$: Laplace radius

R_m : Mechanical resistance of bubble

s : bubble stiffness

S : Water salinity [PSU]

S_V : Volume backscattering strength

Δt_i : Time necessary to fill the volume sample *V* with N_i bubbles of r_i radius [sec]

T : Water temperature [°C]

Tp : Time period of one cycle of bubble oscillation

TS : Target strength

$\overline{TS}$: Geometrical average of target strength [dB]

TS_i : Target strength of different samples inside the (selected layer [dB]

U_i	:	Average bubble rising speed of i-size bubble [m/sec]
$U(r)$	:	Bubble rising speed in function of the bubble radius [m/sec]
V		Bubble volume; $V = \frac{4}{3}\pi r^3$
v_R	:	Radial velocity of bubble
$\Delta x, \Delta y$	:	cell size in x and y direction (here related to UTM coordinates) [m]
z	:	Value associated to the bubble damping, bubble resonance and frequency of the incident wave (Thuraisingham, 1997)
Z	:	Average depth of layer at each acoustic flare [m bsl]
β	:	Constant in Wildt (1946) related to thermal damping
β_D	:	Function defined in Medwin (1977)
γ	:	Specific heat ratio of gas (dimensionless)
Γ	:	Complex politropic index
$\Delta\sigma_{bs}$	:	total backscattering cross-section [m^2]
δ	:	Dimensionless damping
δ_R	:	Dimensionless damping at resonance
δ_{rad}	:	Dimensionless re-radiation damping term
$\delta_{rad}R$	:	Dimensionless re-radiation damping term at resonance
δ_{therm}	:	Dimensionless thermal damping term
$\delta_{therm}R$	:	Dimensionless thermal damping term at resonance
δ_{visc}	:	Dimensionless viscous damping term
$\delta_{visc}R$	:	Dimensionless viscous damping term at resonance
η_B	:	Bulk viscosity [Pa][s]
η_S	:	Shear viscosity [Pa][s]
θ	:	Phase lag between the plane wave and the surface displacement
ξ	:	Bubble radial displacement
ξ_r	:	Real radial displacement of bubble
ξ_0	:	Amplitude of bubble displacement function
Π_S	:	Scattered power
ρ_{G0}	:	Atmospheric CH_4 density [kg/m^3]
ρ_G	:	Gas density of the bubble at the respective water depth [kg/m^3]
ρ_w	:	Liquid density[kg/m^3]
σ	:	Surface tension water[N/m]
$\sigma_{\mathrm{bs}}(r)$	:	Acoustical backscattering cross-section of a single bubble (m^2)
σ_{bsi}	:	Backscattering cross-section of a single bubble of *i*-size (m^2)
$\sigma_{bs}total$	:	Summation of acoustical cross-sections of several bubbles
σ_S	:	Acoustical scattering cross-section
σ_V	:	Differential acoustical cross-section per unit of volume
τ	:	Sample interval [sec]

υ	:	Dimensionless parameter related to the Laplace radius
φ	:	Angle of the radius vector measured from the direction of the incident beam
$\emptyset_V$	:	Volumetric bubble flow rate [vol/time]
$\emptyset_M$	:	Mass bubble flow rate [vol/time]
$\emptyset_{M,V}^{i}$	:	Flow rate (volumetric or in mass) of an *i*-acoustic flare [vol/time]
$\emptyset_{M,V}^{C}$	:	Cluster flow rate [vol/time]
$\emptyset_{M,V}^{T}$	:	Total flow rate [vol/time]
$\emptyset_{M,V}^{C,i}$	:	Flow rate (volumetric or in mass) of *i*-cluster or *i*-isolated flare [vol/time]
$\emptyset_{RF}$	:	Representative flow rate of common area [vol/time]
Ψ	:	Constant factor used to calculate flow rate (inverse method)
X	:	Thermal diffusion ratio
ω	:	Angular frequency
ω_{AD}	:	Adiabatic frequency
ω_b	:	Natural frequency of bubble system
ω_{ISO}	:	Isothermal frequency
ω_M	:	Minnaert frequency
ω_{RES}	:	Exact resonance frequency
ω_{RES_D}	:	Bubble resonance frequency corrected by Devin
$\Omega_{M,V}^{C}$	:	average bubble flux [(mass or vol)(time^{-1})(area^{-1})]

1. Introduction

1.1. Methane in carbon cycle

Carbon is regarded as an essential element because it is present in all life forms on Earth. In addition, it plays an important role in many biogeochemical processes as it is being exchanged between the biosphere, hydrosphere, atmosphere and lithosphere. In the atmosphere, carbon mainly exists in the form of carbon dioxide (CO_2) or of methane (CH_4). Both of them are considered greenhouse gases because of their capability to absorb and retain heat in the atmosphere. CO_2 is more abundant in the atmosphere and has a longer lifetime than methane. Methane, however, is 28 times more efficient in trapping heat than CO_2 over 100 years (Myhre et al., 2013) and therefore its greenhouse effect and its influence on climate is considerable. The main sink of atmospheric CH_4 is through its reaction with the hydroxyl radical (OH) in the troposphere generated by the photodissociation of ozone, followed by the reaction with water vapor (Myhre et al., 2013). Additional sinks such as bacterial uptake in soils and halogen chemistry in the troposphere also contribute to the CH_4 loss but on a minor scale (Myhre et al., 2013). The average residence time of CH_4 in the atmosphere with respect to OH is about one decade (Prather et al., 2012). Evidence of correlation between changes in atmospheric concentrations of methane and atmospheric temperature has been well studied from ice cores extending ca. 800.000 years into the past (Fig. 1.2; e.g. Loulergue et al., 2008). Atmospheric methane concentration has more than doubled since pre-industrial times due to anthropogenic emissions. Reconstructions between 1850 and the 1970s using air trapped in polar ice cores and firn have revealed an increase in atmospheric concentrations from 830 ppbv to 1500 ppbv (Buizert et al., 2012). Nisbet (2002) estimated the long-term variability in atmospheric methane concentration from the late glacial (0.35 ppmv = ∼800 Tg), over the early Holocene (0.65-0.8 ppm*v* = ∼1500 Tg) to 2002 (1.75 ppm*v* = ∼4000 Tg). Nowadays the globally averaged methane concentration is over 1.8 ppmv (Figs 1.1 and 1.3; Nisbet et al., 2014). Today, global CH_4 atmospheric concentrations are well known and measurements are carried out using discrete and continuous air analyses at the surface of the troposphere (Blake et al., 1982; Cunnold et al., 2002; Brenninkmeijer et al., 2007; Wecht, et al., 2012), as well as remotely sensed measurements of atmospheric CH_4 columns from the surface or from space (Crevoisier et al., 2009; Morino et al., 2011). In the past three decades the atmospheric methane concentration has increased but the rate of increase has slowed down in the 1990s (e.g. Dlugokencky et al., 2011), and from 1999 to 2006 the methane concentration was nearly constant. From 2007 onwards the methane concentrations have started to rise again (Fig. 1.3, Nisbet et al. 2014). Montzka et al. (2011) have suggested that the renewed atmospheric CH_4 increase observed during 2007 and 2008 is the consequence of enhanced natural wetland emissions, as a result of high temperatures in the Arctic and higher than average precipitation in the tropics associated with a persistent La Niña (Dlugokencky et al., 2009). Causes of the continued rise of atmospheric CH_4 from 2009 and 2010 could be also related to the strong La Niña that started in early 2010. It is clear that although most sources and sinks of methane have been identified, their relative contributions to atmospheric methane budget are still highly uncertain (Kirschke et al., 2013). While this is still not known, also the anthropogenic influence in the global climate change remains uncertain.

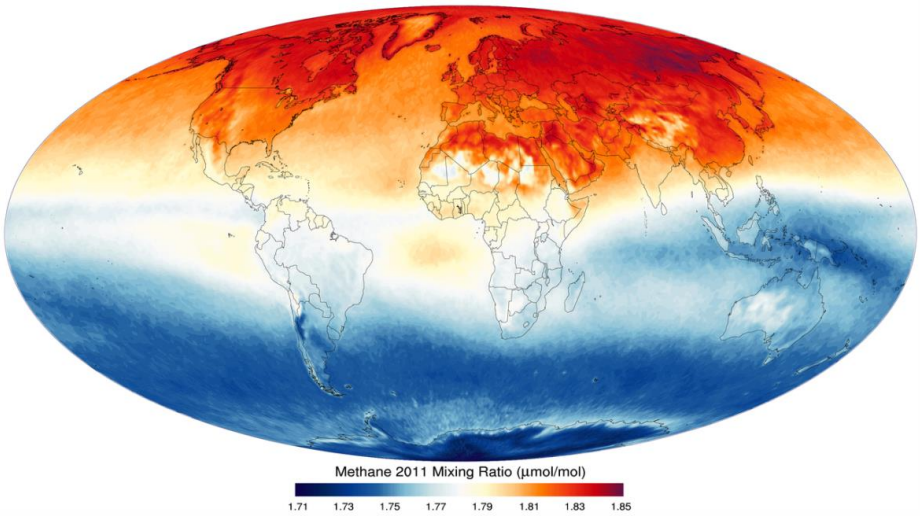

Figure 1.1. Annual mean upper troposphere (359 Hpa) CH_4 mixing ratio, 2011. Atmospheric Infrared Sounder (AIRS). Data source: http://daac.gsfc.nasa.gov/giovanni/.

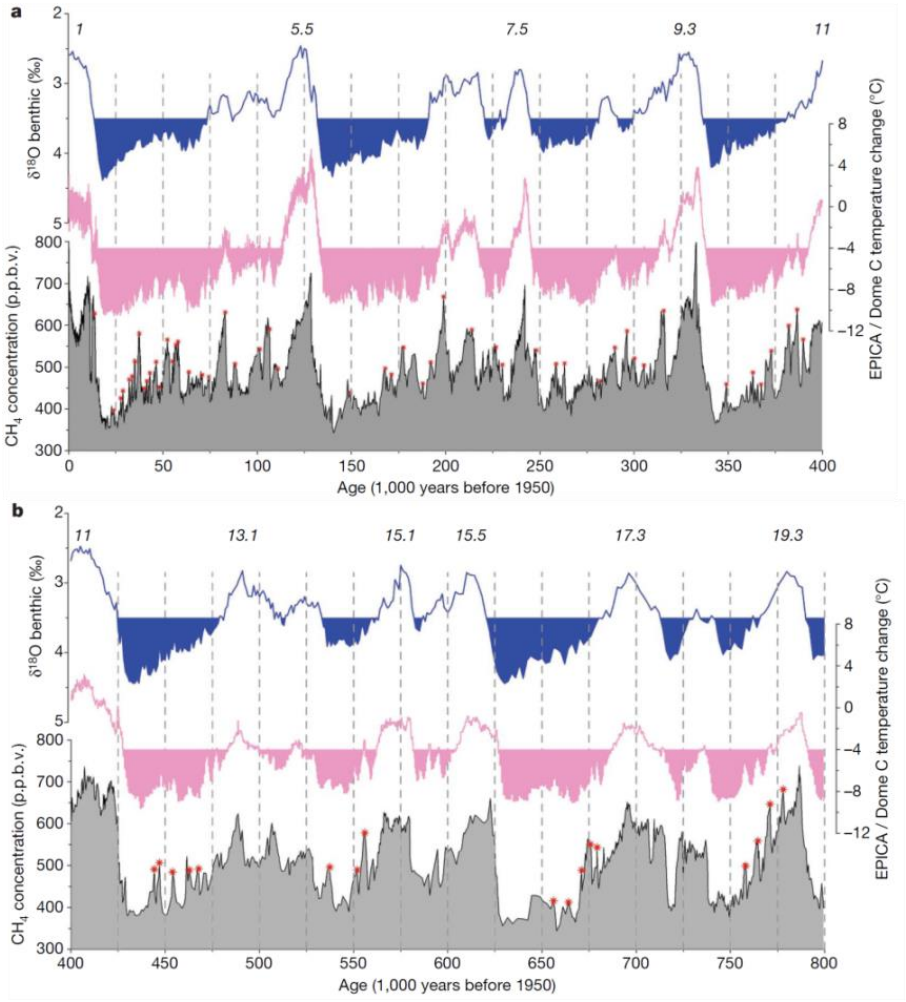

Figure 1.2. Atmospheric temperature and methane concentration (Loulergue et al., 2008)

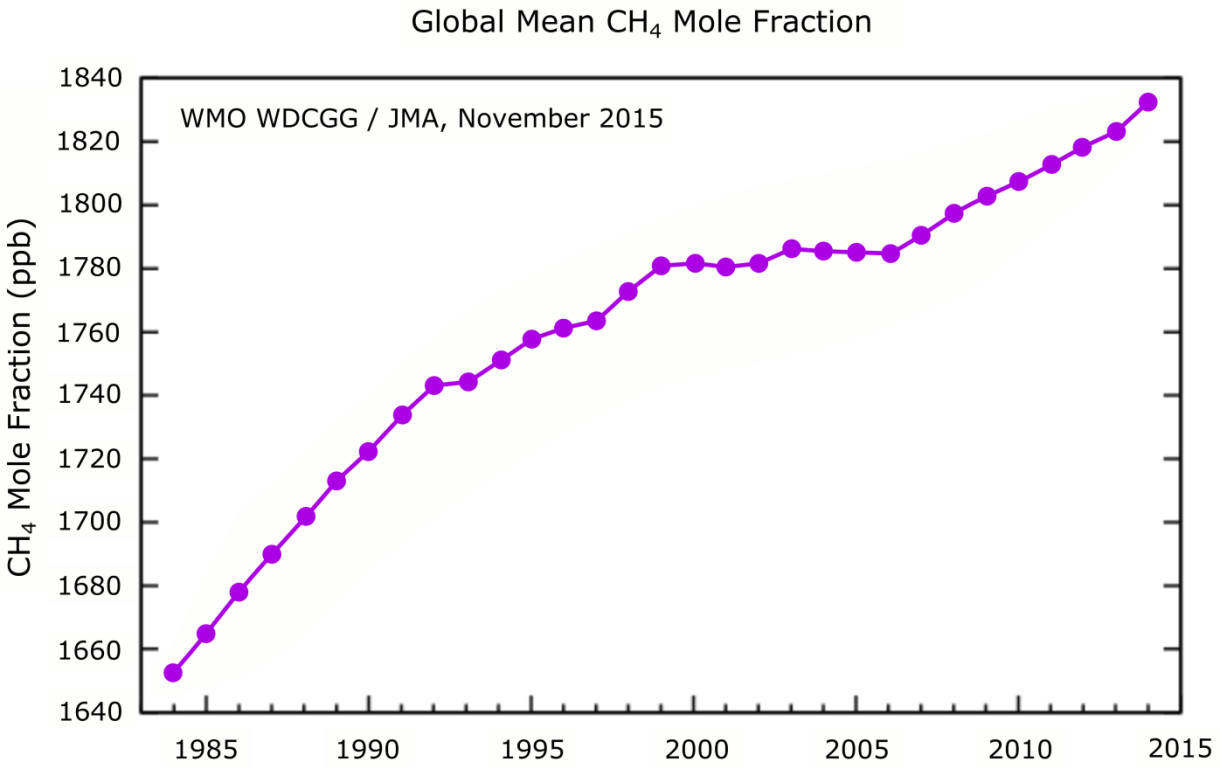

Figure 1.3. Global averaged atmospheric methane concentrations from 1984 to the present. Ref: WMO Greenhouse Gas Bulletin No. 11 (http://www.wmo.int/pages/prog/arep/gaw/ghg/GHGbulletin.html).

1.2. Atmospheric methane budget

Although the individual contribution of sources and sinks is not precise, uncertainties of total global sources and sinks of CH_4 are well constrained (Prather et al., 2012; Denman et al., 2007). Several assessments have been made in order to know the total annual input of CH_4 in the atmosphere. According to the IPCC 2013 report (Myhre et al., 2013) bottom-up estimates of present CH_4 emissions during the decade of the 2000s range from 542 to 852 $TgCH_4\ yr^{-1}$, while top-down estimates range from 526 to 569 Tg $CH_4\ yr^{-1}$ (Table 1.1). During this decade, anthropogenic sources of CH_4 account for 50% to 60% of the decadal mean global emissions (Table 1.1; Ciais et al., 2013). Evaluations of the atmospheric methane budget show imbalances among the global sources and the global sinks of CH_4. For instance, the IPCC 2013 report (Ciais et al., 2013) show an imbalance of 14 Tg $CH_4\ yr^{-1}$ (sources: 556 Tg $CH_4\ yr^{-1}$, sinks: 542 Tg $CH_4\ yr^{-1}$) for the CH_4 atmospheric global budget of 2011 (Table 1.2), which is added to the atmosphere each year. The causes of the residual atmospheric CH_4 can be evaluated only in case there is a correct individual assessment of the sources and sinks involved in the atmospheric methane budget.

1.2.1 Sources

A classification of the different sources of methane, from the perspective of human influence on climate change, can be done (Table. 1.1; Ciais et al., 2013):

- ***Natural sources:*** Contribution to the atmospheric methane from wetlands, termites, oceans and fresh water (anaerobic methanogenesis in the sediments and aerobic production in the water column), wild ruminants, terrestrial and submarine permafrost thawing, natural forest fires and gas hydrate dissociation.

- ***Anthropogenic sources:*** Contribution to the atmospheric methane coming from domesticated ruminants, rice agriculture, energy use, landfill and waste treatment, and biomass burning. Human emissions of CH_4 are mainly generated by the use of fossil fuels (e.g. coal mining, petroleum, natural gas) or from biogenic origin (e.g. enteric fermentation in animals).

Table 1.1. Top-Down and Bottom-Up estimates of the atmospheric methane budget for the last decade (2000-2009) (IPCC report 2013; Ciais et al., 2013)

$Tg(CH_4)\ yr^{-1}$	Top-Down	Bottom-Up
Natural Sources	**218 [179–273]**	**347 [238–484]**
Natural wetlands	**175 [142– 208]**	**217 [177–284]**
Other sources	**43 [37–65]**	**130 [61–200]**
Freshwater (lakes and rivers)		40 [8–73]
Wild animals		15 [15–15]
Wildfires		3 [1–5]
Termites		11 [2–22]
Geological (incl. oceans)		54 [33–75]
Hydrates		6 [2–9]
Permafrost (excl. lakes and wetlands)		1 [0–1]
Anthropogenic Sources	**335 [273–409]**	**331 [304–368]**
Agriculture and waste	**209 [180– 241]**	**200 [187–224]**
Rice		36 [33–40]
Ruminants		89 [87–94]
Landfills and waste		75 [67–90]
Biomass burning (incl. biofuels)	**30 [24–45]**	**35 [32–39]**
Fossil fuels	**96 [77– 123]**	**96 [85–105]**
Sinks		
Total chemical loss	**518 [510– 538]**	**604 [483–738]**
Tropospheric OH		528 [454–617]
Stratospheric OH		51 [16–84]
Tropospheric Cl		25 [13–37]
Soils	**32 [26–42]**	**28 [9–47]**
Global		
Sum of sources	**553 [526–569]**	**678 [542–852]**
Sum of sinks	**550 [514–560]**	**632 [592–785]**
Imbalance (sources minus sinks)	**3 [–4–19]**	
Atmospheric growth rate	**6**	

Table 1.2. Top-Down estimate of the atmospheric methane budget for year 2011 IPCC report 2013; Ciais et al., 2013)

Global top-down	
Burden (Tg CH_4)	4954±10
Atmospheric loss (Tg CH_4 yr^{-1})	542±56
Atmos. increase (Tg CH_4 yr^{-1})	14±3
Total source (Tg CH_4 yr^{-1})	556±56
Anthropogenic source (Tg CH_4 yr^{-1})	354±45
Natural source (Tg CH_4 yr^{-1})	202±35

A second classification of the sources of atmospheric CH_4 can be made according to their source origin. Methane in nature can be generated through different processes. Methane can be generated from organic matter (i.e. biogenic methane) or by processes that do not involve the presence of organic matter (i.e. abiogenic methane). Biogenic sources can be further sub-divided in microbial, thermogenic and pyrogenic (Schoell 1988). Nowadays, the origin of atmospheric samples methane can be traced back to the source process based on the isotopic signature (e.g. Dawson and Siegwolf, 2011). A brief description of each source is given below.

Abiogenic sources

Abiogenic (or abiotic) methane is formed by chemical reactions which do not directly involve organic matter and is produced in much smaller amounts on a global scale (Etiope and Sherwood Lollar, 2013). Abiogenic methane can be produced by either high-temperature magmatic processes in volcanic and geothermal areas, or via low-temperature (<100°C) gas-water-rock reactions in continental settings, even at shallow depths (Etiope and Sherwood Lollar, 2013). In present-day Earth, there are three main sources of abiotic methane: water-rock interactions at mid-ocean ridges, volcanic activity and geothermal systems (Emmanuel and Ague, 2007).

MIcrobial sources (biogenic)

Microbial CH_4 is generated by methanogenesis, a process carried out by microorganisms belonging to the group (or domain) of Archaea. These CH_4 sources span anaerobic environments, such as natural wetlands and rice paddies, digestive systems of ruminants and termites, oxygen-poor water reservoirs, and organic waste deposits (e.g. Kirschke et al. 2013) and aerobic environments such as terrestrial plants, soils, marine algae and animals (e.g. Keppler et al., 2009). Most of the sources in the global CH_4 budget are the result of active biological processes (Kvenvolden and Rogers, 2005).

Thermogenic or geological sources (biogenic)

CH_4 generated from fossil fuel formed over thousands of years through geological processes. Methane is expelled from the subsurface into the atmosphere through natural geological processes (e.g. natural seepage in terrestrial and marine environments, mud volcanism) and through the exploitation of coal, oil and natural gas. Estimates of the atmospheric methane budget just recently considered the contribution of geological methane sources, considering seeps as the possible major contributors. According to Etiope et al. (2008) these sources are estimated to be as large as 30 to 80 Tg CH_4 yr^{-1} (Table 1.3). A summary of the estimates of geological methane sources, as proposed by different scientific groups is shown in Table 1.3 (Etiope et al., 2008)

Pyrogenic sources or biomass burning (biogenic)

CH_4 is produced by the incomplete combustion of organic (non-fossil) matter (e.g. wildfires and combustion of agricultural waste and biofuels). A recent estimate considers that pyrogenic sources of methane contribute in between 4% to 6% to the total atmospheric methane budget (Neef et al., 2010)

Table 1.3. Global Emissions of Methane From Geologic Source Categories (Etiope et al., 2008)

	Emission, Tg yr^{-1}	References
Mud volcanoes	5–10	Etiope and Klusman (2002)
	10.3–12.6	Dimitrov (2002)
	6	Milkov et al. (2003)
	6–9	Etiope and Milkov (2004)
Other macro-seeps	3–4	Etiope et al. (2008)
Marine seepage	18–48	Hornafius et al. (1999)
	10–30 (20)	Kvenvolden et al. (2001)
Microseepage	>7	Klusman et al. (1998)
	10–25	Etiope and Klusman (2010)
Geothermal/volcanic areas	1.7–9.4	Lacroix (1993)
	2.5–6.3[a]	Etiope and Klusman (2002)
	<1[b]	Etiope et al. (2008)
Total[c]	30–70	Etiope and Klusman (2002)
	13–36[d]	Judd (2004)
	35–45[e]	Etiope and Milkov (2004)
	45[e]	Kvenvolden and Rogers (2005)
	40–60	Etiope et al. (2004); Etiope and Klusman (2010)
	42–64	Etiope et al. (2008)– best estimate
	30–80	Etiope et al. (2008) – extended range

(a) Volcanoes not considered; (b) Only volcanoes; (c) Gas hydrates not considered; (d) Microseepage not considered.; (e) Included former microseepage estimate.

1.2.2. Sinks

The main sink for the atmospheric methane (90 % of the global CH_4 sink) is the oxidation with hydroxyl radicals in the troposphere (Kirschke et al. 2013). Additional oxidation sinks are methanotrophic bacteria in aerated soils (~4 %, Simpson et al., 2012; Thoning et al., 1989), reactions with chlorine radicals and atomic oxygen in the stratosphere (~3 %, Crevoisier et al., 2009) and reactions with chlorine radicals from sea salt in the marine boundary layer (~3 %, Montzka et al., 2011). However, it is necessary to highlight that microbial oxidation processes on Earth play an important role in removing CH_4 before it reaches the atmosphere. The reduction of CH_4 carried out by methanotrophs located in aerobic and aerobic environments is considered to be more than the 50 % of the generated CH_4 before it reaches the atmosphere (Reeburgh, 2007). An example of that is the ocean, which has the potential to produce largest quantities of CH_4 but at the same time has effective oxidation processes (aerobic and anaerobic) in sediments and the water column that results in the ocean being one of the net global CH_4 budget's smallest terms (Reeburgh, 2007). In the same way, microbial oxidation has also an important effect on CH_4 emissions from wetlands, rice production, landfills, and underwater leaks from methane distribution systems, such as pipelines (Reeburgh, 2007; Kvenvolden and Rogers, 2005).

1.3. Arctic methane sources from the sediment to the water column

The Arctic has a large potential to influence climate dynamics because it represents a large reservoir of methane stored in natural gas deposits, permafrost, and submarine gas hydrates (e.g. Walter Anthony et al., 2012; O'Connor et al., 2010; Sergienko et al., 2012; Shakhova et al., 2014). Methane stored in Arctic and sub-Arctic marine sediments has been estimated to be 30-9000 Gt CH_4 stored in methane hydrates and 2–1400 Gt CH_4 trapped beneath submerged permafrost either as hydrate, or as free gas (bubbles) (James et al., 2016). Moreover, methane emissions could easily increase with the rising of global temperatures because these reservoirs are highly vulnerable to temperature changes. Evidence shows that Arctic sea-ice coverage has decreased in recent decades (Maslanik et al. 2007) reaching a record low in ice extent in September 2012 (James et al., 2016). Furthermore, the Arctic has been prognosticated to be seasonally ice-free by 2050 (Stroeve et al. 2008; Wang and Overland 2009). As it has been hypothesized, this warming trend could cause the release of important amounts of CH_4 coming from submarine reservoirs (clathrate gun theory, e.g. Maslin et al., 2004). In order to understand how influential Arctic warming over submarine reservoirs of methane could be, it is necessary to identify the different CH_4 sources in marine sediments together with the mechanisms that control their possible release. The aim of this section is to provide a brief description of the main methane sources from the sediment to the water column in the Arctic.

1.3.1. Microbial methane production

Microbial or biogenic methane is the methane derived by anaerobic, microbial degradation of organic matter within the sediment (Fleischer et al., 2011). Biogenic methane predominates within shallow subbottom deposits (Fleischer et al., 2011). Usually the biogenic methane production occurs in the top few meters of the sediment, however, evidence of bacterial activity hundreds of meters down in the sediment has also been found (e.g. Parkes et al., 1990). Biogenic gases are produced at temperatures comparable with their formational environments (< 50 °C; Stolper et al., 2014). Assuming an 'average' geothermal gradient of about 30 °C per kilometer, methanogenesis could continue to a depth of about 2 km (Judd, 2004). Only some species of microorganisms are able to produce methane. They all belong to an ancient group called archaea. Methanogenic archaea are present in soils such as marshland, paddy fields, fresh water and marine muds, as well as the intestines of animals (Zeikus, 1977). Biogenic methane can be produced in the sedimentary column and migrate as free gas through permeable sediments often following lateral extensions of strata boundaries or vertical extension of faults (Rajan et al., 2012a). In the Arctic, microbial production of methane has been evidenced by several authors (e.g. Solheim and Larsson, 1987; Solheim and Elverhoi, 1985; Vogt et al., 1997; Knies et al., 2004; Sahling et al., 2014).

1.3.2. Thermogenic gas production

Thermogenic gas is produced from the breakdown of organic molecules at high temperatures and pressure, and therefore it is produced at depths greater than 1000 m (Floodgate and Judd, 1992). The formation of methane and other thermogenic gases is kinetically controlled by time, temperature, and organic matter composition (Seewald 2003). Thermogenic gas is generated from thermal cracking of both residual kerogen or/and oil (Tissot and Welte, 1984; Rooney et al., 1995). Methane and other

petroleum species may migrate towards the surface or be trapped in reservoirs (such as shallow gas accumulations or in form of gas hydrates). Thermogenic gases have formation temperatures ranging between 157 and 221 °C (Stolper et al., 2014). Most thermogenic hydrocarbons are formed in fine-grained sedimentary rocks (mudstones, claystones, shales and certain limestones, e.g. algal limestones). In the Arctic, methane release coming from thermogenic sources has been reported by several authors (Knies et al., 2004; Shakhova et al., 2010; Walter Anthony et al., 2012; Smith et al., 2014).

1.3.3 Abiotic methane production

Abiotic methane has been recently recognized as an additional sub-seafloor gas source generated in slow to ultraslow spreading mid-ocean ridge environments (Proskurowski et al., 2008; Cannat et al., 2010). The formation of abiotic methane is the result of the interaction between the crust, mantle, and oceans causing the serpentinization of ultramafic rocks (Kelley et al., 2005; Vance et al., 2007; Proskurowski et al., 2008). Serpertinization, that is the hydration of olivine and/or pyroxene, produces H_2 which may react with C-gases (CO_2 or CO) to finally form CH_4 (Etiope and Sherwood, 2013). Studies have demonstrated that the abiotic synthesis of hydrogen and hydrocarbons may occur in deep-sea environments in the presence of ultramafic rocks, water, and moderate amounts of heat by Fischer-Tropsch-type reactions (Proskurowski et al., 2008). In the Arctic at the ultraslow spreading Knipovich Ridge offshore NW Svalbard, seismic evidence indicates the possibility of gas delivery for gas hydrates from an abiotic, serpentinized mantle source of methane. Rajan et al. (2012b) e.g. have shown evidence of bottom simulating reflectors (BSRs) that indicate the base of the gas hydrate stability zone (GHSZ), identified in seismic sections above interpreted serpentinized ultramafic diapirs on the sediment-covered eastern flank of Knipovich Ridge. Johnson et al. (2015) based on seismic evidence, describes the buildup of a 2 Myr gas hydrate and free gas–charged drift system that may be fed and maintained by an abiotic methane source at the Molloy Transform Fault located between the Knipovich and the Molloy ridges offshore Svalbard. Their study suggests that future scientific ocean drilling and isotopic characterization of the recovered gases is necessary to proof the existence of abiotic sources of gas stored in deep-water reservoirs.

1.3.4. Dissociation of methane hydrates

Methane (biogenic or thermogenic) can be stored in sediments as gas hydrates and remain stable at high pressures and low temperatures (Kvenvolden, 1993). A gas hydrate is a class of clathrate formed by an arrangement of complex cage-like structures of water molecules with gas molecules trapped within. Methane hydrates are the most common natural hydrates on Earth. Some researchers postulate that the amount of carbon stored in methane hydrates is larger than that stored in all other fossil fuels combined (Henriet and Mienert, 1998; Sloan and Koh, 2007). A theoretical GHSZ can be defined by assuming CH_4 concentration, temperature and pressure (Fig. 1.6).

It has been postulated that methane hydrates can be implicated in climate change (e.g., Dickens et al., 1995; Kennett et al., 2000) and hence they are considered to play an important role in the present/future climate dynamics. The stability of the hydrate reservoirs is determined by temperature and pressure, and changes in ambient temperature and pressure conditions, e.g. due to changes in climate, may lead to dissociation of the hydrates, release of methane and an enhanced CH_4 flux to the atmosphere. There is evidence that methane hydrate reservoirs may have destabilized in the geological

past. Kennett et al. (2000) found anomalies in the carbon isotopic signature of benthic and planktic foraminifera in sediment cores that sampled the Late Pleistocene deposits in Santa Barbara Basin. These anomalies were interpreted as resulting from the release of large amounts of CH_4 from marine sediments caused by thermal dissociation of CH_4 hydrates. Alternatively, methane hydrate dissociation has also been attributed to sea level falls (Maslin et al., 2004). On the other hand, the evidence from the isotopic signature (e.g. hydrogen) recorded in ice cores suggest that methane emission triggered by hydrate dissociation was not the cause of the rise in atmospheric methane concentration (e.g. Bock et al., 2010; Fischer et al., 2008).

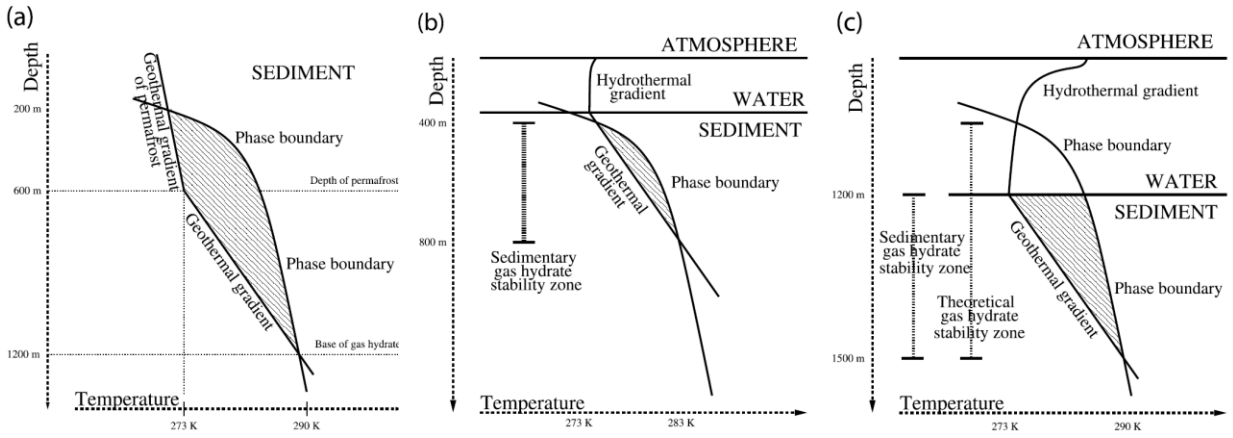

Figure 1.4. Illustration of the GHSZ related to (a) terrestrial permafrost, (b) shallow offshore regions, and (c) deep ocean (O'Connor et al., 2010)

The scientific community is concerned that the ongoing global warming could in the future lead to global hydrate instability, which would give a positive feedback in the warming process because of an enhanced CH_4 flux to the atmosphere (Kennett et al., 2003). Arctic regions are expected to be influenced more severely than the rest of the globe. Buffet and Archer (2004) estimate a reduction of approximately 15 % of the present-day hydrate reservoir if ocean temperatures would warm by 3 °C. Lamarque (2008) estimated the amount of methane that would be released by destabilizing hydrates in function of the increase in atmospheric greenhouse gases. He used the IPCC's 4th assessment report 1%-CO_2 increase per year to estimate the potential destabilization of CH_4 hydrates. His estimation gave a flux of 560-2140 Tg CH_4 yr^{-1} into the ocean with a flux of 5-21 Tg CH_4 yr^{-1} reaching the atmosphere.

1.3.5. Subsea permafrost thawing

Permafrost is a permanently frozen soil, rock or sediment below the freezing point of water 0 °C for two or more years. Permafrost can extend to a depth of 50 m in the "discontinuous" zone and may be 350–650 m thick in the "continuous" zone (Schuur et al., 2008). Here, the continuous and discontinuous zones represent the permafrost with a lateral continuity and a lateral discontinuity beneath the exposed land surface throughout a geographic region, respectively (NRCC, 1988). The lower limit of the permafrost is defined by the Earth's geothermal gradient, which causes a temperature increase with depth (Fig. 1.7).

A big concern lies in the possible degradation and thawing of this permafrost due to climate change within the coming decades. Permafrost thawing could result in the release of large amounts of carbon into the atmosphere (Goulden et al., 1998) and recent observations have demonstrated that this process has started to take place (Jorgenson et al., 2006). Permafrost can be formed in terrestrial and submarine environments. Here are discussed only the submarine permafrost formations and the methane release associated to their thawing. Subsea permafrost is created either in response to the negative mean annual seabed temperature or as the result of sea level rise, when terrestrial permafrost becomes covered by seawater. It is believed that there are large areas of subsea permafrost underlying the Arctic shelves down to a water depth of about 100 m (Rachold et al., 2007).

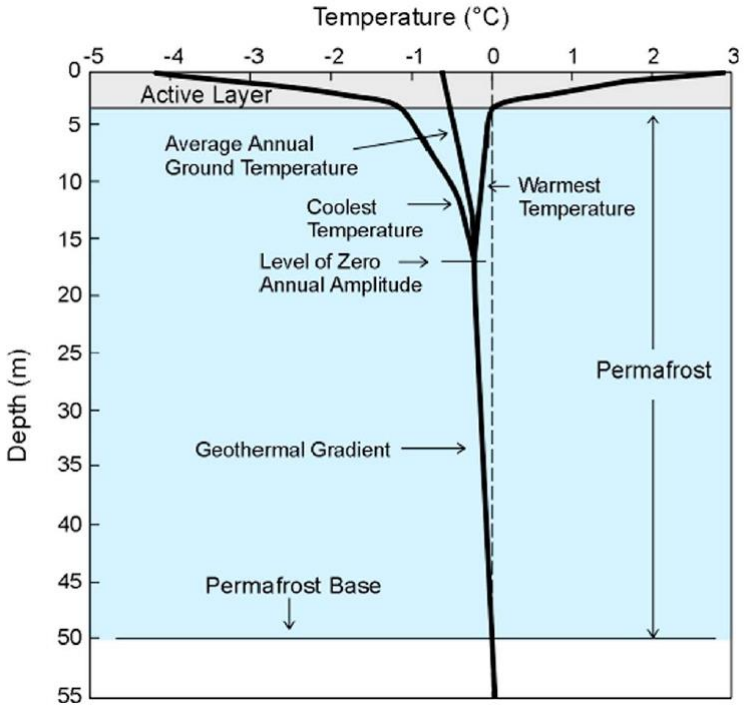

Figure 1.5. Temperatures experienced at different depths in the ground during the year. The active layer above thaws in summer and freezes in winter, while the permafrost layer below remains below 0 °C (O'Connor et al., 2010)

Subsea permafrost thawing can release methane to the water column in three different ways (Thornton and Crill, 2015): (a) freeze-locked organic carbon can become available for microbial degradation leading to biogenic methane production; (b) submarine permafrost may act as a cap on the upward diffusion of biogenic and/or thermogenic gas and permafrost degradation could facilitate the migration of this gas; (c) methane may be stored into the permafrost as gas hydrates and hydrate dissociation could happen when permafrost is thawing. It is known that subsea permafrost warming started in the early Holocene when this shelf was inundated by sea water (Soloviev et al., 1998; Romanovskii et al. 2005). Evidence of significant quantities of CH_4 escaping from the East Siberian Shelf (Fig. 1.8) as a result of the degradation of submarine permafrost has been found by Shakhova et al. (2014). As is explained in this study, degraded permafrost leads to the formation of migration pathways for seabed gaseous CH_4 and

increases the bubble-induced fluxes in annual atmospheric emissions. Hydroacoustic data have shown that acoustic flares extend upward from the seafloor, at water depths of < 50 m, to near to the sea surface. Shakhova et al. (2014) found that storms enhance the sea–air CH_4 flux, suggesting that such events accelerate the ventilation process of CH_4 bubbles released at the seafloor and dissolved in the water column producing high emission rates to the atmosphere. Based on their observations and measurements, Shakhova et al. (2014) calculated that 17 Tg CH_4 yr^{-1} are released into the atmosphere over the East Siberian Shelf.

1.4. Seabed surface anomalies associated to gas venting

Migration of CH_4 and other fluids through the sediments towards the seabed is mainly driven by the buoyancy of fluids, the overpressure generated at depth, and compaction-driven upward flow of pore fluids. When fluids are released at the seabed into the water column, the expulsion process can generate different features at the seafloor. At the same time the consumption of methane utilized by microorganisms at the seafloor can leave some evidence of methane release. The present section describes some of the seafloor anomalies historically associated to gas seepage in the water sediment-interface.

1.4.1. Seepages

Submarine gas seeps are sources located on the seabed where gas, coming from sub-bottom reservoirs, is released. Gas seepage may occur with or without the formation of pockmarks (Judd and Hovland, 2009). The submarine bubble release can be associated with shallow gas in the sediments or with underlying gas hydrate deposits. Gas/fluid migration towards the seabed can take place along several types of pathways, such as faults and so-called 'chimneys', and also along stratigraphically controlled pathways. Estimates of the total global methane contribution to the atmosphere from oceans are still poorly constrained, but 20 Tg CH_4 yr^{-1} can be considered as the first realistic approximation (Judd, 2004). In Arctic regions, bubble release has been attributed to GHSZ displacement and submarine permafrost degradation, both caused by the rise in water temperature produced by the climate change (e.g. Westbrook et al. 2009, Shakhova et al., 2014).

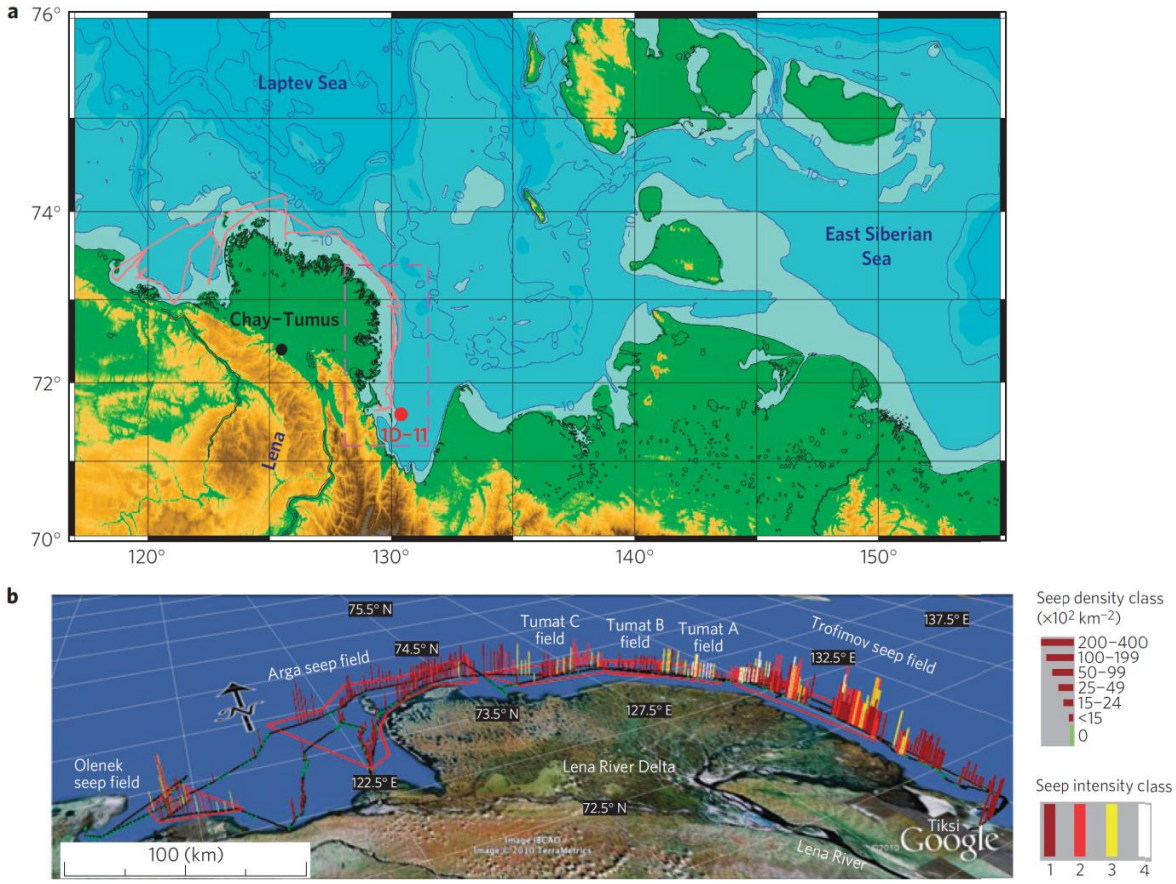

Figure 1.6. a) Bathymetric map of the East Siberian Arctic Shelf (50 m bsl). The area studied by Shakhova et al. (2014) was located inside the dashed rectangle. The red line specifies the ship track of their multibeam survey referred also in b. b) Seepage intensity and spatial density distribution (specified in different colors and heights) in the study area.

1.4.2. Submarine domes and pockmarks

Past, actual and potential future release of gas and fluids can be associated to geomorphological expressions at the seafloor such as domes and pockmarks. A seabed dome is a deformation of the seabed surface in a shape of a dome associated to shallow gas accumulations in near-seabed sediments. Seabed domes are formed when gas displaces water in the pore spaces of the upper sediments, causing a local volume increase (Judd and Hovland, 1992). Gas domes usually appear as minor topographic highs with diameters ranging from 10 m to 1000 m (Koch et al. 2015, Judd and Hovland, 2009; Hovland and Judd, 1988). Gas accumulation can lead to overpressure build-up, doming, and eventually gas break-through, which might occur in dense clusters of individual gas bubble pathways (Haeckel et al., 2007). Seabed domes have been evidenced at different places around the world and have been interpreted as the result of focused fluid migration reaching the shallow sub-seafloor (Hasiotis et al., 1996; Lee and Chough, 2002). Methane seeps associated to submarine domes have been published by several researchers (e.g. Niemann et al., 2005; Naudts et al., 2006; Weber et al., 2014).

The next stage after doming formation is the pockmark, a crater in the sediment surface produced by escape of gas and interstitial water from muddy and unconsolidated sediment (Hovland and Judd, 1988; Judd and Hovland, 1992). The conceptual model of Judd and Hovland (2009) that describes the

pockmark formation can be summarized as following: Fluids pressure builds in a shallow porous layer below a sealing layer and later the excess pressure is relieved by the doming formation at the seabed. Fluids erupt due to overpressure in the sediments, fluidising the sediments. Finally, gas, water, and sediment are ejected into the water column. Part of the suspended sediment is transported away by currents.

Pockmarks size ranges from few meters to hundreds of meters in diameter and up to 30 m in relief (Kelley et al., 1994). Some examples in the Arctic are the seep-related pockmarks studied at the Vestnesa ridge (Fig. 1.9; Hustoft et al., 2009; Bunz et al. 2012; Smith et al, 2014). Presence of a non-active pockmarks field at Prins Karl Forland has been reported by Rajan et al. (2012a), who associated them to gas expulsion through older prograding glacigenic sequences or because they were fed from a yet unknown source area.

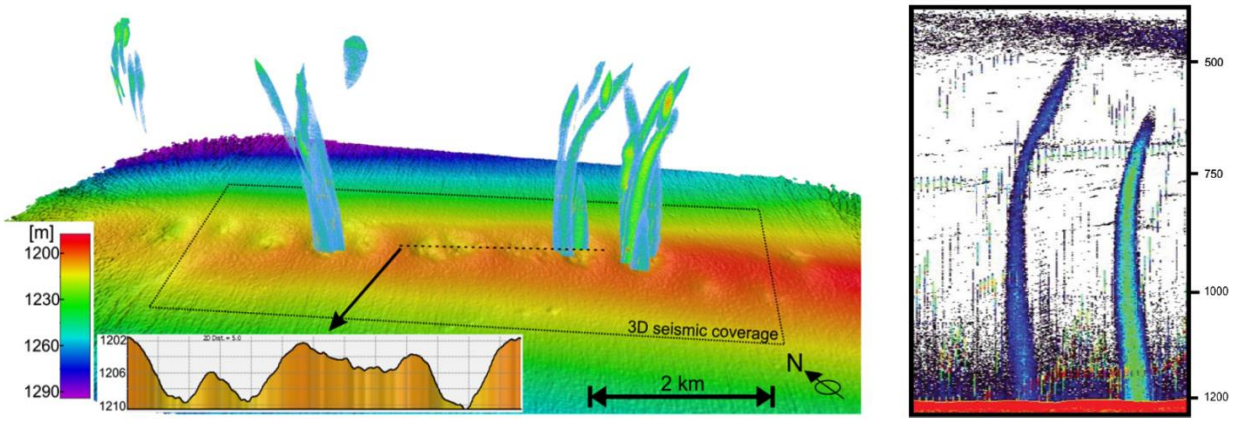

Figure 1.7. a) Bathymetry at the Vestnesa Ridge visualized together with acoustic gas flares. b) Echogram showing an example of the acoustic flares that have been continuously active during the survey in 2010 (Bunz et al., 2012).

1.4.3. Submarine Mud volcanoes

Although the formation of mud volcanoes comprises a process more complex than only the upward migration of gas to the seafloor, gas seepage has been associated to this geomorphological feature (e.g, Sauter et al., 2006; Barnard et al., 2015). A submarine mud volcano is defined as a topographically expressed surface edifice from which solid material (at least mud, but generally also breccia comprising clasts of solid rock in a mud matrix) and fluids (water, brine, gas, oil) flow or erupt at the sea floor (Judd and Hovland, 2009). The large number of submarine mud volcanoes is considered to contribute significantly to the oceanic methane pool (Milkov et al., 2003). A special case in the Arctic is the Håkon Mosby Mud Volcano (HMMV), a structure of approximately 1.5 km in diameter, located at 1250 m water depth on the Norwegian–Barents–Spitzbergen continental margin. Sauter et al. (2006) presented hydro-acoustic, visual, and geochemical evidence of the release of gas hydrate-coated methane bubbles and gas hydrate flakes that extend from 1250 m water depth (bottom) up to 750 m high into the water column (Fig. 1.10).

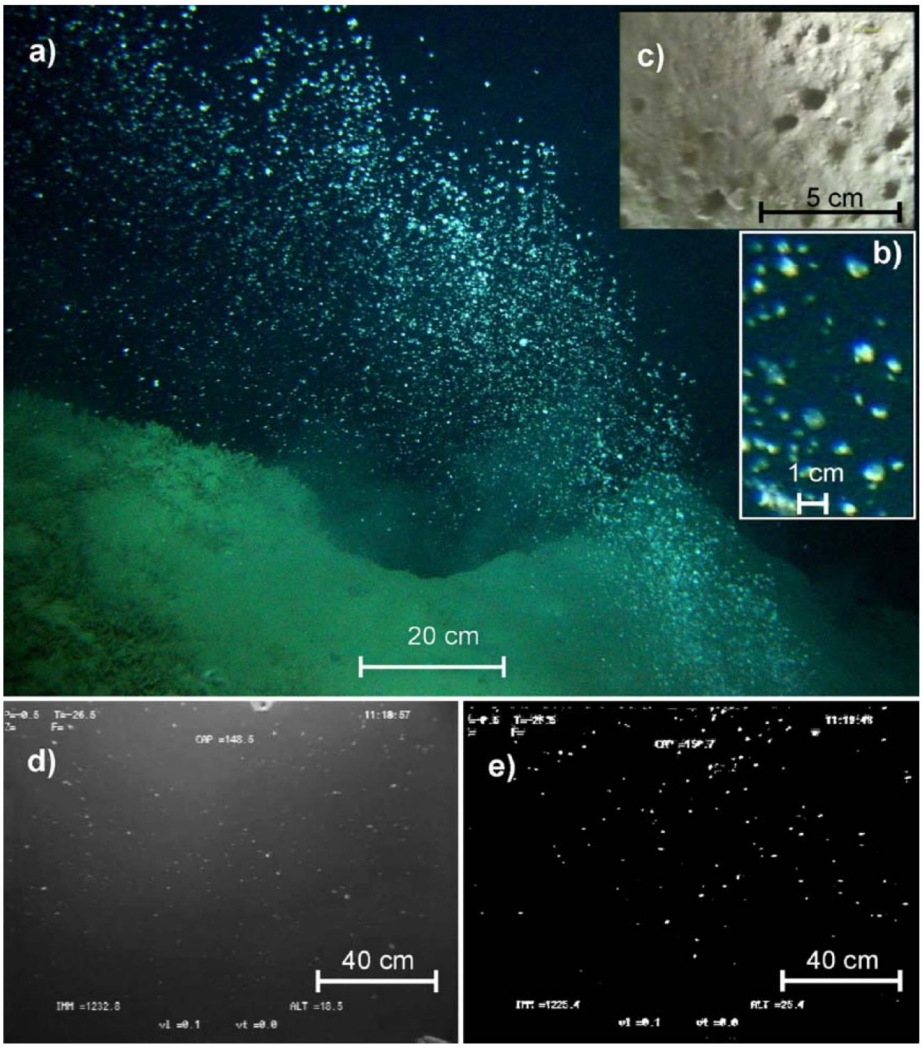

Figure 1.8. a) Picture of bubble release at the Håkon Mosby Mud Volcano b) Zoomed photograph showing released bubbles ~1 m above the seafloor. c) Video image of sediments perforated by bubble release. e) and d) Bubbles at 18.5 and 25.4 m above the seafloor (e) was thresholded to binary (Sauter et al 2006).

1.4.4. Methane-derived carbonates

The presence of methane near to the seafloor may be indicated by the presence of authigenic carbonates. These carbonates are the result of the anaerobic methane oxidation (AOM) coupled with sulfate reduction by consortia of methanotrophic archaea and sulphate-reducing bacteria (Greinert et al., 2001; Magalhães et al., 2012). As methane ascends is oxidized as CO_2 that is then mostly precipitated as authigenic carbonates, which form carbon crusts within the anoxic sediments and above the seafloor. The analysis of authigenic carbonates isotopic signature is valuable information to reveal e.g. the origin and age of carbon incorporated during carbonate precipitation and to evaluate the temperature and origin of fluids from which authigenic carbonates are precipitated (Naehr et al., 2000; Loyd et al., 2016).The occurrence of authigenic carbonates associated to methane release at the seafloor has been reported by many researchers at different regions around the world (e.g. Bohrmann et al., 1998; Sassen et al., 2004, Skarke et al., 2014; Berndt et al., 2014).

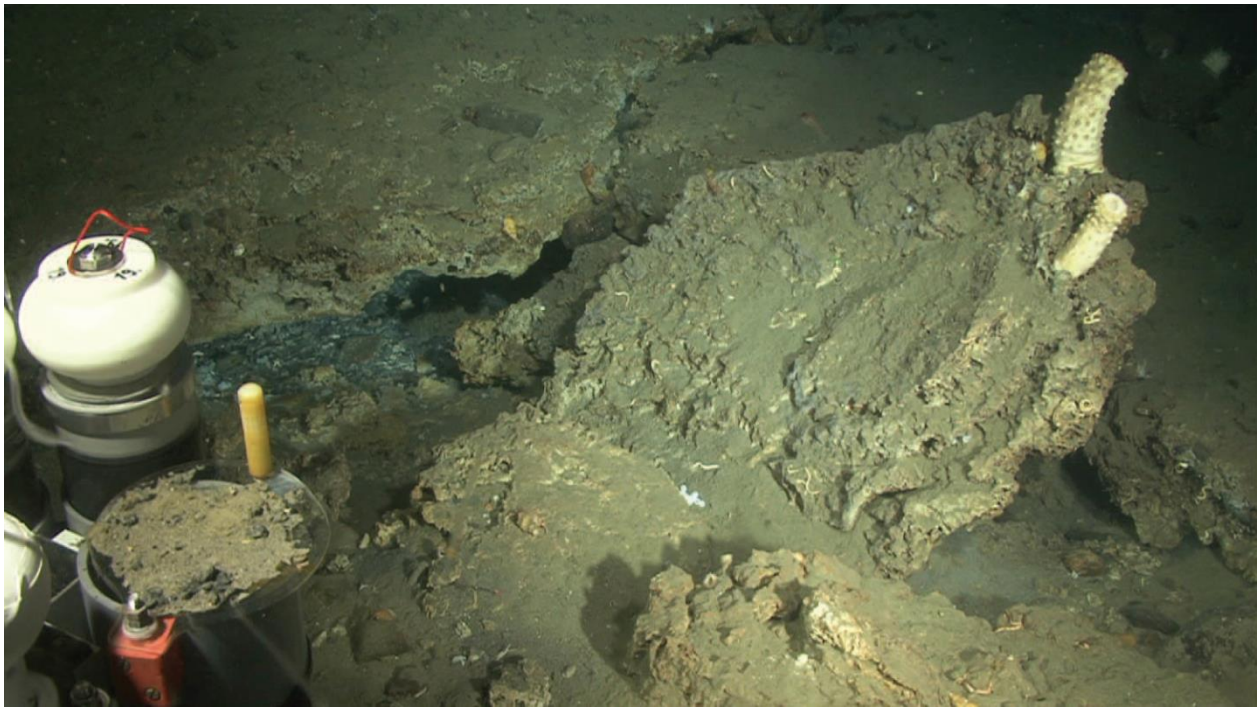

Figure 1.9. Photograph of authigenic carbonate crusts observed at Prins Karl Forland (HyBIS site, 385 m bsl, Berndt et al., 2014)

1.4.5. Biological activity associated to methane release

Seepage areas may be characterized by biological activity. Sulfide, methane and non-methane hydrocarbons are utilized by free-oxidizing bacterial mats and endosymbiotic thiotrophic and methanotrophic bacteria associated with tubeworms, clams and mussels (Gilhooly et al., 2007). Evidence of biological communities associated to methane release has been reported by several researchers (Fig. 1.12; e.g. Greinert et al., 2010; Niemann et al., 2005; Treude et al., 2007). When the rate of methane production and migration exceeds the rate of use, seepage occurs (Judd, 2004). Hovland (2002) has suggested that CH_4 utilization increased over time because pathways are progressively being blocked by bacterial mats and authigenic carbonates.

1.5. Fate of released CH_4 from the seabed

In order to evaluate if submarine sources of methane contribute significantly to the atmospheric methane budget, it is essential to understand the fate of methane released from the seabed. CH_4 solubility in seawater is considered to be low (~ 27 times less than CO_2), increasing with increasing pressure (0.0263, 0.0400 and 0.0514 mol/kg at c.a. 24, c.a. 37 and c.a. 51 atm respectively in seawater at 25 °C; Stoessell and Byrne, 1982). At shallow depths (low pressure), CH_4 dissolves in water, and if the CH_4 concentration exceeds the solubility, the excess CH_4 could become a bubble (O'Connor et al., 2010). On the other hand, at greater depth (high pressure) and inside the GHSZ excess of CH_4 could be stored in the hydrate phase. Analyses have been made to verify if methane is released at the seafloor in gas or hydrate phase. Zhang (2003) suggests that methane released as hydrate, may rises through the water column depending on how much sediment is attached to it. If the admixture of sediment is small, hydrate blocks/flakes would ascend through the water column (due to the lower density than the

seawater) undergoing dissolution and dissociation on their path towards the surface. Zhang and Xu (2003) suggested that hydrates larger than 100 mm in radius would be able to survive dissociation over a 530 m long ascend.

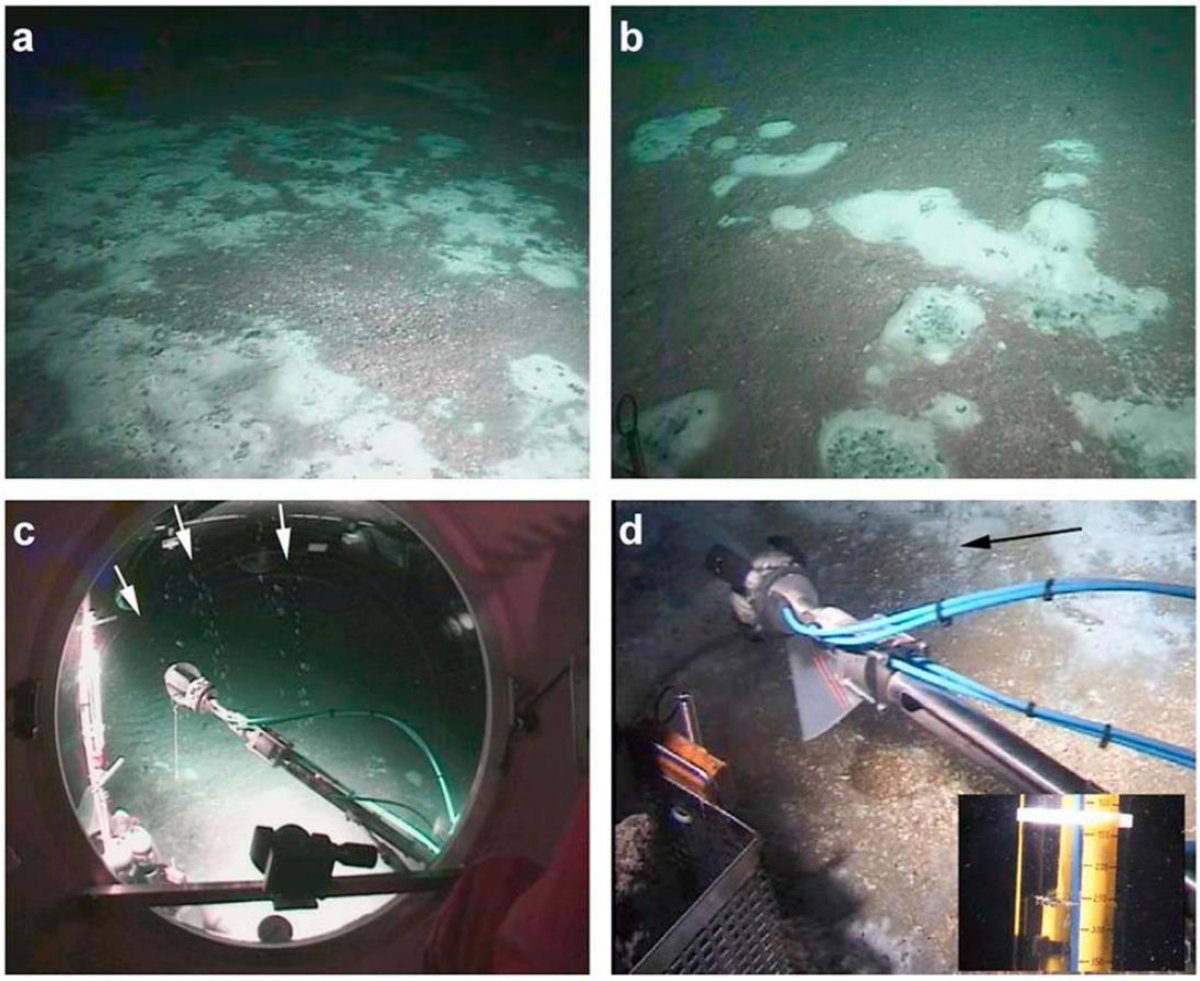

Figure 1.9. (a and b) Beggiatoa mats at the seafloor around seep sites. c) Bubble streams evidence a few tens of cm apart. (d) Inverted funnel technique over a bubble stream during flux measurements (Greinert et al., 2010).

If methane is released as free gas, bubbles will experience expansion, as the static pressure decreases, but also dissolution as the bubble ascends towards the surface. Zhang (2003) has calculated that the critical radius for a bubble that originally contained methane to survive a 50 m rise is 0.9 mm. Bubbles could transport methane directly to the surface. The amount of methane released at the sea surface will depend on the release depth, the initial amount of methane in the bubble, bubble size, dissolved gas concentrations in the surrounding liquid, temperature, surface-active substances, and bulk fluid motions (Leifer and Patro, 2002). Additionally, if a methane bubble is released into the GHSZ, a hydrate coating forms around the bubble decreasing its rate of dissolution and therefore the bubble can survive longer distances (Rehder et al., 2009). Hydrate skin formation at the bubble-water interface has been evidenced in lab experiments for water saturated with methane (Maini and Bishnoi, 1981) and proved in

situ to slow down methane bubble dissolution in the undersaturated open ocean (Rehder et al., 2002). Large acoustic flares have been visualized in places where the GHSZ is located within the water column (e.g. Bunz et al. 2012; Smith et al, 2014; Greinert et al., 2006; Sauter et al., 2006). The highly extended bubble life time has been attributed to the formation of a hydrate-coating[1] around the bubbles that decreases the mass transfer between the bubble and the surrounding water (approximately 10 times) as they rise through the GHSZ (Brewer et al., 2002; Rehder et al., 2002).

Another important observation, included in the model of McGinnis et al. (2006) for bubbles rising in the water column, is the amount of methane transported by the bubble towards the surface. McGinnis et al. (2006) indicate that even though bubbles that reach the surface could be larger than their initial size, they will contain less CH_4 than the initial amount due to partial pressure differences. Concentration differences between the methane in the bubble (gas) and in the sea water (dissolved) causes CH_4 to "outflow" the bubble, while dissolved atmospheric gases (O_2 and N_2) "inflow" the bubble (Leifer and Patro, 2002). McGinnis et al. (2006) conclude that a significant contribution to the atmospheric methane is only possible, if free gas is released at shallow water depths.

An increase in the rise velocity of bubbles can be caused if large numbers of bubbles create a plume in which upwelling water and gas bubbles rise together. Zhang (2003) has noted that a larger amount of bubbles would rise faster because bubbly water has a lower density than the surrounding seawater, which causes a rapid buoyant rise effect in the bubble cloud. This process considerably enhances the fraction of CH_4 emitted at the seafloor to reach the ocean surface.

In the same way that methane is reduced in the sediment due to microbial anaerobic oxidation (more than 50% of the production), it can also be consumed by microbial aerobic oxidation in the water column. Scranton and Brewer (1978) show a rapid decrease of CH_4 concentrations with depth in the North Atlantic and North Pacific. They observed that CH_4 consumption is very rapid in "young water" (shallow water depth) but in older water, e.g. 100 years after water mass formation (water mass isolated from the surface), this consumption almost cease. Mau et al. (2007) suggest that most of the dissolved methane seems to be transported and oxidized below the sea surface.

1.6. Study Area

1.6.1. Gas seepage offshore Prins Karl Forland

Hydroacoustic data presented in this thesis have been collected offshore Prins Karl Forland (PKF; ~ 78 ° N) along the western continental margin of Svalbard, in an area prone to hydrocarbon seepage. The acoustically detected flares can be grouped into three main sub-areas according to their water depth (Fig.1.10): Area 1 (shelf break, ~200 m bsl); Area 2 (upper slope, 300-400 m bsl) and Area 3 (shelf, ~90 m bsl).

[1] The growth of hydrate on the gas-water interface requires the initial formation of a hydrate nucleus, and growth of hydrate after the nucleation site has formed (Rehder et al., 2002)

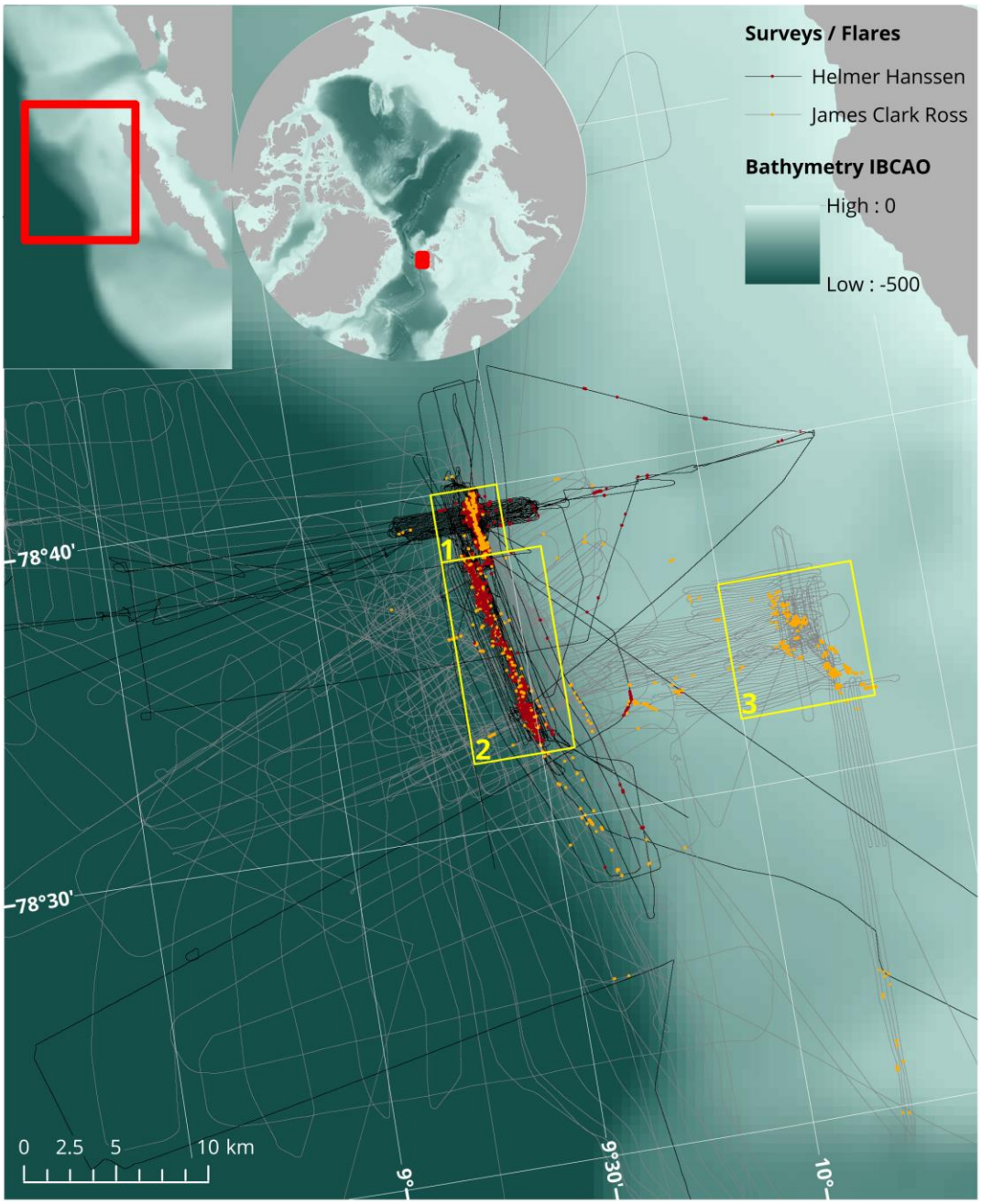

Figure 1.10. Study area located at **PKF**. The figure illustrates the flare positions found from EK60 echosounder data acquired on board R/V James Clark (orange dots) Ross and R/V Helmer Hanssen (red dots) during the 11 hydroacoustic surveys considered in this study. Seep site locations are grouped according to their depth: Area 1 (~200 m bsl), Area 2 (~300-400 m bsl) and Area 3 (~90 m bsl). Additionally, the map shows the GPS track of both vessels during the complete set of surveys.

Evidence of methane seepage in the area was first described by Knies et al. (2004).They observed sulfide-oxidizing bacterial mats, which profit from hydrogen sulfide associated with AOM in the shallow sediment. This is indicative of methane seepage at the sediment surface. The study area has received increased attention since it was observed that some of the gas seeps (Area 2) were located in the proximity of the current landward limit of the theoretical GHSZ (~400 m bsl). Because the Fram Strait is the gateway of Atlantic waters into the Arctic Ocean, it is expected that changes in global temperature

could affect the western margin of Svalbard more than elsewhere in the Arctic (Berndt et al., 2014). As such, seepage at the study area has been initially hypothesized to be a consequence of gas hydrate dissociation induced by ocean warming (Westbrook et al., 2009). Since then, several scientific groups have been investigating the area in order to reveal the origin of the gas, define sub-seabed pathway mechanisms of fluids, fate of gas released in the water column, transfer of gas to the atmosphere and the relationship of bubble release and ocean warming. Although evidence shows that methane seepage is occurring since at least 3000 yr B.P (Berndt et al., 2014) the hypothesis of a possible rising in amount of bubble release as a consequence of hydrate dissociation (triggered by ocean warming) is still debated. The area has been monitored hydroacoustically since 2008 when acoustic flares were recorded for the first time (Westbrook et al., 2009). Hydroacoustic evidence of methane seepage has been reported in several publications by different scientific groups (Berndt et al., 2014; Graves et al., 2015; Lund Myhre et al., 2016; Panieri et al., 2016; Rajan et al., 2012a; Sahling et al., 2014; Sarkar et al., 2012; Steinle et al., 2015; Westbrook et al., 2009). The present research encompasses a large part of the hydroacoustic data collected during 11 'flarehunting' surveys carried out between 2008 and 2014 by different research groups on board R/V Helmer Hanssen and R/V James Clark Ross.

1.6.2. Geological setting

The formation of the western Svalbard continental margin (Fig. 1.11) dates back to Early Eocene resulting from the continental breakup in the south of the Norwegian-Greenland Sea (Eldholm et al., 1987; Sundvor and Austegard, 1990; Vanneste et al., 2007) followed by several rifting episodes in the Late Paleocene/Early Eocene (Eldholm et al., 1987; Mosar et al., 2002). The highly heterogeneous geomorphology of the western margin of Svalbard is mainly a result of glacial activity during the Pliocene and Pleistocene transition (Knies et al., 2009; Solheim et al., 1998). During this geological time, the Svalbard-Barents Sea ice sheet advanced and retreated repeatedly reaching the shelf break (Knies et al., 2009; Solheim et al., 1996). The analysis of prograding glacigenic sequences suggests that major glacier advances at the Svalbard continental margin happened at peak glaciations during the last 3.2 million years (Chabert et al., 2011; Landvik et al., 1998; Rajan et al., 2012a; Solheim et al., 1998). The continental shelf was flooded as the ice sheet retreated 13,000 years ago (Landvik et al., 2005).The actual Svalbard continental shelf break marks the approximate maximum extent of Barents Sea ice sheet (Sarkar et al., 2012).

The western continental margin of Svalbard is characterized by a narrow shelf and a steep slope with a gradient of 4° to 5° (Andersen et al., 1994). This shelf is cut by wide troughs resulting from the action of fast-flowing ice streams over the existent sediment (Ottesen et al., 2007). Two of these features are the Kongsfjorden and Isfjorden cross-shelf troughs (KT and IT respectively, Fig. 1.11), which are the respective northern and southern limits of the study area. Fast-flowing ice streams produced major erosion on the shelf and sediment deposition in prograding glacigenic sequences on the adjacent slope (Rajan et al., 2012a; Solheim et al., 1998). Till deposits are absent within troughs on the inner shelf but they are abundant on the shelf bank areas (Andersson et al., 2000; Solheim et al., 1998). Unlike the glacial dynamic influence in the sedimentation of the shelf and upper continental slope, the distal continental slope was highly influenced by bottom currents, originating the development of contourite deposits (Eiken and Hinz, 1993).

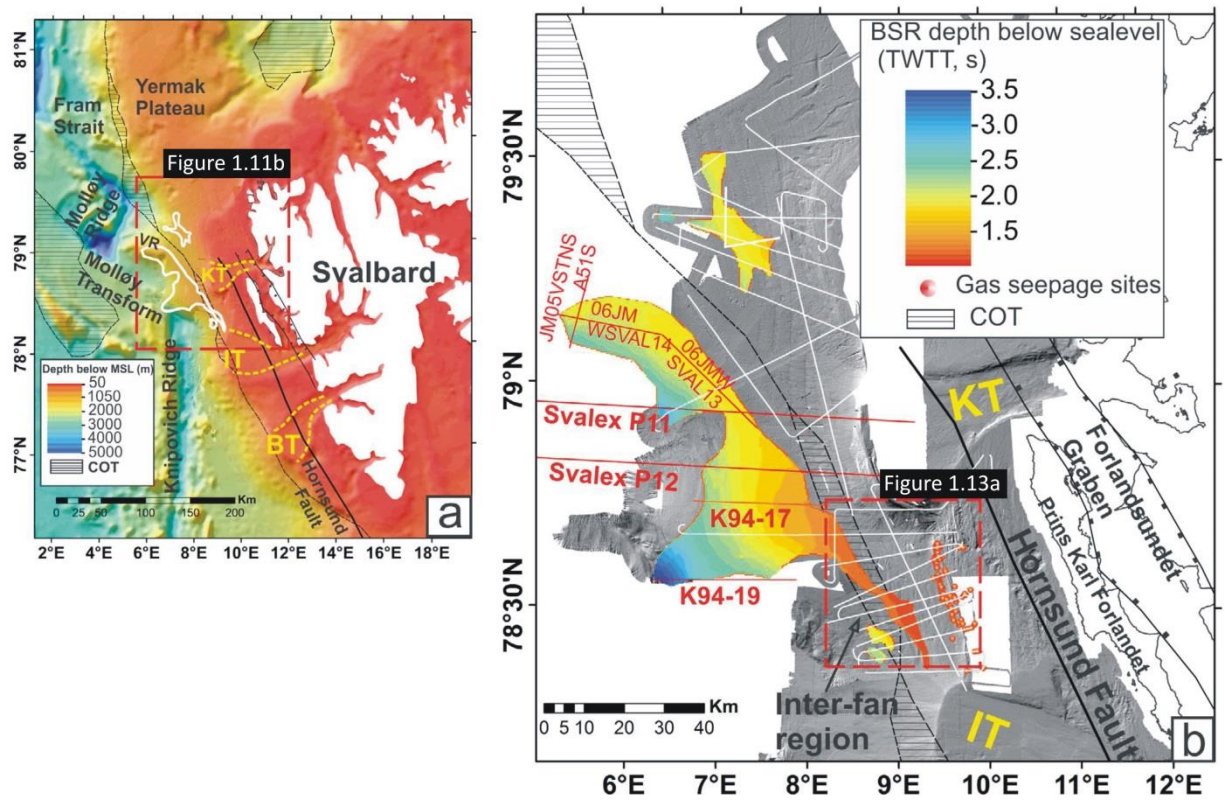

Figure 1.11. Geomorphological map of the West Svalbard continental margin and study area of research carried out by Sarkar et al. (2012). a) The figure illustrates the mid-oceanic ridge and the transform fault system constituted by the Knipovich Ridge, Molloy Transform and the Molloy Ridge. Vestnesa Ridge (VR; contouritic drift system) is also illustrated. Additionally, the currently known BSR area and the western cross-shelf troughs (Kongsfjorden troughs, KT; Isfjorden troughs, IT; Bellsund troughs, BT) are indicated in the figure. b) The BSR extent and depth map (s, Two Way Travel Time) displayed on shaded relief bathymetric image.

The sub-sea geomorphological features of the study area have been well characterized and described by several authors (e.g. Rajan et al., 2012a; Sarkar et al., 2012) in order to detect possible spatial correlations between seeps and those features. From high resolution bathymetry, Sarkar et al. (2012) have reported the existence of a convex upward bulge in the northeastern part of the study area (Figs. 4a and 4b). From seismic and morphological information this topographical expression has been interpreted as a slump. No gas seepage has been associated to this feature and seismic data suggest that the slump may inhibit rising of gas to the seafloor. In the same study, features such as furrows (ploughmarks), circular and elliptical crater-like depressions and small pits are also described (Fig. 1.12). Those features have been interpreted to be a consequence of the drifting of iceberg keels (Bass and Woodworth-Lynas, 1988; Sarkar et al., 2012). Gas seeps coincided with parts of ploughmarks in the inter-fan region and with some craters near to the shelf break (Fig. 1.12). A cluster of craters or pockmarks are also visible on the shelf eastward to the seeps of Area 1 located at ~200 m bsl. The formation of those features has been associated to past gas seepage (Rajan et al., 2012a). No morphological features associated to the current gas seepage have been found.

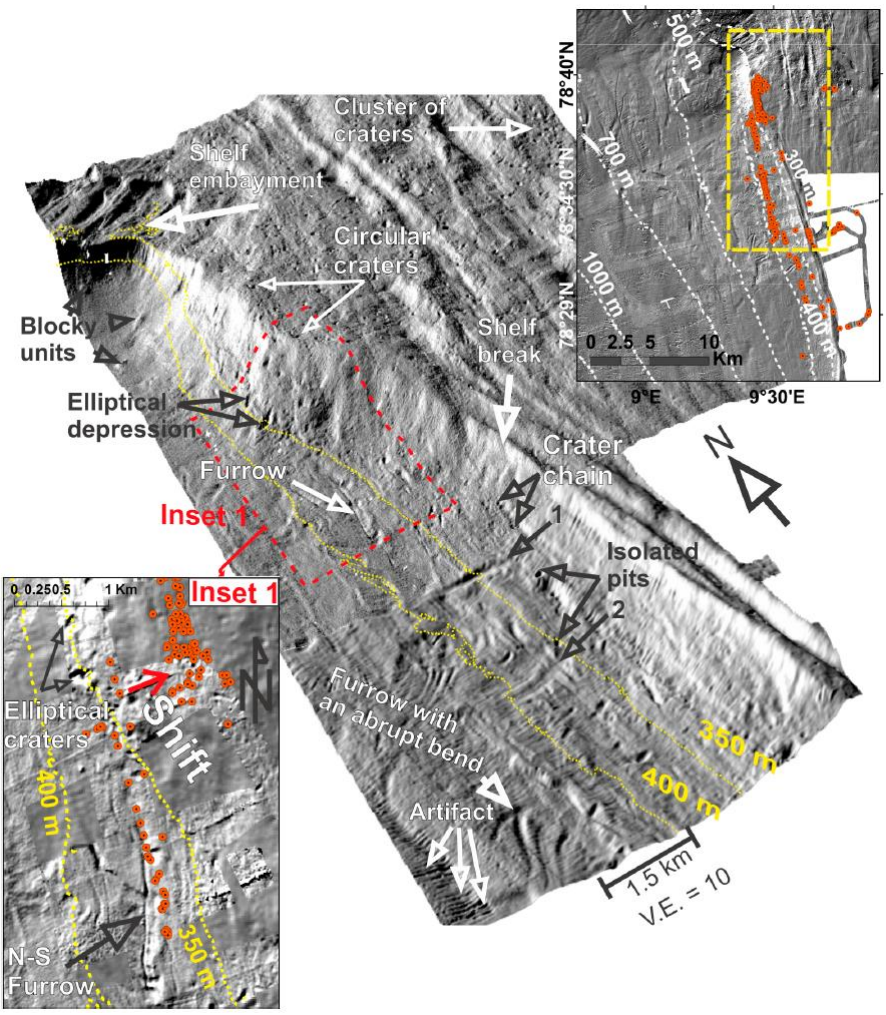

Figure 1.12. Geomorphology of the study area (Sarkar et al., 2012). The image illustrates different morphological features including e.g, ploughmarks and circular and elongated craters. Additionally, the location of the acoustic flares detected during the JR211 survey carried out in 2009 on board R/V James Clark Ross (hydroacoustic data also included in the presented thesis) are illustrated

BSRs that are the seismically inferred expressions of the base of the GHSZ have been identified in several places at the continental slope of Svalbard (Figs. 1.11 and 1.13; e.g. Chabert et al., 2011; Vogt et al., 1994; Westbrook et al., 2008). The currently known BSR distribution is confined to a region west of the seepage areas in a region of deeper water and it is limited by the Molloy Transform and the Vestnesa Ridge (Figs. 1.11a and 1.13a). The two recent studies carried out by Rajan et al. (2012a) and Sarkar et al. (2012) based on seismic observations have tried to explain the gas expulsion mechanisms describing the possible sub-seafloor fluid flow pathways. In both of these studies, the BSR is mapped down-slope at greater water depths (~ 700 m) than the seepage area. At shallower depths, where the GHSZ is still predicted to exist and pinch out at the seafloor, no BSR has been imaged. However, the absence of the BSR is not necessarily an indication of the absence of gas hydrates (e.g. Chabert et al., 2011; Holbrook et al., 2002).

Sarkar et al. (2012) reported the evidence of gas pockets right below the seepage area (Area 1 and 2) in form of negative-polarity bright spots, zones of low velocity and seismic attenuation and scattering. The major part of these gas pockets were found below the theoretical base of the GHSZ suggesting that gas has reached these pockets through permeable glacimarine strata and fractures. Because the numerous seismic evidence of gas and the presence of BSR at deeper water depths it was concluded that gas is coming dominantly from deep sedimentary sections. Though the existence of gas hydrates at shallower water depths has not been confirmed yet, their presence was inferred by comparing seismic anomalies such as bright spots between the actual GHSZ and the one from 30 years ago. Therefore the study supports the possibility that gas ebullition could be consequence of hydrate destabilization in response of bottom-water warming. Finally this study concludes that the uppermost slope is constituted by a mixture of low-permeable glacigenic sediments and more permeable marine sediment, that in combination influence the gas seeps locations, zones of gas hydrate formation, as well as the gas/fluids migration pathways.

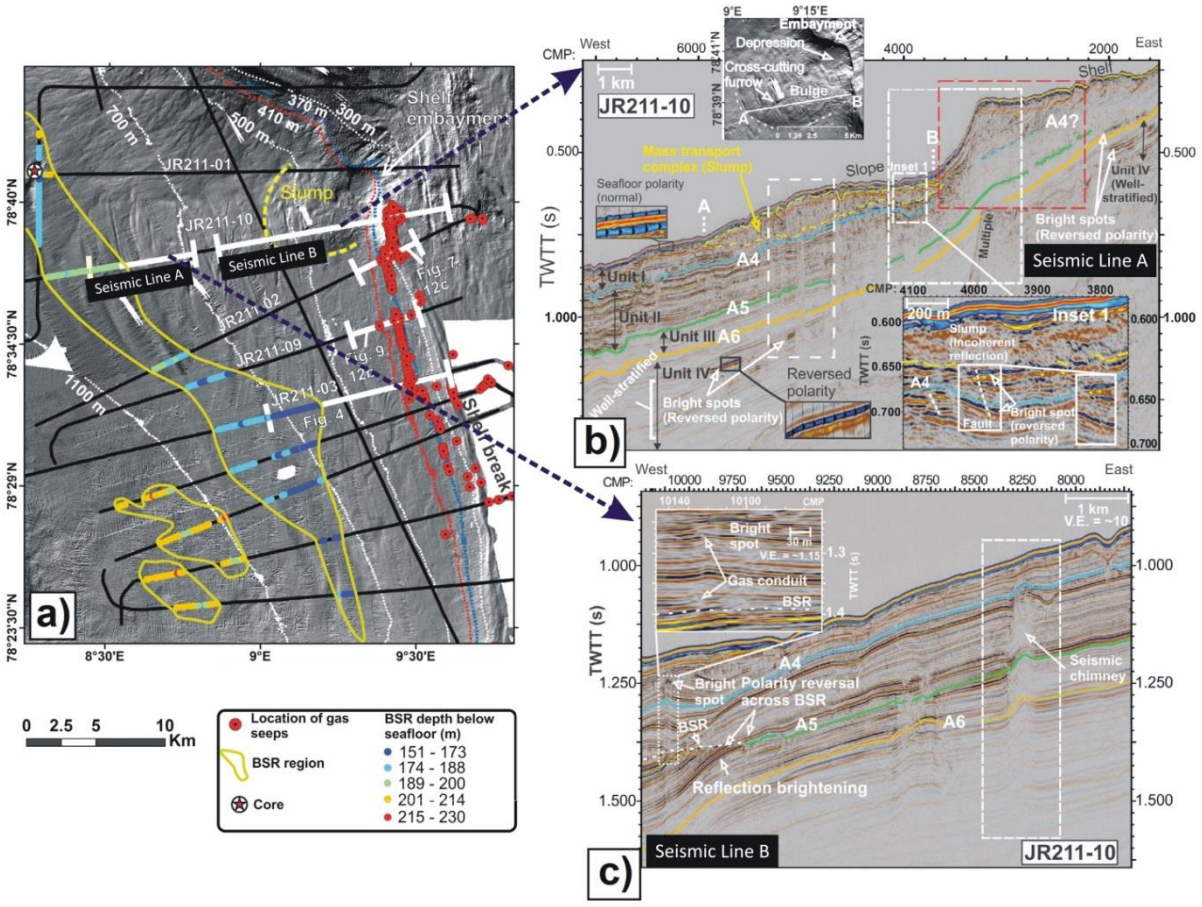

Figure 1.13. a) Bathymetric map of the study carried out by Sarkar et al. (2012) western **PKF**. The image illustrates the results obtained during the JR211 cruise on board R/V James Clark Ross (2009) including seismic lines, coring position and acoustic flares hydroacoustically detected (hydroacoustic data also used in the presented research). Additionally, the currently known BSR area and the contour lines representing the landward limits of the theoretical GHSZ at 2 °C (˜370 m bsl; c.a. 30 years ago) and 3 °C (~410 m bsl; actual) bottom water temperatures are also illustrated. b) and c) Profiles illustrating the different seismic anomalies found in the JR211-10 seismic line including bright spots, gas conduits, incoherent reflections and BSR.

Rajan et al. (2012a) built a conceptual model (Fig. 1.14) based on the analysis of high resolution 3D and 2D seismic data that summarizes the geologically controlled gas/fluids migration and expulsion at the uppermost slope and the shelf break offshore PKF (Area 1 and 2). From seismic analysis it is deduced that thermogenic-gas migration is potentially coming from deep hydrocarbon reservoirs caused by diffusive processes. Seismic data show that the westward prograding shelf is constituted of spatially confined glacigenic sequences and glacial debris flow deposits. The model shows that fluids are trapped beneath a glacigenic sequences because of their low permeability and continue to migrate upslope along permeable layers. Subsequently, fluids reach the seafloor when the base of the prograding glacigenic sequence intersects the seabed. Because the static pressure decreases as fluids rise, part of this fluid is transformed to bubbles.

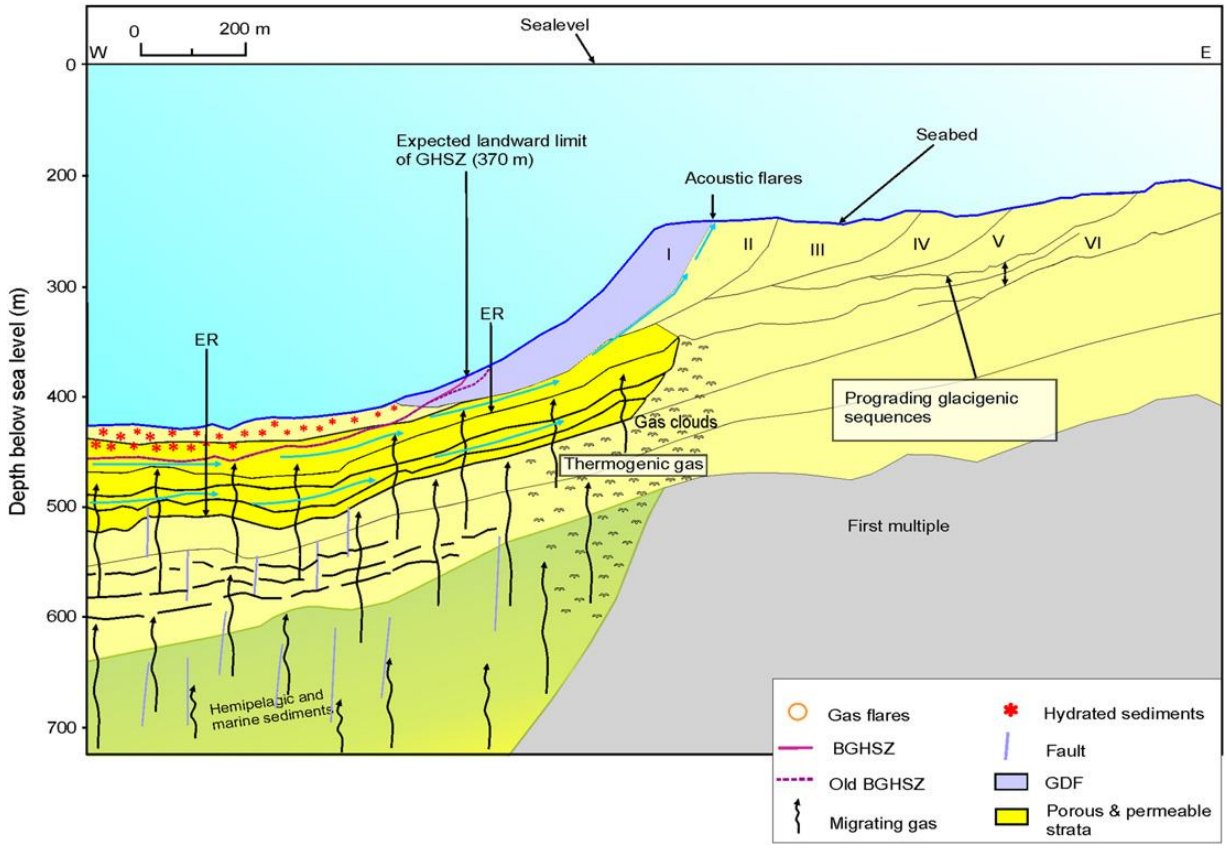

Figure 1.14. Conceptual model of geological mechanisms at the sub-seafloor controlling the fluid migration and bubble release at the seabed into the water column (Rajan et al., 2012a).

During a cruise in 2011 with the R/V James Clarke Ross, gas emissions (included in our hydroacoustic data set) were found at the Area 3 seep site area (Wright, 2012). A plausible explanation for the seepage on the shallow shelf (Area 3) is that during the last glaciation due to ice sheet loading, the pressure was high enough for gas hydrates to form in deep sediments. After the ice retreat, gas hydrates formed during high pressure conditions started to dissociate (Portnov et al., 2016). Age determination of authigenic carbonate collected at these sites (Berndt et al., 2014) indicates that methane seepage has been prevalent here for at least 3000 years B.P. and all collected carbonate crusts were older than 100 years.

1.6.3. Oceanographic setting

The study area is under the influence of two main water currents (Fig.1.15), the West Spitsbergen Current (WSC) and the Coastal Current (CC). The WSC is a shallow northward flowing branch of the North Atlantic Current that introduces warm and saline water into the Arctic Ocean (e.g. Graves et al., 2015; Nilsen et al., 2016; Saloranta and Haugan, 2004). This current is responsible for keeping mean annual temperatures around 10 °C higher than locations at similar latitudes (e.g. Ślubowska-Woldengen et al., 2007). Both, the mean temperature and speed of the WSC increase towards the shelf break (Graves et al., 2015). The WSC can be sub-divided into 3 branches: the Return Atlantic Current (RAC) which is the westernmost branch, re-circulates the northward flowing Atlantic waters in the Fram Strait; the Yermak Branch (YB) which is dominantly baroclinic and circulates along the Yermak Plateau at the north of Svalbard; and the Svalbard Branch (SB) which is dominantly barotropic and circulates along the Svalbard Shelf edge (Nilsen et al., 2016). Part of the Atlantic waters flowing in the SB is forced to circulate into the western shelf and troughs off Svalbard. Nilsen et al. (2016) has named this flow the Spitsbergen Trough Current (STC) which represents a longer and slower route of Atlantic waters toward the Arctic Ocean.

The contribution of fresher and colder Artic water in the surface layer on the West Spitsbergen Shelf is done by the CC also known as Spitsbergen Polar Current (SPC). The CC is a surface current associated with the West Spitsbergen Polar Front along the west coast of Spitsbergen carrying Arctic waters from Storfjorden and the Barents Sea (Nilsen at al., 2016). Additionally, this current is influenced by water discharge from glaciers and rivers at the fjords along the coast (Meredith et al., 2001; Nilsen et al., 2016).

Specifically, surface waters at the study area are mainly provided by the CC while the seafloor at the landward limit of the GHSZ is generally overlain by the warm saline Atlantic Water coming from the westward branch of the WSC. Steinle et al. (2015) describe this process as an oceanographic switch, altering methane oxidation rates according to different methanotrophic microbial communities that are characteristic of the two water masses and the microbial capacity for oxidizing methane. In addition, seasonal events such as sea ice melting and formation, surface heating and cooling and storms influence the hydrography of the study area (Gentz et al., 2014). These local processes change the density stratification and subsequently control the vertical turbulent diffusion of dissolved methane. Strong vertical density stratification impedes diapycnal and favors isopycnal diffusion. Dissolved methane concentration gradients are thus much stronger in the vertical direction than in the horizontal, in the vicinity of local methane sources. This implies that dissolved methane is prone to flow along constant density surfaces at the velocity of the momentary current (Gentz et al., 2014).

The variability of the water temperature at the study area has received increased attention since Westbrook et al. (2009) postulated a possible increase in gas release caused by hydrate destabilization in response to ocean warming. Multi decadal-scale records of ocean temperature variations during the past 2000 years derived from marine sediments off Western Svalbard show that the current Fram Strait ocean temperatures represent a maximum over the last 2000 years (Spielhagen et al., 2011). The latter accompanied to the warming trend of the WSC observed since 1975 in the historical temperature measurements (Ferré et al., 2012; Westbrook et al., 2009), supports a gas flux-rising scenario triggered

by hydrate destabilization. In addition, short term records from bottom-water temperatures at the landward limit of the GHSZ show high seasonal variability (0.6 °C to 4.9 °C) suggesting that methane seepage could also be affected by hydrate formation and dissociation caused by seasonally large lateral shifts of the GHSZ (Berndt et al., 2014)

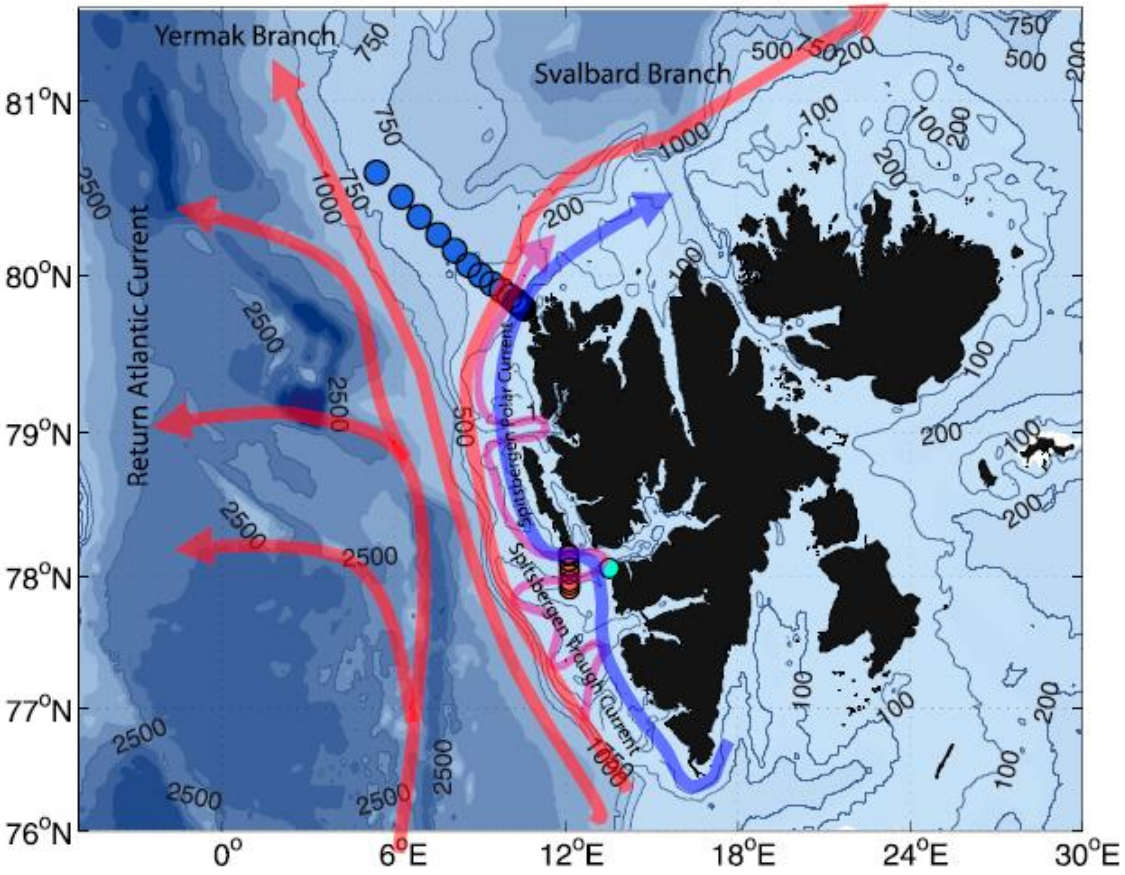

Figure 1.15. Dominating current systems on the western Svalbard continental margin (Nilsen et al., 2016). The continental margin is influenced by the WSC (red arrow) and the CC (blue arrow). The WSC can be sub-divided in three branches: the RAC, the YB and the SB. The figure also illustrates the STC which represents a longer and slower route of the SB.

1.7. Motivation and outline of this thesis

The need to identify the sources of atmospheric methane in order to evaluate the influence of human activities in climate change has become increasingly important. The IPCC (Intergovernmental Panel on Climate Change) established that global warming has been mainly induced by human activities (Stocker et al., 2013). A clear identification of all the sources that contribute to the atmospheric methane budget is the key to create a mitigation plan of anthropogenic greenhouse gas emissions and to stimulate the manufacturing of new clean technology to diminish the atmospheric greenhouse gases input.

Underwater sources of natural methane (seawater and freshwater) are considered to be an important component of the atmospheric methane budget (Kvenvolden and Rogers, 2005). Moreover, methane

emissions from underwater sources could possible increase due to e.g. long-term hydrate dissociation process in response of an eventual ocean warming. A rise in methane release related to hydrate dissociation could lead ocean temperatures to rise, triggering the destabilization of a major amount of hydrates and therefore initiating an irreversible process (clathrate gun hypothesis; e.g, Maslin et al., 2004). Additionally, in recent years the oil and gas industry has been confronted with the need to have better gas leak detection and monitoring systems in order to satisfy the regulations associated to marine environmental pollution (Veritas 2010). Consequently, there is an increasing need for monitoring and quantifying submarine sources of gas.

In this thesis work, the main focus is the quantification of the flow rate of submarine methane in gas phase, from gas seep sites, within the water column, associated to climate change studies. The use of hydroacoustic techniques to detect and monitor methane venting has shown to be efficient by virtue of its non-invasive nature and the capability to scan remotely large seep sites areas (e.g. Nikolovska et al., 2008; Greinert, 2008, Sahling et al., 2014).

The aim of this thesis work is the creation of a consistent method for quantification of gas venting at the seafloor over large seep areas using hydroacoustic information of the release in the water column. Furthermore, this work intends to determine the gas emission changes (temporal and spatial) at the study area by using the hydroacoustic technique and hydroacoustic information from different surveys. The main objectives of this work can be defined as following:

General objectives

- Implement a hydroacoustic inverse method to quantify the emission of free gas in the water
- Evaluate the methane emission over large seep site areas using the implemented method

Specific objectives

- Quantify the total flow rate of a large seep site area susceptible to global warming at the Arctic (PKF) using hydroacoustic data from a singlebeam echosounder system and the inverse hydroacoustic method.
- Evaluate the spatial and temporal variability of methane release at the study area using a hydroacoustic dataset from different years.
- Create an user-friendly software for echosounder data analysis including the implemented inverse hydroacoustic method.

The presented work is a mixture between theoretical review chapters (chapter 1- chapter 3) and 3 scientific articles (chapter 4 – chapter 6). Finally, a general conclusion and outlook is presented (chapter 7). A brief description of each chapter is given below:

Chapter 1 (Introduction) presents a theoretical background in which the main topic is methane as a greenhouse gas. The atmospheric methane sources and sinks of methane are presented. Because the study area where this work has been carried out is located in the Arctic, common submarine sources of methane in the Arctic coming from the seabed are defined. Finally, a literature review associated with the evidence of the methane release at the seafloor and the fate of this methane is presented.

Chapter 2 (Optic and hydroacoustic techniques for locating, monitoring and quantifying gas) presents a brief review about the optic and acoustic systems for detection, monitoring and quantification of gas released at the seafloor.

Chapter 3 (Acoustic theory of bubbles) describes the theory of bubbles in liquid media in presence of an acoustic wavefront related to active acoustic systems. The chapter also presents an introduction of an inverse problem associated to the bubble flux quantification.

Chapter 4 (Article 1 published at Limnology and Oceanography methods) shows the interpretation of hydroacoustic data coming from echosounders. Here is also presented a new inverse method for flow rate quantification of free gas, and a technique to quantify the flow rate a large seep site area located in the Arctic (PKF, Svalbard, ~78 N).

Chapter 5 (Article 2, submitted at SoftwareX journal) describes the Graphical User Interface (GUI) for analysis and post-proccessing of hydroacoustic data (Flarehunter GUI) and the GUI with the implemented inverse method to quantify the flow rate (FlareFlowModule). The chapter shows some examples of the functionality of the GUI and the quantification of the flow rate coming from single acoustic flares.

Chapter 6 (Article, to be submitted, Nature Geosciences) present a large dataset of hydroacoustic echosounder information from the study area coming from 11 surveys and the evaluation of the spatio/temporal variability of the methane fluxes at the study area. Results are shown together with the favorable and the unfavorable factors using hydroacoustic data coming from echosunder systems. Finally, recommendations are given in order to optimize a hydroacoustic survey.

Chapter 7 (Conclusions) shows the main achievements, limitations and challenges of this work together with the proposed future work.

References

Andersen, E.S., Solheim, A., Elverhøi, A., 1994. Development of a glaciated Arctic continental margin: exemplified by the western margin of Svalbard, in: International Conference on Arctic Margins, Proceedings: Anchorage, AK (US Dept. of the Interior), MMS. pp. 94–40.

Andersson, T., Forman, S.L., Ingólfsson, Ó., Manley, W.F., 2000. Stratigraphic and Morphologic Constraints on the Weichselian Glacial History of Northern Prins Karls Forland, Western Svalbard. Geogr. Ann. Ser. Phys. Geogr. 82, 455–470. doi:10.1111/j.0435-3676.2000.00134.x

Aydin, M., Verhulst, K.R., Saltzman, E.S., Battle, M.O., Montzka, S.A., Blake, D.R., Tang, Q., Prather, M.J., 2011. Recent decreases in fossil-fuel emissions of ethane and methane derived from firn air. Nature 476, 198–201. doi:10.1038/nature10352

Barnard, A., Sager, W.W., Snow, J.E., Max, M.D., 2015. Subsea gas emissions from the Barbados Accretionary Complex. Mar. Pet. Geol. 64, 31–42. doi:10.1016/j.marpetgeo.2015.02.008

Bass, D.W., Woodworth-Lynas, C., 1988. Iceberg crater marks on the sea floor, Labrador Shelf. Mar. Geol. 79, 243–260. doi:10.1016/0025-3227(88)90041-2

Berndt, C., Feseker, T., Treude, T., Krastel, S., Liebetrau, V., Niemann, H., Bertics, V.J., Dumke, I., Dünnbier, K., Ferré, B., Graves, C., Gross, F., Hissmann, K., Hühnerbach, V., Krause, S., Lieser, K.,

Schauer, J., Steinle, L., 2014. Temporal Constraints on Hydrate-Controlled Methane Seepage off Svalbard. Science 343, 284–287. doi:10.1126/science.1246298

Blake, D.R., Mayer, E.W., Tyler, S.C., Makide, Y., Montague, D.C., Rowland, F.S., 1982. Global increase in atmospheric methane concentrations between 1978 and 1980. Geophys. Res. Lett. 9, 477–480. doi:10.1029/GL009i004p00477

Bock, M., Schmitt, J., Möller, L., Spahni, R., Blunier, T., Fischer, H., 2010. Hydrogen Isotopes Preclude Marine Hydrate CH4 Emissions at the Onset of Dansgaard-Oeschger Events. Science 328, 1686–1689. doi:10.1126/science.1187651

Bohrmann, G., Greinert, J., Suess, E., Torres, M., 1998. Authigenic carbonates from the Cascadia subduction zone and their relation to gas hydrate stability. Geology 26, 647–650. doi:10.1130/0091-7613(1998)026<0647:ACFTCS>2.3.CO;2

Brenninkmeijer, C.A.M., Crutzen, P., Boumard, F., Dauer, T., Dix, B., Ebinghaus, R., Filippi, D., Fischer, H., Franke, H., Frieβ, U., Heintzenberg, J., Helleis, F., Hermann, M., Kock, H.H., Koeppel, C., Lelieveld, J., Leuenberger, M., Martinsson, B.G., Miemczyk, S., Moret, H.P., Nguyen, H.N., Nyfeler, P., Oram, D., O'Sullivan, D., Penkett, S., Platt, U., Pupek, M., Ramonet, M., Randa, B., Reichelt, M., Rhee, T.S., Rohwer, J., Rosenfeld, K., Scharffe, D., Schlager, H., Schumann, U., Slemr, F., Sprung, D., Stock, P., Thaler, R., Valentino, F., van Velthoven, P., Waibel, A., Wandel, A., Waschitschek, K., Wiedensohler, A., Xueref-Remy, I., Zahn, A., Zech, U., Ziereis, H., 2007. Civil Aircraft for the regular investigation of the atmosphere based on an instrumented container: The new CARIBIC system. Atmos Chem Phys 7, 4953–4976. doi:10.5194/acp-7-4953-2007

Buffett, B., Archer, D., 2004. Global inventory of methane clathrate: sensitivity to changes in the deep ocean. Earth Planet. Sci. Lett. 227, 185–199. doi:10.1016/j.epsl.2004.09.005

Buizert, C., Martinerie, P., Petrenko, V.V., Severinghaus, J.P., Trudinger, C.M., Witrant, E., Rosen, J.L., Orsi, A.J., Rubino, M., Etheridge, D.M., Steele, L.P., Hogan, C., Laube, J.C., Sturges, W.T., Levchenko, V.A., Smith, A.M., Levin, I., Conway, T.J., Dlugokencky, E.J., Lang, P.M., Kawamura, K., Jenk, T.M., White, J.W.C., Sowers, T., Schwander, J., Blunier, T., 2012. Gas transport in firn: multiple-tracer characterisation and model intercomparison for NEEM, Northern Greenland. Atmos Chem Phys 12, 4259–4277. doi:10.5194/acp-12-4259-2012

Bünz, S., Polyanov, S., Vadakkepuliyambatta, S., Consolaro, C., Mienert, J., 2012. Active gas venting through hydrate-bearing sediments on the Vestnesa Ridge, offshore W-Svalbard. Mar. Geol., Hydrocarbon leakage through focused fluid flow systems in continental margins 332–334, 189–197. doi:10.1016/j.margeo.2012.09.012

Cannat, M., Fontaine, F., EscartíN, J., 2010. Serpentinization and Associated Hydrogen And Methane Fluxes at Slow Spreading Ridges, in: Rona, P.A., Devey, C.W., Dyment, J., Murton, B.J. (Eds.), Diversity Of Hydrothermal Systems On Slow Spreading Ocean Ridges. American Geophysical Union, pp. 241–264.

Chabert, A., Minshull, T.A., Westbrook, G.K., Berndt, C., Thatcher, K.E., Sarkar, S., 2011. Characterization of a stratigraphically constrained gas hydrate system along the western continental margin of Svalbard from ocean bottom seismometer data. J. Geophys. Res. Solid Earth 116, B12102. doi:10.1029/2011JB008211

Crevoisier, C., Nobileau, D., Fiore, A.M., Armante, R., Chédin, A., Scott, N.A., 2009. Tropospheric methane in the tropics – first year from IASI hyperspectral infrared observations. Atmos Chem Phys 9, 6337–6350. doi:10.5194/acp-9-6337-2009

Cunnold, D.M., Steele, L.P., Fraser, P.J., Simmonds, P.G., Prinn, R.G., Weiss, R.F., Porter, L.W., O'Doherty, S., Langenfelds, R.L., Krummel, P.B., Wang, H.J., Emmons, L., Tie, X.X., Dlugokencky, E.J., 2002. In situ measurements of atmospheric methane at GAGE/AGAGE sites during 1985–2000 and resulting source inferences. J. Geophys. Res. Atmospheres 107, ACH 20-1. doi:10.1029/2001JD001226

Dawson, T.E., Siegwolf, R.T.W. (Eds.), 2007. Stable isotopes as indicators of ecological change, 1st ed. ed, Terrestrial ecology series. Academic, Oxford.

Denman, K.L., Brasseur, G.P., Chidthaisong, A., Ciais, P., Cox, P.M., Dickinson, R.E., Hauglustaine, D.A., Heinze, C., Holland, E.A., Jacob, D.J., Lohmann, U., Ramachandran, S., Leite da Silva Dias, P., Wofsy, S.C., Zhang, X., Steffen, W., 2007. Couplings Between Changes in the Climate System and Biogeochemistry. Cambridge University Press.

Dickens, G.R., O'Neil, J.R., Rea, D.K., Owen, R.M., 1995. Dissociation of oceanic methane hydrate as a cause of the carbon isotope excursion at the end of the Paleocene. Paleoceanography 10, 965–971. doi:10.1029/95PA02087

Dimitrov, L.I., 2002. Mud volcanoes—the most important pathway for degassing deeply buried sediments. Earth-Sci. Rev. 59, 49–76. doi:10.1016/S0012-8252(02)00069-7

Dlugokencky, E.J., Bruhwiler, L., White, J.W.C., Emmons, L.K., Novelli, P.C., Montzka, S.A., Masarie, K.A., Lang, P.M., Crotwell, A.M., Miller, J.B., Gatti, L.V., 2009. Observational constraints on recent increases in the atmospheric CH4 burden. Geophys. Res. Lett. 36, L18803. doi:10.1029/2009GL039780

Dlugokencky, E.J., Nisbet, E.G., Fisher, R., Lowry, D., 2011. Global atmospheric methane: budget, changes and dangers. Philos. Trans. R. Soc. Lond. Math. Phys. Eng. Sci. 369, 2058–2072. doi:10.1098/rsta.2010.0341

Eiken, O., Hinz, K., 1993. Contourites in the Fram Strait. Sediment. Geol. 82, 15–32. doi:10.1016/0037-0738(93)90110-Q

Eldholm, O., Faleide, J.I., Myhre, A.M., 1987. Continent-ocean transition at the western Barents Sea/Svalbard continental margin. Geology 15, 1118–1122. doi:10.1130/0091-7613(1987)15<1118:CTATWB>2.0.CO;2

Emmanuel, S., Ague, J.J., 2007. Implications of present-day abiogenic methane fluxes for the early Archean atmosphere. Geophys. Res. Lett. 34, L15810. doi:10.1029/2007GL030532

Etheridge, D.M., Pearman, G.I., Fraser, P.J., 1992. Changes in tropospheric methane between 1841 and 1978 from a high accumulation-rate Antarctic ice core. Tellus B 44, 282–294. doi:10.1034/j.1600-0889.1992.t01-3-00006.x

Etiope, G., 2004. New directions: GEM—geologic emissions of methane, the missing source in the atmospheric methane budget. Atmos. Environ. 38, 3099–3100.

Etiope, G., Klusman, R.W., 2010. Microseepage in drylands: Flux and implications in the global atmospheric source/sink budget of methane. Glob. Planet. Change, Quaternary and Global Change: Review and Issues Special issue in memory of Hugues FAURE 72, 265–274. doi:10.1016/j.gloplacha.2010.01.002

Etiope, G., Klusman, R.W., 2002. Geologic emissions of methane to the atmosphere. Chemosphere 49, 777–789. doi:10.1016/S0045-6535(02)00380-6

Etiope, G., Lassey, K.R., Klusman, R.W., Boschi, E., 2008. Reappraisal of the fossil methane budget and related emission from geologic sources. Geophys. Res. Lett. 35, L09307. doi:10.1029/2008GL033623

Etiope, G., Milkov, A.V., 2004. A new estimate of global methane flux from onshore and shallow submarine mud volcanoes to the atmosphere. Environ. Geol. 46, 997–1002. doi:10.1007/s00254-004-1085-1

Etiope, G., Sherwood Lollar, B., 2013. Abiotic Methane on Earth. Rev. Geophys. 51, 276–299. doi:10.1002/rog.20011

Ferré, B., Mienert, J., Feseker, T., 2012. Ocean temperature variability for the past 60 years on the Norwegian-Svalbard margin influences gas hydrate stability on human time scales. J. Geophys. Res. Oceans 117, C10017. doi:10.1029/2012JC008300

Fischer, H., Behrens, M., Bock, M., Richter, U., Schmitt, J., Loulergue, L., Chappellaz, J., Spahni, R., Blunier, T., Leuenberger, M., Stocker, T.F., 2008. Changing boreal methane sources and constant biomass burning during the last termination. Nature 452, 864–867. doi:10.1038/nature06825

Fleischer, P., Orsi, T., Richardson, M., Anderson, A., 2001. Distribution of free gas in marine sediments: a global overview. Geo-Mar. Lett. 21, 103–122. doi:10.1007/s003670100072

Floodgate, G.D., Judd, A.G., 1992. The origins of shallow gas. Cont. Shelf Res., Methane in Marine Sediments 12, 1145–1156. doi:10.1016/0278-4343(92)90075-U

Forster, P., Ramaswamy, V., Artaxo, P., Berntsen, T., Betts, R., Fahey, D.W., Haywood, J., Lean, J., Lowe, D.C., Myhre, G., Nganga, J., Prinn, R., Raga, G., Schulz, M., Van Dorland, R., 2007. Changes in Atmospheric Constituents and in Radiative Forcing. Chapter 2.

Fung, I., John, J., Lerner, J., Matthews, E., Prather, M., Steele, L.P., Fraser, P.J., 1991. Three-dimensional model synthesis of the global methane cycle. J. Geophys. Res. 96, 13033. doi:10.1029/91JD01247

Gentz, T., Damm, E., Schneider von Deimling, J., Mau, S., McGinnis, D.F., Schlüter, M., 2014. A water column study of methane around gas flares located at the West Spitsbergen continental margin. Cont. Shelf Res. 72, 107–118. doi:10.1016/j.csr.2013.07.013

Goulden, M.L., Wofsy, S.C., Harden, J.W., Trumbore, S.E., Crill, P.M., Gower, S.T., Fries, T., Daube, B.C., Fan, S.-M., Sutton, D.J., Bazzaz, A., Munger, J.W., 1998. Sensitivity of Boreal Forest Carbon Balance to Soil Thaw. Science 279, 214–217. doi:10.1126/science.279.5348.214

Graves, C.A., Steinle, L., Rehder, G., Niemann, H., Connelly, D.P., Lowry, D., Fisher, R.E., Stott, A.W., Sahling, H., James, R.H., 2015. Fluxes and fate of dissolved methane released at the seafloor at the landward limit of the gas hydrate stability zone offshore western Svalbard. J. Geophys. Res. Oceans 120, 6185–6201. doi:10.1002/2015JC011084

Greinert, J., Artemov, Y., Egorov, V., De Batist, M., McGinnis, D., 2006. 1300-m-high rising bubbles from mud volcanoes at 2080 m in the Black Sea: Hydroacoustic characteristics and temporal variability. Earth Planet. Sci. Lett. 244, 1–15. doi:10.1016/j.epsl.2006.02.011

Greinert, J., Bohrmann, G., Suess, E., 2001. Gas Hydrate-Associated Carbonates and Methane-Venting at Hydrate Ridge: Classification, Distribution, and Origin of Authigenic Lithologies, in: Paull, C.K., Dillon, W.P. (Eds.), Natural Gas Hydrates: Occurrence, Distribution, and Detection. American Geophysical Union, pp. 99–113.

Greinert, J., McGinnis, D.F., Naudts, L., Linke, P., De Batist, M., 2010. Atmospheric methane flux from bubbling seeps: Spatially extrapolated quantification from a Black Sea shelf area. J. Geophys. Res. 115. doi:10.1029/2009JC005381

Haeckel, M., Boudreau, B.P., Wallmann, K., 2007. Bubble-induced porewater mixing: A 3-D model for deep porewater irrigation. Geochim. Cosmochim. Acta 71, 5135–5154. doi:10.1016/j.gca.2007.08.011

Harris, S.A., Permafrost Subcommittee, Associate Committee on Geotechnical Research, National Research Council of Canada (Eds.), 1988. Glossary of permafrost and related ground-ice terms, Technical Memorandum / National Research Council, Canada. Ottawa,Ontario,Canada.

Hasiotis, T., Papatheodorou, G., Kastanos, N., Ferentinos, G., 1996. A pockmark field in the Patras Gulf (Greece) and its activation during the 14/7/93 seismic event. Mar. Geol. 130, 333–344. doi:10.1016/0025-3227(95)00131-X

Heimann, M., 2011. Atmospheric science: Enigma of the recent methane budget. Nature 476, 157–158. doi:10.1038/476157a

Henriet, J.-P., Mienert, J. (Eds.), 1998. Gas hydrates: relevance to world margin stability and climate change, Geological Society special publication. Geological Society, London.

Holbrook, W.S., Lizarralde, D., Pecher, I.A., Gorman, A.R., Hackwith, K.L., Hornbach, M., Saffer, D., 2002. Escape of methane gas through sediment waves in a large methane hydrate province. Geology 30, 467–470. doi:10.1130/0091-7613(2002)030<0467:EOMGTS>2.0.CO;2

Hornafius, J.S., Quigley, D., Luyendyk, B.P., 1999. The world's most spectacular marine hydrocarbon seeps (Coal Oil Point, Santa Barbara Channel, California): Quantification of emissions. J. Geophys. Res. Oceans 104, 20703–20711. doi:10.1029/1999JC900148

Houghton, J.T., Intergovernmental Panel on Climate Change (Eds.), 2001. Climate change 2001: the scientific basis: contribution of Working Group I to the third assessment report of the Intergovernmental Panel on Climate Change. Cambridge University Press, Cambridge ; New York.

Hovland, M., 2002. On the self-sealing nature of marine seeps. Cont. Shelf Res., Gas in Marine Sediments: Contributions from the 5th International Conference orgainsed by the Shallow Gas Group, Bologna, Italy, September 1998 22, 2387–2394. doi:10.1016/S0278-4343(02)00063-8

Hovland, M., Judd, A., 1988. Seabed pockmarks and seepages: impact on geology, biology, and the marine environment. Springer.

Hustoft, S., Bünz, S., Mienert, J., Chand, S., 2009. Gas hydrate reservoir and active methane-venting province in sediments on < 20 Ma young oceanic crust in the Fram Strait, offshore NW-Svalbard. Earth Planet. Sci. Lett. 284, 12–24. doi:10.1016/j.epsl.2009.03.038

James, R.H., Bousquet, P., Bussmann, I., Haeckel, M., Kipfer, R., Leifer, I., Niemann, H., Ostrovsky, I., Piskozub, J., Rehder, G., Treude, T., Vielstädte, L., Greinert, J., 2016. Effects of climate change on methane emissions from seafloor sediments in the Arctic Ocean: A review. Limnol. Oceanogr. n/a-n/a. doi:10.1002/lno.10307

Johnson, J.E., Mienert, J., Plaza-Faverola, A., Vadakkepuliyambatta, S., Knies, J., Bünz, S., Andreassen, K., Ferré, B., 2015. Abiotic methane from ultraslow-spreading ridges can charge Arctic gas hydrates. Geology G36440.1. doi:10.1130/G36440.1

Jorgenson, M.T., Shur, Y.L., Pullman, E.R., 2006. Abrupt increase in permafrost degradation in Arctic Alaska. Geophys. Res. Lett. 33, L02503. doi:10.1029/2005GL024960

Judd, A.G., 2004. Natural seabed gas seeps as sources of atmospheric methane. Environ. Geol. 46, 988–996. doi:10.1007/s00254-004-1083-3

Judd, A.G., Hovland, M., 2009. Seabed fluid flow: the impact of geology, biology and the marine environment, Digitally print. version. ed. Cambridge Univ. Press, New York, NY.

Judd, A.G., Hovland, M., 1992. Methane in Marine SedimentsThe evidence of shallow gas in marine sediments. Cont. Shelf Res. 12, 1081–1095. doi:10.1016/0278-4343(92)90070-Z

Kai, F.M., Tyler, S.C., Randerson, J.T., Blake, D.R., 2011. Reduced methane growth rate explained by decreased Northern Hemisphere microbial sources. Nature 476, 194–197. doi:10.1038/nature10259

Kelley, D.S., Karson, J.A., Früh-Green, G.L., Yoerger, D.R., Shank, T.M., Butterfield, D.A., Hayes, J.M., Schrenk, M.O., Olson, E.J., Proskurowski, G., Jakuba, M., Bradley, A., Larson, B., Ludwig, K., Glickson, D., Buckman, K., Bradley, A.S., Brazelton, W.J., Roe, K., Elend, M.J., Delacour, A., Bernasconi, S.M., Lilley, M.D., Baross, J.A., Summons, R.E., Sylva, S.P., 2005. A Serpentinite-Hosted Ecosystem: The Lost City Hydrothermal Field. Science 307, 1428–1434. doi:10.1126/science.1102556

Kelley, J.T., Dickson, S.M., Belknap, D.F., Barnhardt, W.A., Henderson, M., 1994. Giant sea-bed pockmarks: Evidence for gas escape from Belfast Bay, Maine. Geology 22, 59–62. doi:10.1130/0091-7613(1994)022<0059:GSBPEF>2.3.CO;2

Kennett, J.P., Cannariato, K.G., Hendy, I.L., Behl, R.J., 2000. Carbon Isotopic Evidence for Methane Hydrate Instability During Quaternary Interstadials. Science 288, 128–133. doi:10.1126/science.288.5463.128

Kennett, J.P., Cannariato, K.G., Hendy, I.L., Behl, R.J., Kennett, J.P., Cannariato, K.G., Hendy, I.L., Behl, R.J., 2003. Methane Hydrates in Quaternary Climate Change: The Clathrate Gun Hypothesi, in: Methane Hydrates in Quaternary Climate Change: The Clathrate Gun Hypothesis. American Geophysical Union, pp. 1–9.

Kirschke, S., Bousquet, P., Ciais, P., Saunois, M., Canadell, J.G., Dlugokencky, E.J., Bergamaschi, P., Bergmann, D., Blake, D.R., Bruhwiler, L., Cameron-Smith, P., Castaldi, S., Chevallier, F., Feng, L., Fraser, A., Heimann, M., Hodson, E.L., Houweling, S., Josse, B., Fraser, P.J., Krummel, P.B., Lamarque, J.-F., Langenfelds, R.L., Le Quéré, C., Naik, V., O'Doherty, S., Palmer, P.I., Pison, I., Plummer, D., Poulter, B., Prinn, R.G., Rigby, M., Ringeval, B., Santini, M., Schmidt, M., Shindell, D.T., Simpson, I.J., Spahni, R., Steele, L.P., Strode, S.A., Sudo, K., Szopa, S., van der Werf, G.R., Voulgarakis, A., van Weele, M., Weiss, R.F., Williams, J.E., Zeng, G., 2013. Three decades of global methane sources and sinks. Nat. Geosci. 6, 813–823. doi:10.1038/ngeo1955

Klusman, R.W., Jakel, M.E., LeRoy, M.P., 1998. Does microseepage of methane and light hydrocarbons contribute to the atmospheric budget of methane and to global climate change. Assoc. Pet. Geochem. Explor. Bull. 11, 1–56.

Knies, J., Damm, E., Gutt, J., Mann, U., Pinturier, L., 2004. Near-surface hydrocarbon anomalies in shelf sediments off Spitsbergen: Evidences for past seepages. Geochem. Geophys. Geosystems 5, Q06003. doi:10.1029/2003GC000687

Knies, J., Matthiessen, J., Vogt, C., Laberg, J.S., Hjelstuen, B.O., Smelror, M., Larsen, E., Andreassen, K., Eidvin, T., Vorren, T.O., 2009. The Plio-Pleistocene glaciation of the Barents Sea–Svalbard region: a new model based on revised chronostratigraphy. Quat. Sci. Rev. 28, 812–829. doi:10.1016/j.quascirev.2008.12.002

Koch, S., Berndt, C., Bialas, J., Haeckel, M., Crutchley, G., Papenberg, C., Klaeschen, D., Greinert, J., 2015. Gas-controlled seafloor doming. Geology 43, 571–574. doi:10.1130/G36596.1

Kort, E.A., Wofsy, S.C., Daube, B.C., Diao, M., Elkins, J.W., Gao, R.S., Hintsa, E.J., Hurst, D.F., Jimenez, R., Moore, F.L., Spackman, J.R., Zondlo, M.A., 2012. Atmospheric observations of Arctic Ocean methane emissions up to 82° north. Nat. Geosci. 5, 318–321. doi:10.1038/ngeo1452

Kvenvolden, K.A., 1993. Gas hydrates—geological perspective and global change. Rev. Geophys. 31, 173–187.

Kvenvolden, K.A., Lorenson, T.D., Reeburgh, W.S., 2001. Attention turns to naturally occurring methane seepage. Eos Trans. Am. Geophys. Union 82, 457–457. doi:10.1029/01EO00275

Kvenvolden, K.A., Rogers, B.W., 2005. Gaia's breath—global methane exhalations. Mar. Pet. Geol., Near-Surface Hydrocarbon Migration: Mechanisms and Seepage Rates 22, 579–590. doi:10.1016/j.marpetgeo.2004.08.004

Lacroix, A.V., 1993. Proceedings of the NATO advanced research workshop Unaccounted-for sources of fossil and isotopically-enriched methane and their contribution to the emissions inventory. Chemosphere 26, 507–557. doi:10.1016/0045-6535(93)90441-7

Lamarque, J.-F., 2008. Estimating the potential for methane clathrate instability in the 1%-CO2 IPCC AR-4 simulations. Geophys. Res. Lett. 35, L19806. doi:10.1029/2008GL035291

Landvik, J.Y., Bondevik, S., Elverhøi, A., Fjeldskaar, W., Mangerud, J., Salvigsen, O., Siegert, M.J., Svendsen, J.-I., Vorren, T.O., 1998. The last glacial maximum of Svalbard and the Barents Sea area: ice sheet extent and configuration. Quat. Sci. Rev. 17, 43–75. doi:10.1016/S0277-3791(97)00066-8

Landvik, J.Y., Ingólfsson, Ó., Mienert, J., Lehman, S.J., Solheim, A., Elverhøi, A., Ottesen, D., 2005. Rethinking Late Weichselian ice-sheet dynamics in coastal NW Svalbard. Boreas 34, 7–24. doi:10.1111/j.1502-3885.2005.tb01001.x

Lee, S.H., Chough, S.K., 2002. Distribution and origin of shallow gas in deep-sea sediments of the Ulleung Basin, East Sea (Sea of Japan). Geo-Mar. Lett. 22, 204–209. doi:10.1007/s00367-002-0114-x

Leifer, I., Patro, R.K., 2002. The bubble mechanism for methane transport from the shallow sea bed to the surface: A review and sensitivity study. Cont. Shelf Res. 22, 2409–2428. doi:10.1016/S0278-4343(02)00065-1

Loulergue, L., Schilt, A., Spahni, R., Masson-Delmotte, V., Blunier, T., Lemieux, B., Barnola, J.-M., Raynaud, D., Stocker, T.F., Chappellaz, J., 2008. Orbital and millennial-scale features of atmospheric CH4 over the past 800,000 years. Nature 453, 383–386. doi:10.1038/nature06950

Loyd, S.J., Sample, J., Tripati, R.E., Defliese, W.F., Brooks, K., Hovland, M., Torres, M., Marlow, J., Hancock, L.G., Martin, R., Lyons, T., Tripati, A.E., 2016. Methane seep carbonates yield clumped isotope signatures out of equilibrium with formation temperatures. Nat. Commun. 7, 12274. doi:10.1038/ncomms12274

Lund Myhre, C., Ferré, B., Platt, S.M., Silyakova, A., Hermansen, O., Allen, G., Pisso, I., Schmidbauer, N., Stohl, A., Pitt, J., Jansson, P., Greinert, J., Percival, C., Fjaeraa, A.M., O'Shea, S., Gallagher, M., Le Breton, M., Bower, K., Bauguitte, S., Dalsøren, S., Vadakkepuliyambatta, S., Fisher, R.E., Nisbet, E. g., Lowry, D., Myhre, G., Pyle, J., Cain, M., Mienert, J., 2016. Extensive release of methane from Arctic seabed west of Svalbard during summer 2014 does not influence the atmosphere. Geophys. Res. Lett. 2016GL068999. doi:10.1002/2016GL068999

Magalhães, V.H., Pinheiro, L.M., Ivanov, M.K., Kozlova, E., Blinova, V., Kolganova, J., Vasconcelos, C., McKenzie, J.A., Bernasconi, S.M., Kopf, A.J., Díaz-del-Río, V., González, F.J., Somoza, L., 2012. Formation processes of methane-derived authigenic carbonates from the Gulf of Cadiz. Sediment. Geol. 243–244, 155–168. doi:10.1016/j.sedgeo.2011.10.013

Maini, B.B., Bishnoi, P.R., 1981. Experimental investigation of hydrate formation behaviour of a natural gas bubble in a simulated deep sea environment. Chem. Eng. Sci. 36, 183–189. doi:10.1016/0009-2509(81)80062-0

Maslin, M., Owen, M., Day, S., Long, D., 2004. Linking continental-slope failures and climate change: Testing the clathrate gun hypothesis. Geology 32, 53–56. doi:10.1130/G20114.1

Mau, S., Valentine, D.L., Clark, J.F., Reed, J., Camilli, R., Washburn, L., 2007. Dissolved methane distributions and air-sea flux in the plume of a massive seep field, Coal Oil Point, California. Geophys. Res. Lett. 34, L22603. doi:10.1029/2007GL031344

McGinnis, D.F., Greinert, J., Artemov, Y., Beaubien, S.E., Wüest, A., 2006. Fate of rising methane bubbles in stratified waters: How much methane reaches the atmosphere? J. Geophys. Res. Oceans 111, C09007. doi:10.1029/2005JC003183

Meredith, M., Heywood, K., Dennis, P., Goldson, L., White, R., Fahrbach, E., Schauer, U., Østerhus, S., 2001. Freshwater fluxes through the Western Fram Strait. Geophys. Res. Lett. 28, 1615–1618. doi:10.1029/2000GL011992

Milkov, A.V., Sassen, R., Apanasovich, T.V., Dadashev, F.G., 2003. Global gas flux from mud volcanoes: A significant source of fossil methane in the atmosphere and the ocean. Geophys. Res. Lett. 30, 1037. doi:10.1029/2002GL016358

Montzka, S.A., Krol, M., Dlugokencky, E., Hall, B., Jöckel, P., Lelieveld, J., 2011. Small Interannual Variability of Global Atmospheric Hydroxyl. Science 331, 67–69. doi:10.1126/science.1197640

Morino, I., Uchino, O., Inoue, M., Yoshida, Y., Yokota, T., Wennberg, P.O., Toon, G.C., Wunch, D., Roehl, C.M., Notholt, J., Warneke, T., Messerschmidt, J., Griffith, D.W.T., Deutscher, N.M., Sherlock, V., Connor, B., Robinson, J., Sussmann, R., Rettinger, M., 2010. Preliminary validation of column-averaged volume mixing ratios of carbon dioxide and methane retrieved from GOSAT short-wavelength infrared spectra. Atmos Meas Tech Discuss 3, 5613–5643. doi:10.5194/amtd-3-5613-2010

Mosar, J., Eide, E.A., Osmundsen, P.T., Sommaruga, A., Torsvik, T.H., 2002. Greenland – Norway separation: A geodynamic model for the North Atlantic. Presented at the Norwegian Journal of Geology, p. 282.

Naehr, T.H., Rodriguez, N.M., Bohrmann, G., Paull, C.K., Botz, R., 2000. 29. Methane-derived authigenic carbonates associated with gas hydrate decomposition and fluid venting above the Blake Ridge Diapir, in: Proceedings of the Ocean Drilling Program. Scientific Results. Ocean Drilling Program, pp. 285–300.

Naudts, L., Greinert, J., Artemov, Y., Staelens, P., Poort, J., Van Rensbergen, P., De Batist, M., 2006. Geological and morphological setting of 2778 methane seeps in the Dnepr paleo-delta, northwestern Black Sea. Mar. Geol. 227, 177–199. doi:10.1016/j.margeo.2005.10.005

Neef, L., van Weele, M., van Velthoven, P., 2010. Optimal estimation of the present-day global methane budget. Glob. Biogeochem. Cycles 24, GB4024. doi:10.1029/2009GB003661

Niemann, H., Elvert, M., Hovland, M., Orcutt, B., Judd, A., Suck, I., Gutt, J., Joye, S., Damm, E., Finster, K., Boetius, A., 2005. Methane emission and consumption at a North Sea gas seep (Tommeliten area). Biogeosciences Discuss. 2, 1197–1241.

Nilsen, F., Skogseth, R., Vaardal-Lunde, J., Inall, M., 2016. A Simple Shelf Circulation Model: Intrusion of Atlantic Water on the West Spitsbergen Shelf. J. Phys. Oceanogr. 46, 1209–1230. doi:10.1175/JPO-D-15-0058.1

Nisbet, E.G., 2002. Have sudden large releases of methane from geological reservoirs occurred since the Last Glacial Maximum, and could such releases occur again? Philos. Trans. R. Soc. Lond. Math. Phys. Eng. Sci. 360, 581–607. doi:10.1098/rsta.2001.0958

Nisbet, E.G., Dlugokencky, E.J., Bousquet, P., 2014. Methane on the Rise—Again. Science 343, 493–495. doi:10.1126/science.1247828

NRCC, 1988. Glossary of permafrost and related ground-ice terms. Assoc. Comm. Geotech. Res. Natl. Res. Counc. Can. Ott. 156.

O'Connor, F.M., Boucher, O., Gedney, N., Jones, C.D., Folberth, G.A., Coppell, R., Friedlingstein, P., Collins, W.J., Chappellaz, J., Ridley, J., Johnson, C.E., 2010. Possible role of wetlands, permafrost, and methane hydrates in the methane cycle under future climate change: A review. Rev. Geophys. 48, RG4005. doi:10.1029/2010RG000326

Panieri, G., Graves, C.A., James, R.H., 2016. Paleo-methane emissions recorded in foraminifera near the landward limit of the gas hydrate stability zone offshore western Svalbard: PALEO-METHANE SEEPS OFF WESTERN SVALBARD. Geochem. Geophys. Geosystems 17, 521–537. doi:10.1002/2015GC006153

Parkes, R.J., Cragg, B.A., Fry, J.C., Herbert, R.A., Wimpenny, J.W.T., Allen, J.A., Whitfield, M., 1990. Bacterial Biomass and Activity in Deep Sediment Layers from the Peru Margin [and Discussion]. Philos. Trans. R. Soc. Lond. Math. Phys. Eng. Sci. 331, 139–153. doi:10.1098/rsta.1990.0061

Portnov, A., Vadakkepuliyambatta, S., Mienert, J., Hubbard, A., 2016. Ice-sheet-driven methane storage and release in the Arctic. Nat. Commun. 7, 10314. doi:10.1038/ncomms10314

Proskurowski, G., Lilley, M.D., Seewald, J.S., Früh-Green, G.L., Olson, E.J., Lupton, J.E., Sylva, S.P., Kelley, D.S., 2008. Abiogenic Hydrocarbon Production at Lost City Hydrothermal Field. Science 319, 604–607. doi:10.1126/science.1151194

Rachold, V., Bolshiyanov, D.Y., Grigoriev, M.N., Hubberten, H.-W., Junker, R., Kunitsky, V.V., Merker, F., Overduin, P., Schneider, W., 2007. Nearshore arctic subsea permafrost in transition. Eos Trans. Am. Geophys. Union 88, 149–150. doi:10.1029/2007EO130001

Rajan, A., Mienert, J., Bünz, S., 2012a. Acoustic evidence for a gas migration and release system in Arctic glaciated continental margins offshore NW-Svalbard. Mar. Pet. Geol. 32, 36–49. doi:10.1016/j.marpetgeo.2011.12.008

Rajan, A., Mienert, J., Bünz, S., Chand, S., 2012b. Potential serpentinization, degassing, and gas hydrate formation at a young (<20 Ma) sedimented ocean crust of the Arctic Ocean ridge system. J. Geophys. Res. Solid Earth 117, B03102. doi:10.1029/2011JB008537

Reeburgh, W.S., 2007. 4.03 - Global Methane Biogeochemistry, in: Turekian, H.D.H.K. (Ed.), Treatise on Geochemistry. Pergamon, Oxford, pp. 1–32.

Rehder, G., Brewer, P.W., Peltzer, E.T., Friederich, G., 2002. Enhanced lifetime of methane bubble streams within the deep ocean. Geophys. Res. Lett. 29, 21–1. doi:10.1029/2001GL013966

Rehder, G., Leifer, I., Brewer, P.G., Friederich, G., Peltzer, E.T., 2009. Controls on methane bubble dissolution inside and outside the hydrate stability field from open ocean field experiments and numerical modeling. Mar. Chem. 114, 19–30. doi:10.1016/j.marchem.2009.03.004

Romanovskii, N.N., Hubberten, H.-W., Gavrilov, A.V., Eliseeva, A.A., Tipenko, G.S., 2005. Offshore permafrost and gas hydrate stability zone on the shelf of East Siberian Seas. Geo-Mar. Lett. 25, 167–182. doi:10.1007/s00367-004-0198-6

Rooney, M.A., Claypool, G.E., Moses Chung, H., 1995. Modeling thermogenic gas generation using carbon isotope ratios of natural gas hydrocarbons. Chem. Geol., Processes of Natural Gas Formation 126, 219–232. doi:10.1016/0009-2541(95)00119-0

Sahling, H., Römer, M., Pape, T., Bergès, B., dos Santos Fereirra, C., Boelmann, J., Geprägs, P., Tomczyk, M., Nowald, N., Dimmler, W., Schroedter, L., Glockzin, M., Bohrmann, G., 2014. Gas emissions at the continental margin west off Svalbard: mapping, sampling, and quantification. Biogeosciences Discuss. 11, 7189–7234. doi:10.5194/bgd-11-7189-2014

Saloranta, T.M., Haugan, P.M., 2004. Northward cooling and freshening of the warm core of the West Spitsbergen Current. Polar Res. 23, 79–88. doi:10.1111/j.1751-8369.2004.tb00131.x

Sarkar, S., Berndt, C., Minshull, T.A., Westbrook, G.K., Klaeschen, D., Masson, D.G., Chabert, A., Thatcher, K.E., 2012. Seismic evidence for shallow gas-escape features associated with a retreating gas hydrate zone offshore west Svalbard. J. Geophys. Res. Solid Earth 117, B09102. doi:10.1029/2011JB009126

Sassen, R., Roberts, H.H., Carney, R., Milkov, A.V., DeFreitas, D.A., Lanoil, B., Zhang, C., 2004. Free hydrocarbon gas, gas hydrate, and authigenic minerals in chemosynthetic communities of the northern Gulf of Mexico continental slope: relation to microbial processes. Chem. Geol., Geomicrobiology and Biogeochemistry of Gas Hydrates and Hydrocarbon Seeps 205, 195–217. doi:10.1016/j.chemgeo.2003.12.032

Sauter, E.J., Muyakshin, S.I., Charlou, J.-L., Schlüter, M., Boetius, A., Jerosch, K., Damm, E., Foucher, J.-P., Klages, M., 2006. Methane discharge from a deep-sea submarine mud volcano into the upper water column by gas hydrate-coated methane bubbles. Earth Planet. Sci. Lett. 243, 354–365. doi:10.1016/j.epsl.2006.01.041

Schoell, M., 1988. Origins of Methane in the Earth Multiple origins of methane in the Earth. Chem. Geol. 71, 1–10. doi:10.1016/0009-2541(88)90101-5

Schuur, E.A.G., Bockheim, J., Canadell, J.G., Euskirchen, E., Field, C.B., Goryachkin, S.V., Hagemann, S., Kuhry, P., Lafleur, P.M., Lee, H., Mazhitova, G., Nelson, F.E., Rinke, A., Romanovsky, V.E., Shiklomanov, N., Tarnocai, C., Venevsky, S., Vogel, J.G., Zimov, S.A., 2008. Vulnerability of Permafrost Carbon to Climate Change: Implications for the Global Carbon Cycle. BioScience 58, 701–714. doi:10.1641/B580807

Scranton, M.I., Brewer, P.G., 1978. Consumption of dissolved methane in the deep ocean. Limnol Ocean. 23, 1207–1213.

Seewald, J.S., 2003. Organic–inorganic interactions in petroleum-producing sedimentary basins. Nature 426, 327–333. doi:10.1038/nature02132

Sergienko, V.I., Lobkovskii, L.I., Semiletov, I.P., Dudarev, O.V., Dmitrievskii, N.N., Shakhova, N.E., Romanovskii, N.N., Kosmach, D.A., Nikol'skii, D.N., Nikiforov, S.L., Salomatin, A.S., Anan'ev, R.A., Roslyakov, A.G., Salyuk, A.N., Karnaukh, V.V., Chernykh, D.B., Tumskoi, V.E., Yusupov, V.I., Kurilenko, A.V., Chuvilin, E.M., Bukhanov, B.A., 2012. The degradation of submarine permafrost and the destruction of hydrates on the shelf of east arctic seas as a potential cause of the

"Methane Catastrophe": some results of integrated studies in 2011. Dokl. Earth Sci. 446, 1132–1137. doi:10.1134/S1028334X12080144

Shakhova, N., Semiletov, I., Leifer, I., Sergienko, V., Salyuk, A., Kosmach, D., Chernykh, D., Stubbs, C., Nicolsky, D., Tumskoy, V., Gustafsson, Ö., 2014. Ebullition and storm-induced methane release from the East Siberian Arctic Shelf. Nat. Geosci. 7, 64–70. doi:10.1038/ngeo2007

Shakhova, N., Semiletov, I., Salyuk, A., Yusupov, V., Kosmach, D., Gustafsson, Ö., 2010. Extensive Methane Venting to the Atmosphere from Sediments of the East Siberian Arctic Shelf. Science 327, 1246–1250. doi:10.1126/science.1182221

Simpson, I.J., Sulbaek Andersen, M.P., Meinardi, S., Bruhwiler, L., Blake, N.J., Helmig, D., Rowland, F.S., Blake, D.R., 2012. Long-term decline of global atmospheric ethane concentrations and implications for methane. Nature 488, 490–494. doi:10.1038/nature11342

Skarke, A., Ruppel, C., Kodis, M., Brothers, D., Lobecker, E., 2014. Widespread methane leakage from the sea floor on the northern US Atlantic margin. Nat. Geosci. 7, 657–661. doi:10.1038/ngeo2232

Sloan, E.D., Koh, C.A., 2008. Clathrate hydrates of natural gases, 3rd ed. ed, Chemical industries. CRC Press, Boca Raton, FL.

Ślubowska-Woldengen, M., Rasmussen, T.L., Koç, N., Klitgaard-Kristensen, D., Nilsen, F., Solheim, A., 2007. Advection of Atlantic Water to the western and northern Svalbard shelf since 17,500 cal yr BP. Quat. Sci. Rev. 26, 463–478. doi:10.1016/j.quascirev.2006.09.009

Smith, A.J., Mienert, J., Bünz, S., Greinert, J., 2014. Thermogenic methane injection via bubble transport into the upper Arctic Ocean from the hydrate-charged Vestnesa Ridge, Svalbard. Geochem. Geophys. Geosystems 15, 1945–1959. doi:10.1002/2013GC005179

Solheim, A., Andersen, E.S., Elverhøi, A., Fiedler, A., 1996. Impact of Glaciations on Basin Evolution: Data and Models from the Norwegian Margin and Adjacent AreasLate Cenozoic depositional history of the western Svalbard continental shelf, controlled by subsidence and climate. Glob. Planet. Change 12, 135–148. doi:10.1016/0921-8181(95)00016-X

Solheim, A., ELVERHøI, A., 1985. A pockmark field in the Central Barents Sea; gas from a petrogenic source? Polar Res. 3, 11–19. doi:10.1111/j.1751-8369.1985.tb00492.x

Solheim, A., Faleide, J.I., Andersen, E.S., Elverhøi, A., Forsberg, C.F., Vanneste, K., Uenzelmann-Neben, G., Channell, J.E.T., 1998. Late Cenozoic seismic stratigraphy and glacial geological development of the East Greenland and Svalbard–Barents sea continental margins. Quat. Sci. Rev. 17, 155–184. doi:10.1016/S0277-3791(97)00068-1

Solheim, A., Larsson, F.R., 1987. Seismic indications of shallow gas in the Northern Barents Sea.

Soloviev, V.A., Ginzburg, G.D., Telepnev, E.V., Mikhaluk, Y.N., 1987. Cryothermia and gas hydrates in the Arctic Ocean. Sevmorgeologias Leningr. 150pp.

Spielhagen, R.F., Werner, K., Sørensen, S.A., Zamelczyk, K., Kandiano, E., Budeus, G., Husum, K., Marchitto, T.M., Hald, M., 2011. Enhanced Modern Heat Transfer to the Arctic by Warm Atlantic Water. Science 331, 450–453. doi:10.1126/science.1197397

Steinle, L., Graves, C.A., Treude, T., Ferré, B., Biastoch, A., Bussmann, I., Berndt, C., Krastel, S., James, R.H., Behrens, E., Böning, C.W., Greinert, J., Sapart, C.-J., Scheinert, M., Sommer, S., Lehmann, M.F., Niemann, H., 2015. Water column methanotrophy controlled by a rapid oceanographic switch. Nat. Geosci. 8, 378–382. doi:10.1038/ngeo2420

Stoessell, R.K., Byrne, P.A., 1982. Salting-out of methane in single-salt solutions at 25°C and below 800 psia. Geochim. Cosmochim. Acta 46, 1327–1332. doi:10.1016/0016-7037(82)90268-X

Stolper, D.A., Lawson, M., Davis, C.L., Ferreira, A.A., Neto, E.V.S., Ellis, G.S., Lewan, M.D., Martini, A.M., Tang, Y., Schoell, M., Sessions, A.L., Eiler, J.M., 2014. Formation temperatures of thermogenic and biogenic methane. Science 344, 1500–1503. doi:10.1126/science.1254509

Stroeve, J., Serreze, M., Drobot, S., Gearheard, S., Holland, M., Maslanik, J., Meier, W., Scambos, T., 2008. Arctic Sea Ice Extent Plummets in 2007. Eos Trans. Am. Geophys. Union 89, 13–14. doi:10.1029/2008EO020001

Sundvor, E., Austegard, A., 1990. The Evolution of the Svalbard Margins: Synthesis and New Results, in: Bleil, U., Thiede, J. (Eds.), Geological History of the Polar Oceans: Arctic versus Antarctic, NATO ASI Series. Springer Netherlands, pp. 77–94.

Thoning, K.W., Tans, P.P., Komhyr, W.D., 1989. Atmospheric carbon dioxide at Mauna Loa Observatory: 2. Analysis of the NOAA GMCC data, 1974–1985. J. Geophys. Res. Atmospheres 94, 8549–8565. doi:10.1029/JD094iD06p08549

Thornton, B.F., Crill, P., 2015. Arctic permafrost: Microbial lid on subsea methane. Nat. Clim. Change 5, 723–724. doi:10.1038/nclimate2740

Tissot, B.P., Welte, D.H., 1978. Petroleum Formation and Occurrence a New Approach to Oil and Gas Exploration. Springer Berlin Heidelberg, Berlin, Heidelberg.

Treude, T., Orphan, V., Knittel, K., Gieseke, A., House, C.H., Boetius, A., 2007. Consumption of Methane and CO2 by Methanotrophic Microbial Mats from Gas Seeps of the Anoxic Black Sea. Appl. Environ. Microbiol. 73, 2271–2283. doi:10.1128/AEM.02685-06

Vance, S., Harnmeijer, J., Kimura, J., Hussmann, H., deMartin, B., Brown, J.M., 2007. Hydrothermal Systems in Small Ocean Planets. Astrobiology 7, 987–1005. doi:10.1089/ast.2007.0075

Vanneste, M., Berndt, C., Laberg, J.S., Mienert, J., 2007. Large shelf embayments between cross-shelf troughs west of Svalbard-Glaciodynamics vs. slope failure processes. Quat. Sci. Rev. 26, 2406–2419.

Vogt, P.R., Cherkashev, G., Ginsburg, G., Ivanov, G., Milkov, A., Crane, K., Sundvor, A., Pimenov, N., Egorov, A., 1997. Haakon Mosby Mud Volcano provides unusual example of venting. Eos Trans. Am. Geophys. Union 78, 549–557. doi:10.1029/97EO00326

Vogt, P.R., Crane, K., Sundvor, E., Max, M.D., Pfirman, S.L., 1994. Methane-generated(?) pockmarks on young, thickly sedimented oceanic crust in the Arctic: Vestnesa ridge, Fram strait. Geology 22, 255–258. doi:10.1130/0091-7613(1994)022<0255:MGPOYT>2.3.CO;2

Walter Anthony, K.M., Anthony, P., Grosse, G., Chanton, J., 2012. Geologic methane seeps along boundaries of Arctic permafrost thaw and melting glaciers. Nat. Geosci. 5, 419–426. doi:10.1038/ngeo1480

Weber, T.C., Mayer, L., Jerram, K., Beaudoin, J., Rzhanov, Y., Lovalvo, D., 2014. Acoustic estimates of methane gas flux from the seabed in a 6000 km 2 region in the Northern Gulf of Mexico. Geochem. Geophys. Geosystems 15, 1911–1925. doi:10.1002/2014GC005271

Wecht, K.J., Jacob, D.J., Wofsy, S.C., Kort, E.A., Worden, J.R., Kulawik, S.S., Henze, D.K., Kopacz, M., Payne, V.H., 2012. Validation of TES methane with HIPPO aircraft observations: implications for inverse modeling of methane sources. Atmos Chem Phys 12, 1823–1832. doi:10.5194/acp-12-1823-2012

Westbrook, G.K., Chand, S., Rossi, G., Long, C., Bünz, S., Camerlenghi, A., Carcione, J.M., Dean, S., Foucher, J.-P., Flueh, E., Gei, D., Haacke, R.R., Madrussani, G., Mienert, J., Minshull, T.A., Nouzé, H., Peacock, S., Reston, T.J., Vanneste, M., Zillmer, M., 2008. Estimation of gas hydrate concentration from multi-component seismic data at sites on the continental margins of NW Svalbard and the Storegga region of Norway. Mar. Pet. Geol. 25, 744–758. doi:10.1016/j.marpetgeo.2008.02.003

Westbrook, G.K., Thatcher, K.E., Rohling, E.J., Piotrowski, A.M., Pälike, H., Osborne, A.H., Nisbet, E.G., Minshull, T.A., Lanoisellé, M., James, R.H., Hühnerbach, V., Green, D., Fisher, R.E., Crocker, A.J., Chabert, A., Bolton, C., Beszczynska-Möller, A., Berndt, C., Aquilina, A., 2009. Escape of methane gas from the seabed along the West Spitsbergen continental margin. Geophys. Res. Lett. 36, L15608. doi:10.1029/2009GL039191

Wright, I.C., et al, 2012. RRS James Clark Ross Cruise 253, 26 Jul -25 Aug 2011. Arctic methane hydrates [WWW Document]. URL http://nora.nerc.ac.uk/439241/ (accessed 2.25.16).

Zeikus, J.G., 1977. The biology of methanogenic bacteria. Bacteriol. Rev. 41, 514–541.

Zhang, Y., 2003. Methane escape from gas hydrate systems in marine environment, and methane-driven oceanic eruptions. Geophys. Res. Lett. 30, 1398. doi:10.1029/2002GL016658

Zhang, Y., Xu, Z., 2003. Kinetics of convective crystal dissolution and melting, with applications to methane hydrate dissolution and dissociation in seawater. Earth Planet. Sci. Lett. 213, 133–148. doi:10.1016/S0012-821X(03)00297-8

2. Optical and hydroacoustic techniques for locating, monitoring and quantifying gas

Several techniques and methodologies have been developed to locate, monitor and quantify the released methane into the water column. These techniques have been shown to be useful for tracking methane gas bubbles in the water column and investigating the fate of the methane. Commonly used techniques are visual observations and hydroacoustic methods to detect gas bubbles in the water column. These were the main techniques used in this thesis. A brief description of these techniques is presented below:

2.1. Photo-optical systems

Optical imaging systems are commonly used in marine sciences in general and have been widely applied in gas seep studies. Video recording of seep sites has been focused on studying the dynamics of bubble release, gas quantification, characterization of microbial communities and seafloor classification. Visual evidence (photography and video) of gas release has been acquired by using underwater video-camera systems mounted on remotely operated underwater vehicles (ROV) or towed frames (Fig. 2.2; e.g. Greinert et al., 2006; Thomanek et al., 2010; Römer et al. 2012b; Sahling et al. 2014). Visual information of methane bubbles has been utilized to e.g. derive bubble size distributions (BSD; Römer et al., 2012b; McGovern, 2012; Ostrovsky et al., 2008; Leifer et al., 2002, Greinert and Nützel, 2004) which can be used to estimate/determine the amount of transported gas, bubble rising speeds values (e.g. see McGinnis et al., 2006) or to estimate the scattered sound produced by the bubble cloud (e.g. Medwin, 1977). Image scaling is usually done by placing objects of known dimensions next to the bubbles. Visual observations of bubble sizes have been shown to be very consistent in different seep areas and release depth. Although one of the main goals is to determine the gas transport in the water column, which is mainly carried out by large bubbles, it is necessary to highlight the limitation in resolution of this technique in identifying microbubbles. Alternatively, hydroacoustic passive systems, which will be mentioned in the next section, could be a good option to improve the resolution problem.

Bubble rising speeds (BRSs) are essential to establish the flow rate/flux of gas seeps. Observations of ascending bubbles using photo-optical systems have already been documented by several researchers e.g. Greinert et al., 2006; Römer et al. 2012b; Sahling et al. 2014). Results from visual bubble rising velocity studies have been used to validate bubble rising speed models (BRSMs) or create empirical relationships between BRS and bubble sizes (e.g. Mendelson 1967; Woolf and Thorpe 1991; Leifer and Patro 2002; Greinert et al., 2006). Using the optical information, bubble fluxes can be determined (e.g. Römer et al. 2012b; Greinert et al., 2010; Sahling et al. 2014). Usually flux measurements are accompanied by trapping bubbles with an inverted-funnel for direct flux measurements (Fig. 2.1) and gas sampling for later geochemical analyses.

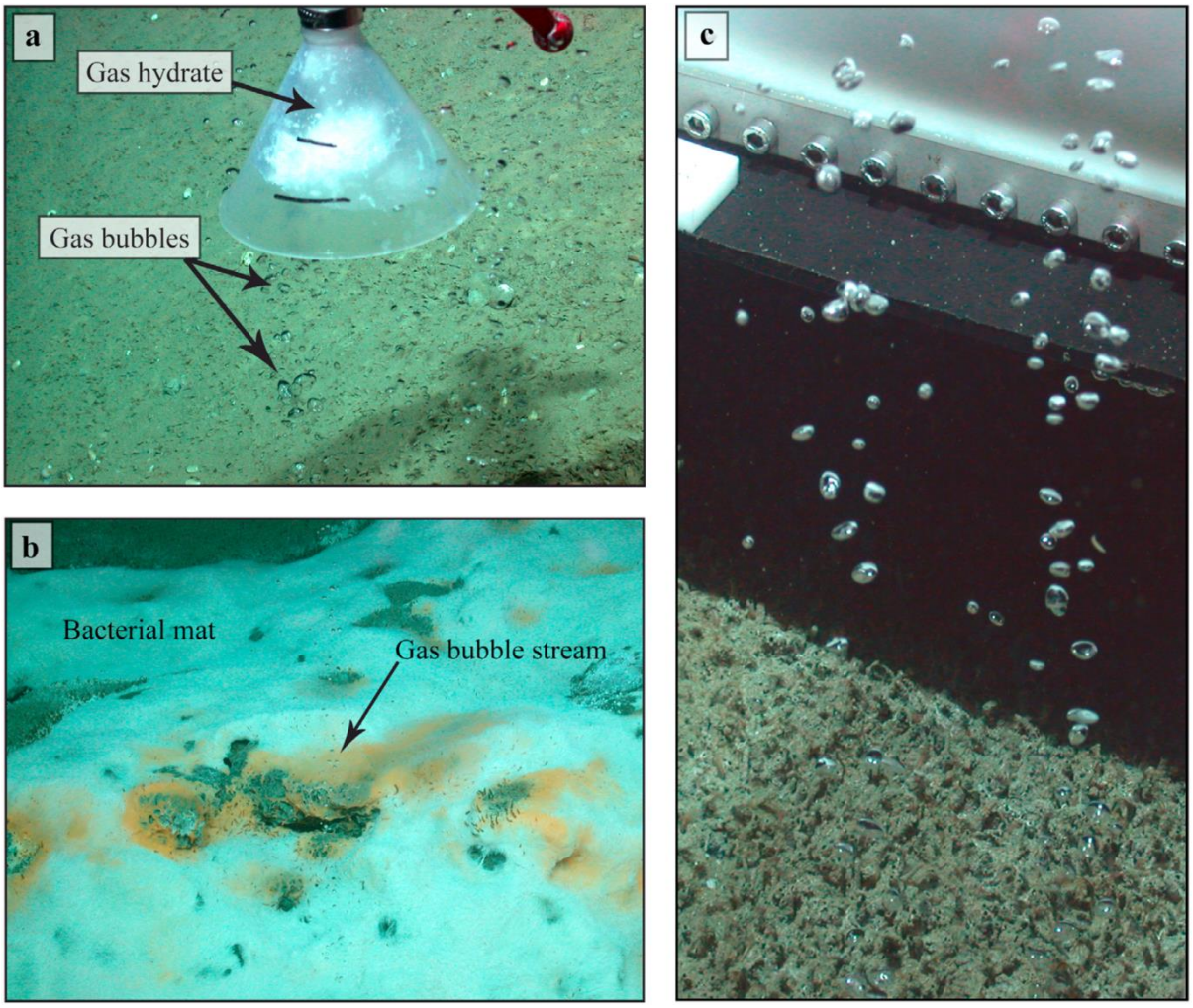

Figure 2.1. a) Gas bubbles collected with the inverted funnel of a Gas Bubble Sampler. The figure shows the gas hydrate skin formation around the bubbles when they were trapped. b) Bubbles release through a thick mat of sulfide-oxidizing filamentous bacteria. c) Two gas bubble streams released at the seafloor (Roemer et al. 2012b).

Several reports in the literature describe image-based and funnel-trapping measurements of bubbles. Leifer and Boles (2005) designed a diver operated device able to optically measure flow rates and bubble size distributions simultaneously for shallow water applications down to 30 m. Leifer and MacDonald (2003) employed a manned submersible to record image data at a seep field in the Gulf of Mexico. At Håkon Mosby mud volcano, optical flux estimation has been carried out using ROV cameras (Sauter, 2006). Sahling et al. (2009) estimated gas fluxes at the Vodyanitskii mud volcano in the Black Sea also using visual information collected with ROV cameras. Greinert et al. (2010) used the submersible JAGO to estimate fluxes of seep sites at a Black Sea shelf area. At Hydrate Ridge in situ flow rate estimations were carried out using the time required to displace the fluid inside the gas collector (Torres et al., 2002). Thomanek et al. (2010) presented a deployable system ('Bubblemeter') for in situ automated image processing and data management (Fig. 2.2).

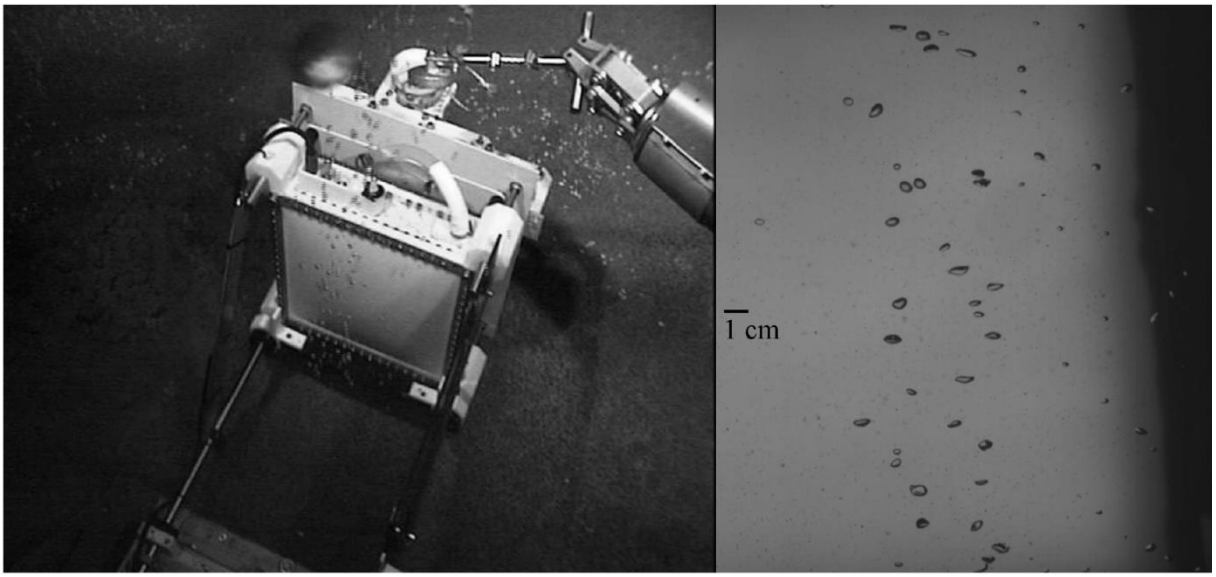

Figure 2.2. Left: Bubblemeter positioned and ready to be triggered by the ROV manipulator. Right: Gas bubbles rising between the camera and the illumination device (Thomanek et al., 2010).

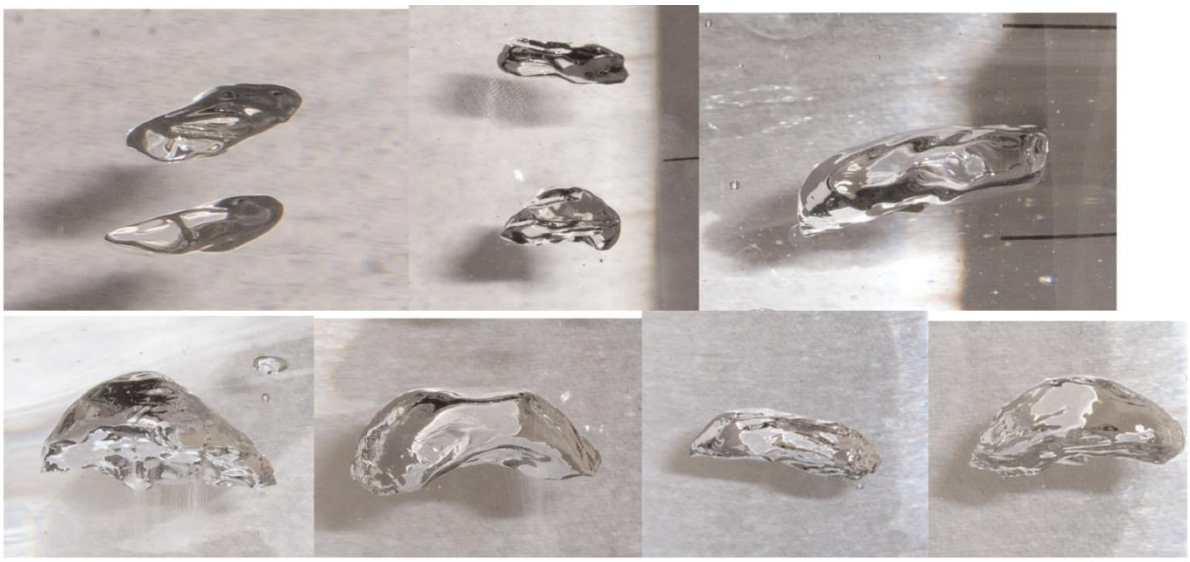

Figure 2.3. Images of rising bubbles ranging from 1 to 3 mL showing the variability in shape (Ostrovsky et al., 2008).

Optical observations of bubble allometry reported that ascending bubbles get more deformed as they increase their size (Fig. 2.3; Ostrovsky et al., 2008; Thomanek et al., 2010). Clift et al. (1978) classifies rising bubbles in a fluid of gravitational forces according to their sizes in three regimes: spherical, ellipsoidal, and spherical cap (see also Amaya-Bower and Lee, 2010). Their observations also show that the BRS is also affected by bubble deformation.

2.2. Hydroacoustics

Visual estimates of bubble fluxes are precise but not practical when it is necessary to evaluate the flux from an entire seep field that covers a large area. A more efficient alternative for calculating fluxes but less precise due to errors introduced by e.g. the theoretical inversion or instrumental accuracy, is the use of hydroacoustics methods that are able to map larger areas in shorter time. Hydroacoustic systems used for monitoring/quantification of free gas released into the water column can be divided in active and passive systems. Active systems transmit a wavefront and receive the scattered signal while passive systems just listen without transmitting. A brief description of the use of these systems in bubble venting research is detailed below.

2.2.1. Active systems

Underwater acoustic systems have been used for detecting and analyzing free gas release into the water column for already some decades (e.g. Watkins and Worzel, 1978; Merewether et al., 1985). Among of them, hydroacoustic active systems such as singlebeam and multibeam echosounder systems (SBES and MBES respectively; Fig. 2.4) have the ability to map large areas without interfering with the dynamics of the bubble release itself (non-invasive method). The use of active hydroacoustic systems has mainly focused on localization, monitoring and flux quantification of gas seepage. Active systems are considered to be highly sensitive, detecting free gas in the water owing to the strong impedance difference between the free gas phase and the water.

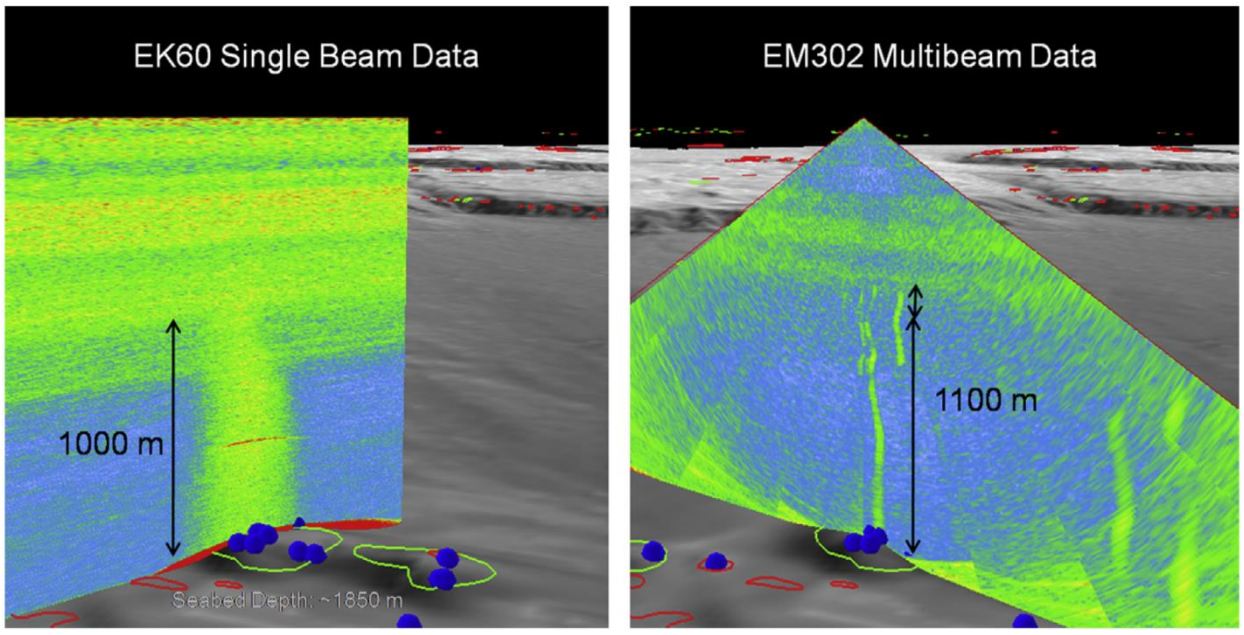

Figure 2.4. Visualization of the SBES (left) and MBES (right) curtains that contain acoustic flares (Colbo et al., 2014).

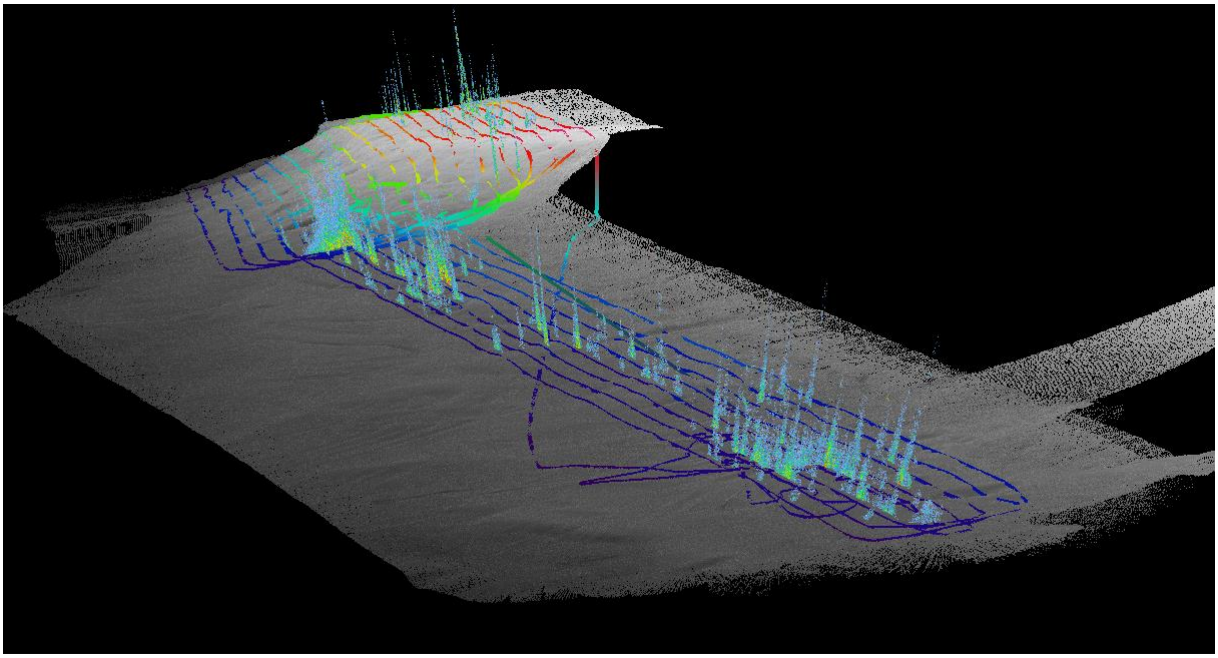

Figure 2.5. Acoustic flares detected at **PKF** detected with the EK60 split-beam echosounder. Echogram curtains have been located over the bathymetric surface. Acoustic flares are coming from the dataset presented in this thesis.

SBES and MBES (Figs. 2.4 and 2.5) are usually mounted in the hull of the ship or in ROV (e.g. Nikolovska et al., 2008) with the beam axis oriented downward, or in deployable systems with the beam axis oriented horizontally to vertically insonify the bubble release path (e.g. Greinert a, 2008). Bubbles can produce strong scattering if they are insonified close to their resonance frequency (see chapter theory). Flux estimates can be inferred from the scattering produced by bubbles when they are insonified by a wavefront, produced by the system. There are several publications that report gas flux estimates from bubble release by using inverse hydroacoustics methods. Artemov et al. (2007) related the backscattering produced by bubble jets with bubble sizes and seep productivity (number of bubbles/vertical distance), estimating the emitted methane in an area located at the Black Sea. Ostrovsky et al. (2008) used an empirical method to establish a relationship between the volumes and acoustical backscattering cross-section of individual bubbles. They calculated the bubble fluxes emitted into the water column from a seep site area located at Lake Kinneret using a combination of established relationships and bubble rise velocity measurements. Nikolovska et al. (2008) estimated the gas flux of a seep area located at the eastern Black Sea using an inverse model based on the principle of finding the ‘‘acoustic mass’’. Muyakshin and Sauter (2010) presented an inverse hydroacoustic method to calculate the flux emitted from bubble plumes. The method involves theoretical scattering from bubbles, volume backscattering strength (S_V) values calculated in situ and BRS values (for more detail see chapter 3). The method was successfully applied to quantify the total convective methane flux at the HMMV at 1280 m water depth. Inverse methods are only applicable with data obtained from active systems that can be calibrated, because parameters such as transducer gain or equivalent beam angle are needed to calculate target strength (TS) or volume backscattering strength values (S_V).

MBES just recently have started to be used in submarine gas seeps analysis, since initially they were designed to map the seafloor only. New system developments now allow extracting information from the water column as well (e.g. Fig. 2.6; e.g. Schneider et al., 2007). So far, MBES have been used commonly for the detection of seep sites, for determining seep field extent and for flare number estimations, for the analysis of the spatial and temporal variability of gas release, and for the final depth evaluation of bubbles in the water column (e.g. Nikolovska et al. 2008; Greinert, 2008, Schneider et al., 2007). Additionally, extrapolated flux estimates of large seep areas have been carried out by using the combination of gas flow rates visually calculated and flare numbers extracted from MBES observations (e.g. Römer et al. 2012a, Sahling et al., 2014).

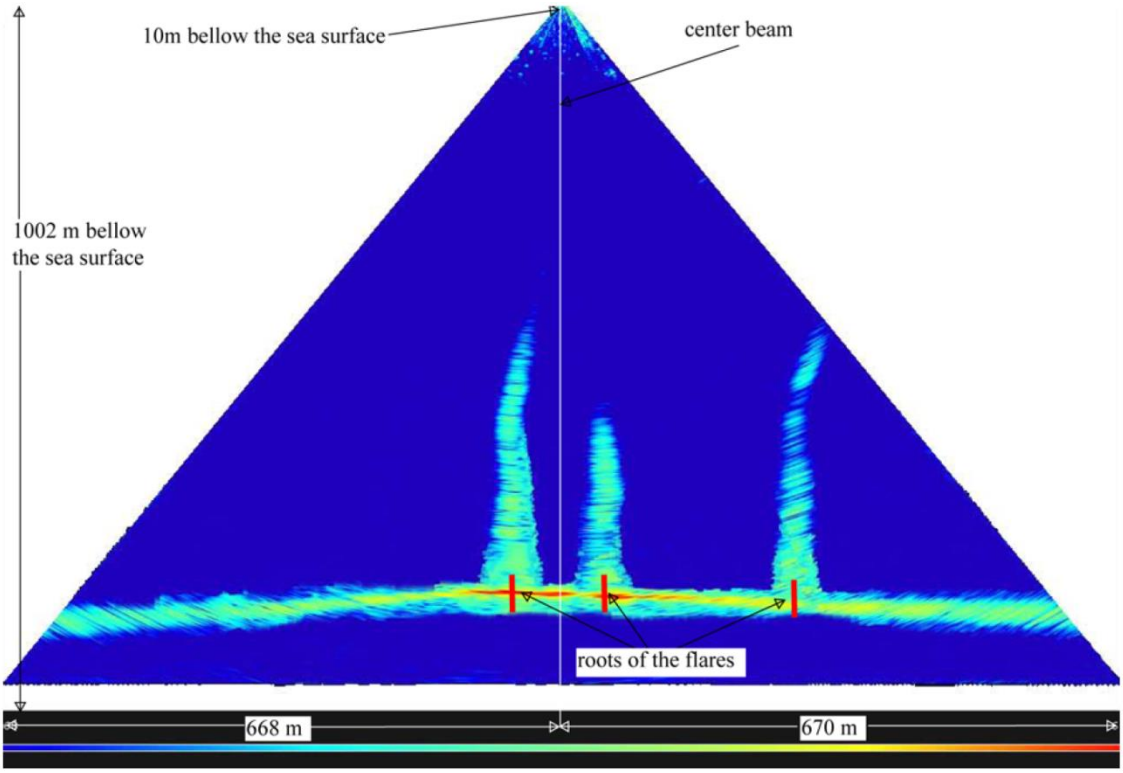

Figure 2.6. MBES echogram showing bubble streams rising from the seafloor. (Nikolovska et al.2008)

Improvements in the MBES technology have been triggered in response to the needs of the scientific community. An example of that is the lander-based system is the GasQuant system (Fig. 2.7) developed by J. Greinert in cooperation with ELAC Nautik in Kiel, Germany (Greinert and Nützel, 2004; Greinert, 2008). GasQuant uses a modified SeaBeam 1000 MBES with a horizontally oriented swath (21 beams, 63° swath angle, 180 kHz) to detect bubbles that rise through the swath from the seabed. The system has been designed to constantly monitor seep activity to understand the bubble release dynamics. Greinert and Nützel (2004) demonstrate by using a SBES, that bubble flux is proportional to the backscatter of the insonified volume at flow rates up to 20 L/min. The GasQuant lander has been deployed already at several places as the Black Sea (Greinert, 2008) and the North Sea (Schneider et al., 2010).

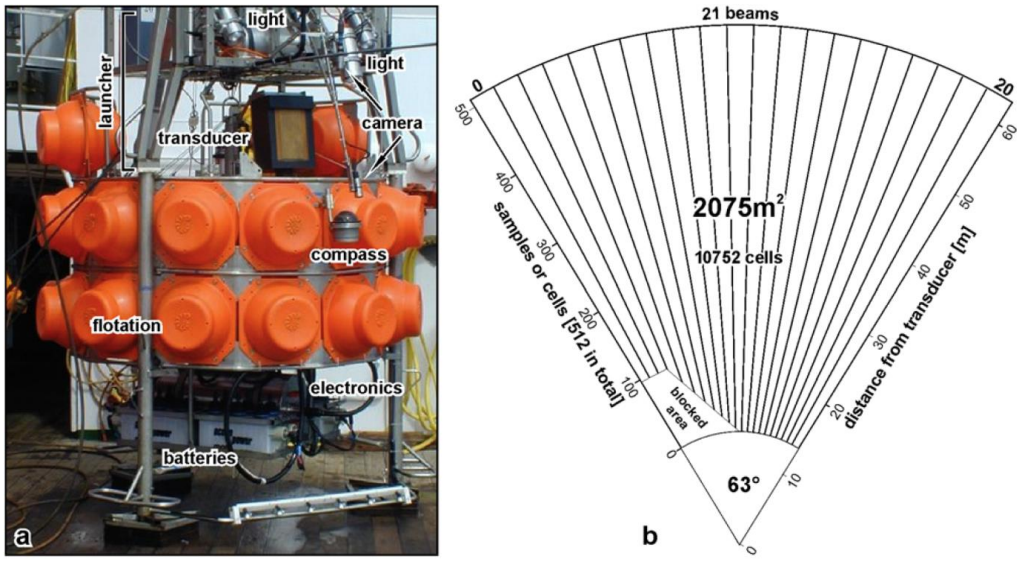

Figure 2.7. a) Image of the GasQuant lander with launcher system ready for deployment. b) Size of the hydroacoustic swath showing the 21 beams and positions of the analyzed samples per beam (Greinert and Nützel, 2004).

Kongsberg recently developed the Simrad ME70 system which groups EK60 split-beam echosounders to form a kind of MBES. Such a system allows obtaining both TS and S_V values coming from scatterers in the water column as with normal SBES but with a much larger coverage. This enormously decreases survey time. Hydroacoustic data coming from this system could be used as an input of inverse hydroacoustics methods like the one presented in this thesis (chapter 4).

Finally, Acoustic Doppler Current Profilers (ADCP) have been also used to describe the dynamics of bubble emissions from the seafloor. Data describe the temporal variability of bubble emissions and are used estimating BRSs (Fig. 2.8; Vagle et al. 2010; McGinnis et al., 2006; Linke et al., 2010; Salmi et al., 2011; Kannberg et al., 2013; Schmidt et al., 2013).

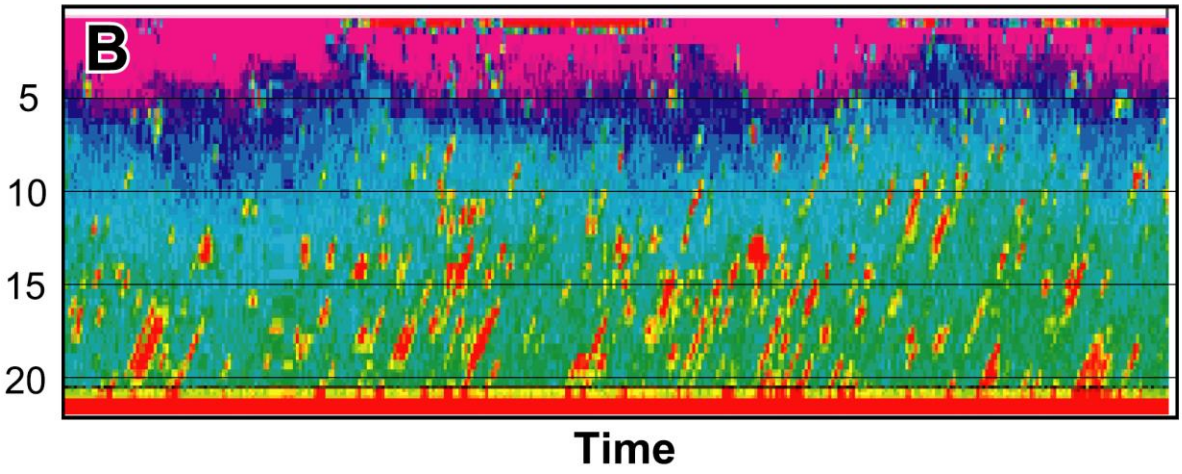

Figure 2.8. ADCP backscatter measurements from Iron Gate I dam on the Danube River (Romania). The strong backscatter data in the water column represent the bubble release from the sediment. Image taken from McGinnis et al., (2006).

2.2.2. Passive Systems

In addition to all the different active acoustic methods discussed above, passive techniques have also been applied when studying bubble release from the seafloor. It is well known that bubbles oscillate at their natural frequency when they are formed (e.g. detached from the seafloor, produced at the sea surface by breaking waves), producing as a result a sound field in the surrounding media (Minnaert, 1933; Leighton and Walton, 1987). Minnaert (1933) as a pioneer established the relationship between the resonance frequency of a bubble and its size (radius) assuming simple harmonic motion. The acoustic signature that bubbles leave when they are formed has been used in studies related with BSD and flux quantification of bubble release. Leighton and Walton (1987) developed an experiment to analyze the frequency, pressure amplitude, and decay characteristics during the formation of bubbles, by 'listening' to them with hydrophones. Their measurements agreed with the natural oscillation frequency of the bubble (Minnaert frequency) and theoretical bubble damping values (e.g. Prosperetti, 1977). Nikolovska and Waldmann (2006) designed a passive hydroacoustic system to measure the gas flux from gas seepage. Their method was based on a Morlet wavelet analysis of the recorded sound signal series. Data were in agreement with their optical observations (see also Nikolovska et al., 2007). Leifer and Tang (2007) measured acoustical signatures at the La Goleta Seeps (Coal Oil Point; California) obtaining that bubble radii were lower than predicted by the Minnaert formula. They also observed frequency shifts attributed to coupling of neighboring bubbles and surfactants. Greene and Wilson (2011) presented a mathematical model for active hydroacoustic systems to study the behavior of natural gas bubbles emitted at the seafloor taking into account the physical ambient conditions (Fig. 2.9).

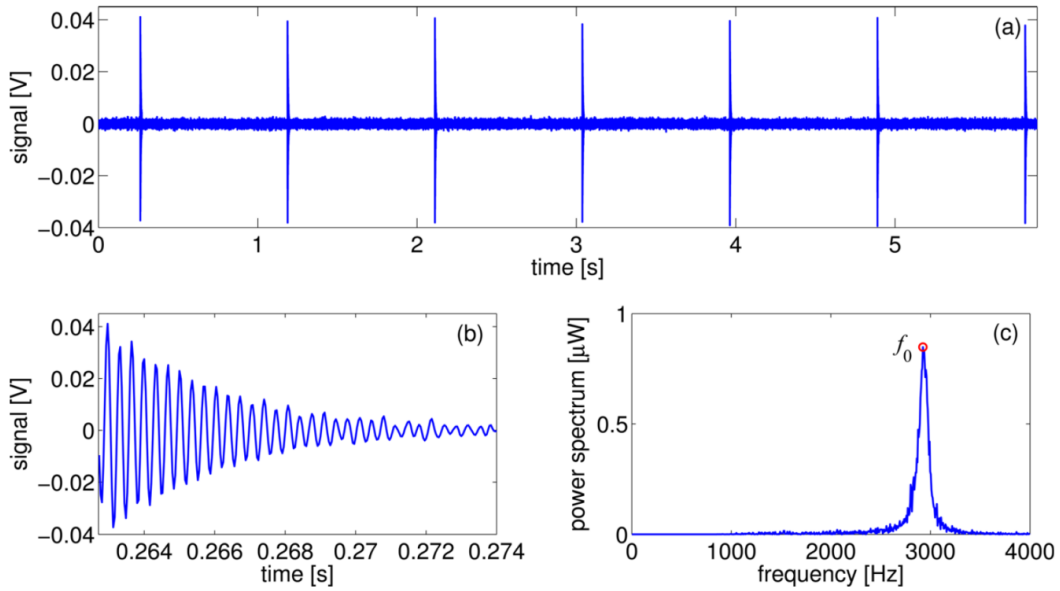

Figure 2.9. Example of passive acoustic recording of air-bubble release in water tank showing (a) first 6 s of recording; (b) zoomed-in plot of the first recorded bubble—exponential decay; and (c) FFT of recorded signal of first bubble (with zero-padding) (Greene and Wilson, 2012).

Maksimov et al. (2014) have recently proposed a new theoretical model for bubble volume pulsations at relatively small distances from the rigid-bottom boundary. They suggest that the model is more

appropriate to bubble releasing at the seafloor and that it has to be considered when using passive acoustic techniques in marine seep studies. Leighton and White (2012) describe a method for quantifying the gas flux and bubble size distribution injected into liquid from high flux leaks using their acoustic emissions. The method considers the signature overlapping produced by the release of a large amount of bubbles when they are released. Leighton and White (2012) suggest that the most important unknown is the acoustic energy released by an individual bubble. Berges et al (2015) have proven the accuracy and applicability of the method (Leighton and White, 2012) against experimental data, showing an agreement at a practically useful level for high flow rates. In summary, hydroacoustic techniques play an important role in the research field of submarine gas release, being even stronger when they are combined.

The following table summarizes the applicability, advantanges and disadvantages of the techniques for locating, monitoring and quantifying gas seepage in underwater environments.

Table 2.1. Summary of optical and hydroacoustic techniques

Techniques			**Applicability**	**Advantages**	**Disadvantages**
Photo-optical systems			-Quantification of bubble flow rates -Determination of BRSs and BSDs -Monitoring of gas seeps	-Direct observations of the bubble release	-Short range -Limitation in resolution to detect microbubbles -Limitation in coverage
Hydroacoustic systems	**Passive**	**Hydrophones**	-Monitoring of gas seeps -Measurement of bubble flow rates through inversion	-Non-invasive -Wide Bandwidth -Low energy -Portable	-Short range -Received signal can be easily overlapped by background noise
	Active	**SBES**	-Location of seepage at the seafloor -Monitoring of gas seeps -Quantification of bubble flow rates through inversion -Determination of BRSs	-Non-invasive -Long range -Calibrated systems useful for quantification of bubble fluxes of large seep sites areas	-Not able to identify the amount of bubble vents within the footprint -Narrow Bandwidth Limited in spatial coverage
		MBES	-Location of seepage at the seafloor -Monitoring of gas seeps -Determination of BRSs	-Long range -Large spatial coverage	-Usually non-calibrated systems (except Simrad ME70) -Narrow Bandwidth
		ADCP	-Evaluation of temporal variability of bubble emission (e.g., bubble periodicity and BRSs)	-Long range -Able to locate targets in the water column	-Non-calibrated system -Narrow Bandwidth -Limited in spatial coverage

References

Amaya-Bower, L., Lee, T., 2010. Single bubble rising dynamics for moderate Reynolds number using Lattice Boltzmann Method. Comput. Fluids 39, 1191–1207. doi:10.1016/j.compfluid.2010.03.003

Artemov, Y.G., Egorov, V.N., Polikarpov, G.G., Gulin, S.B., 2007. Methane emission to the hydro- and atmosphere by gas bubble streams in the Dnieper paleo-delta, the Black Sea. Morskyji ehkologichnyji zhurnal (Marine Ecological Journal) 6, 5–26.

Bergès, B.J.P., Leighton, T.G., White, P.R., 2015. Passive acoustic quantification of gas fluxes during controlled gas release experiments. Int. J. Greenh. Gas Control 38, 64–79. doi:10.1016/j.ijggc.2015.02.008

Clift, R., Grace, J.R., Weber, M.E., 2013. Bubbles, drops, and particles. Dover Publ, Mineola, NY.

Colbo, K., Ross, T., Brown, C., Weber, T., 2014. A review of oceanographic applications of water column data from multibeam echosounders. Estuar. Coast. Shelf Sci. 145, 41–56. doi:10.1016/j.ecss.2014.04.002

Greene, C.A., Wilson, P.S., 2012. Laboratory investigation of a passive acoustic method for measurement of underwater gas seep ebullition. J. Acoust. Soc. Am. 131, EL61–EL66. doi:10.1121/1.3670590

Greinert, J., 2008. Monitoring temporal variability of bubble release at seeps: The hydroacoustic swath system GasQuant. J. Geophys. Res. Oceans 113, C07048. doi:10.1029/2007JC004704

Greinert, J., Artemov, Y., Egorov, V., De Batist, M., McGinnis, D., 2006. 1300-m-high rising bubbles from mud volcanoes at 2080 m in the Black Sea: Hydroacoustic characteristics and temporal variability. Earth Planet. Sci. Lett. 244, 1–15. doi:10.1016/j.epsl.2006.02.011

Greinert, J., McGinnis, D.F., Naudts, L., Linke, P., De Batist, M., 2010. Atmospheric methane flux from bubbling seeps: Spatially extrapolated quantification from a Black Sea shelf area. J. Geophys. Res. 115. doi:10.1029/2009JC005381

Greinert, J., Nützel, B., 2004. Hydroacoustic experiments to establish a method for the determination of methane bubble fluxes at cold seeps. Geo-Mar. Lett. 24, 75–85. doi:10.1007/s00367-003-0165-7

Kannberg, P.K., Tréhu, A.M., Pierce, S.D., Paull, C.K., Caress, D.W., 2013. Temporal variation of methane flares in the ocean above Hydrate Ridge, Oregon. Earth Planet. Sci. Lett. 368, 33–42. doi:10.1016/j.epsl.2013.02.030

Leifer, I., Boles, J., 2005. Measurement of marine hydrocarbon seep flow through fractured rock and unconsolidated sediment. Mar. Pet. Geol., Near-Surface Hydrocarbon Migration: Mechanisms and Seepage Rates 22, 551–568. doi:10.1016/j.marpetgeo.2004.10.026

Leifer, I., MacDonald, I., 2003. Dynamics of the gas flux from shallow gas hydrate deposits: interaction between oily hydrate bubbles and the oceanic environment. Earth Planet. Sci. Lett. 210, 411–424. doi:10.1016/S0012-821X(03)00173-0

Leifer, I., Patro, R.K., 2002. The bubble mechanism for methane transport from the shallow sea bed to the surface: A review and sensitivity study. Cont. Shelf Res., Gas in Marine Sediments: Contributions from the 5th International Conference orgainsed by the Shallow Gas Group, Bologna, Italy, September 1998 22, 2409–2428. doi:10.1016/S0278-4343(02)00065-1

Leifer, I., Tang, D., 2007. The acoustic signature of marine seep bubbles. J. Acoust. Soc. Am. 121, EL35–EL40. doi:10.1121/1.2401227

Leighton, T.G., Walton, A.J., 1987. An experimental study of the sound emitted from gas bubbles in a liquid. Eur. J. Phys. 8, 98. doi:10.1088/0143-0807/8/2/005

Leighton, T.G., White, P.R., 2012. Quantification of undersea gas leaks from carbon capture and storage facilities, from pipelines and from methane seeps, by their acoustic emissions. Proc. R. Soc. Math. Phys. Eng. Sci. 468, 485–510. doi:10.1098/rspa.2011.0221

Linke, P., Sommer, S., Rovelli, L., McGinnis, D.F., 2010. Physical limitations of dissolved methane fluxes: The role of bottom-boundary layer processes. Mar. Geol., Methane seeps at the Hikurangi Margin, New Zealand 272, 209–222. doi:10.1016/j.margeo.2009.03.020

Maksimov, A.O., Burov, B.A., Salomatin, A.S., Chernykh, D.V., 2014. Sounds of marine seeps: A study of bubble activity near a rigid boundary. J. Acoust. Soc. Am. 136, 1065–1076. doi:10.1121/1.4892753

McGinnis, D.F., Greinert, J., Artemov, Y., Beaubien, S.E., Wüest, A., 2006. Fate of rising methane bubbles in stratified waters: How much methane reaches the atmosphere? J. Geophys. Res. Oceans 111, C09007. doi:10.1029/2005JC003183

McGovern, C., 2012. Video-based quantification of gas bubble fluxes from the seafloor offshore western Svalbard (Msc. thesis). Univ. of Bremen.

Medwin, H., 1977. Counting bubbles acoustically: a review. Ultrasonics 15, 7–13. doi:10.1016/0041-624X(77)90005-1

Memery, L., Merlivat, L., 1985. Modelling of gas flux through bubbles at the air-water interface. Tellus B 37B, 272–285. doi:10.1111/j.1600-0889.1985.tb00075.x

Mendelson, H.D., 1967. The prediction of bubble terminal velocities from wave theory. AIChE J. 13, 250–253. doi:10.1002/aic.690130213

Merewether, R., Olsson, M.S., Lonsdale, P., 1985. Acoustically detected hydrocarbon plumes rising from 2-km depths in Guaymas Basin, Gulf of California. J. Geophys. Res. Solid Earth 90, 3075–3085. doi:10.1029/JB090iB04p03075

Minnaert, M., 1933. XVI. On musical air-bubbles and the sounds of running water. Lond. Edinb. Dublin Philos. Mag. J. Sci. 16, 235–248. doi:10.1080/14786443309462277

Muyakshin, S.I., Sauter, E., 2010. The hydroacoustic method for the quantification of the gas flux from a submersed bubble plume. Oceanology 50, 995–1001. doi:10.1134/S0001437010060202

Nikolovska, A., Manasseh, R., Ooi, A., 2007. On the propagation of acoustic energy in the vicinity of a bubble chain. J. Sound Vib. 306, 507–523. doi:10.1016/j.jsv.2007.05.025

Nikolovska, A., Sahling, H., Bohrmann, G., 2008. Hydroacoustic methodology for detection, localization, and quantification of gas bubbles rising from the seafloor at gas seeps from the eastern Black Sea: HYDROACOUSTIC GAS QUANTIFICATION. Geochem. Geophys. Geosystems 9, n/a–n/a. doi:10.1029/2008GC002118

Nikolovska, A., Waldmann, C., 2006. Passive acoustic quantification of underwater gas seepage, in: OCEANS 2006. Presented at the OCEANS 2006, pp. 1–6. doi:10.1109/OCEANS.2006.306926

Ostrovsky, I., McGinnis, D.F., Lapidus, L., Eckert, W., 2008. Quantifying gas ebullition with echosounder: the role of methane transport by bubbles in a medium-sized lake. Limnol. Oceanogr. Methods 6, 105–118. doi:10.4319/lom.2008.6.105

Prosperetti, A., 1977. Thermal effects and damping mechanisms in the forced radial oscillations of gas bubbles in liquids. J. Acoust. Soc. Am. 61, 17–27. doi:10.1121/1.381252

Römer, M., Sahling, H., Pape, T., Bahr, A., Feseker, T., Wintersteller, P., Bohrmann, G., 2012a. Geological control and magnitude of methane ebullition from a high-flux seep area in the Black Sea—the Kerch seep area. Mar. Geol. 319–322, 57–74. doi:10.1016/j.margeo.2012.07.005

Römer, M., Sahling, H., Pape, T., Bohrmann, G., Spieß, V., 2012b. Quantification of gas bubble emissions from submarine hydrocarbon seeps at the Makran continental margin (offshore Pakistan). J. Geophys. Res. Oceans 117, C10015. doi:10.1029/2011JC007424

Sahling, H., Bohrmann, G., Artemov, Y.G., Bahr, A., Brüning, M., Klapp, S.A., Klaucke, I., Kozlova, E., Nikolovska, A., Pape, T., Reitz, A., Wallmann, K., 2009. Vodyanitskii mud volcano, Sorokin trough, Black Sea: Geological characterization and quantification of gas bubble streams. Mar. Pet. Geol. 26, 1799–1811. doi:10.1016/j.marpetgeo.2009.01.010

Sahling, H., Römer, M., Pape, T., Bergès, B., dos Santos Fereirra, C., Boelmann, J., Geprägs, P., Tomczyk, M., Nowald, N., Dimmler, W., Schroedter, L., Glockzin, M., Bohrmann, G., 2014. Gas emissions at the continental margin west off Svalbard: mapping, sampling, and quantification. Biogeosciences Discuss. 11, 7189–7234. doi:10.5194/bgd-11-7189-2014

Salmi, M.S., Johnson, H.P., Leifer, I., Keister, J.E., 2011. Behavior of methane seep bubbles over a pockmark on the Cascadia continental margin. Geosphere 7, 1273–1283. doi:10.1130/GES00648.1

Schneider von Deimling, J., Brockhoff, J., Greinert, J., 2007. Flare imaging with multibeam systems: Data processing for bubble detection at seeps. Geochem. Geophys. Geosystems 8, Q06004. doi:10.1029/2007GC001577

Schneider von Deimling, J., Greinert, J., Chapman, N.R., Rabbel, W., Linke, P., 2010. Acoustic imaging of natural gas seepage in the North Sea: Sensing bubbles controlled by variable currents. Limnol. Oceanogr. Methods 8, 155–171. doi:10.4319/lom.2010.8.155

Thomanek, K., Zielinski, O., Sahling, H., Bohrmann, G., 2010. Automated gas bubble imaging at sea floor – a new method of in situ gas flux quantification. Ocean Sci 6, 549–562. doi:10.5194/os-6-549-2010

Torres, M.E., McManus, J., Hammond, D.E., de Angelis, M.A., Heeschen, K.U., Colbert, S.L., Tryon, M.D., Brown, K.M., Suess, E., 2002. Fluid and chemical fluxes in and out of sediments hosting methane hydrate deposits on Hydrate Ridge, OR, I: Hydrological provinces. Earth Planet. Sci. Lett. 201, 525–540. doi:10.1016/S0012-821X(02)00733-1

Vagle, S., Hume, J., McLaughlin, F., MacIsaac, E., Shortreed, K., 2010. A methane bubble curtain in meromictic Sakinaw Lake, British Columbia. Limnol. Oceanogr. 55, 1313–1326. doi:10.4319/lo.2010.55.3.1313

Watkins, J.S., Worzel, J.L., 1978. Serendipity Gas Seep Area, South Texas Offshore: GEOLOGIC NOTES. AAPG Bull. 62, 1067–1074.

Woolf, D.K., Thorpe, S.A., 1991. Bubbles and the air-sea exchange of gases in near-saturation conditions. J. Mar. Res. 49, 435–466. doi:10.1357/002224091784995765

3. Acoustic theory of bubbles

3.1. Bubbles and acoustics

The theoretical background of the acoustics related with bubbles has its origin in the early 1920's, when physical concepts and properties (e.g. acoustical scattering cross-section, acoustical extinction cross-section, resonance frequency, bubble damping) had been properly defined. Nowadays, the behavior of acoustic waves in liquids that either interact or are generated by bubbles is a topic of interest for several research fields. To name a few: medical applications such as ultrasound imaging, lithotripsy and histotripsy (e.g. Chen et al., 2009; Cleveland and McAteer, 2007; Maxwell et al. 2011); ultrasonic cleaning using cavitation (e.g. Niemczewski, 2007); fishery (e.g. MacLennan and Simmonds, 1992); oil industry (e.g. Pedersen et al., 2014); marine geology (e.g. Greinert et al. 2006). Because bubbles in liquids are considered to be strong scatterers due to the large difference in acoustic impedance across the liquid-gas interface (e.g. acoustic impedance of water is ~3500 times higher than that of air), bubbles located in liquid media can easily be sensed remotely. The acoustic scattering is strongly enhanced when the frequency of the acoustic field insonifying the bubble is close to its resonance. As a reference, acoustical cross-sections can reach values of three to four orders of magnitude greater than its geometrical cross-section.

Hydroacoustic systems (active and passive) have recently been used to locate and monitor the release of bubbles from sources at the seafloor (see chapter 2). Experimental results have clearly shown a relationship between acoustical response and bubble flux rate intensities (e. g. Greinert and Nützel, 2004; Ostrovsky et al. 2008). Using the theoretical formulations of bubble acoustic response and real acoustic data, inverse hydroacoustic methods for bubble flux estimation have been developed and they have proven to be reliable (e.g. Nikolovska et al., 2008; Artemov, 2007; Muyakshin and Sauter 2010). The theoretical inverted formulation used and implemented in this research work is based on the total backscattering as a product of the constructive interference of single targets (bubbles) when a bubble cloud is insonified.

The goal of this chapter is to summarize the "foundations" of the acoustic theory involved in the hydroacoustic inverse method for bubble flux estimations presented in this thesis. Bubble resonance, damping and acoustical scattering cross-section of bubbles, which are the essential parts of this inverse method, are subsequently defined. Finally, the relationship between bubble flux and the backscattering produced by the bubble cloud is explained.

3.2. Bubble resonance

3.2.1. Minnaert resonance

A first approximation to calculate the resonance frequency of a spherical bubble in a liquid can be done by assuming that damping is negligible, that there are no effects due to surface tension or thermal

conductivity and that $kr \ll 1$ (which is the condition where the bubble is driven by the virtually uniform acoustic pressure over its surface). Here k represents the wave number and r the bubble radius.

The motion of a pulsating bubble can be represented with the mechanical equation of a mass-stiffness system:

$$m\frac{\partial^2 \xi}{\partial t^2} + s\xi = 0 \tag{3.1}$$

Where,

m: Equivalent bubble mass
s: Bubble stiffness
ξ: Bubble radial displacement

Equation [3.1] has the following solution,

$$\xi = \xi_0 e^{i\omega_b t} \tag{3.2}$$

If equation [3.2] is substituted in [3.1], an expression for the system natural frequency ω_b is obtained,

$$\omega_b = \sqrt{\frac{s}{m}} \tag{3.3}$$

Considering that the compressions and rarefactions of the bubble inner gas follow the adiabatic relation $p_i V^{\gamma} = constant$ and differentiating this we obtain,

$$\frac{dp_i}{dV} = -\frac{\gamma P_a}{V} \tag{3.4}$$

Where,

p_i : Inner bubble pressure

P_a : Static surrounding pressure

γ : Ratio of specific heats

V : Bubble volume; $V = \frac{4}{3}\pi r^3$

dV: Incremental bubble volume; $dV = 4\pi r^2 dr$

r: Bubble radius

The equation [3.4] can be rewritten in terms of the bubble radius, obtaining,

$$4\pi r^2 dp_i = -(12\pi\gamma P_a r)dr \tag{3.5}$$

Equation [3.5] has the form of Hook's law, showing that the stress is proportional to the strain. Then, bubble stiffness s (proportionality constant) is expressed by,

$$s = 12\pi\gamma P_a r \tag{3.6}$$

The equivalent bubble mass, which is related to the entrained water that surrounds the bubble, is calculated using the inertial force experienced by the radiating bubble.

Let us consider the bubble as an isotropic source. Then the pressure emitted by this source p_S, which is the scattered pressure, can be represented by,

$$p_S = \frac{P_{0S} r}{R} e^{i(\omega_b t - kR)} \tag{3.7}$$

Where k is the wave number and P_{0S} is the pressure amplitude at $R = r$.

In addition, the acoustic force equation (e.g. Medwin and Clay, 1998) for radial motion is defined by,

$$\rho_w \frac{\partial^2 \xi}{\partial t^2} = -\frac{\partial p_S}{\partial R} \tag{3.8}$$

Where ρ_w is the water density.

Replacing equation [3.7] in equation [3.8], it is obtained,

$$\rho_w \frac{\partial^2 \xi}{\partial t^2}\Big]_{R=r} = \frac{P_{0S} r}{R^2}(1 + ikR)e^{i(\omega_b t - kR)}\Big]_{R=r} \tag{3.9}$$

Because $kr \ll 1$, Eq. [3.9] can be simplified,

$$\rho_w \frac{\partial^2 \xi}{\partial t^2}\Big]_{R=r} = \frac{p_S}{r}\Big]_{R=r} \tag{3.10}$$

Then, using Newton's second law, the inertial force at the surface F_m can be obtained (Eq. 3.11) and the effective mass m identified (Eq. 3.12)

$$F_m]_{R=a} = -4\pi r^2 p_S]_{R=r} = -4\pi r^3 \rho_w \frac{\partial^2 \xi}{\partial t^2}\Big]_{R=r} \tag{3.11}$$

$$m = 4\pi r^3 \rho_w \tag{3.12}$$

Replacing equation [3.12] and equation [3.6] in [3.3], an expression of the harmonic breathing frequency of a small bubble ($kr \ll 1$) is obtained,

$$\omega_M = \frac{1}{r}\sqrt{\frac{3\gamma P_a}{\rho_w}} \tag{3.13}$$

This expression is also known as the Minnaert frequency, as Minnaert (1933) was the first to publish it.

3.2.2. Exact resonance frequency of a spherical bubble

Approximations for the exact resonance values have been described by Ainslie and Leighton (2010). The approximations have been developed using the concept of thermal diffusion length L_{th} and defining different regimes according to the rate between the bubble size and this term. The thermal diffusion length $L_{th}$is defined as following,

$$L_{th}(\omega, r) = \sqrt{\frac{D_P(r)}{2\omega}} \tag{3.14}$$

Where,

ω : Angular frequency

D_P : Thermal diffusivity of the gas inside the bubble

To define regimes of the different approximations of bubble resonance it is also necessary to introduce the thermal diffusion ratio,

$$X(\omega, r) = \frac{r}{L_{th}(\omega, r)} \tag{3.15}$$

Thermally large bubble

For a bubble thermally large at resonance, its resonance frequency ω_{RES} can be approximated to the "adiabatic resonance" ω_{AD} (Fig. 1; Neppiras, 1980), defined by,

$$\omega_{AD} = \omega_M \sqrt{1 + \frac{R_{Laplace}}{r}\left(1 - \frac{1}{3\gamma}\right)} \tag{3.16}$$

Where,

$$R_{Laplace} = \frac{2\sigma}{P_a} \tag{3.17}$$

$R_{Laplace}$: Laplace radius

σ : Surface tension

The $\omega_{RES} \approx \omega_{AD}$ approximation is valid for $X(\omega_{RES}, r) \gg 1$, which is approximately equivalent to $X(\omega_{AD}, r) \gg 1$.

Bubble with intermediate thermal size

An exact solution for the resonance frequency ω_{RES} of bubbles with intermediate thermal size is given by the followed iterative solution (Chapman and Plesset, 1971; Prosperetti, 1977; Aislie and Leighton, 2010),

$$\left(\frac{\omega_N^{RES}}{\omega_{AD}}\right)^2 = 1 - \left(1 - \frac{Re\Gamma\left(\omega_{N-1}^{RES}\right)}{\gamma}\right)\upsilon \tag{3.18}$$

Where,

$$\Gamma(\omega) = \frac{\gamma}{1 - \left\{\frac{(1+i)\,X/2}{\tan[(1+i)\,X/2]} - 1\right\}\frac{6i(\gamma-1)}{X^2}} \tag{3.19}$$

$$\upsilon = \upsilon(r) = \frac{1 + \frac{R_{Laplace}}{r}}{1 + \frac{R_{Laplace}}{r}\left(1 - \frac{1}{3\gamma}\right)} \tag{3.20}$$

Γ : Complex polytropic index (Chapman and Plesset, 1971; Prosperetti, 1984; Prosperetti, 1988)

υ : Dimensionless parameter related to the Laplace radius

The exact value of the resonance frequency can be obtained by repeated application of equation [3.14] until it converges. The solution can be obtained by seeding equation [3.19] with the adiabatic resonance frequency ($\omega_0^{RES} = \omega_{AD}$; Fig.1).

Thermally small bubble

For thermally small values ($r \ll L_{th}(\omega_{RES})$), the bubble is considered to pulsate isothermally at resonance, and the resonance frequency ω_{RES} can be approximated to the isothermal resonance frequency ω_{ISO} (Fig. 3.1; Neppiras, 1980) defined by,

$$\omega_{ISO} = \frac{\omega_M}{\sqrt{\gamma}}\sqrt{1 + \frac{4\tau}{3P_a r}}$$

The approximation $\omega_{RES} \approx \omega_{ISO}$ holds for $X < 3$ values

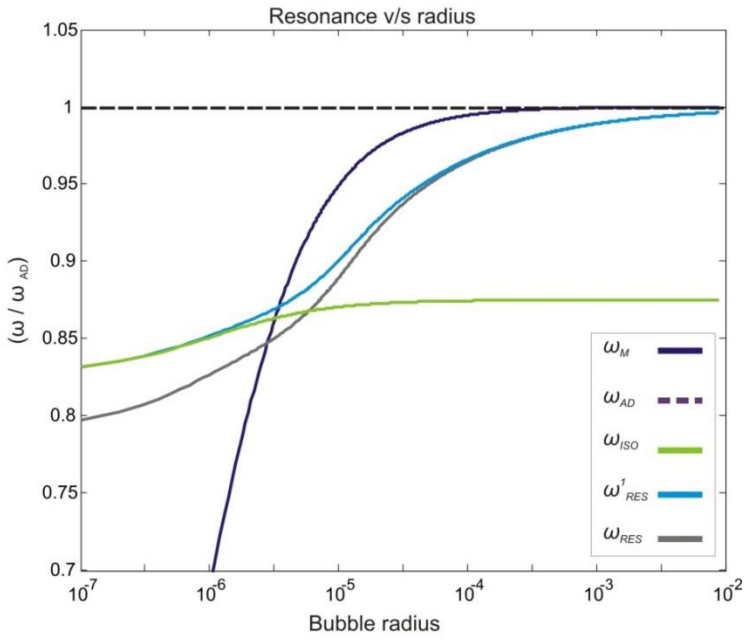

Figure 3.1. Illustration of different approximations of resonance frequency for bubbles near to the surface

3.3. Scattering cross-section of spherical bubbles

The first expression of the acoustical scattering cross-section for a spherical bubble was published by Wildt (1946). The expression is limited for small bubbles in comparison to the wavelength of the sound in water $kr \ll 1$.

3.3.1. Ideal bubble (scattering without absorption)

Wildt (1946) considers a plane pressure wave p_0 of amplitude A traveling toward to the bubble in the Cartesian $+x$ axis,

$$p_0 = Ae^{i(\omega t - kx)} \tag{3.21}$$

and a bubble scattered field represented by a divergent spherical pressure wave p_S (see also Eq. [3.7]) whose amplitude is inversely proportional to distance R from the bubble center,

$$p_S = \frac{B}{R} e^{i(\omega t - kR)} \tag{3.22}$$

Where,

ω: Angular frequency of incident plane wave
k: Wave number of incident plane wave
A: Amplitude of incident plane wave
B: Amplitude of scattered spherical wave multiplied by distance from center of symmetry

The root mean square (RMS) acoustic intensity of p_i and p_S are represented by the following equations,

$$I_0 = \frac{|A|^2}{2\rho_w c_w} \tag{3.23}$$

$$I_S = \frac{|B|^2}{2\rho_W c_W r^2} \tag{3.24}$$

Where,

c_W: Sound propagation in liquid media
I_0: RMS acoustic intensity of incident sound field
I_S: RMS acoustic intensity of scattered sound field

The acoustical cross-section σ_S is defined as the total scattered power divided by the incident plane-wave intensity (Medwin and Clay, 1998). Considering the bubble as an isotropic source, the total scattered power at r_0 (bubble radius equilibrium) from the center of the bubble is represented by,

$$\Pi_S = \frac{4\pi|B|^2}{2\rho_W c_w} \tag{3.25}$$

And then,

$$\sigma_S = \frac{\Pi_S}{I_0} = 4\pi\left|\frac{B}{A}\right|^2 \tag{3.26}$$

The ratio B/A is obtained through the following steps. A mathematical expression for volume velocity is found by differentiating the ideal gas law with respect to time. In addition, Euler's equation is applied to the scattered wave and the result evaluated at the bubble wall, yielding an equation for the volume velocity. Both of them are solved for the pressure in the interior of the bubble which is matched to the sum of incident and scattered pressures, evaluated at the bubble wall.

Considering the vibrations are so rapid that there is no heat exchange between the bubble and its surroundings, bubble pulsations can be assumed to be adiabatic changes of state.

Using the adiabatic relationship $PV^\gamma = constant$, (where P is the pressure inside the bubble, V the Volume and γ the ratio of the specific heats) denoting by P_a the average hydrostatic pressure in the water, by V_0 and r_0 the volume and radius of the bubble in equilibrium and, dP and dV small departures from the equilibrium pressure and volume, the following relationships can be obtained,

$$\frac{dP}{P_a} = -\gamma\frac{dV}{V_0}; \qquad \frac{1}{P_a}\frac{dP}{dt} = -\frac{\gamma}{V_0}\frac{dV}{dt} \tag{3.27}$$

Expressing the bubble volume in terms of its radius, it is found that

$$V_0 = \frac{4}{3}\pi r_0^3; \quad \frac{dV}{dt} = 4\pi r_0^2\frac{dr}{dt}; \quad \frac{dr}{dt} = v_R \tag{3.28}$$

Where v_R is defined as the radial velocity of the bubble. If p_i represents the acoustic pressure and A_{iB} the pressure amplitude inside the bubble, the forced vibrations of the gas inside the bubble are described by,

$$p_i = A_{iB} e^{i\omega t}; \qquad \frac{dp_i}{dt} = i\omega A_{iB} e^{i\omega t} \tag{3.29}$$

The internal pressure p_i is associated to the excess of gas pressure inside the bubble dP (Eq. [3.27]). Then, equations [3.29] and [3.28] can be substituted in [3.27], giving as a result,

$$v_R = -\frac{i\omega r_0 A_{iB}}{3\gamma P_a} e^{i\omega t} \tag{3.30}$$

Amplitudes A_{iB} and B are calculated from the given pressure amplitude A of the incident wave plane using boundary conditions. These boundary conditions require that the pressure p and the component v_R of the particle velocity normal to the surface have continuity at the surface. The first condition is given by,

$$p_i = p_{EXT} \quad \text{or} \quad p_i = p_0 + p_S \tag{3.31}$$

Assuming that the bubble is small compared with the wavelength λ, the term kR in the equation [3.22] is much smaller than the unity in the vicinity of the bubble. Then, p_S and its derivate can be approximated to,

$$p_S = \left(\frac{B}{R_0} - \frac{2\pi i}{\lambda} B\right) e^{i\omega t}; \qquad \frac{dp_S}{dr} = -\frac{B}{R^2} e^{i\omega t} \tag{3.32}$$

Replacing equations [3.21], [3.29] and [3.32] in equation [3.31], the following relationship is obtained,

$$A + \frac{B}{R_0} - \frac{2\pi i}{\lambda} B - A_{iB} = 0 \tag{3.33}$$

The second condition is the continuity of the normal component of the velocity. The normal component of the fluid velocity inside the bubble is already known from equation [3.30]. In order to evaluate the normal component of the velocity outside the bubble, Euler's force equation (conservation of momentum; see also Eq. 3.8) is used,

$$\frac{\partial p}{\partial r} = -\rho_W \frac{\partial v_R}{\partial t} \tag{3.34}$$

Substituting equation [3.34] in the derivate of the scattered pressure in [3.32], with r set equal to r_0 and integrating over dt, it is obtained,

$$v_R = -\frac{Bi}{\omega \rho_W r_0^2} e^{i\omega t} \tag{3.35}$$

The continuity of v_R now can be formulated using equations [3.30] and [3.35], obtaining the following relationship,

$$\frac{B}{\omega \rho_W r_0^2} = \frac{\omega r_0 A_{iB}}{3\gamma P_a} \tag{3.36}$$

From equations [3.33] and [3.36], A_{iB} can be eliminated and a relation between A and B obtained. The variable r_0 is substituted by r which is the bubble radius in equilibrium. From equation [3.13], ω_M is also replaced.

$$B = \frac{rA}{\frac{\omega_M^2}{\omega^2} - 1 + \frac{2\pi i r}{\lambda}} \tag{3.37}$$

Then, σ_S is calculated by computing $|A|^2 = AA^*$ and $|B|^2 = BB^*$, where A^* and B^* are the complex conjugates of A and B respectively. Then, using equation [3.26], the scattering cross-section of a spherical bubble σ_S is obtained,

$$\sigma_S = \frac{4\pi r^2}{\left[\left(\frac{\omega_M}{\omega}\right)^2 - 1\right]^2 + (kr)^2} \tag{3.38}$$

Where k represents the wave number ($k = 2\pi/\lambda$)

3.3.2. Real bubble

A real bubble-water system must include the extraction of sound energy and dissipation into the surrounding water in the form of heat. To solve that, the continuity of pressures at the bubble surface (Eq. [3.31]) must include a frictional force term that modifies the behavior of the bubble.

$$p_0 + p_S - p_i = -C_1 \frac{dr}{dt};$$

or (3.39)

$$A + \frac{B}{r} - ikB - A_{iB} = \frac{iC_1 B}{\omega \rho_W r^2}$$

Where C_1 represent a constant value related to the friction effect and the $C_1\, dr/dt$ term represents the net pressure on the bubble.

In addition, in order to include the heat transfer, the condition of continuity of velocities at the bubble surface (Eq. [3.36]) also has to be modified. This process involves the existent phase shift between the pressure and temperature in one hand and volume and radial velocity of the bubble on the other hand (Wildt, 1946). To include this process in the mathematical formulation, Wildt (1946) inserted a complex factor $1 - i\beta$ in the right side of equation [3.36], where β is a positive constant much smaller than one.

$$\frac{B}{\omega \rho_W r_0^2} = \frac{\omega r_0 A_{iB}}{3\gamma P_a}(1 - i\beta) \tag{3.40}$$

Relating equations [3.39] and [3.40], the following new expression is obtained,

$$B = \frac{rA}{\left(\frac{\omega_M^2}{\omega^2}\frac{1}{(1+\beta^2)} - 1\right) + i\left(\frac{\omega_M^2}{\omega^2}\frac{\beta}{(1+\beta^2)} + kr + \frac{C_1}{\omega \rho_W r}\right)} \tag{3.41}$$

Because $\beta^2 \ll 1$

$$B = \frac{rA}{\left(\frac{\omega_M^2}{\omega^2} - 1\right) + i\delta(\omega, r)} \tag{3.42}$$

Where

$$\delta(\omega, r) = \beta\frac{\omega_M^2}{\omega^2} + kr + \frac{C_1}{\omega \rho_W r} \tag{3.43}$$

The term δ is known as the dimensionless damping. Then, a scattering cross-section of a real bubble can be defined from equation [3.26] (Fig. 3.6),

$$\sigma_S = \frac{4\pi r^2}{\left[\left(\frac{\omega_M}{\omega}\right)^2 - 1\right]^2 + \delta^2(\omega, r)} \tag{3.44}$$

3.4. Damping

The dimensionless damping depends on the physical parameters of the bubble gas, the host liquid and the interface between them. Medwin (1959) subdivided the dimensionless damping in three terms calculated by Devin (1967), the re-radiation term δ_{rad} , the damping associated to thermal conductivity δ_{therm} and the damping related to the viscosity δ_{visc} .

$$\delta = \delta_{rad} + \delta_{therm} + \delta_{visc} \tag{3.45}$$

Each damping component was defined as follows (Fig. 3.2; Medwin, 1977),

$$\delta_{rad} = kr; \tag{3.46a}$$

$$\delta_{therm} = \frac{d}{b}\left(\frac{\omega_{RES\_D}}{\omega}\right)^2; \tag{3.46b}$$

$$\delta_{visc} = \frac{4\eta_S}{\rho_W \omega r^2} \tag{3.46c}$$

Where

$$\frac{d}{b} = 3(\gamma - 1)\left[\frac{X(\sinh X + \sin X) - 2(\cosh X - \cos X)}{X^2(\cosh X - \cos X) + 3(\gamma - 1)X(\sinh X - \sin X)}\right]; \tag{3.47}$$

and X is thermal diffusion ratio previously defined in equation [3.18] and η_S is the shear viscosity. Devin (1959) also gave a corrected expression of the resonance frequency taking into account that the oscillation of bubbles with small radii is nearly isothermal. The correction also includes the effect of surface tension, which becomes a significant additional restoring force for bubbles with small radii (Medwin, 1977). Then, some of the terms of the Minneart frequency ω_M (Eq. [3.13]) were modified. The static pressure P_a is replaced by a term that includes the surface tension ($\beta_D P_a$) and the rate of specific heats γ is replaced by the effective ratio of specific heats in the presence of thermal conductivity (γb). Then, the corrected expression ω_{RES_D} (Fig. 3.3) is defined by,

$$\omega_{RES\_D} = \frac{1}{r}\sqrt{\frac{3\gamma b\beta_D P_a}{\rho_w}} = \omega_M\sqrt{b\beta_D} \tag{3.48}$$

Where,

$$b = \left[1 + \left(\frac{d}{b}\right)^2\right]^{-1}\left[1 + \frac{3(\gamma-1)}{X}\left(\frac{\sinh X - \sin X}{\cosh X - \cos X}\right)\right]^{-1} \tag{3.49}$$

$$\beta_D = 1 + \frac{2\tau}{P_a r}\left(1 - \frac{1}{3\gamma b}\right) \tag{3.50}$$

The most important values of the damping constants occur when the incident wave front of the sound wave has a frequency equal to the resonance frequency of the bubble at resonance, $\omega = \omega_{RES\_D}$. Then the damping term at resonance (Fig. 3.4) is defined by,

$$\delta_R = \delta_{rad}R + \delta_{therm}R + \delta_{visc}R \tag{3.51}$$

$$\delta_{rad}R = k_R r_R; \tag{3.52a}$$

$$\delta_{therm}R = \frac{d}{b}; \tag{3.52b}$$

$$\delta_{visc}R = \frac{4\eta_S}{\rho\omega r_R^2} \tag{3.52c}$$

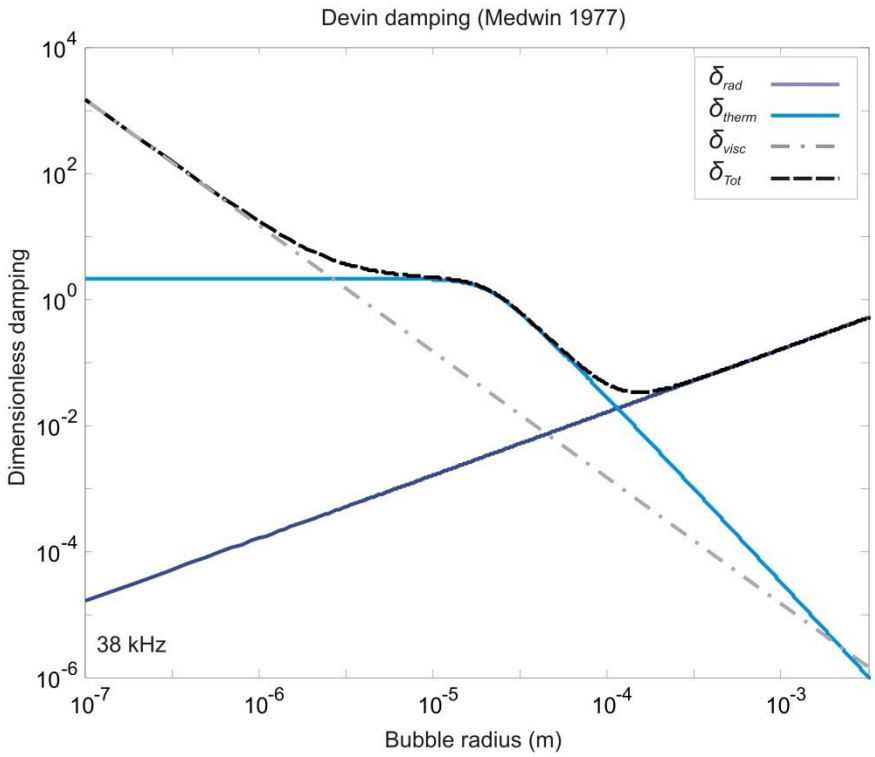

Figure 3.2. Dimensionless "Devin" damping (Medwin, 1977) for bubbles at the water surface. (sound speed=1500; specific heat ratio=1.3; sound frequency wave front: 38 kHz.

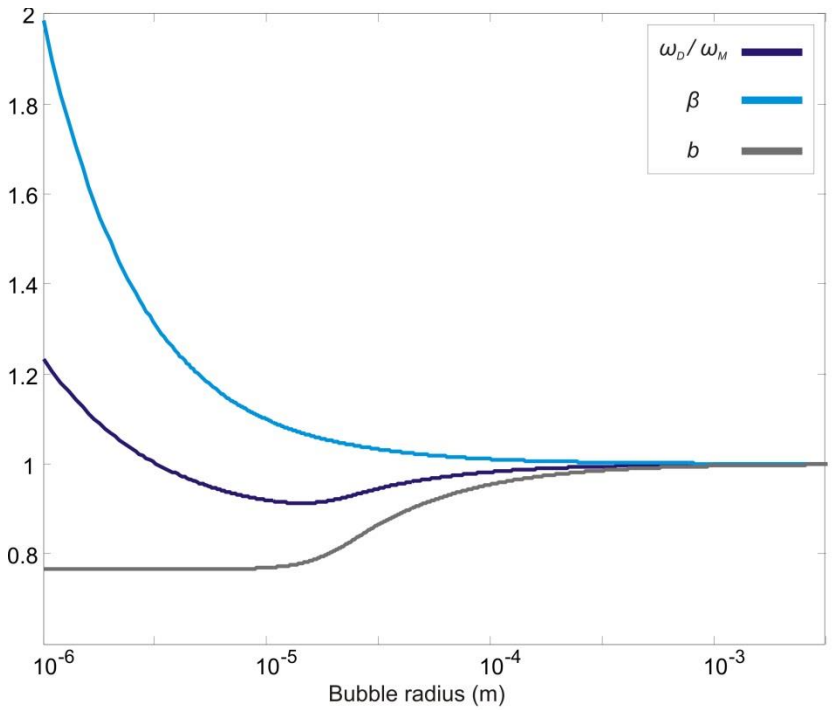

Figure 3.3. Correction constants for resonance frequency, for methane bubbles near to the water surface.

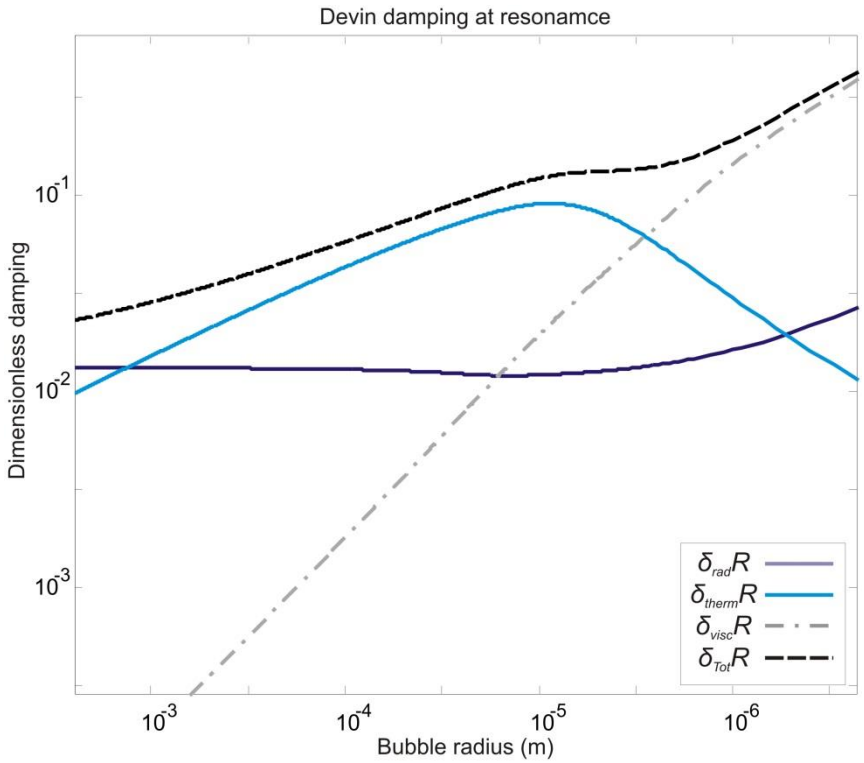

Figure 3.4. Devin damping constants at resonance, for methane bubbles near to the water surface

Simple approximations for damping δ has been given by Ainslie (e.g. see Ainslie, 2010) valid for moderately large bubbles (radius exceeding 100 μm), are presented in equations [3.48a-c] (Fig. 3.5).

$$\delta_{rad} = \omega_M r / c_w \qquad [3.53a]$$

$$\delta_{therm} = \frac{3(\gamma - 1)}{r}\left(\frac{D_p}{2\omega_M}\right)^{\frac{1}{2}} \qquad [3.53b]$$

$$\delta_{visc} = \frac{(\eta_S + 3\eta_B)}{\rho_W \omega_M r^2} \qquad [3.53c]$$

Where,

η_B : Bulk viscosity [Pa][s]

ρ_W : Water density [kg/m^3]

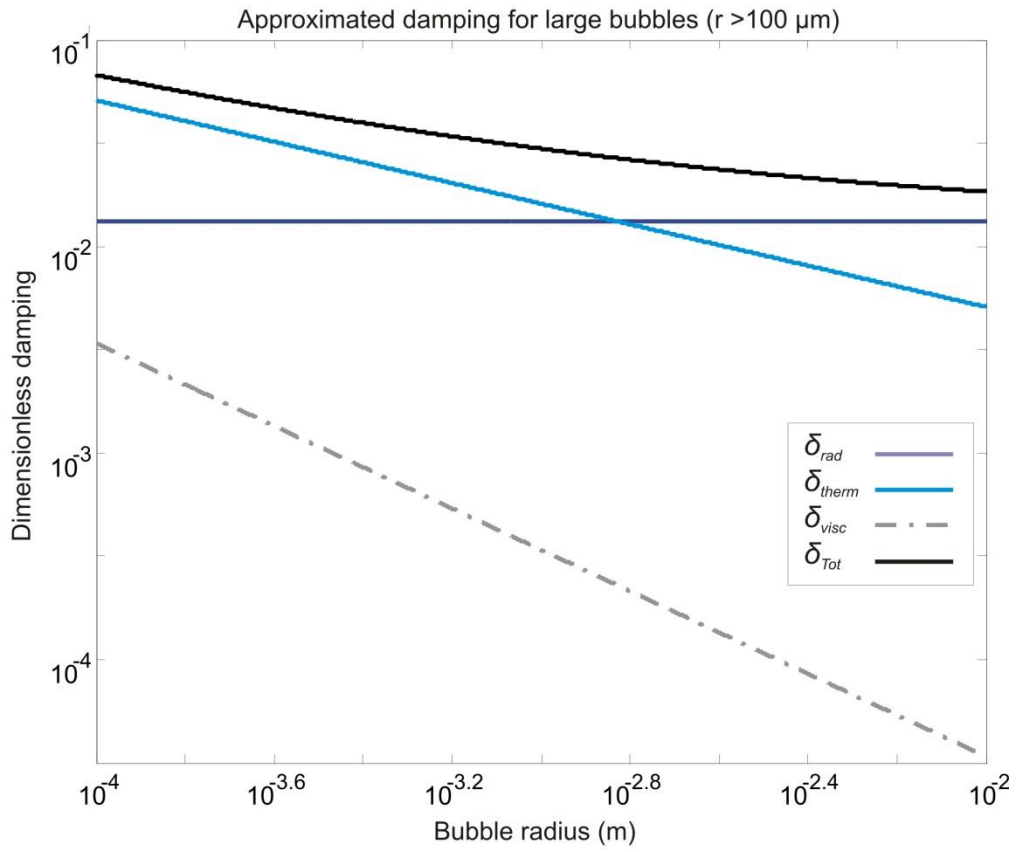

Figure 3.5. Approximated damping values for large bubbles near to the water surface

3.5. Scattering cross-section for all kr

Thuraisingham (1997) derived a new expression for the scattering produced by spherical bubbles insonified by a wave plane when the condition of $kr \ll 1$ is not reached and therefore the lumped constant approximation cannot be used.

Considering a plane wave of angular frequency ω incident on a bubble of radius r, the motion of the bubble in the radius-force frame can be described by,

$$m\frac{\partial^2\xi}{\partial t^2} + R_m\frac{\partial\xi}{\partial t} + s\xi = F_{ext}, \tag{3.54}$$

Where ξ is the radial displacement; m is the effective mass (Eq. [3.12]); s is the bubble stiffness (Eq. [3.6]); F_{ext} is the total external force applied on the bubble by the plane wave; R_m is the mechanical resistance equal to $\delta\omega m$, where δ represents the dimensionless damping.

For $kr \ll 1$, the F_{ext} has been replaced by $4\pi a^2\sqrt{2}P_p e^{i\omega t}$, where P_p represent the root mean square pressure of the incident wave, and the solution of equation [3.54], address to the classical mathematical expression of scattering for a spherical bubbles presented in equation [3.44].

Thuraisingham (1997) included the case for values $kr \geq 1$ in order to obtain a scattering expression valid for all kr, replacing F_{ext} by,

$$F_{ext} = \int_0^{\pi} \sqrt{2}P_p e^{i\omega t} e^{ik(r+\xi)\cos\varphi} 2\pi\,(r+\xi)\sin\varphi\,(r+\xi)d\varphi \tag{3.55}$$

Where φ represents the angle of the radius vector measured from the direction of the incident beam. Equation [3.55] is the integral of the force applied by the plane wave over a small elemental area of the bubble. The integral solution can be simplified to,

$$F_{ext} = 4\pi(r+\xi)^2\sqrt{2}P_p e^{i\omega t}\frac{\sin k(r+\xi)}{k(r+\xi)} \tag{3.56}$$

Since $\xi \ll r$,

$$F_{ext} = 4\pi r^2\sqrt{2}P_p e^{i\omega t}\frac{\sin kr}{kr} \tag{3.57}$$

For $kr \ll 1$, equation [3.57] reduces to $4\pi r^2\sqrt{2}P_p e^{i\omega t}$

Then, a solution of the radial displacement of the bubble ξ is obtained by replacing the equation [3.57] in [3.54]. The solution is given by,

$$\xi(r) = |\xi|e^{-i\theta}e^{i\omega t}, \tag{53.8}$$

Where θ represents the phase lag between the plane wave and the surface displacement and $|\xi|$ is given by,

$$|\xi| = \frac{4\pi r^2 P_p}{\omega m\sqrt{z}}\left(\frac{\sin kr}{kr}\right) \tag{3.59}$$

Where,

$$z = \left[\delta^2 + \left(\frac{\omega_M^2}{\omega^2} - 1\right)^2\right] \tag{60}$$

The real displacement ξ_r and the velocity $\dot{\xi}_r$ are given by,

$$\xi_r = |\xi|\cos(\omega t - \theta)\,; \qquad \dot{\xi}_r = -\omega|\xi|\sin(\omega t - \theta) \tag{3.61}$$

The resistive component of this impedance evaluated at the bubble surface was introduced by Leighton (1993) and defined as,

$$b_r = 4\pi r^2 \rho_W c_W \frac{(kr)^2}{[1+(kr)^2]} \tag{3.62}$$

The time average rate of energy loss due to scattering is the product of the radiative resistance b_r with the square of the velocity $\dot{\xi}_r$ over one cycle period ($Tp = 2\pi/\omega$) which is given by,

$$\frac{1}{Tp}\int_0^T b_r|\xi|^2\omega^2\sin^2(\omega t-\theta)\,dt = \frac{b_r\omega^2|\xi|^2}{2} \tag{63}$$

As it is defined, the scattering cross-section of a single bubble σ_S is the ratio of the time average rate of energy loss from scattering to the incident intensity (see also Eq. [3.26]). Then σ_S is given by,

$$\sigma_S = \frac{b_r\omega^2|\xi|^2}{2}\left[\frac{P_p^2}{\rho_w c_W}\right]^{-1} \tag{3.64}$$

An equivalent form of σ_S is obtaining replacing equations [3.59] and [3.62] in [3.64]. Then σ_S is represented by,

$$\sigma_S = \frac{4\pi r^2}{\left[\left(\frac{\omega_{res}}{\omega}\right)^2 - 1\right]^2 + \delta^2(\omega, r)} \frac{[\sin(kr)/kr]^2}{1+(kr)^2} \tag{3.65}$$

3.6. Bubble backscattering

Underwater active acoustic systems are designed to send an acoustic signal and receive “echoes” from the target (Lurton, 2002).When the wave front impacts the target, energy is scattered in all directions of space and just a portion of this is captured by the system‘s transceiver. The energy sent back towards to the transceiver receives the name of “backscattering”. A spherical bubble pulsating in the “breathing” mode is considered to be an isotropic source of energy. Then, the acoustical “backscattering” cross-section σ_{bs} can be defined as the scattering cross section per steradian (Medwin, 1977),

$$\sigma_{bs} = \frac{\sigma_S}{4\pi} \tag{3.66}$$

Additionally, the term of "target strength" TS, which is commonly used in sonar active systems, can be defined

$$TS = 10 \log \sigma_{bs} \tag{3.67}$$

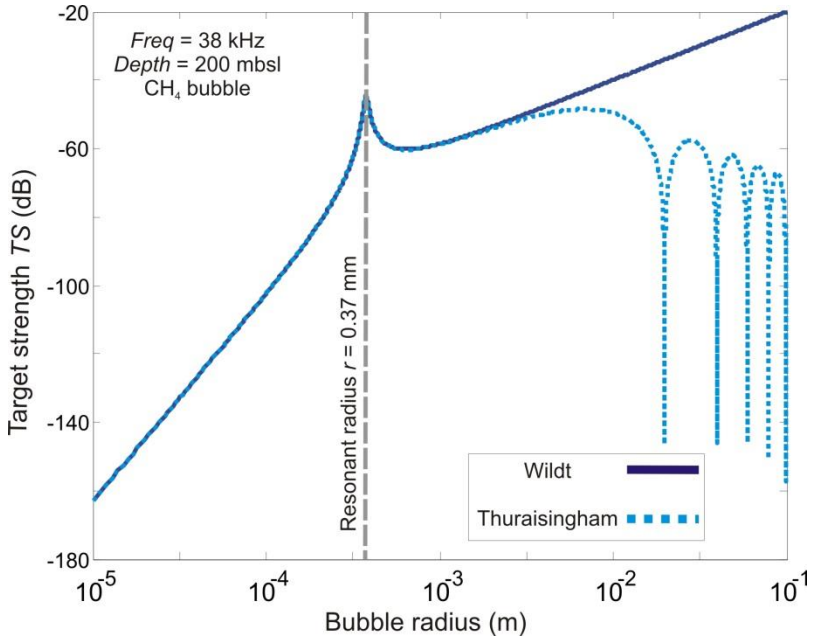

Figure 3.6. Representation of target strength (*TS*) produced by bubbles obtained by using Wildt and Thuraisingham models of acoustical scattering cross-section. The acoustical responses represent bubbles located at 200 m below the sea level (m bsl) insonified by a sound field of 38 kHz.

3.7. Backscattering from multiple bubbles

If the backscattering is produced by multiple bubbles is possible to approximate the total scattering to the constructive interference of the bubble cloud. A simple approximation can be obtained by the sum of the contributions of each bubble,

$$\sigma_{bs}total = \sum_{j}^{N} n_j \, \sigma_{bsj} \tag{3.68}$$

Where, n_j represents the number of bubbles of a certain radius and $\sigma_{bs}total$ the total backscattering cross-section produced by the group of bubbles. Fig. 3.7, shows the total backscattering produced by a group of bubbles with different sizes.

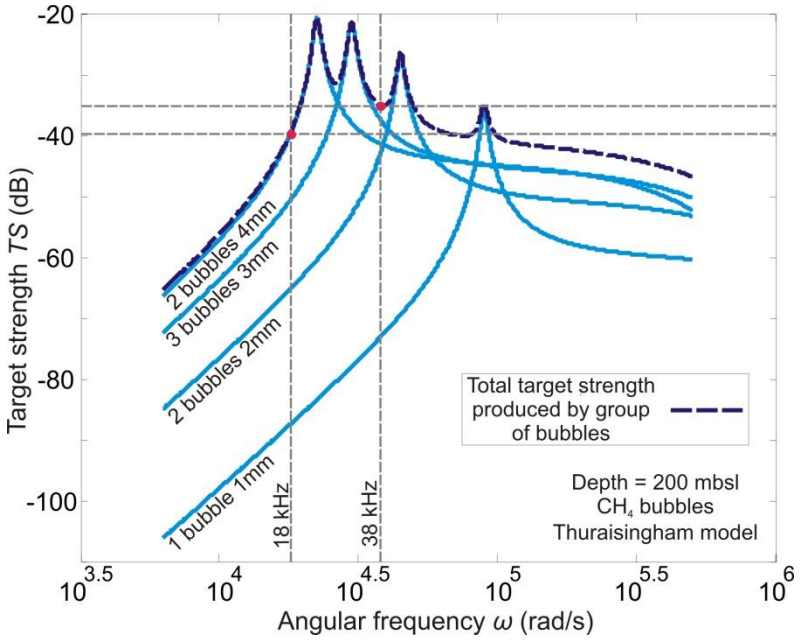

Figure 3.7. Representation of the *TS* produced by the contribution of 8 methane bubbles of different sizes (1x1 mm, 2x2 mm, 3x3 mm, 2x4 mm) located at 200 m bsl using Thuraisingham model of acoustical scattering cross-section. Bubbles are insonified with a sound field at different frequencies. Frequencies of 18 kHz and 38 kHz (frequencies of echosunder system using to capture the data in situ, see chapter 4) gave TS values of -40 dB and -35 dB respectively.

Considering a continuous distribution of bubbles inside a water volume full with bubbles, a new expression of the total backscattering normalized by the insonified sample volume , also known as a "volume backscattering coefficient" (MacLennan and Simmonds, 1992) can be defined as,

$$\sigma_V = \int_{r^1}^{r^2} \sigma_{bs}(r,\omega) N_b(r) dr \, ; \tag{3.69}$$

Where $N_b(r)$ is the bubble size distribution inside the water volume and the total bubble concentration (number of bubbles per volume) is defined by,

$$N_{0C} = \int_{r^1}^{r^2} N_b(r)dr \tag{70}$$

Where N_{0C} represents the bubble concentration.

The amount $N_b(r)dr$ in equations [3.69] and [3.70] can be seen as the number of bubbles, with radius values between r and $r + dr$, per unit volume (Medwin and Clay, 1998). Equation [3.60] can be found in the literature as the differential backscattering cross-section per unit of volume. A typical value that is used in active sonar systems is the "volume backscattering strength" defined as follows,

$$S_V = 10 \log \sigma_V \tag{3.71}$$

3.8. Relation between backscattering and bubble flux (inverse method)

Bubbles released from the seabed rise upwards to the surface due to buoyancy. As it is known, bubbles with different sizes rise at different speeds. When considering a volume containing bubbles with a defined continuous bubble size distribution, the bubble flux can be defined as following,

$$Q = \int_{r^1}^{r^2} N_b(r)U(r)dr \tag{3.72}$$

Where, Q is the bubble flux and it represents the number of bubbles per unit of time and per unit of area and $U(r)$ is the bubble velocity function which depends on the bubble size.

If the gas density ρ_G is known and bubbles are considered to be spherical an equivalent expression of the mass flux Q_m can be defined,

$$Q_m = \frac{4}{3}\pi\rho_G \int_{r^1}^{r^2} r^3 N_{0C} f(r)U(r)dr \tag{3.73}$$

Where Q_m is expressed in units of mass per time per square meters.

If the bubble size distribution is assumed to be $N_b(r) = N_{0C} f(r)$, with $f(r)$ as the probability density function of the bubble distribution and combining equations [3.69] and [3.73], a relationship between the mass flux of bubbles and the backscattering can be obtained (Muyakshin and Sauter, 2010),

$$Q_m = \rho_G \sigma_V K \tag{3.74}$$

Where,

$$K = \frac{\frac{4}{3}\pi \int_{r_1}^{r_2} U(r) r^3 f(r) dr}{\int_{r_1}^{r_2} \sigma_{bs} f(r) dr} \tag{3.75}$$

As it can be seen in equations [3.74] and [3.75], the mass flux of a bubble jet can be obtained by knowing differential backscattering cross-section per unit of volume σ_V, the bubble gas density ρ_G, bubble rising speed $U(r)$ which is a function of the bubble radius and the probability density function of the bubble distribution $f(r)$ inside the bubbly water volume.

The mathematical expression of mass flux (equation [3.73]) works only when the insonified sample volume is totally filled with bubbles, which is not the case in most of the studied areas where free gas is released. Places like the study area presented in this thesis, release methane in groups of bubble streams that can be separated by several meters between each other. As a result, bubble streams occupy only a narrow region within the echosounder beam. Then, the use of the backscattering coefficient is not appropriate because this value represent the normalization of the backscatter for the entire sample volume.

Alternatively, a new inverse hydroacoustic method is introduced in chapter 4 which uses the total acoustical backscattering cross-section (equation [3.66]), or its equivalent logarithmic value (target strength, equation [3.67]) to derive the mass bubble flow rate (mass per time) of an insonified sample volume. Additionally, the calculated flow rate for of a large area using this mathematical inversion is presented.

References

Ainslie, M. A. and T.G. Leighton. 2011. Review of theory for scattering and extinction cross-sections, damping factors and resonance frequencies of spherical gas bubbles, J. Acoust. Soc. Am., 130(5): 3184-3208, [doi: 10.1121/1.3628321]

Artemov, Y. G., V. Egorov, G. Polikarpov, and S. Gulin. 2007. Methane emission to the hydro-and atmosphere by gas bubble streams in the Dnieper paleo-delta, the Black Sea. Mar. Ecol. J. 3: 5–26, [doi:10.0.0.194:8080/dspace/handle/99011/622].

Chapman, R. B. and M. S. Plesset. 1971. Thermal effects in the free oscillation of gas bubbles, J. Basic Eng. (Trans. ASME) 93, 373–376.

Chen, J., K. S., Hunter, and R., Shandas. 2009. Wave scattering from encapsulated microbubbles subject to high-frequency ultrasound: Contribution of higher-order scattering modes. The Journal of the Acoustical Society of America, 126(4), 1766-1775.

Cleveland, R. O., and J. A., McAteer. 2007. The physics of shock wave lithotripsy. Smith's Textbook on Endourology, 1, 529-558.

Devin, Jr. C. 1959. Survey of thermal, radiation, and viscous damping of pulsating air bubbles in water. The Journal of the Acoustical Society of America, 31(12), 1654-1667.

Greinert, J. and B., Nützel. 2004. Hydroacoustic experiments to establish a method for the determination of methane bubble fluxes at cold seeps, Geo. Mar. Lett., 24, 75–85.

Greinert, J., Y., Artemov, V., Egorov, M., De Batist, and D. McGinnis. 2006. 1300-m-high rising bubbles from mud volcanoes at 2080m in the Black Sea: Hydroacoustic characteristics and temporal variability. Earth and Planetary Science Letters, 244(1), 1-15.

Lurton, X. 2002. An Introduction to Underwater Acoustics: Principles and Applications. Springer, [doi:10.1121/1.1639324.

MacLennan, D. N., and E. J., Simmonds. 1992. Fisheries acoustics. London: Chapman & Hall.

Maxwell, A. D., T. Y., Wang, C. A., Cain, J. B., Fowlkes, O. A., Sapozhnikov, M. R., Bailey, and Z., Xu. 2011. Cavitation clouds created by shock scattering from bubbles during histotripsy. The Journal of the Acoustical Society of America, 130(4), 1888-1898.

Medwin, H. 1977. Counting bubbles acoustically: A review. Ultrasonics 7:13, [doi:10.1016/0041-624X(77)90005-1]

Medwin, H. and C. S. Clay. 1998. Fundamentals of Acoustical Oceanography. Chapter 8 - Bubbles, p. 287-347. Academic Press, [doi:10.1046/j.1365-2419.1999.00096.x]

Minnaert, M. 1933. XVI. On musical air-bubbles and the sounds of running water. Philos. Mag. 16:235-248, [doi:10.1080/14786443309462277]

Muyakshin, S., and E. Sauter. 2010. The hydroacoustic method for the quantification of the gas flux from a submersed bubble plume. Oceanology 50:995-1001, [doi:10.1134/S0001437010060202]

Neppiras, E. A. 1980. Acoustic cavitation, Phys. Rep. 61(3), 159–251.

Niemczewski, B. 2007. Observations of water cavitation intensity under practical ultrasonic cleaning conditions. Ultrasonics sonochemistry, 14(1), 13-18.

Nikolovska, A., H., Sahling, G., Bohrmann. 2008. Hydroacoustic methodology for detection, localization, and quantification of gas bubbles rising from the seafloor at gas seeps from the eastern Black Sea. Geochem. Geophys. Geosyst. 9, Q10010 http://dx.doi.org/10.1029/2008GC002118

Ostrovsky, I., D. Mcginnis, L. Lapidus, and W. Eckert. 2008. Quantifying gas ebullition with echosounder: the role of methane transport by bubbles in a medium-sized lake. Limnol. Oceanogr-Meth.6:18, . [doi:10.4319/lom.2008.6.105]

Pedersen G, R., Hauge, R., Kubilius. 2014. Active acoustic detection of subsea oil and gas leaks; model prediction and measurements J Acoust Soc Am, 135 (4), 2303.

Prosperetti, A. 1977. Thermal effects and damping mechanisms in the forced radial oscillations of gas bubbles in liquids, J. Acoust. Soc. Am. 61, 17–27 (1977).

Prosperetti, A. 1984. Bubble phenomena in sound fields: Part one, Ultrasonics 22, 69–77

Prosperetti A., L. A. Crum, and K. W. Commander. 1988. Nonlinear bubble dynamics, J. Acoust. Soc. Am. 83, 502–514.

Thuraisingham, R. A. 1997. New expressions of acoustic cross-sections of a single bubble in the monopole bubble theory. Ultrasonics, 35(5): 407-409,[doi:10.1016/S0041-624X(97)00021-8]

Wildt, R., 1946. Acoustic theory of bubbles, Chap. 28, Physics of Sound in the Sea, NDRC Summary Technical Report Div. 6, 8: 460-477.

4. A new methodology for quantifying bubble flow rates in deep water using splitbeam echosounders: Examples from the Arctic offshore NW-Svalbard

Mario E. Veloso-Alarcón, J. Greinert, J. Mienert, M. De Batist

(Published at L&O Methods)

Abstract

Quantifying marine methane fluxes of free gas from the seafloor into the water column is of importance for climate related studies e.g. in the Arctic, reliable methodologies are also of interest for studying man-made gas and oil leakage systems at hydrocarbon production sites. Hydroacoustic surveys with singlebeam and nowadays also multibeam systems have been proven to be a successful approach to detect bubble release from the seabed. A number of publications used singlebeam echosounder data to indirectly quantify free gas fluxes via empirical correlations between gas fluxes observed at the seafloor and the hydroacoustic response. Others utilize the hydroacoustic information in an inverse modeling approach to derive bubble fluxes.

Here we present an advanced methodology using data from splitbeam echosounder systems for analyzing gas release water depth (> 100 m)**.** We introduce a new MATLAB-based software for processing and interactively editing data and we present how bubble size distribution, BRS and the model used for calculating the backscatter response of single bubbles influence the final gas flow rate calculations. As a result we highlight the need for further investigations on how large, wobbly bubbles, bubble clouds and multi-scattering influence target strength. The results emphasize that detailed studies of bubble size distributions and rising speeds need to be performed in parallel to hydroacoustic surveys to achieve realistic mediated methane flow rate and flux quantifications.

Contributions: The manuscript was written by MV and revised by JG, JM and MDB. Fieldwork was conducted by MV, JG and facilitated by JM. Discussion of results and interpretation were done by MV and JG. The formulation of the inverse method was done by MV.

4.1. Introduction

Because unique ecosystems thrive in direct proximity to methane release sites, but also because methane is a greenhouse gas that creates a positive climate warming feedback when reaching the atmosphere, methane release in the marine environment has been studied for several decades now. Recent publications about ‘massive’ methane releases from the Eastern Siberian Arctic Shelf (Shakhova et al., 2013) highlight the need for a standardized methodology for free gas flux quantifications.

This paper provides a brief review of how 'large' bubbles released from seep sites can be detected and analyzed with SBES and it presents an advanced methodology to quantify bubble flow rates.

Reports on 'flares' seen on various hydroacoustic systems date back to the 1980s, sometimes not linking the 'plumes' clearly to their bubble origin (Merewether et al. 1985; Paull et al. 1995; Lewis and Marshall 1996). Studies in the Black Sea (Polikarpov 1989; Naudts et al. 2006), the Sea of Okhotsk (Obzhirov et al. 2004), Hydrate Ridge (Heeschen et al. 2003), the Barents Sea (Sauter et al. 2006, Chand et al., 2012), the Fram strait offshore NW Svalbard (Smith et al., 2014), Lake Baikal (Granin et al. 2012), the Gulf of Mexico (Solomon et al., 2009; Talukder et al., 2013; Weber at al., 2014) and the area offshore Santa Barbara (Hornafius et al. 1999; Leifer and Culling, 2010) underline the usefulness of SBES observations to find active seep sites, map their extent and even get an idea of their temporal variability (Quigley et al. 1999; Greinert et al. 2006). First attempts to quantify gas flow rates from SBES were difficult because of limitations of digital data storage capacity (Hornafius et al. 1999) and computer power for data processing. Today, this is not a problem anymore and singlebeam as well as multibeam water column data (Nikolovska et al. 2008; Lorenson et al., 2011; Weber et al., 2013) are commonly used to visualize gas release and increasingly more often to quantify gas flow rates and fluxes (Granin et al. 2012; Römer et al. 2012b).

Successful attempts have been made to measure free gas flow rates at the seafloor and model the transport towards the sea surface or into the mixed layer (Leifer and Patro 2002; Greinert et al. 2010; Schneider Von Deimling et al. 2011), accounting for gas dissolution while bubbles rise (Leifer and Patro 2002; McGinnis et al. 2006; Rehder et al. 2009). In those attempts, the amount of gas reaching the mixed layer (where it ultimately equilibrates with the atmosphere) was between 4 and 19 % of the initially released gas in water depths of less than 100 m. The total methane flux shows large variations, depending on seep area, bubble sizes and bubble release intensity. Flow rates range from 1.5 to 18.5 x 10^6 mol/yr for the respective areas; much higher fluxes have been presented for the Eastern Siberian Arctic Shelf (Shakhova and Semiletov 2007; Shakova et al., 2014) or the Gulf of Mexico (Solomon et al. 2008).

Although the number of such research activities concerned with flow rate and flux estimates is currently increasing, the total amount of methane reaching the atmosphere from marine seep sources is far from being reliably determined. Also, estimates from basic modeling approaches have limited data for validation, particularly in Arctic areas (Archer et al. 2009; Biastoch et al. 2011). Extrapolations over large areas need to be made with great caution as local environmental conditions that are highly variable (temperature, depth, wind and wave activity, ice cover) is distinctly influencing flow rates.

Here we present a methodology that allows SBES-based flow rate estimates in water depth of more than > 100 m, where no or a very limited release of single bubbles can be observed during ship-based SBES surveys. Our approach provides an easy-to-use methodology allowing a better comparison of data from repeated surveys and/or groups for analyzing long-term changes in methane flow rates and fluxes from the ocean floor through the water column.

4.2. Bubble detection in SBES echograms

4.2.1. What bubbles look like in echograms

The approach for detecting and quantifying free gas is based on SBE data recorded with a splitbeam system. For the correct detection of single bubbles and bubble clouds, the recognition and classification of different backscattering targets in the water column is essential. Slow sailing speed (< 5 kn) and a 'silent' ship with additional acoustic sources being turned off (e.g. multibeam systems, sub-bottom profilers) significantly enhance the quality of data and the opportunity to discriminate bubbles from other signals such as fish, fish larvae, plankton or suspended sediment. The recognition of free gas release essentially depends on the pattern of the backscattering in echograms (Greinert et al., 2006; Judd and Hovland, 2007). Because of the typical "flare" shape in echograms (for non-single bubbles), these features are referred to as "flares" (Greinert at al., 2006; Römer at al., 2012), but the term 'bubble plume' or 'hydroacoustic plume of bubbles' is also used (e.g. Westbrook et al., 2008; Fig. 4.1 and 4.2).

How bubbles (> 1 mm in diameter) in the water column can be identified and distinguished from other signal sources has been described previously (e.g. Judd et al. 1997; Greinert et al. 2006). The visual representation of bubbles in echograms strongly depends on vessel speed, water currents influencing the bubble rising path, and on how the bubbles have been insonified by the acoustic beam (Fig. 2). As echograms are usually displays of echo intensity per depth (y-axis) over time (x-axis) different vertical exaggeration might stretch fish schools in the y-axis that can result in false flare detection. 'Rooted' flares (Fig. 2 d and e) and the observation of single bubbles rising (Fig. 2 f) give ultimate proof. Side lobe effects specific to different transducers may clearly show in echograms if the backscattering of the target is strong enough. One example is given in Fig. 4.3; others have been presented by e.g. Nikolovska et al. (2008) and Schneider Von Deimling et al. (2011).

In comparison to the flares in Fig. 3 that were recorded at sites that more or less continuously release bubbles, backscattering of single bubbles or small bubble clouds can be reasonably well detected at a slow vessel speed (< 2 kn) and low background noise. Such conditions existed for flow rate quantifications at shallow water depths, e.g. in lakes and shelf areas (Ostrovsky 2003; Delsontro et al. 2011). A single bubble or an isolated bubble cloud appears as an almost straight line with a positive slope in echograms (Fig. 4.4). Unfortunately, in deeper water (> 100 m) observations of single bubble targets are very limited in the literature. This is most likely due to the lack of good quality data that could track bubbles inside the acoustic beam for a high enough number of pings (over time). Being stationary at one site or going slowly helps to acquire more information from the same target with the reduced ping rate in deeper water and the increased possibility of additional backscatteres in the larger insonified water volume. As a consequence, there is a lack of BRS measurements and bubble size estimates needed for flow rate quantifications.

It should be pointed out that faster survey speeds (~10 kn) would cover larger areas giving a better regional view on the distribution of gas release sites. Choosing between coverage (fast and thus wider coverage, less data per seep, more noise from the ship or sea state) and high quality data (slow and thus less coverage, less noise, more data per seep) depends on the research question (overview mapping vs.

detailed flow rate and temporal variability studies), time and money constrains or commercial requirements.

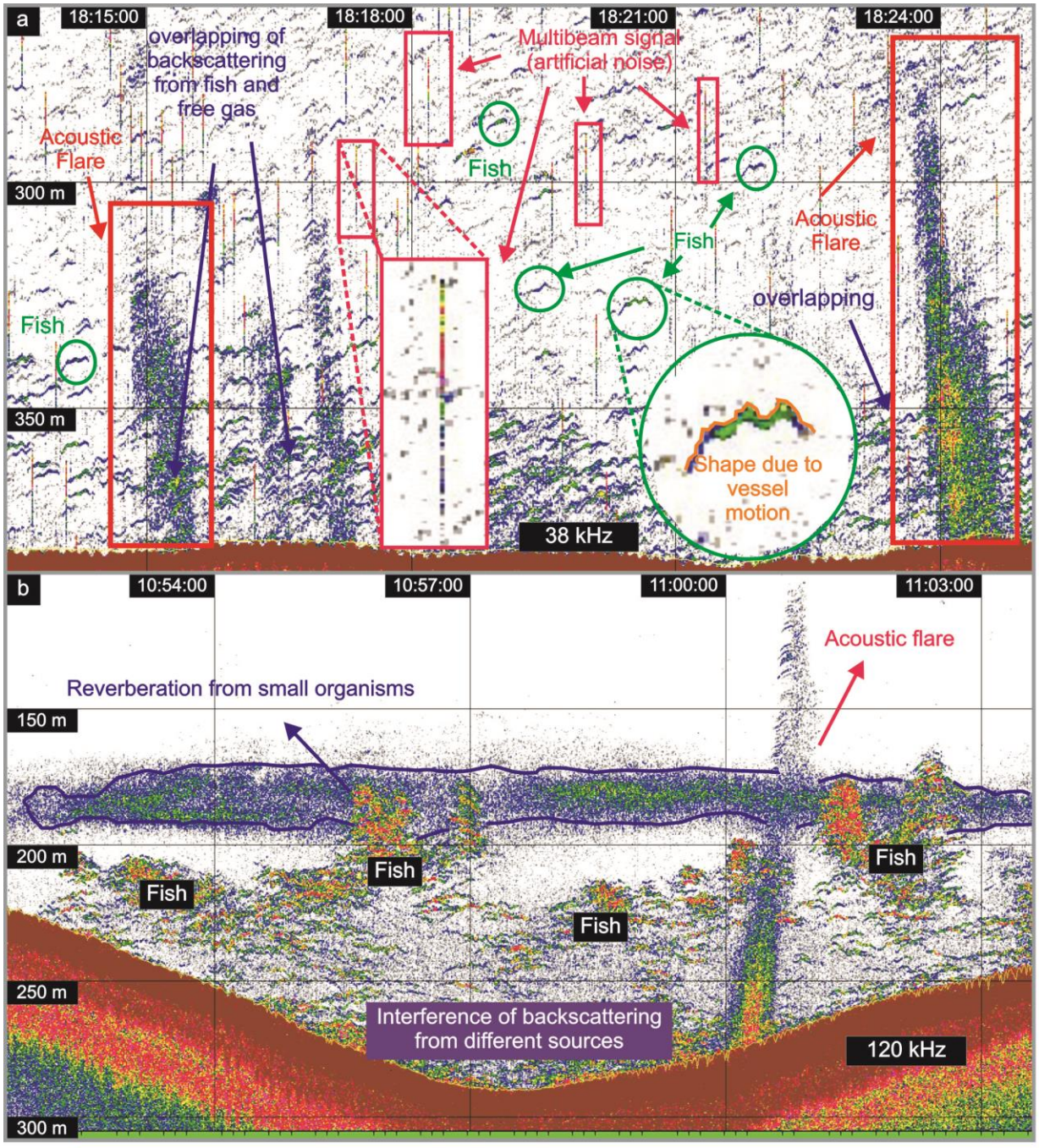

Figure 4.1. a) Echograms (38 kHz) showing flares as manifestation of rising bubbles and sources of noise (multibeam) and reverberation (fish). This complicates the identification of free gas fluxes as the interference of the different signal sources results in wrong backscattering values for bubbles, which again may result in flux overestimations. The image shows the effect of the vessel motion on the acoustic data i.e. the shape of backscatter signals of fish (wobbly shape). b) Echogram (120 kHz) showing the interference of hydroacoustic signals from bubbles (flares) and sources of reverberation (fish and plankton). Here, the plankton layer shows more distinctly because of the higher frequency used. The illustrated echograms are part of the hydroacoustic dataset acquired at the study area offshore PKF.

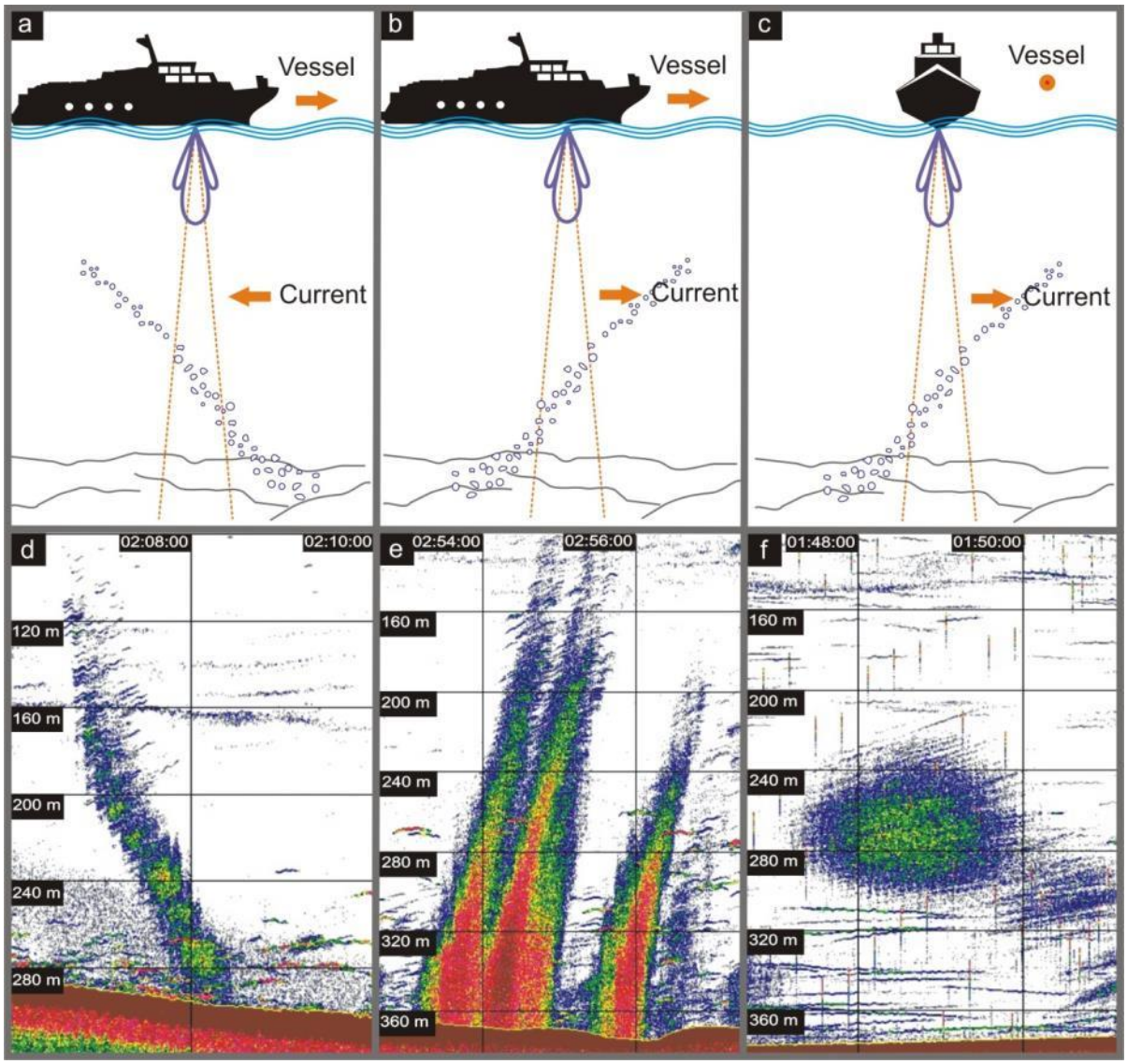

Figure 4.2. Three typical examples for how bubbles influenced and shifted by currents are depicted: a) current from the opposite direction of the ship's movement; b) current from the same direction as the ship's movement; c) current oblique to the ship's movement, which can easily be misinterpreted as fish or vice versa. Almost all echograms will represent a mix of two of these possibilities. The illustrated information is part of the hydroacoustic dataset acquired at the study area, offshore PKF.

4.2.2. Disturbance by noise

Fish is the main source of disturbances/reverberation during hydroacoustic bubble studies and have been observed repeatedly to interfere with flow rate estimates (Ostrovsky 2009; Delsontro et al. 2011). To obtain "pure" backscattering from bubbles, signals from fish need to be clearly identified, separated and automatically or manually removed from the data prior to quantitative processing. Single fish can be recognized by their concave shape (Lefeuvre 2002) when the fish pass the acoustic beam, but they also show artifacts depicting the vessel motion as a 'wobbly' shape (see example Fig. 4.1a). Fish schools that show up as 'clouds' are sometimes difficult to discriminate from strong gas release, depending on the total number of fish and the distance between them (Fig. 4.1b). For unambiguous identification of fish shoals, the observer needs a good understanding of the local fish populations and their behavior (Simmonds and MacLennan 2005).

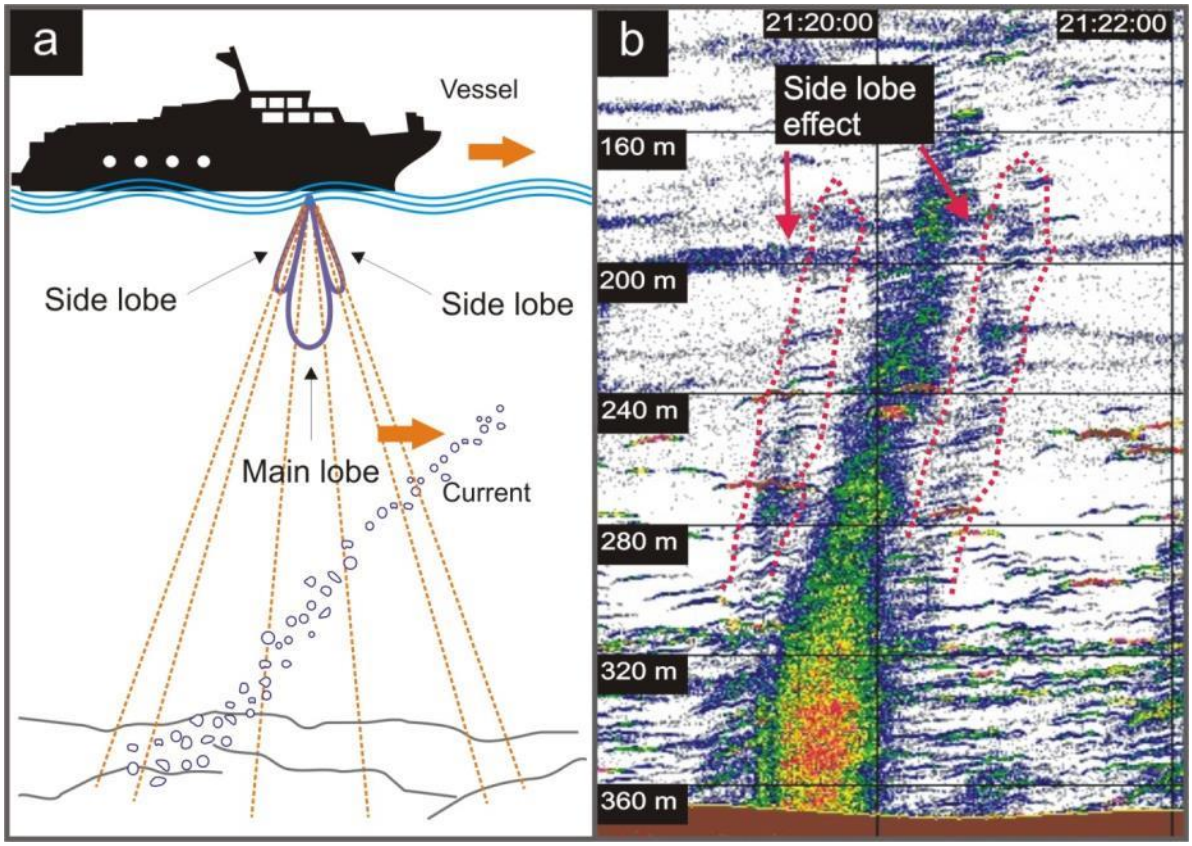

Figure 4.3. Side lobe effects when rising bubbles have been insonified with the current. The illustrated information is part of the hydroacoustic dataset acquired at the study area, offshore PKF.

Small organisms as plankton and micronekton are another source of reverberation often accumulating in the deep scattering layer (Lurton, 2002). Large amounts of small organisms cause strong echoes that could interfere with the backscattering from free gas, making quantitative analyses impossible (see example Fig. 4.1b). Plankton often concentrates at density layers increasing the backscatter signal in a certain water depth range and can influence signals from bubbles in a similar way as seafloor multiples do. A good understanding of the daily vertical migration of these microorganisms and respective adjustment of the time for data acquisition will result in better data for gas flow rate estimates. However, this might contradict monitoring efforts to estimate the gas flow or flux over tidal cycles or longer periods. Once bubbles have been identified, data need to be cleaned from noise or unwanted backscattering. This can be done by 'simple' threshold filtering, speckle noise removal or manual editing in 3D space as used here.

4.2.3. Bubble rising speed, terminal bubble rising height and water currents

Gas flow rate estimates depend on several parameters such as initial gas composition, pressure and temperature conditions that affect gas density as well as bubble size and rising speed. BRSs depend on the bubble size and the amount and kind of surfactants on the bubble surface including a potential oil or gas hydrate coating (Leifer and Patro 2002; Rehder et al. 2009, Salmi et al., 2010). Further, the number

of bubbles rising together influences their rising speed, as they are forming a bubble plume in which water and bubbles are upwelling together (Leifer and Culling, 2010).

To estimate the BRS of single bubbles the rise path needs to be identified from echograms. The quality of the results strongly depends on the resolution of the echogram, which is related to the sampling rate of the received echo signal, the pulse length of the transmitted signal and the bandwidth during receive. In short, longer pulses as needed in greater water depth give lower resolution in the y-axis (depth) but shorter pulses result in more noisy data. The resolution in the x-axis (time axis) depends on the ping rate as function of water depth (as deeper as slower the pin grate) and the relative speed between the bubble and the moving vessel. At slow-mode sampling (< 2 kn, Ostrovsky 2009), the number of pings on the bubble target is higher, improving identification and accurate measurements of the depth change of a bubble over time (pings) without a significant effect of distance/depth changes caused by position changes inside the acoustic beam (see Fig. 4.4).Such measurements have been successfully employed by several authors (Artemov 2006; Ostrovsky et al. 2008; Delsontro et al. 2011). However, in deep water the identification of single bubbles or bubble clouds is difficult and very often only the typical flares are seen, unless the ship stays stationary over one seep or is drifting very slowly (< 1 kn). This is due to the increasing foot print size of the insonified water volume and the increasing chance of recording several bubble streams simultaneously. Salmi et al (2011) present another mooring-based technique to monitor BRS and indirectly bubble sizes. The group deployed an upward-looking 200 kHz echosounder next to several bubble vents. They determined bubble size spectra from BRS measurements, assuming either clean or dirty bubble[2] rise behavior. Such stationary observations certainly help to understand the temporal changes in released bubble sizes as well as the activity fluctuations.

Bubbles are moved laterally by ocean currents as they rise through the water column. The horizontal displacement of a single target during a known time interval can be tracked using a splitbeam echosounder if motion, ship's heading and ray tracing are considered appropriately, assuming the horizontal displacement equals the water current speed. Using the corrected locations of the backscattered signal geo-referenced provides the direction of the water current. Fig. 4.5a shows the horizontal current speed calculated from five bubble traces at similar water depths (Fig. 4.5b). In this example, all bubbles are displaced towards WNW with a speed varying from 0.5 to 0.72 m/s (independent of ship's movement and heading).

As bubbles gradually dissolve as they move upwards through the water column, most eventually disappear and do not reach the mixed layer or sea surface. The height at which this happens is the terminal rising height which is critical for estimating the amount of methane transported into the atmosphere/upper mixed layer. The terminal height is often derived from the height of the flare in an echogram (Römer et al. 2012a). The respective values must be used with caution because only a conical volume of the water column is insonified, due to the hydroacoustic beam pattern and the backscattering strength of bubbles decreases quickly when bubbles become smaller than the resonance frequency at a

[2] The terms clean and dirty refer to the assumption of a bubble surface to be liquid and solid respectively. Hydrodynamical conditions of the water surrounding a risingbubble change according to the bubble type. For example, the velocity field becomes equal to zero at a solid liquid interface, whereas only the normal component of the velocity tends to zero at a liquid-liquid interface (Memery and Merlivat, 1985)

particular depth (Medwin et al., 1998). A flare height should only be called “terminal” if all bubbles are definitely inside the acoustic lobe. Greinert et al. (2010) provide an example where transducers with different frequencies depict the terminal flare height very differently although the recording happened simultaneously. In shallow water, the chance that only parts of the rising bubble stream are insonified is high, in particular if ocean currents shift bubbles laterally away from their point of origin (Fig. 4.2f). Using multibeam systems overcomes this problem, but performing SBES surveys over the same seep site from different directions and comparing flare heights may also provide accurate information. Recording SBES water column data simultaneously with MBES would help to determine the terminal rising height. A disadvantage may be the introduction of additional noise in the SBES data.

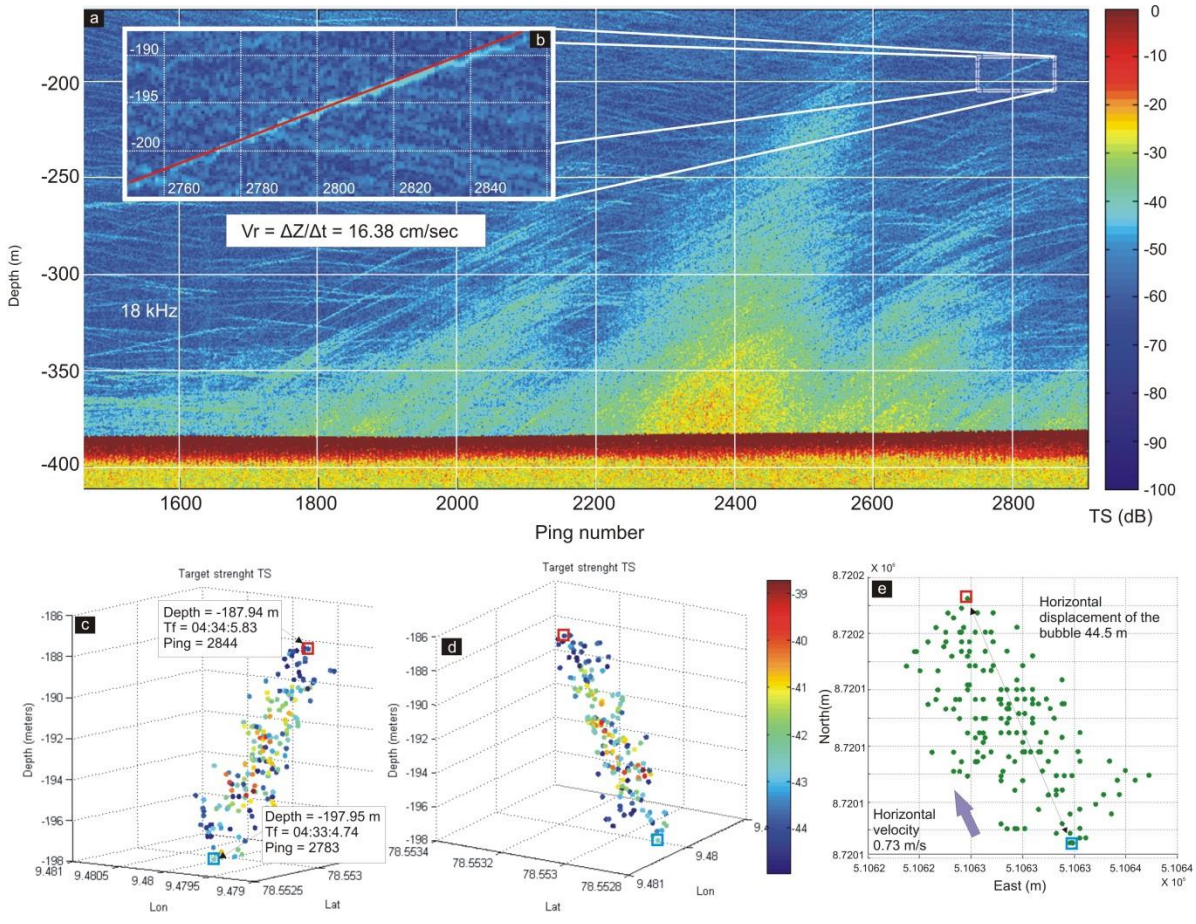

Figure 4.4. a) Echogram showing backscattering from a single bubble captured during slow-mode-sampling. b) Enlarged signal of the rising bubble; the slight wavy pattern is caused by the ship movements (pitch, roll, heave). Images c) and d) show two 3D views of the backscattering positions produced by a rising bubble in a latitude-longitude-depth coordinate system. Colors in images a), b), c), d) represent the target strength (*TS*). Image e) shows a top-down view of the spatial distribution in UTM coordinates (Zone 33). The image clearly shows the current effect that causes the horizontal displacement of the bubble for a certain time and depth interval (here ~0.5 m/s towards the NE).

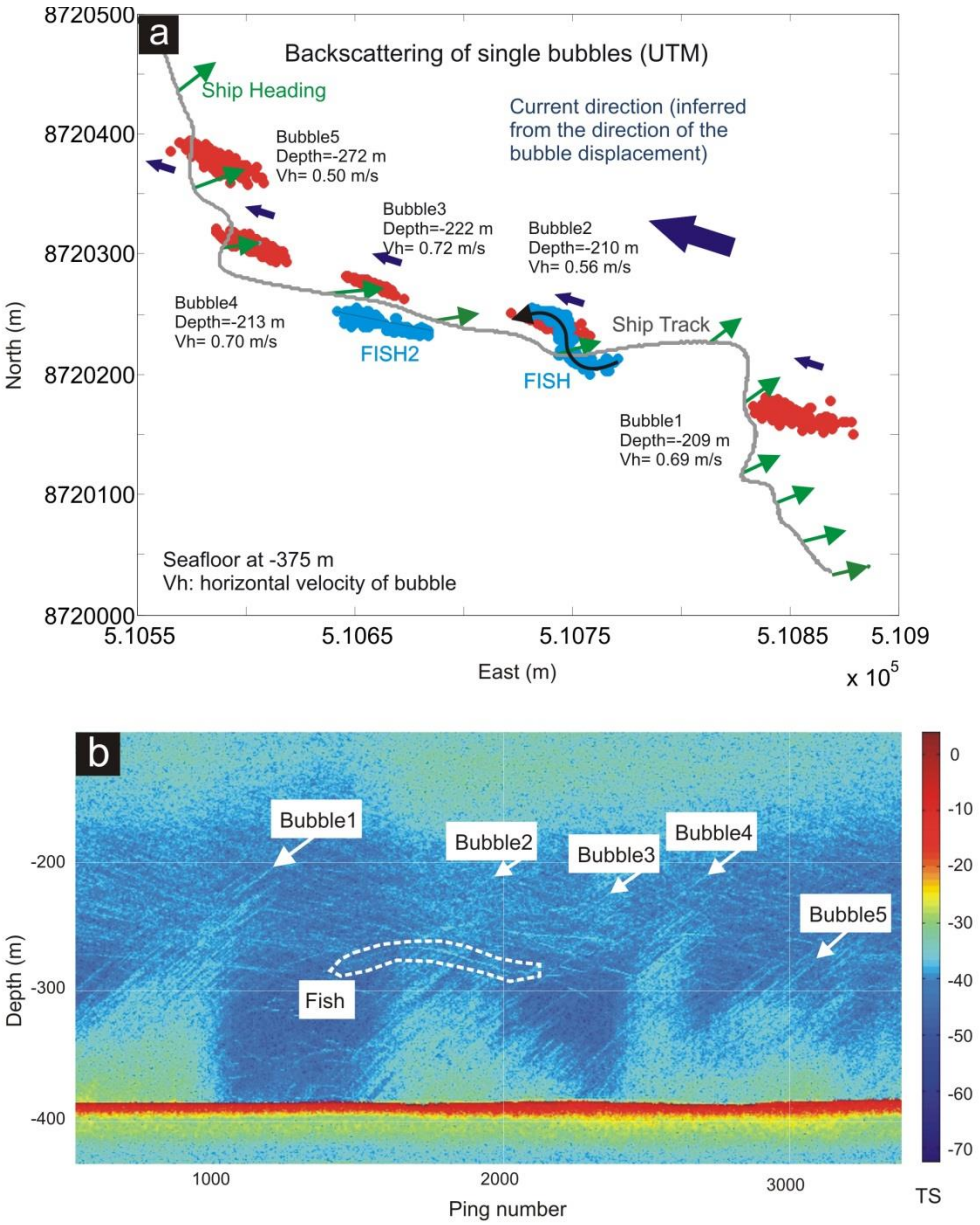

Figure 4.5. Evaluation of current speed using hydroacoustic information of single bubbles captured by a splitbeam echosounder. a) Red spots represent the position of the backscattering produced by bubbles during a certain time interval (horizontal bubble displacement). Blue arrows show the displacement direction. The track of the vessel is shown as a line with green arrows indicating the vessel heading. The horizontal speed of each bubble is specified. b) Gas release in ~375 m water depth; the five bubble lines measured are indicated. Low angle lines that show increasing depth with ping number, are diving fish (e.g. inside dashed line)

4.3. Study area

The study area lies west of Prins Karls Forland (PKF) offshore NW Svalbard (Fig. 6), where two data sets have been recorded in July 2009 and 2012 onboard RV Helmer Hanssen from UiT (The Arctic University of Norway). Methane seepage offshore Svalbard has first been described by Knies et al. (2004) and later by Westbrook et al. (2009). Since then, the area has been annually revisited by several research groups.

Three distinct depth intervals of bubble release have been determined. The deeper area, at about 400 m water depth, appears to be associated with the top of the gas hydrate stability zone (TGHZ) and the dissociation of gas hydrate in response to increasing bottom water temperatures (Westbrook et al. 2009). However, Berndt et al. (2013) have shown that methane release is not a short-term but a long-term process, active for more than several thousands years that started after the last glacial period. At shallower water depth at 240 m, methane-charged fluids migrate along a sedimentologically defined permeable pathway beneath an impermeable glacial debris flow, a specific fluid-focussing mechanism for this area (Rajan et al. 2012). A third and very active area has been recently described by Sahling et al. (2014) on the shelf at only 90 m water depth.

Data from the area at 240 m water depth are used here to present our quantification method and strategies for gas release monitoring. Hydrographically, the area is influenced by the WSC, which is a warm water branch of the North Atlantic Current (NAC) flowing northward together with the CC, which is a continuation of the East Spitsbergen Current (ESC; Fig. 4.6). The CC brings less saline water into the area. Seasonal driven ice formation impacts the hydrographical changes, influencing the water stratification and thus the transport of dissolved and gaseous methane through the water column.

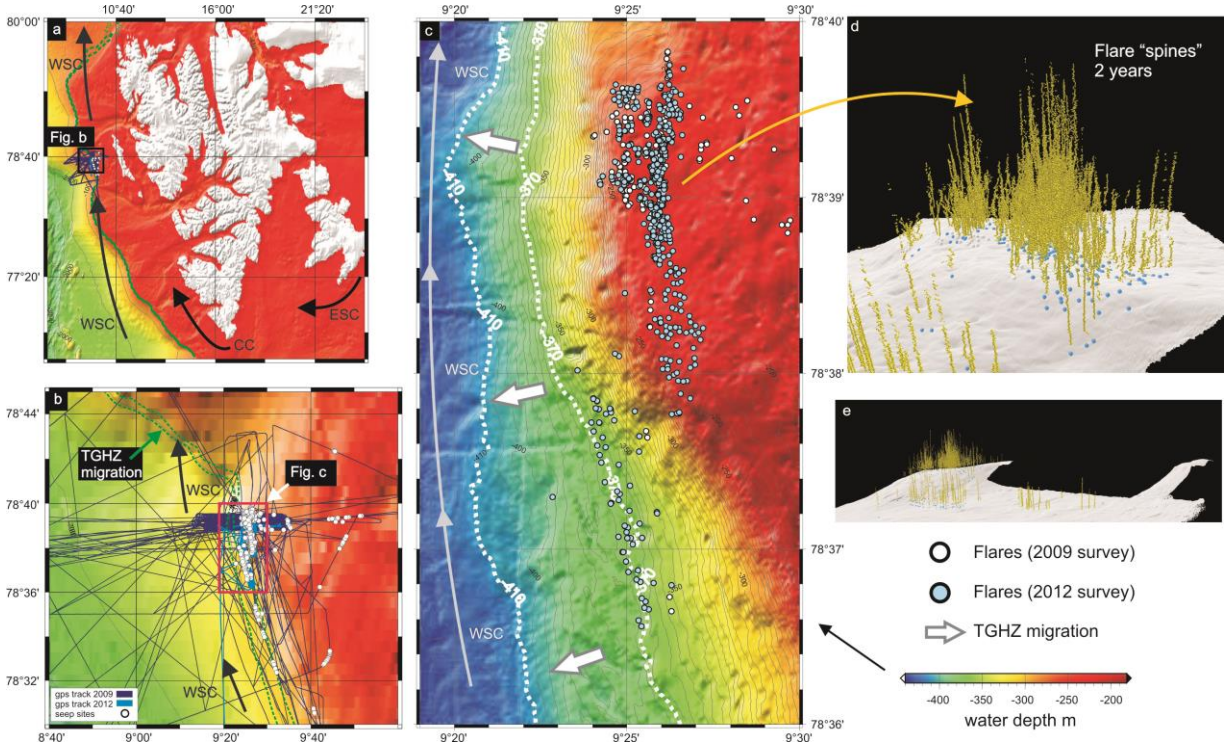

Figure 4.6. a) Bathymetric map of the Svalbard archipelago and dominating currents in the area (WSC; CC; East Spitsbergen Current ESC). b) Track of the hydroacoustic surveys carried out in 2009 and 2012. c) Distribution of detected seeps in the study region; yellow arrows indicate the migration of the TGHZ during the last 30 years from 370 m down to 410 m water depth (Westbrook et al, 2009) assuming a bottom water temperature increase from 2° to 3° C; the area densely covered with seeps at the shelf edge is the focus of our studies. Images d) and e) show a three-dimensional view of the "flare spines" in the study area.

4.4. Methods

4.4.1. Data acquisition and processing

The data presented here have been recorded with an EK60 scientific SBES which applies splitbeam technology; it was operated with three frequencies simultaneously (18, 38 and 120 kHz). In the following, we concentrate on the 38 kHz frequency data because the echogram quality was superior compared to the other frequencies (e.g. less artificial noise and unwanted reverberation, strong backscattering of bubbles); the beam width of this transducer is 6.7°. For data acquisition and online visualization, we used the ER60 software developed by Kongsberg. Post-processing is based on the FM-Midwater tool of the Fledermaus software suite (QPS, now member of the SAAB Group) and a self-written MATLAB-based software package called FlareHunter. FlareHunter calculates target strength *TS* and backscattering volume strength S_V (Appendix 1) and allows three-dimensional visualization and analysis for each depth bin per ping using the mechanical angle information of the split-beam system. Ship motion compensation, static offset correction and where necessary ray-tracing needs to be carried out before further processing and interpretation can be done. This is implemented in FlareHunter.

4.4.2. Seep localization

Flares were identified based on the criteria presented above and manually selected in FlareHunter. The selected ping and depth interval was filtered by a user-definable threshold and cleaned manually to exclude unwanted signals from other sources (fish, plankton) and noise (seafloor multiple, other hydroacoustic systems). Seafloor signals were also excluded to derive a clean and undisturbed water column data set. Each depth bin value of this pre-cleaned data set was geo-referenced to receive the correct position in 3D volume. Static offsets between transducers and the GPS antenna, motion compensation (pitch, roll, yaw and heave) were considered during post-processing (Appendix 2: Workflow diagram). In addition, ray tracing has been implemented in FlareHunter to consider refraction of the acoustic wave with changing sound velocity in the water column. Because of the acquired sound velocity profiles (Appendix 3), the water depth of only 240 m at the chosen seep area and the rather small pitch and roll angles (< 9°), ray tracing was deemed unnecessary to achieve a better positioning accuracy for our specific data set.

Backscattering recorded as a flare is usually caused by multiple targets/bubbles in the acoustic beam released from localized bubble releasing vents at the seafloor. Depending on the areal extend of these vents at the seafloor and current induced spreading of bubbles while rising, bubbles in most cases fill only a small portion of the beam volume at a certain depth (Fig. 4.7), in shallow water wide spread bubbling can fill the beam completely. To better pinpoint the center of the bubble release site on the seafloor, geometric averaging was applied to the edited and position-corrected data. The geometric mean is calculated for each set of backscatter values for a certain depth range, providing a line with only one position per depth range, the 'flare spine' (Fig. 4.7d). The lowermost point just at the seafloor can be seen as the center of the bubble release. This does not mean that each flare is the result of only one bubble vent at the seafloor, but that the centre of the seep site (which most likely consists of multiple bubble vents scattered over a certain area) is the base of the flare spine.

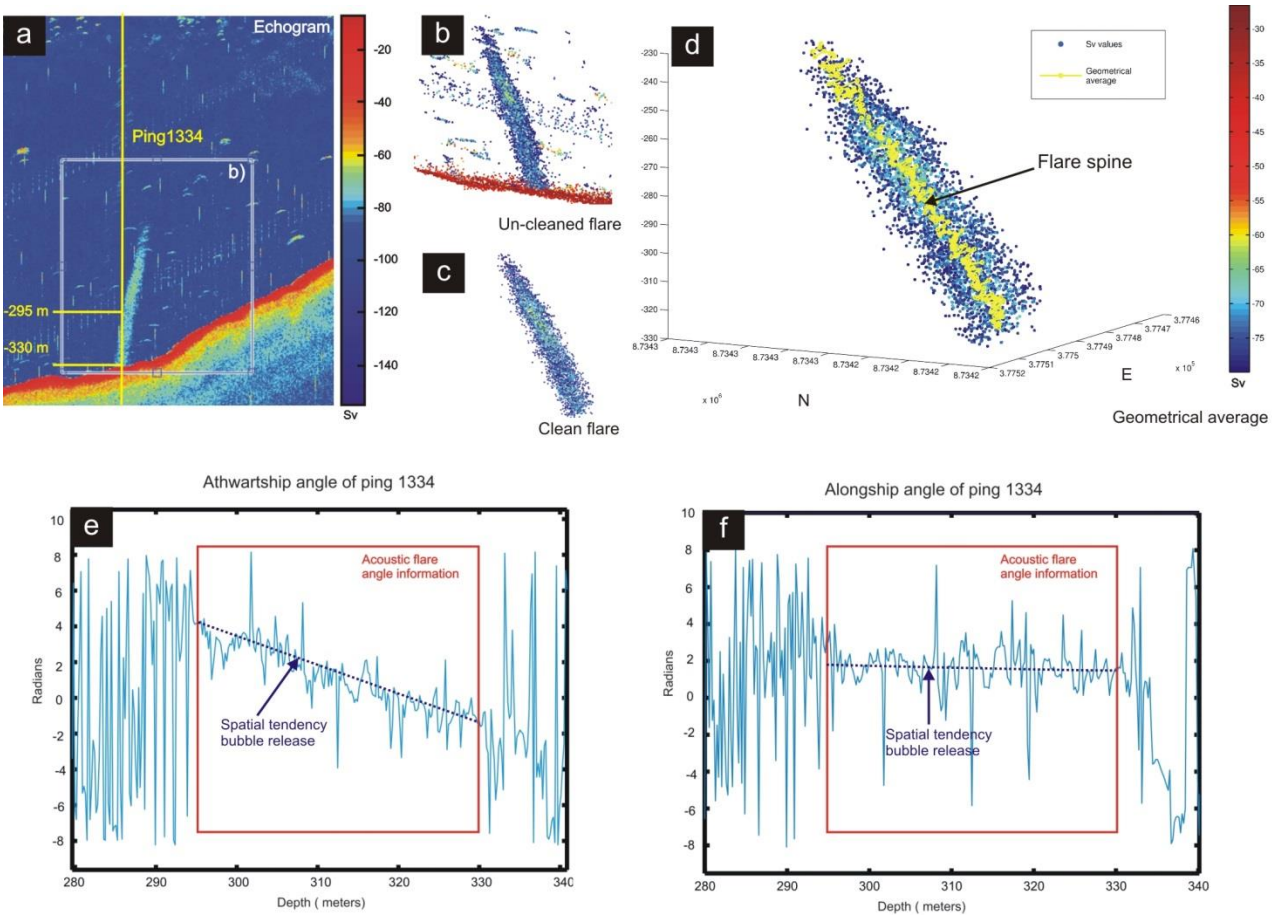

Figure 4.7. Processing steps for flare analysis. a) Identification of the acoustic flare in the echogram (38 kHz) and processing of the backscatter values inside the selected area above a specific threshold of S_V. Images b) and c) show the 3D visualization of the backscatter data of un-cleaned and cleaned data. d) 3D representation of the geometric mean calculated flare-spine. Images e) and f) represent the athwart- and along-ship angle information respectively versus the depth of one selected ping (1334) inside the flare (see image (a)). Data inside the red boxes are from bubble backscattering; for both angles, the more or less linear trend shows that the system correctly identifies the position of the bubbles inside the beam. Spatial uncertainties have been further decreased by calculating the geometric mean over several pings.

Video footage from seep sites in the study area shows little to moderate bubble release activity of single or multiple bubble chains or clouds being released over few to tens of square meters. This means that backscattering could have been produced by single and multiple targets (bubbles) in the beam. Because the splitbeam processing of the EK60 SBES was designed to locate single targets inside the beam, bubble positioning could be faulty due to signals from multiple targets. A faulty identification of multiple targets as single target would most likely result in a random distribution. However, when averaging the target positions by calculating the geometric mean from several consecutive pings, it was shown that the angle information from single targets (with a spatial tendency in the beam lobe) is predominant over randomly distributed data from multiple targets (see Fig. 4.7e, 4.7f).

4.4.3. Inverse method and flow rate estimation

Accurately calculating gas flow rates using hydroacoustic methods is needed but different research groups still use very different approaches (Artemov et al. 2007; Nikolovska et al.2008; Ostrovsky et al.

2008; Muyakshin et al., 2010; Jerram et al., 2014). To date, no standard methodology exists for analyzing free gas flow rates of large bubbles in deep water (> 100 m) with ship-based hydroacoustic systems alone.

Gas flow rate calculations become even more complicated and uncertain if one lacks detailed information about the bubble size distribution. The method that we introduce estimates the bubble flow rate of a group of bubble streams by using the backscattering produced when insonified. The total acoustical backscattering received by the echosounder is assumed to be the contribution of single backscattering produced by several spherical bubbles of different sizes. The inversion relates the flow rate produced by the bubble streams inside the beam with the differential backscattering cross-section (e.g. see Medwin and Clay, 1988) produced by the group of bubbles. The final mathematical expression of the flow rate requires as inputs the target strength (*TS*) values of the acoustic flare at a pre-determined depth; a probability density function of the bubble sizes that have been ideally observed at the respective seep site; BRSs; environmental properties (e.g. densities, sound speed); as well as a number of echosounder specific parameters.

4.4.3.1. Inverse Method

The insonified area of a singlebeam echosounder at the seafloor (the echosounder footprint) can cover several hundreds of square meters (a beam width of 7° covers ~760 m^2 at 220 m bsl) and thus the backscattering signal collected can be produced by several bubble streams (Fig. 4.8).

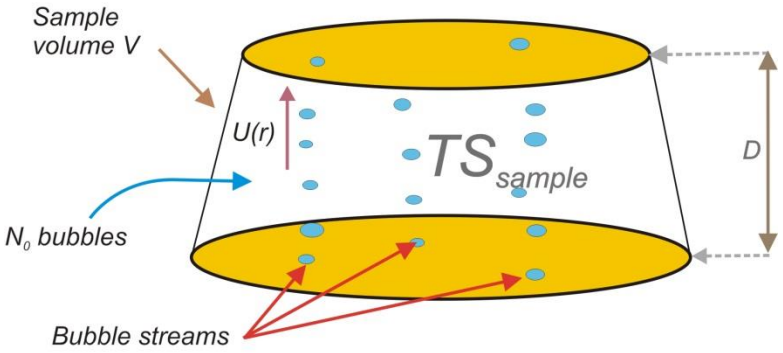

Figure 4.8. Illustration of bubble streams covered by the sample volume *V* of the echosounder at a specific depth. Here $\boldsymbol{N_0}$ represents the total number of bubbles inside the sample volume *V*; $\boldsymbol{TS_{sample}}$ represents the target strength of the sample volume *V*; $\boldsymbol{U(r)}$ is the BRS as function of the bubble size; and $\boldsymbol{D}$ the height of the sample volume *V*.

The available information obtained from the echosounder is given in terms of target strength (*TS*) which is the logarithmic version of the total backscattering cross-section $\Delta\sigma_{bs}$ (also known as differential backscattering cross-section, e.g. see Medwin and Clay, 1988) of the scatterers in the insonified volume (Equation 4.1).

$$TS = 10 \log \Delta\sigma_{bs} \tag{4.1}$$

TS is calculated for each sample of each ping (e.g. Fig. 4) and therefore each *TS* value represents the backscattering produced by the targets located at the approximated truncated conical volume with a depth given by the time sample interval of the received signal (sample volume *V*; Fig. 4.8).

If multi-scattering effects are neglected, the total backscattering cross-section of the sample volume can be simply assumed as the summation of single backscattering cross-sections produced by the scatterers within the sample volume *V*. If the scatterers are considered to be bubbles with different sizes, the total backscattering cross-section coming from a sample volume is given by,

$$\Delta\sigma_{bs} = N_1\sigma_{bs1} + N_2\sigma_{bs2} + \cdots N_n\sigma_{bsn} = \sum_{i}^{n} N_i\sigma_{bsi} \tag{4.2}$$

Where σ_{bsi} represents the backscattering cross-section of a single bubble of *i*-size and N_i the number of bubbles of *i*-size inside the sample volume.

The equivalent of equation [4.2] in the continuous domain can be expressed as,

$$\Delta\sigma_{bs} = \int_{r_1}^{r_2} N(r)\sigma_{bs}(r)dr \tag{4.3}$$

where,

$$N_0 = \int_{r_1}^{r_2} N(r)dr \tag{4.4}$$

N_0	:	Total number of bubbles inside the sample volume *V*
$N(r)$	:	Distribution of bubbles in function of the radius size [1/m]
r_1, r_2	:	Lower and upper limit of the bubble size distribution

In equation [4.3], σ_{bs} represents the theoretical backscattering cross-section of a single bubble. In this work, we use the equation given by Thuraisingham (1997; Fig. 4.9a) to calculate σ_{bs} as this expression is valid for all kr values, where k represents the wave number, and r the bubble radius [4.5].

$$\sigma_{bs} = \frac{r^2}{\left[\left(\left(\frac{r_0}{r}\right)^2 - 1\right)^2 + \delta(r, f_{echo})^2\right]} \frac{(\sin kr/kr)^2}{1 + (kr)^2} \tag{4.5}$$

where,

r_0	:	Bubble resonant radius at echosounder frequency and specific static pressure [m]
k	:	Wave number ($\frac{2\pi f_{echo}}{c}$)
f_{echo}	:	Echosounder frequency [Hz]
δ	:	Dimensionless damping

Expressions for the damping δ (Ainslie, 2010) and the resonance frequency ω_M (Minnaert, 1933) valid for moderately large bubbles (radius exceeding 100 μm), are presented in equations [4.6] and [4.7a-c] and [4.8], respectively (Appendix 4).

$$\delta(r,\omega) = \delta_{rad} + \delta_{therm} + \delta_{visc} \quad (4.6)$$

$$\delta_{rad} = \omega_M r / c_w \quad (4.7a)$$

$$\delta_{therm} = \frac{3(\gamma-1)}{r}\left(\frac{D_a}{2\omega_M}\right)^{\frac{1}{2}} \quad (4.7b)$$

$$\delta_{visc} = \frac{(\eta_S + 3\eta_B)}{\rho_W \omega_M r^2} \quad (4.7c)$$

$$\omega_M = \left(\frac{3\gamma P_{st}}{\rho_W r^2}\right)^{\frac{1}{2}} \quad (4.8)$$

where,

δ_{rad}	:	Re-radiation damping term (dimensionless)
δ_{therm}	:	Thermal damping term (dimensionless)
δ_{visc}	:	Viscous damping term (dimensionless)
ω_M	:	Minnaert frequency [rad/s]
c_w	:	Speed of sound in the seawater [m/s]
γ	:	Specific heat ratio of gas (dimensionless)
D_a	:	Thermal diffusivity [m^2/s]
η_S	:	Shear viscosity [Pa][s]
η_B	:	Bulk viscosity [Pa][s]
ρ_W	:	Water density [kg/m^3]
P_{st}	:	Static pressure [Pa]

The value of r_0 in [4.5] was calculated using the breathing frequency expression [4.9] developed by Minnaert (Minnaert 1933; Medwin and Clay 1998). Fig. 4.9b depicts r_0 values at different depths for a 38 kHz frequency,

$$r_0 = \frac{1}{2\pi f_{ECHO}}\left(\frac{3\gamma P_{st}}{\rho_W}\right)^{\frac{1}{2}} \quad (4.9)$$

where,

γ	:	Specific heat ratio of gas (dimensionless)
ρ_W	:	Water density [kg/m^3]
f_{ECHO}	:	Echosounder frequency [Hz]
P_{st}	:	Static pressure [Pa]

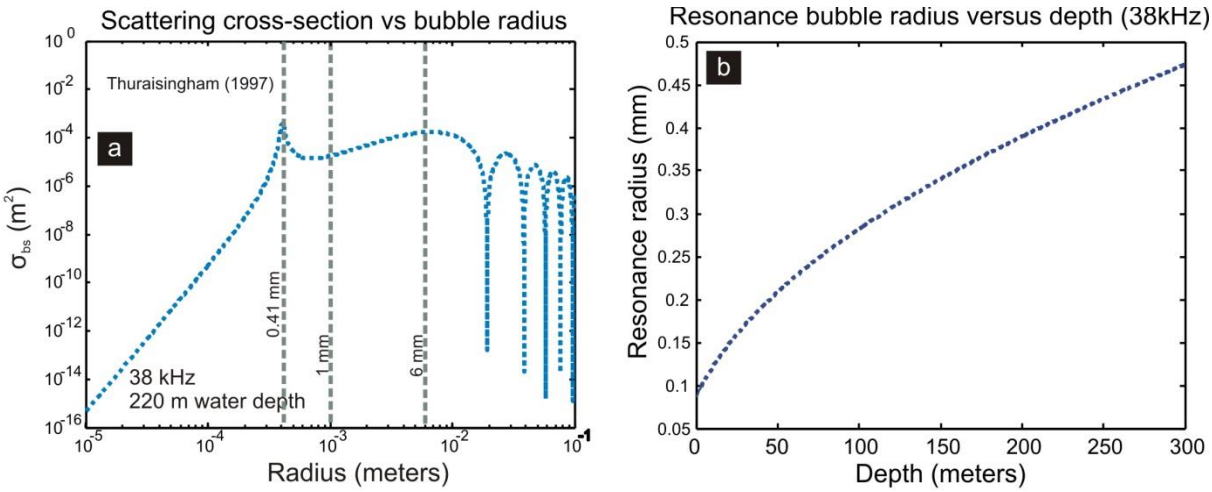

Figure 4.9. a) Acoustic backscattering cross section σ_{bs} as function of the bubble radius using the mathematical expressions of Thuraisingham (1997) for a single bubble, considering bubbles at 220 m and using the Minnaert frequency (Minnaert 1933) as resonance frequency. b) Representation of the Minneart resonance radius at different depths for a pure methane bubble insonified with 38 kHz.

As stated above, singlebeam echosounders can cover an area with several bubble streams. Therefore, the mathematical expression of the total flow rate linked to the obtained acoustical backscattering must represent the backscattering produced by these several bubble streams. If it is assumed that all the bubbles released are approximately spherical the volumetric bubble flow rate of a group of bubble streams can be defined as following,

$$\emptyset_V = \frac{4\pi}{3}\sum_{i}^{n} r_i^3 N_i/\Delta t_i \tag{4.10}$$

And its equivalent mass bubble flow rate as,

$$\emptyset_M = \rho_G \frac{4\pi}{3}\sum_{i}^{n} r_i^3 N_i/\Delta t_i \tag{4.11}$$

where,

r_i : Bubble radius of i-size [m]
N_i : Number of bubbles of i-size inside the volume sample *V*
Δt_i : Time necessary to fill the volume sample *V* with N_i bubbles of r_i radius [sec]
ρ_G : Gas density of the bubble at the respective water depth [kg/m^3]

In order to relate the flow rate with the volume sample (Fig. 4.8) we assume that the time Δt_i is necessary to fill the volume sample *V* with N_i bubbles of r_i radius. If we consider U_i as the average BRS of a bubble of r_i radius and *D* the vertical distance that the bubble needs to travel from the lower to the upper limit of the sample volume *V*, the massive flow rate (equation [4.11]) can be replaced by,

$$\emptyset_M = \rho_G \frac{4\pi}{3D} \sum_{i}^{n} r_i^3 N_i U_i \tag{4.12}$$

Where,

U_i : Average BRS of i-size bubble (m/sec)
D : Height of volume sample [m]

The equivalent expression of equation [4.11] in the continuous domain can be expressed as following,

$$\emptyset_M = \rho_G \frac{4\pi}{3D} \int_{r_1}^{r_2} r^3 N(r) U(r) dr \tag{4.13}$$

Where,
$U(r)$: BRS in function of the bubble radius [m/sec]

To obtain our inverted expression of the total mass flow rate $\emptyset_M$ related to the backscattering $\Delta\sigma_{bs}$coming from the sample volume *V*, equations [4.3] and [4.13] are combined. The total mass flow rate of the bubble streams inside the sample volume is then given by:

$$\emptyset_M = \rho_G \Delta\sigma_{bs} \frac{4\pi}{3D} \frac{\int_{r_1}^{r_2} r^3 N(r) U(r) dr}{\int_{r_1}^{r_2} N(r)\sigma_{bs}(r) dr} \tag{4.13a}$$

Or its equivalent using the *TS* value (equation [4.1])

$$\emptyset_M = \rho_G 10^{\frac{TS}{10}} \frac{4\pi}{3D} \frac{\int_{r_1}^{r_2} r^3 N(r) U(r) dr}{\int_{r_1}^{r_2} N(r)\sigma_{bs}(r) dr} \tag{4.13b}$$

It can be assumed that the distribution of bubbles $N(r)$ inside the volume sample is equal to the total number of bubbles N_0 multiplied by the probability density function $f(r)$ of the bubble size distribution. As we further know that D represents the depth of the volume sample which can also be expressed as a function of the sample interval τ and the sound propagation speed c_w. in the water, equation [4.13b] can be re-written as:

$$\emptyset_M = \rho_G 10^{\frac{TS}{10}} \Psi \tag{4.14}$$

where,

$$\Psi = \frac{8\pi}{3c_w\tau} \frac{\int_{r_1}^{r_2} r^3 f(r) U(r) dr}{\int_{r_1}^{r_2} f(r)\sigma_{bs}(r) dr} \tag{4.15}$$

$f(r)$: Probability density function of the bubble size distribution [1/m]
τ : Sample interval [sec]

4.4.3.2. Flow rate estimation

TS average values were extracted from flares visualized in echograms using FlareHunter. All *TS* values in echograms were compensated for their position in the beam using the Simrad split-beam method described by Echoview (Echoview webpage: http://www.echoview.com/).

Acoustic flares were identified within the *TS* echograms and *TS* average values ($\overline{TS}$) of each flare at the source near the seafloor were stored together with additional information as e.g. water depth, footprint at the specific depth, geographic coordinates or sound speed. To decrease the effect of background noise, data below -70 dB were threshold filtered for the entire echogram (Fig. 4.10a). In order to isolate single flares, the backscattering surrounding the flare was manually removed (Figs. 4.10b and 4.10c). Backscattering coming clearly from fish (shape with stronger signal than the flare) was manually removed (edited in 3D using MATLAB functionality) in order to avoid overestimation of flow rates. To evaluate the flow rate of the flares the *TS* values coming from a 5 m thick layer with the lower boundary 5 m above the seafloor were used (Fig. 4.10d). *TS* values coming from this layer of a single flare were geometrically averaged in order to obtain one representative $\overline{TS}$ value for the strength of bubble release close to the source at the seafloor. We choose this layer from 5 to 10 m above the bottom to be as close as possible to the source (and with as little as possible changes in bubble size due to bubble dissolution while rise) but avoiding reverberation effects of the signals at the seafloor. The $\overline{TS}$value was calculated using the following mathematical equation,

$$\overline{TS} = 10\log\left(\left[\prod_{i=1}^{n_P} 10^{\frac{TS_i}{10}}\right]^{\frac{1}{n_P}}\right) \tag{4.16}$$

where,

TS_i : Target strength of different samples inside the (selected layer [dB]
n_P : Number of samples

The final flow rate (mass and volumetric) of each of the detected acoustic flares was estimated using equation [4.14].

As defined in equation [4.14], the parameter Ψ depends on *f(r)*, *U(r)*, r_0 and *δ.* The probability density function *f(r)* was calculated from a polynomial fit of the bubble size distribution (BSD) visually obtained during the during surveys carried out in 2011 and 2012 (McGovern, 2012; solid green line in Fig. 4.11).

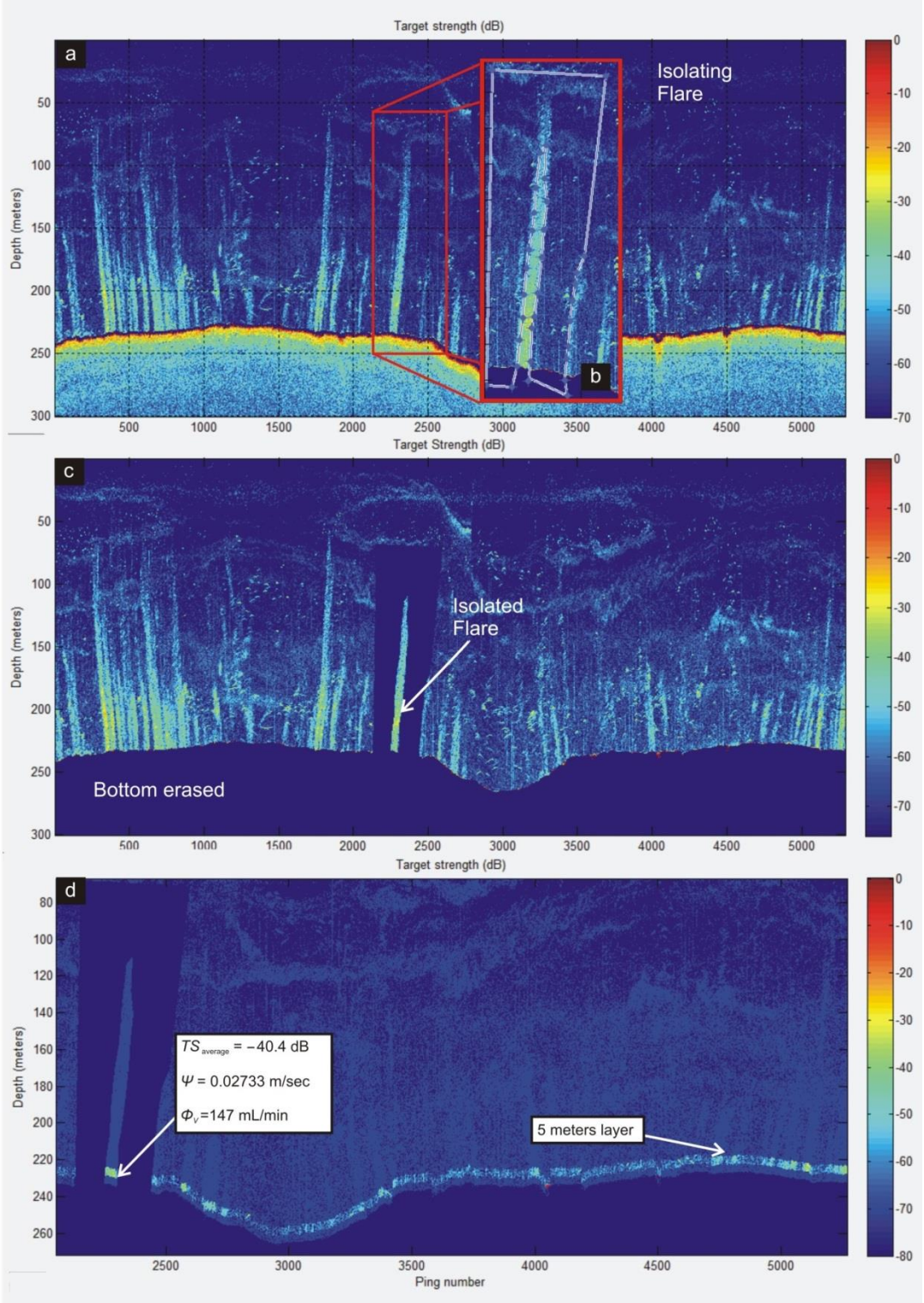

Figure 4.10. Acoustic flare detection and flow rate estimation processing using FlareHunter GUI; a) TS echogram (beam compensated) filtered with a lower threshold of -70 dB; b) Removal of 'noise' surrounding an isolate flare; c) Isolated flare with removed signals from the seafloor and below; d) Layer selection to calculate $\overline{TS}$ at near the seafloor of the flare. The figure shows Ψ value and the estimated flow rate using the Leifer model for clean bubbles to estimate BRS.

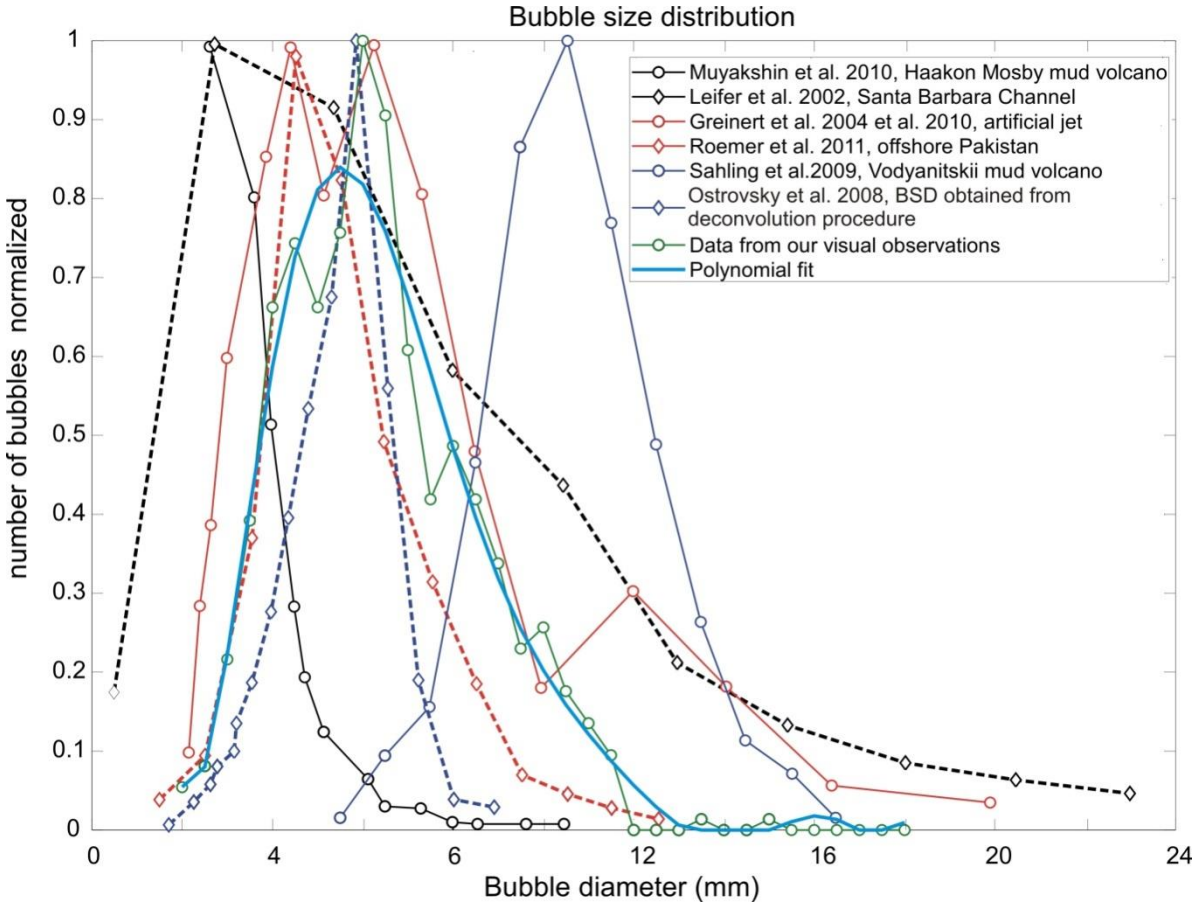

Figure 4.11. BSD from our video observations (green line with circles) in comparison to other published data. For our gas flow rate estimation we considered bubbles with a radius from 1 to 6 mm; none of them is resonant in 220 m water depth (Fig. 9b).

U(r) was calculated for bubbles of 1 to 6 mm in diameter using a MATLAB-based script kindly provided by Ira Leifer (Fig. 4.12; Bubbleology Research International). This script considers bubble rise models of Mendelson (1967), Woolf and Thorpe (1991), Woolf (1993), Leifer et al. (2000), and Leifer and Patro (2002).

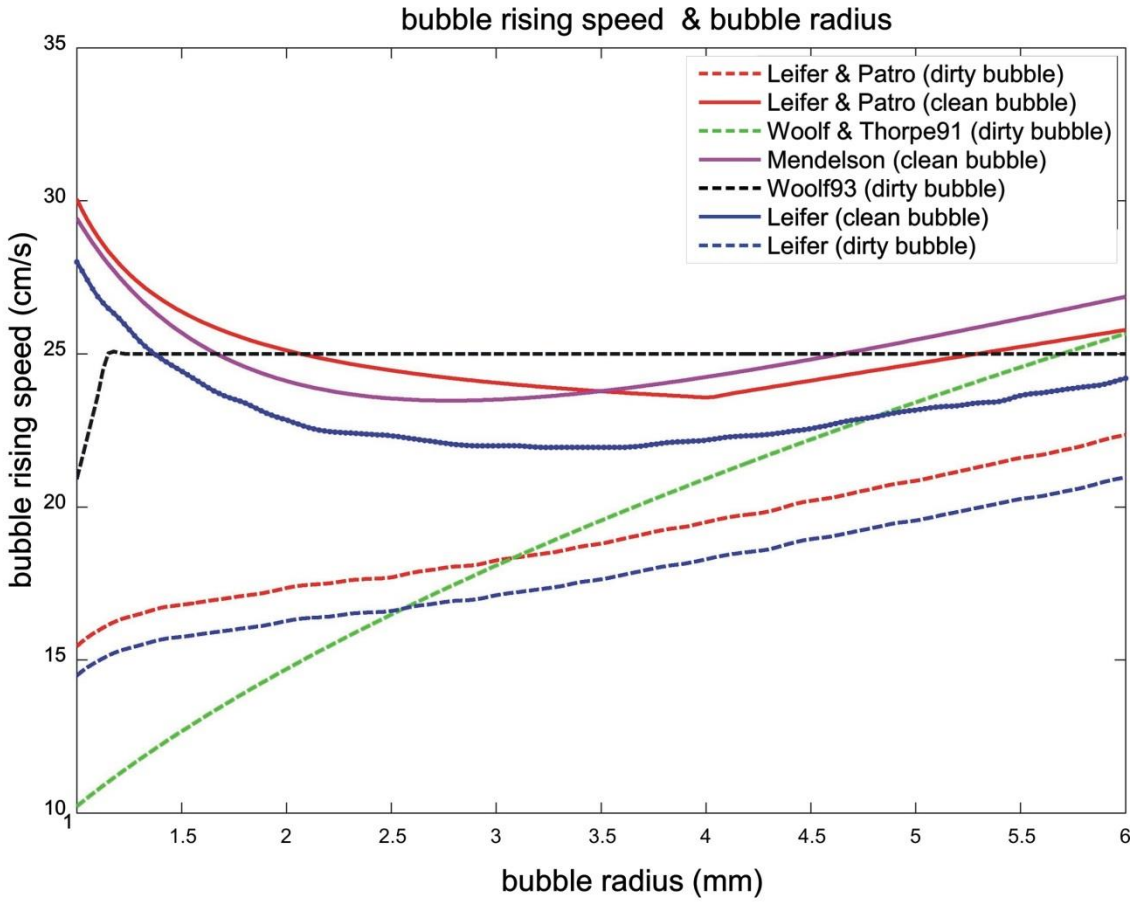

Figure 4.12. Representation of the BRS as function of the bubble radius (1 to 6 mm) using different published models (Mendelson 1967; Woolf and Thorpe 1991;Woolf 1993; Leifer et al. 2000; Leifer and Patro 2002).

Temperature and salinity are necessary input parameters in those models. Based on CTD profiles, we used 4 °C and a salinity of 35 PSU at 220 m water depth (see profiles Appendix 3). Radii r_0 for each flare were estimated using the corresponding average layer depth following equation [4.9]. The damping δ and Minnaert frequency ω_M were calculated for bubble sizes between 1 and 6 mm using equations [4.6], [4.7] and [4.8], and the needed constants detailed in Table 4.1. The gas density ρ_G at different water depth for pure methane was calculated using the simplified equation given by (Medwin and Clay (1988), with atmospheric density of methane ρ_{G0} of 0.66 kg/m^3.

$$\rho_G = \rho_{G0}\left(1 + \frac{2\sigma}{P_{st} r_{av}}\right)(1 + 0.1Z) \qquad (4.17)$$

where,

ρ_{G0} : Atmospheric CH_4 density
σ : Surface tension water[N/m]
r_{av} : Most frequent bubble radius BSD (m)
Z : Average depth of layer at each acoustic flare

A more precise density can be calculated using the SUGAR toolbox by Kossel et al. (2013).

Table 4.1. Constants values used to evaluate flow rates of each acoustic flare

Constant	Symbol	Value
Atmospheric CH_4 density	ρ_{G0}	0.66 [kg/m^3]
Surface tension water	σ	0.074 [N/m]
Most frequent bubble radius BSD	r_{av}	0.003 [m]
Average sound velocity seawater	c_w	1467 [m/s](from sound speed profiles, Appendix 3)
Specific heat ratio of gas	γ	1.4
Thermal diffusivity	D_a	9.19e-7 [m^2/s^{-1}]
Shear viscosity	η_S	1.519e-3 [Pa/s]
Bulk viscosity	η_B	2.2η_S [Pa/s]
Water density	ρ_W	1028 [kg/m^2] (derived from CTD casts)
Echosounder frequency	f_{ECHO}	38000 [Hz]
Atmospheric pressure	P_{st0}	101325 [Pa]
Acceleration of gravity	g	9.8 [m/s^2]
Static pressure at bubble depth	P_{st}	$P_{st0} + \rho_W g Z$ [Pa]
Water depth of bubbles	Z	Average depth of layer at each acoustic flare
Average temperature	T	4 °C (used in BRS models; from temperature profiles, Appendix 3)
Salinity	S	35 PSU (used in BRS models; from salinity profiles, Appendix 3)

To assign an average flow rate to a cluster of flares forming a seep site, flares were clustered if the footprints overlap (Fig. 4.13). Once the clustering is done, the average bubble flux $\Omega^C_{M,V}$ (volumetric or in mass) can be obtained using the following expression,

$$\Omega^C_{M,V} = \frac{\emptyset^1_{M,V}}{A_1} + \frac{\emptyset^2_{M,V}}{A_2} + \frac{\emptyset^3_{M,V}}{A_3} + \cdots + \frac{\emptyset^P_{M,V}}{A_p} = \sum_i^p \frac{\emptyset^i_{M,V}}{A_i} \tag{4.18}$$

where,

$\emptyset^i_{M,V}$: Flow rate (volumetric or massive) of an *i*-acoustic flare [dB]
A_i : Area of echosounder footprint of the source of an *i*-acoustic flare [m^2]
p : Number of acoustic flares that belong to the cluster

In order to evaluate the average flow rate of each cluster $\emptyset^C_{M,V}$, the average bubble flux $\Omega^C_{M,V}$ is multiplied by the area of the cluster A_C (Fig. 4.13c). The cluster area was calculated by gridding all footprints (Fig. 4.13c). The cluster flow rate $\emptyset^C_{M,V}$was then calculated as:

$$\emptyset^C_{M,V} = \Omega^C_{M,V} A_C = \Omega^C_{M,V} N_{Cells} \Delta x \Delta y \tag{4.19}$$

where,

A_C : Cluster area [m^2]
N_{Cells} : Number of cells inside the cluster area
$\Delta x, \Delta y$: cell size in x and y direction (here related to UTM coordinates) [m]

Finally, the estimation of the total flow rate $\emptyset_{M,V}^{T}$ of the study area is done by adding the flow rates of the each cluster and isolated flares (flares without overlapping footprints).

$$\emptyset_{M,V}^{T} = \sum_{i} \emptyset_{M,V}^{C,i} \tag{4.20}$$

where,

$\emptyset_{M,V}^{C,i}$: Flow rate of *i*-cluster or *i*-isolated flare

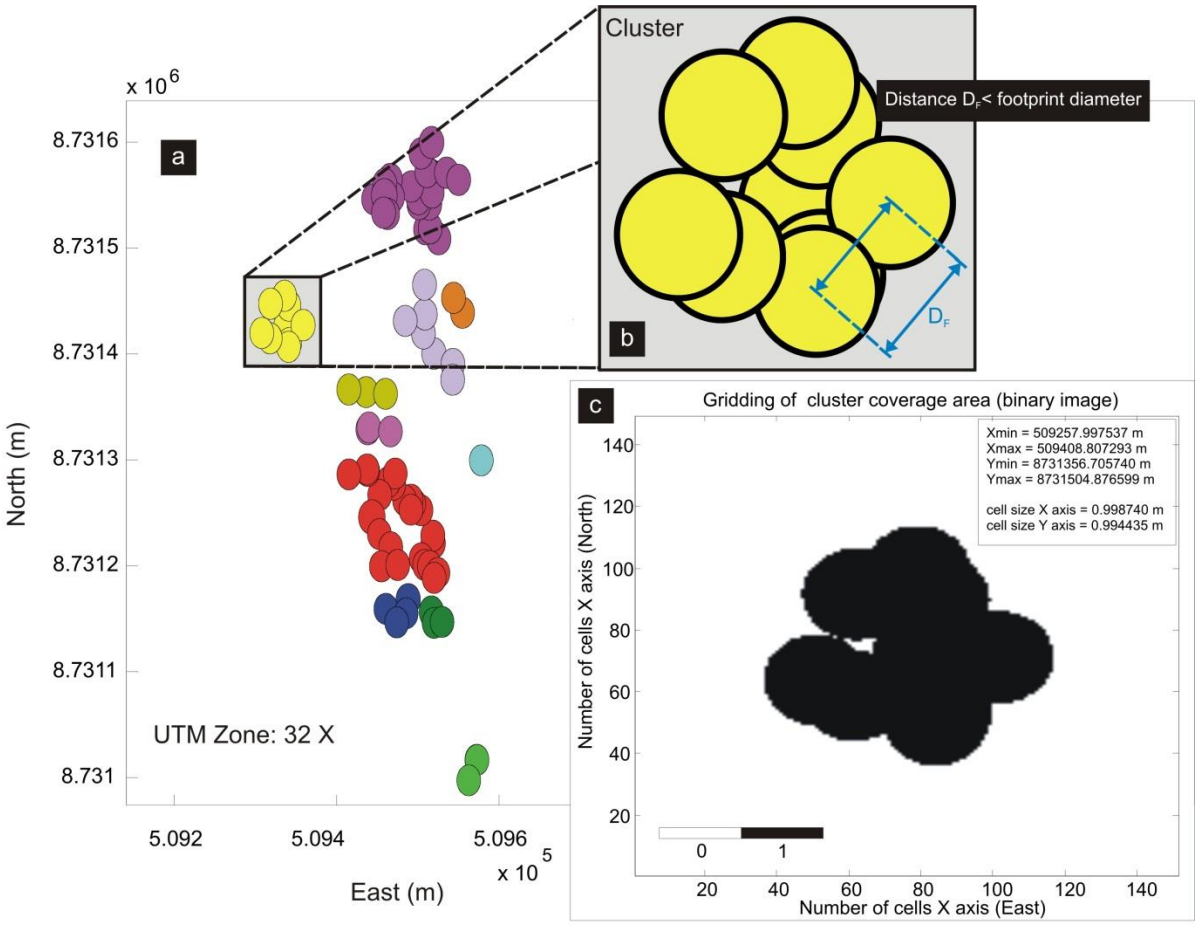

Figure 4.13. Example of the clustering process of detected flares; a) Several clusters in the study area (different colors); sizes of circles are equivalent to the footprint of the echosounder at the layer average depth; b) Zoom in of one cluster example showing the overlap of the footprint; c) combination of the overlapping footprints to estimate the cluster area.

4.5. Results

4.5.1. Methane flow rates and fluxes

During the surveys in 2009 and 2012, the same seep area was investigated. Unfortunately, we could not rerun the same survey lines because of time limitations; the very dense EW line spacing in 2009 was part

of a 3D-seismic survey. However, two slightly oblique surveys covered the main seep area in 2012; slight differences in coverage remain. Fig. 4.14 presents the final acoustic maps from both years of SBES mapping as well as a map where both surveys are merged (Fig. 4.14d).

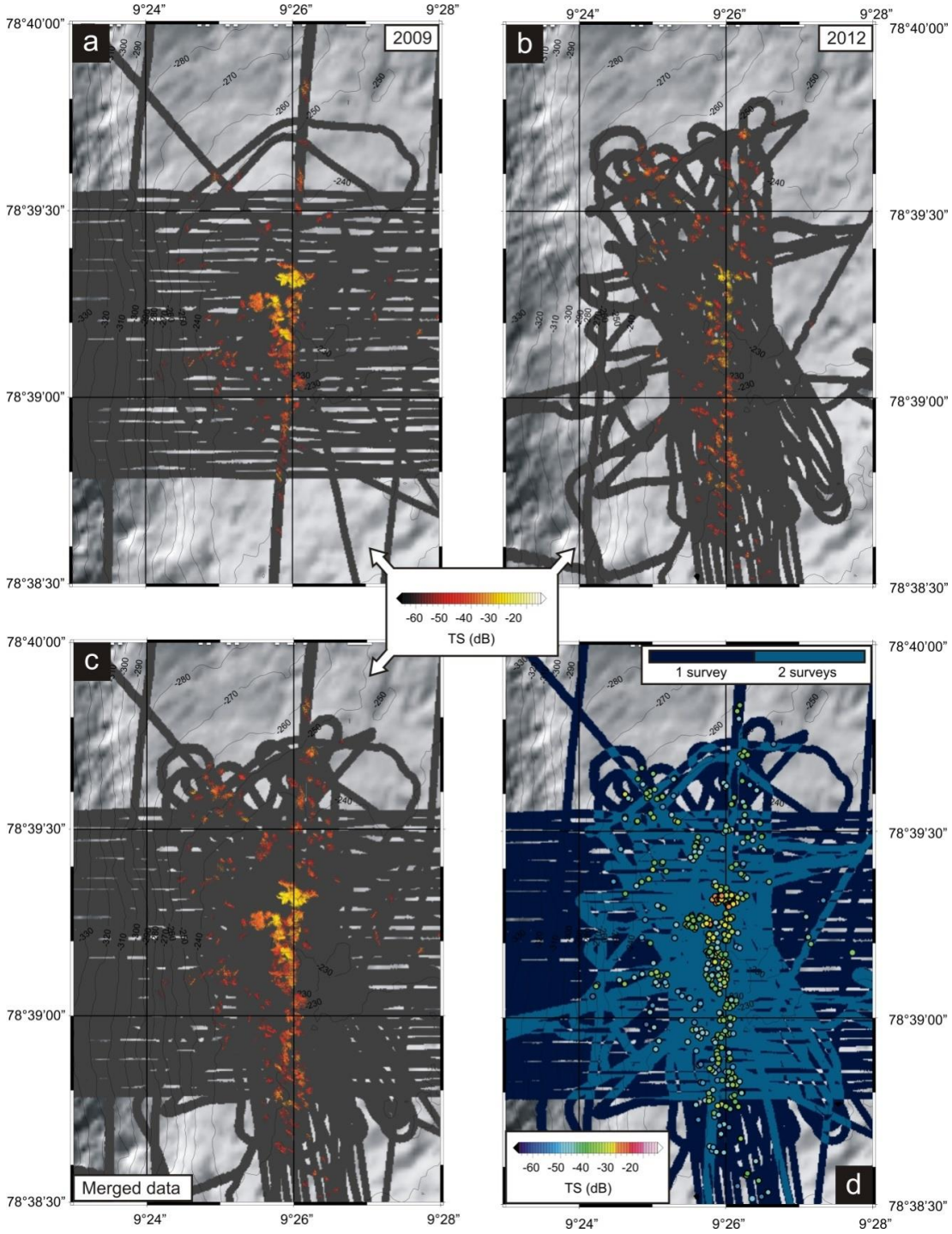

Figure 4.14. a-b) Acoustic maps of bubble induced backscattering (*TS* values) above the seafloor. c) Map of merged backscattering *TS* over 2 years. Grey areas in images (a) to (c) indicate the insonified area/footprint. d) Overlap of the insonified areas in 2009 and 2012. Areas covered once are dark blue, those covered twice are lighter blue. Colored circles represent target strength at the centre of the footprint in the selected depth layer.

Final flow rates and flux estimates (per volume and mass) per minute and extrapolated to one-year are shown in Table 4.2. They are based on the above mentioned inverse method to calculate $\emptyset_{M,V}^{T}$ using the Thuraisingham model of acoustical backscattering cross-section of bubbles and applying different models for calculating BRS. We chose to present flow rates for a one-year period in order to provide data in the same unit as other authors (Judd et al. 1997; Hornafius et al. 1999; Sauter et al. 2006). We think that extrapolating flow rates to "one year" based on short-term one-day observations needs to be treated carefully as they most likely are not a valid representation for the entire year. However, repeated flow rate measurements of one-day or maybe one-hour period provide important information about short time flow variability.

Table 4.2. CH_4 flow rates and fluxes with respect to different BRS models (Mendelson 1967; Woolf and Thorpe 1991; Woolf 1993; Leifer et al. 2000; Leifer and Patro 2002). The table also includes the mean, standard deviation, relative error using the different BRS models and the relative error produced by $\pm$ 1 dB of variation in the *TS* value of the source of the acoustic flare.

Data period	2009		2012		2 years merged	
	Total covered area (m^2)					
	101285.61		158632.36		231930.41	
BRS model						
Clean bubbles	$\emptyset_V^T$ *(L/min)*	$\emptyset_M^T$ *(T/yr)*	$\emptyset_V^T$ *(L/min)*	$\emptyset_M^T$ *(T/yr)*	$\emptyset_V^T$ *(L/min)*	$\emptyset_M^T$ *(T/yr)*
Leifer 'clean bubble' (mean=0.231 *m/s*)	36.58	300.48	42.83	354.38	64.76	534.50
Mendelson 'clean bubble' (mean=0.249 *m/s*)	46.18	379.26	54.06	447.29	81.75	674.63
Leifer&Patro 'clean bubble' (mean=0.249 *m/s*)	45.61	374.65	53.40	441.86	80.76	666.43
Mean	42.79	351.46	50.09	414.51	75.75	625.18
Standard deviation	5.38	44.21	6.30	52.14	9.53	78.64
Relative error, BRS models (%)	$\pm$ 14.53					
Approximated relative error, $\pm$1dB *TS* value (%)	$\pm$ 26.40					
	Mean Flux $(1000 \times \emptyset_{M,V}^{T}/m^2)$					
	0.42	3.47	0.32	2.61	0.33	2.70
Dirty bubbles	$\emptyset_V^T$ *(L/min)*	$\emptyset_M^T$ *(T/yr)*	$\emptyset_V^T$ *(L/min)*	$\emptyset_M^T$ *(T/yr)*	$\emptyset_V^T$ *(L/min)*	$\emptyset_M^T$ *(T/yr)*
Leifer&Patro 'dirty bubble' (mean=0.190 *m/s*)	37.04	304.19	43.36	358.76	65.57	541.11

Table 4.2 (continued)

Woolf & Thorpe 'dirty bubble' (mean=0.191 *m/s*)	39.79	326.79	46.58	385.41	70.44	581.29
Woolf 93'dirty bubble' (mean=0.249 *m/s*)	46.23	379.68	54.12	447.79	81.84	675.37
Leifer 'dirty bubble' (mean=0.178 *m/s*)	30.15	247.60	35.29	292.02	53.37	440.44
Mean	38.30	314.56	44.83	370.99	67.80	559.55
Standard deviation	6.66	54.71	7.80	64.52	11.79	97.32
Relative error, BRS models (%)	$\pm$ 17.39					
Approximated relative error, $\pm$ 1dB *TS* value (%)	$\pm$ 26.40					
	Mean Flux $(1000 \times \emptyset^{T}_{M,V}/m^2)$					
	0.38	3.11	0.28	2.34	0.29	2.41

In addition to the uncertainty described in Table 4.2, another uncertainty is given by the bubble size distribution itself; it is necessary to measure accurate BSD in order to obtain realistic values of the flow rate. Table 4.3 shows an example of the differences of estimated flow rate values based on different published BSD (Ostrovsky et al. 2008; Sahling et al. 2009; Römer et al., 2011). We used an example flare and the average *TS* value at the source near the bottom to calculate the flow rates (Fig. 4.15). In addition the BSD from McGovern (2012) and a uniform bubble size of 6 mm in diameter were used. Uncertainties are given in Table 4.3 and with 60 % of relative error the BSD is more important than rising speed and uncertainties in the absolute *TS* value.

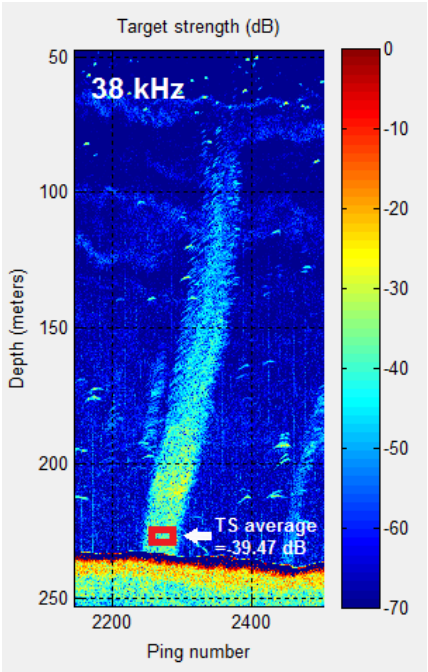

Figure 4.15. Acoustic flare used to evaluate the flow rate at the source using different BSD

Table 4.3. Estimation of flow rates using different BSD

BSD	**Flow rate (ml/min)**
BSD from our visual observations (McGovern, 2012)	181.02
All bubbles same size (diameter: 6 mm, most frequent value of our BSD)	110.38
BSD from Ostrovsky et al. 2008	108.42
BSD from Sahling et al. 2009	412.61
BSD from Römer et al., 2011	136.52
Mean	189.79
Standard deviation	127.95
Relative error (%)	$\pm$ 60.30

4.6. Discussion

The following discussion only deals with the presented methodology. We do not attempt to discuss or even answer the observed changes in fluxes between the two survey years. This will be part of another study where we compare fluxes from yearly surveys between 2008 and 2014 over the same area presented here.

4.6.1. Limitations of the methodology

Methods quantifying free gas flow rates in lakes and oceans using hydroacoustic measurements have recently undergone a series of developments that improved their reliability and accuracy. This is particularly true for shallow-water studies, e.g. in lakes as described by Ostrovsky et al. (2008) and Delsontro et al. (2011). In deep water (> 100 m), methodologies link visual observations and direct flow rate measurements (e.g. inverted funnels) with the larger-scale occurrence of seeps observed in single- or multibeam data (Nikolovska et al., 2008; Greinert et al., 2010; Römer et al., 2012b). Not always are links between the hydroacoustic backscatter intensity and direct flow rate measurements established. This could result in an empirical relationships that allows better extrapolations if applied to the measured acoustic data. Although the flow rate estimates presented still need to be validated using either discrete measurements, visual or high-frequency acoustic measurements by ROV deployments, we are confident that our flux estimates are reasonable and representative for the area at the time of the survey in July 2009 and 2012.

Our approach follows the understanding that the received acoustic signal is generated by the contribution of the backscattering produced by several single targets (Artemov et al., 2006; Muyakshin and Sauter, 2010; Weber et al., 2014). As mentioned earlier, we use a set of assumptions on which our method is based. We assume that a) the targets are spherical bubbles of different sizes, each one being an isotropic scatterer. As the scattering of a single bubble can be related to its radius and therefore its volume (Wildt, 1946), it is b) also assumed that the scattering generated by multiple bubbles is related to the total volume of the bubbles within the insonified volume of water (Medwin, 1977). We are aware that assumptions a) and b) may have a large uncertainty because they “idealize” real conditions and a

purely summation of the backscattered energy coming from single targets has limited application validity. To our knowledge there is no finally validated and conclusive backscatter model for large wobbly bubbles or bubble clouds insonified with low frequency echosounders in water depth > 100 m where multiple backscattering (backscattering of energy that does not directly come from the transducer but from other bubbles, but which is also received by the transducer) might occur as well. Advanced models that describe the backscattering strength of large, none spherical and wobbly bubbles that travel in close distance to each other could easily be included in our methodology by replacing equations [4.5] to [4.9]. Despite the used simplification and the existing uncertainties about BSD and BRS, our results give reasonable approximations for methane flow rates that are in agreement with direct observations (McGovern, 2012; Sahling et al., 2014).

4.6.2. Uncertainties of bubble size and rising speed

Many optical observations at seep sites of different release intensities and in different water depths show that bubbles of 1 to 12 mm in diameter present the most common sizes with a mean diameter of 6 mm that is frequently found (see references in Fig. 4.11). Larger bubbles are neither spheres nor ellipsoids but represent rather irregularly shaped oblate forms that change shape while rising in a wobbly fashion (Ostrovsky et al., 2008; Leifer and Culling, 2010). The shape of the bubble depends on the forces acting on it and only below a certain size where the surface tension force predominates so bubbles become spherical (Bhaga and Weber, 1981); the same is true for larger bubbles if they are gas-hydrate skinned (Rehder et al., 2009).

Flow rate estimates obviously strongly depend on the BSD and the bubble BRS. For our flow rates and flux calculations, the BSD obtained from our optical data was considered to be representative for the release within the study area although only 17 seep locations scattered over the entire area were observed for a very short time and only 641 bubbles in total have been analyzed (McGovern, 2012). The BSD as well as the mean bubble size agree well with results from similar seep settings (see references in Fig. 4.12). Nevertheless, more detailed visual observations are needed to assess the spatial and temporal variability of the BSD in the area to decrease uncertainties in our flow rate calculations. BSD estimates without visual verification leave uncertainties that ideally could be reduced. However, detailed measurements need large and expensive equipment as remotely ROVs and cannot always be conducted. We think that such uncertainties should be clearly stated in any publication.

The final flow rate estimate is very sensitive to BRSs (see Table 4.2). BRSs are ideally obtained directly from optical or hydroacoustic measurements. We used BRSs from various models (see references in Fig. 4.12) that have been verified by direct observations. However, until the BRS has been measured in the field, it remains uncertain if bubbles are ‘dirty’ or ‘clean’ or something in between. Environmental conditions e.g. ocean currents are equally important to measure. Bubble release intensity driven by plume dynamics (bubbles inducing upwelling of water) and thus faster rising speeds need to be considered as well. For our data, final flow rates show up to 53 % difference between the used BRSs (Table 4.2).

4.6.3. Backscatter and resonance of bubbles and bubble clouds

We would like to emphasize the importance of choosing the best model for calculating the backscattering cross-section of natural bubbles. We are aware that our approach for calculating the free gas flow rate is idealized as we assume large, spherical bubbles. It is known that large bubbles deform while rising and assuming an isotropic radiation of the incoming pressure wave adds to the uncertainties. According to literature, rising bubbles can be classified into three main types based on their shape after reaching the terminal velocity: the spherical, ellipsoidal and spherical-cap types (Amaya-Bower and Lee, 2010). The bubbles in our working area belong to the ellipsoidal type (oblate bubbles, 2 to 12 mm in diameter; BRS (Leifer model; clean bubble) 0.19-0.24 [m/sec]; Weber number 1.05-9.77 [dimensionless]); this shape is mainly determined by surface tension. Several theoretical studies give other models/equations to calculate the scattering cross-section and resonance values of non-spherical, especially oblate, bubbles (Strasberg, 1953; Stanton, 1989; Feuillade and Werby, 1994; Leblond et al., 2014). These can be included in future calculations to improve the accuracy of flow rate estimates with our given approach (replacing equation [4.5]).In this study, we considered a scattering cross-section model for spherical bubbles that is based on the monopole bubble theory. The model developed by Thuraisingham (2009) is valid for all *kr* values. The Thuraisingham model might be more appropriate than the one of e.g. Wildt (1946), but it has not been validated for both greater water depths and natural conditions where several bubbles might be very close to each other with clean or dirty surfaces. Multiple scattering effects (Foldy, 1945; Carey and Roy, 1993; Prosperetti et al., 1993) and the generation of a bubble-cloud specific resonance frequency have not been taken into account either, although this might have unforeseen implications.

Apart from these mostly theoretical problems, it remains unclear how the final backscattering could be recorded with state-of-the-art SBES and MBES under natural conditions. Direct flow rate validations in the field would provide answers to some of the questions related to the present simplifications in calculating the scattering cross-section. However, our results show reasonable flow rate values. Improvements could be done by either very accurately observing the shape and behavior of natural bubbles by optical means or by producing bubbles artificially at the seafloor, exactly knowing the BRS and bubble shape from lab experiments (visual confirmation should be also given). The results of such studies would certainly enhance the accuracy of ship-based free gas flow rate quantifications and would help to find a widely accepted model to estimate free gas flow rates and fluxes from the ocean floor through the water column from both deep and shallow water.

References

Ainslie, M. A. 2010. Principles of sonar performance modeling. Springer, [doi: 10.1007/978-3-540-87662-5]

Ainslie, M. A., and T.G. Leighton. 2011. Review of theory for scattering and extinction cross-sections, damping factors and resonance frequencies of spherical gas bubbles, J.Acoust. Soc. Am**.**, 130(5): 3184-3208, [doi: 10.1121/1.3628321]

Amaya-Bower, L., and T. Lee. 2010. Single bubble rising dynamics for moderate Reynolds number using lattice Boltzmann method. Comput. Fluids 39: 1191–1207, [doi:10.1016/j.compfluid.2010.03.003]

Archer, D., B. Buffett, and V. Brovkin. 2009. Ocean methane hydrates as a slow tipping point in the global carbon cycle. P. Natl. Acad. Sci. USA 106:20596-20601, [doi:10.1073/pnas.0800885105]

Artemov, Y. G. 2006. Software support for investigation of natural methane seeps by hydroacoustic method. Mar. Ecol. J. 5: 57–71.

Artemov, Y. G., V. Egorov, G. Polikarpov, and S. Gulin. 2007. Methane emission to the hydro- and atmosphere by gas bubble streams in the Dnieper paleo-delta, the Black Sea. Mar. Ecol. J. 3: 5–26, [doi:10.0.0.194:8080/dspace/handle/99011/622]

Bhaga, D., and M. Weber. 1981. Bubbles in viscous liquids: shapes, wakes and velocities. J. Fluid mech.105**:** 61-85, [doi:10.1017/S002211208100311X]

Biastoch, A.,T. Treude, L. H. Rüpke, U. Riebesell, C. Roth, E. B. Burwicz, W. Park, M. Latif, C. W. Böning, G. Madec and K. Wallmann.2011. Rising Arctic Ocean temperatures cause gas hydrate destabilization and ocean acidification. Geophys. Res. Lett.38:L08602,[doi:10.1029/2011GL047222]

Carey, W. M. and R. A. Roy. 1993. Sound scattering from microbubble distributions near the sea surface. In Ocean Reverberation (pp. 25-43). Springer Netherlands.

Chand, S., T. Thorsnes, L. Rise, H. Brunstad, D. Stoddart, R. Bøe, P. Lågstad and T. Svolsbru. 2012. Multiple episodes of fluid flow in the SW Barents Sea (Loppa High) evidenced by gas flares, pockmarks and gas hydrate accumulation. Earth and Planetary Science Letters 331-332, 305–314. [doi:10.1016/j.epsl.2012.03.021]

Delsontro, T., M. J. Kunz, T. Kempter, A. Wüest, B. Wehrli, and D. B. Senn. 2011. Spatial Heterogeneity of Methane Ebullition in a Large Tropical Reservoir. Envir. Sci. Tech.45**:** 9866-9873, [doi:10.1021/es2005545]

Feuillade, C., and M. F. Werby. 1994. Resonances of deformed gas bubbles in liquids. J.Acoust. Soc. Am.,96: 3684-3692, [doi:10.1121/1.410558]

Foldy, L. L. 1945. The multiple scattering of waves. Phys.Rev. 67:107-119, [doi:10.1103/PhysRev.67.107]

Granin, N. G.,S. Muyakshin, M. Makarov, K. Kucher, I. Aslamov, L.Granina and I.Mizandrontsev. 2012. Estimation of methane fluxes from bottom sediments of Lake Baikal. Geo-mar.Lett.32:427-436,[doi:10.1007/s00367-012-0299-6]

Greinert, J., Y. Artemov, V. Egorov, M. De Batist, and D. Mcginnis. 2006. 1300-m-high rising bubbles from mud volcanoes at 2080 m in the Black Sea: Hydroacoustic characteristics and temporal variability. Earth Planet. Sc. Lett.244:1-15,[doi:10.1016/j.epsl.2006.02.11]

Greinert, J., D. F. Mcginnis, L. Naudts, P. Linke, and M. De Batist. 2010. Atmospheric methane flux from bubbling seeps: Spatially extrapolated quantification from a Black Sea shelf area. J. Geophys. Res-oceans 115:C01002, [doi:10.1029/2009JC005381]

Heeschen, K. U., A. M. Tréhu, R. W. Collier, E. Suess, and G. Rehder. 2003. Distribution and height of methane bubble plumes on the Cascadia Margin characterized by acoustic imaging. Geophys. Res. Lett. 30: 12, [doi:10.1029/2003GL016974]

Hornafius, J. S., D. Quigley, and B. P. Luyendyk. 1999. The world's most spectacular marine hydrocarbon seeps (Coal Oil Point, Santa Barbara Channel, California): Quantification of emissions. . J. Geophys. Res-oceans104:20703-20711, [doi:10.1029/1999JC900148]

Jerrem, K., T.C. Weber, J. Beaudion. 2014. Split-beam echosounder observations of natural methane seep variability in the northern Gulf of Mexico. Geochemistry, Geophysics, Geosystems, DOI 10.1002/2014GC005429

Judd, A., G. Davies, J. Wilson, R. Holmes, G. Baron, and I. Bryden. 1997. Contributions to atmospheric methane by natural seepages on the UK continental shelf. Mar. Geol.137:165-189, [doi: 10.1016/S0025-3227(96)00087-4]

Judd, A. G. and M. Hovland. 2007. Seabed Fluid Flow. Cambridge University Press, New York, 360 pp.

Knies, J., E. Damm, J. Gutt, U. Mann, and L. Ointurier. 2004. Near-surface hydrocarbon anomalies in shelf sediments off Spitsbergen: Evidences for past seepages. Geochem. Geophys. Geosyst., 5, Q06003. [doi:10.1029/2003GC000687].

Kossel, E., N. Bigalke, E. Piñero, and M. Haeckel. 2013. The SUGAR Toolbox - A library of numerical algorithms and data for modelling of gas hydrate systems and marine environments, Bremenhaven, PANGEA. GEOMAR Report (N. Ser.), 8, 160 pp., [doi:10.3289/GEOMAR_REP_NS_8_2013. PANGAEA].

Leblond, I., C. Scalabrin, and L. Berger. 2014. Acoustic monitoring of gas emissions from the seafloor. Part I: quantifying the volumetric flow of bubbles. Mar. Geophys. Res.[doi: 10.1007/s11001-014-9223-y]

Lefeuvre, P. 2002. Fish Species Identification Using Image Analysis of Echo-sounder Images. MSc. Thesis. University of Newfoundland.

Leifer, I., and D. Culling. 2010. Formation of seep bubble plumes in the Coal Oil Point seep field. Geo-mar.Lett. 30: 339-353, [doi:10.1007/s00367-010-0187-x]

Leifer, I., and R. K. Patro. 2002. The bubble mechanism for methane transport from the shallow sea bed to the surface: A review and sensitivity study. Cont. Shelf. Res. 22:2409-2428, [doi:10.1016/S0278-4343(02)00065-1]

Leifer, I., R. K. Patro, and P. Bowyer. 2000. A study on the temperature variation of rise velocity for large clean bubbles. J. Atmos. Ocean. Tech.17:1392-1402,[doi:10.1175/1520-0426(2000)0172.0.CO;2]

Leighton, T. G. 1994. The Acoustic Bubble, Academic Press, Elsevier, [doi:10.1103/PhysRevLett.86.4819]

Lewis, K. B., and B. A. Marshall. 1996. Seep faunas and other indicators of methane-rich dewatering on New Zealand convergent margins. New. Zeal. J. Geol. Geop. 39:181-200, [doi:10.1080/00288306.1996.9514704]

Lurton, X. 2002. An Introduction to Underwater Acoustics: Principles and Applications. Springer, [doi:10.1121/1.1639324]

Macdonald, I. R., I. Leifer, R. Sassen, P. Stine, R. Mitchell, and N. Guinasso. 2002. Transfer of hydrocarbons from natural seeps to the water column and atmosphere. Geofluids 2:95-107,[doi::10.1046/j.1468-8123.2002.00023.x]

McGinnis, D. F., J. Greinert, Y. Artemov, S. E. Beaubien, and A. Wüest. 2006. Fate of rising methane bubbles in stratified waters: How much methane reaches the atmosphere? J.Geophys. Res-oceans 111:C09007, [doi:10.1029/2005JC003183]

McGovern, C. 2012. Video-based quantification of gas bubble fluxes from the seafloor offshore western Svalbard. Msc. thesis, University of Bremen.

Medwin, H. 1977. Counting bubbles acoustically. A review.Ultrasonics7:13, [doi:10.1016/0041-624X(77)90005-1]

Medwin, H., and C. S. Clay. 1998. Chapter 8 - Bubbles, p. 287-347. Fundamentals of Acoustical Oceanography. Academic Press, [doi:10.1046/j.1365-2419.1999.00096.x]

Mendelson, H. D. 1967. The prediction of bubble terminal velocities from wave theory. AIChE J.13:250-253, [doi:10.1002/aic.690130213]

Merewether, R., M. S. Olsson, and P. Lonsdale. 1985. Acoustically detected hydrocarbon plumes rising from 2-km depths in Guaymas Basin, Gulf of California. J. Geophys. Res-sol. Ea.90:3075-3085, [doi:10.1029/JB090iB04p03075]

Minnaert, M. 1933. XVI. On musical air-bubbles and the sounds of running water. Philos. Mag. 16:235-248, [doi:10.1080/14786443309462277]

Muyakshin, S., and E. Sauter. 2010. The hydroacoustic method for the quantification of the gas flux from a submersed bubble plume. Oceanology 50:995-1001, [doi:10.1134/S0001437010060202]

Naudts, L. and J. Greinert, Y. Artemov, P. Staelens, J. Poort, P. Van Rensbergen, Marc De Batist.2006. Geological and morphological setting of 2778 methane seeps in the Dnepr paleo-delta, northwestern Black Sea. Mar. Geol.227:177-199, [doi:10.1016/j.margeo.2005.10.005]

Nikolovska, A., H. Sahling, and G. Bohrmann. 2008. Hydroacoustic methodology for detection, localization, and quantification of gas bubbles rising from the seafloor at gas seeps from the eastern Black Sea. Geochem. Geophy. Geosy. 9:Q10010.[doi:10.1029/2008GC002118]

Obzhirov, A., R. Shakirov, A. Salyuk, E. Suess, N. Biebow, and A. Salomatin. 2004. Relations between methane venting, geological structure and seismo-tectonics in the Okhotsk Sea. Geo-mar. Lett. 24:135-139, [doi:10.1007/s00367-004-0175-0]

Ostrovsky, I. 2003. Methane bubbles in Lake Kinneret: Quantification and temporal and spatial heterogeneity. Limnol.Oceanogr.48(3):1030-1036,[doi:10.4319/lo.2003.48.3.1030]

Ostrovsky, I., D. Mcginnis, L. Lapidus, and W. Eckert. 2008. Quantifying gas ebullition with echosounder: the role of methane transport by bubbles in a medium-sized lake. Limnol. Oceanogr-Meth.6:18, . [doi:10.4319/lom.2008.6.105]

Ostrovsky, I. 2009. Hydroacoustic assessment of fish abundance in the presence of gas bubbles. Limnol. Oceanogr-Meth.**7:** 309-318, [doi:10.4319/lom.2009.7.309]

Paull, C. K., W. Ussler, W. S. Borowski, and F. N. Spiess. 1995. Methane-rich plumes on the Carolina continental rise: associations with gas hydrates. Geology 23:89-92, [doi:10.1130/0091-7613(1995)023<0089:MRPOTC>2.3.CO;2]

Polikarpov, G. G. E., V. N. 1989. Evidence of the gas bubble streams from the Black Sea bottom, Visnik AN. UkrSSR 10:108

Prosperetti, A., N. Q. Lu and H. S. Kim. 1993. Active and passive acoustic behavior of bubble clouds at the ocean's surface. The Journal of the Acoustical Society of America, 93(6), 3117-3127.

Quigley, D. C., J. Scott Hornafius, B. P. Luyendyk, R. D. Francis, J. Clark, and L. Washburn. 1999. Decrease in natural marine hydrocarbon seepage near Coal Oil Point, California, associated with offshore oil production. Geology 27:1047-1050, [doi:10.1130/0091-7613(1999)027<1047:DINMHS> 2.3.CO;2]

Rajan, A., J. Mienert, and S. Bünz. 2012. Acoustic evidence for a gas migration and release system in Arctic glaciated continental margins offshore NW-Svalbard. Mar. Petrol. Geol. 32:36-49, [doi:10,1016/j.marpetgeo.2011.12.008]

Rehder, G., I. Leifer, P. G. Brewer, G. Friederich, and E. T. Peltzer. 2009. Controls on methane bubble dissolution inside and outside the hydrate stability field from open ocean field experiments and numerical modeling. Mar. Chem. 114:19-30, [doi:10.1016/j.marchem.2009.03.004]

Römer, M., H. Sahling, T. Pape, A. Bahr, T. Feseker, P. Wintersteller and G. Bohrmann. 2012a. Geological control and magnitude of methane ebullition from a high-flux seep area in the Black Sea—the Kerch seep area. Mar. Geol.319–322:57-74, [doi:10.1016/j.margeo.2012.07.005]

Römer, M., H. Sahling, T. Pape, G. Bohrmann, and V. Spieß. 2012b. Quantification of gas bubble emissions from submarine hydrocarbon seeps at the Makran continental margin (offshore Pakistan). J. Geophys. Res-oceans117:C10015, [doi:10.1029/2011JC007424]

Sahling, H., G. Bohrmann, Y. G. Artemov, A. Bahr, M. Brüning, S. A. Klapp, I. Klaucke, E. Kozlova, A. Nikolovska, T. Pape, A. Reitz and K. Wallmann. 2009. Vodyanitskii mud volcano, Sorokin trough, Black Sea: Geological characterization and quantification of gas bubble streams. Mar. Petrol. Geol. 26:1799-1811, [doi:10.1016/j.marpetgeo.2009.01.010]

Sahling, H., M. Römer, T. Pape, B. Bergès, C. dos Santos Fereirra, J. Boelmann, P. Geprägs, M. Tomczyk, N. Nowald, W. Dimmler, L. Schroedter, M. Glockzin and G. Bohrmann. 2014. Gas emissions at the continental margin west off Svalbard: mapping, sampling, and quantification. Biogeosciences, 11, 7189–7234.

Salmi, M.S., H.P. Johnson, I. Leifer and J.E. Keister. 2011. Behavior of methane seep bubbles over a pockmark on the Cascadia continental margin. *Geosphere,* 7, 1273-1283. [doi: 10.1130/GES00648.1]

Sauter, E. J., S. Muyakshin, J. Charlou, M. Schlüter, A. Boetius, K. Jerosch, E. Damm, J. Foucher and M. Klages. 2006. Methane discharge from a deep-sea submarine mud volcano into the upper water column by gas hydrate-coated methane bubbles. Earth Planet.Sc. Lett.243: 354-365, [doi:10.1016/j.epsl.2006.01.041]

Schneider Von Deimling, J., G. Rehder, J. Greinert, D. F. Mcginnnis, A. Boetius, and P. Linke. 2011. Quantification of seep-related methane gas emissions at Tommeliten, North Sea. Cont. Shelf res.31: 867-878, [doi:10.1016/j.csr.2011.02.012]

Shakhova, N., and I. Semiletov. 2007. Methane release and coastal environment in the East Siberian Arctic shelf. J. Marine. Syst.66:227-243, [doi:10.1016/j.marsys.2006.06.006]

Shakhova, N., I. Semiletov , I. Leifer, V. Sergienko , A. Salyuk, D. Kosmach, D. Chernykh, C. Stubbs, D. Nicolsky, V. Tumskoy and Ö. Gustafsson. 2014. Ebullition and storm-induced methane release from the East Siberian Arctic Shelf. Nat. Geosci., 7(1): 64-70, [doi:10.1038/ngeo2007]

Simmonds, J., and D. N. Maclennan. 2005. Fisheries Acoustics: Theory and Practice. Wiley, [doi:10.1002/9780470995303]

Smith, A.J.; Mienert, J., Bünz, S., and Greinert, J. 2014. Thermogenic methane injection via bubble transport into the upper Arctic Ocean from the hydrate-charged Vestnesa Ridge, Svalbard.Geochem. Geophys. Geosyst. [doi.org/10.1002/2013GC005179]

Solomon, E. A., M. Kastner, H. Jannasch, G. Robertson, and Y. Weinstein. 2008. Dynamic fluid flow and chemical fluxes associated with a seafloor gas hydrate deposit on the northern Gulf of Mexico slope. Earth planet. Sc. Lett.270:95-105, [doi:10.1016/j.epsl.2008.03.024]

Solomon, E. A., M. Kastner, I. R. MacDonald, and I. Leifer. 2009. Considerable methane fluxes to the atmosphere from hydrocarbon seeps in the Gulf of Mexico. Nat. Geosci., 2(8): 561-565,[doi:10.1038/ngeo574]

Stanton, T. K.,1989. Simple approximate formulas for backscattering of soundby spherical and elongated objects. J. Acoust. Soc. Am. 86: 1499-15 l0, [doi:10.1121/1.398711]

Strasberg, M., 1953. The pulsation frequency of non-spherical gas bubbles in liquids. J. Acoust. Soc. Am. 25: 536–537, [doi:10.1121/1.1907076]

Talukder, R. A., A. Ross, E. Crooke, C. Stalvies, C. Trefry, X. Qi, D. Fuentes, S. Armand, and A. Revill. 2013.Natural hydrocarbon seepage on the continental slope to the east of Mississippi Canyon in the northern Gulf of Mexico. Geochem. Geophy. Geosy. 14(6): 1940-1956, [doi:10.1002/ggge.20130]

Thuraisingham, R. A. 1997. New expressions of acoustic cross-sections of a single bubble in the monopole bubble theory. Ultrasonics, 35(5): 407-409,[doi:10.1016/S0041-624X(97)00021-8]

Weber, T. C., K. Jerram, Y. Rzhanov, L. Mayer, and D. Lovalvo. 2013. Acoustic and optical observations of methane gas seeps in the Gulf of Mexico. In Proceedings of Meetings on Acoustics, Acoustical Society of America 19(1): p075046, [doi:10.1121/1.4799132]

Weber, T.C., L. Mayer, K. Jerram, J. Beaudoin, and Y. Rzhanov.2014: Acoustic estimates of methane gas flux from the seabed in a 6000 km^2 region in the Northern Gulf of Mexico. Geochem. Geophy. Geosy.[doi: 10.1002/2014GC005271

Wessel, P., W. H. F. Smith, R. Scharroo, J. Luis, and F. Wobbe. 2013. Generic MappingTools: Improved Version Released. Eos, Trans. Amer. Geophys. Union94:409-410, [doi:10.1002/2013EO450001]

Westbrook, G. K., K. E. Thatcher, E. J. Rohling, A. M. Piotrowski, H. Pälike, A. H. Osborne, E. G. Nisbet, T. A. Minshull, M. Lanoisellé, R. H. James, V. Hühnerbach, D. Green, R. E. Fisher, A. J. Crocker, A.Chabert, C. Bolton, A. Beszczynska-Möller, C. Berndt and A. Aquilina. 2009. Escape of methane

gas from the seabed along the West Spitsbergen continental margin. Geophys. Res.Lett.36:L15608, [doi:10.1029/2009GL039191]

Wildt, R., 1946. Acoustic theory of bubbles, Chap. 28," Physics of Sound in the Sea, NDRC Summary Technical Report Div. 6, 8: 460-477.

Woolf, D. K. 1993. Bubbles and the air-sea transfer velocity of gases. Atmos. Ocean31:517-540, [doi:10.1080/07055900.1993.9649484]

Woolf, D. K., and S. Thorpe. 1991. Bubbles and the air-sea exchange of gases in near-saturation conditions. J. Mar. Res.49:435-466, [doi:10.1357/002224091784995765]

5. FlareHunter and FlareFlowModule: GUIs for processing split-beam echosounder data to visualize and quantify gas bubble release into the water column

Mario E. Veloso-Alarcón, Tim Weiss, Jens Greinert

(Submitted for publication in SoftwareX)

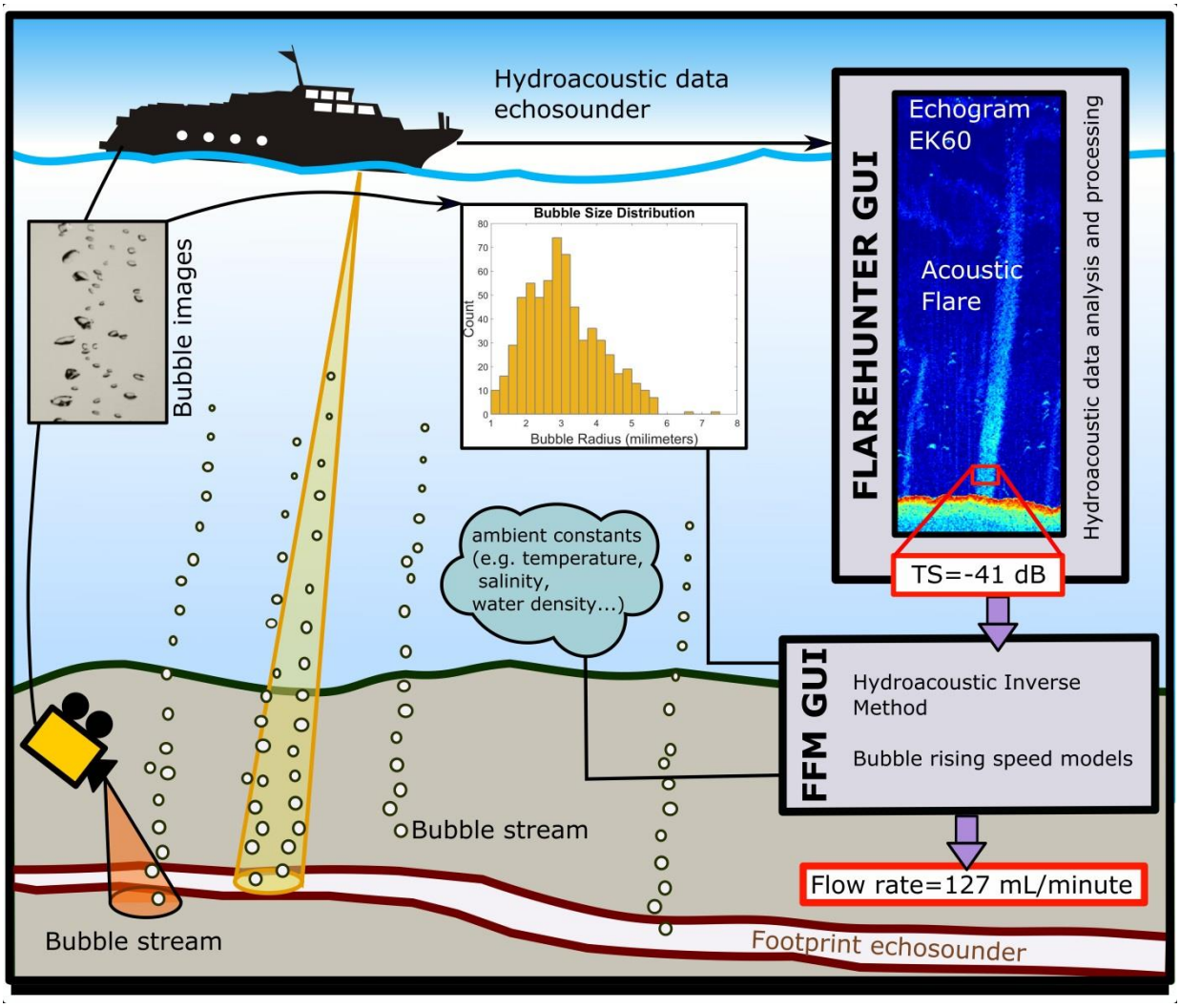

Contributions: The manuscript was written by MV and revised by JG and TW. Discussion of results and interpretation were done by MV and JG. Software development and mathematical formulation was done by MV.

Abstract

Estimates of free gas flow rates (amount of gas per unit of time) and fluxes (flow rate per unit of area) from the seafloor into the water column using hydroacoustic systems are becoming a standard method for studying natural gas release and its potential impact on climate. The same methodology is used to evaluate the amount of unwanted gas release from gas/oil production areas. At the moment there is no agreed on methodology and software to estimate gas flow rates.

We developed 'FlareHunter' and 'FlareFlowModule', two specialized Graphical User Interfaces (GUIs) built in MATLAB for quantifying free gas emissions using echosounder data. FlareHunter allows selecting and editing backscatter signals in echograms using a standard way of processing and thus allows comparisons between different surveys and users. Additionally, FlareHunter can be used to obtain physical properties of acoustic flares such as BRS values, terminal height and average target strength.

'FlareFlowModule' applies an inversion method using backscattering data processed with FlareHunter to derive flow rates of the insonified bubbles. Flow rates of acoustic flares are calculated using bubble size distributions, BRSs (bubble size dependent) and ambient conditions (e.g. temperature, pressure, salinity) as input parameters. The software can easily be advanced to account for new relations between backscattering strength and bubble shape as well as multiple scattering effects once such new relations have been derived.

5.1. Introduction

The release of methane (CH_4), a strong greenhouse gas, from the environment is receiving increasing attention as it has been identified to be a rather unconstrained natural atmospheric source (e.g. Clark et al., 2010; Malakhova et al., 2010; Mau et al., 2007; Solomon et al., 2009). In addition, unwanted gas release from pipelines and gas wells including blow out scenarios (e.g. Marshall, and Strahan, 2012) has further promoted the efforts to create new methods to estimate gas flow rates (volume/time) and gas fluxes (flow rate/unit of area). Different methods and approaches have been developed and used for gas leak detection and monitoring (e.g. Leighton and White, 2012; Murvay and Silea, 2012). One of the main goals of all these methods is to quantify the amount of gas being released from the seafloor as either dissolved or free gas. Furthermore the spatial distribution of gas seeps and the temporal variability of gas release on time scales from seconds to years and beyond are of great interest to better understand the mechanism controlling the gas emission from that type of environment.

The presented software has been developed for post-processing hydroacoustic data containing signals of free gas in the water column and for quantifying gas flow rates using the processed information. To date four different methodologies are commonly used for this purpose. Possible the most accurate method is directly measuring free gas flow rates by trapping gas bubbles with an inverted funnel or similar device. Measuring the time a certain volume is filled or using a flow meter will provide the flow rate (e.g. Greinert et al., 2010; Leifer, 2005; Nikolovska et al., 2008). A more indirect methodology uses video observations and subsequent image analyses to derive the BSD and the amount of bubbles for calculating fluxes (e.g. Römer et al., 2012; Sahling et al., 2009). Optical observations are in general

important as they provide the bubble size distribution and BRSs that are also needed for the here presented flow rate calculations. The two other methods use passive and active hydroacoustic and thus are remote methodologies allowing for covering larger areas at once or in short time. The passive acoustic method inverts the recorded 'sound' produced when bubbles are detached from the seafloor. This inversion is based on the frequencies of the received signal (bubble spectrum) associating the frequency spectrum of the acoustic signal to the bubble size distribution and spectral magnitude of the acoustic emission to the bubble population (e.g. Bergès et al., 2015; Leighton and White, 2012). The active method sends an acoustic signal and uses the received backscattered energy to calculate gas fluxes. This last approach has been used by several groups for almost a decade (e.g. Artemov et al., 2007; Muyakshin and Sauter, 2010; Ostrovsky et al., 2008) relying on singlebeam or splitbeam echosounders but no standard procedure or easily accessible software package exists. A number of software tools for processing of splitbeam echosounder data (EK60 or EK500) have been used to analyze the backscatter signal from ascending bubbles and to estimate gas flow rates and fluxes. Among them are WeaveLens from Artemov (2006) used e.g. by Malakhova et al., (2010), the commercial software package Sonar 5 Pro developed by Lindem Acquisition used by DelSontro et al., (2011) as well as the software code developed by Towler, (2010), e.g. used by Weber et al. 2014. The aim of this publication is to advance the existing capabilities and present a freely accessible software.

The presented software contains two MATLAB-based (Matlab, 2015) modules (FlareHunter and FlareFlowModule) to display and edit hydroacoustic data as well as calculate gas flow rates using the inverse method developed by Veloso et al., (2015; chapter 4). FlareHunter has already been reported at Veloso et al., (2015; chapter 4), as a tool for post-processing hydroacoustic data from a seep site area located west of Prins Karls Forland (PKF) offshore NW Svalbard. The software can be improved and updated according to specific needs of the community and new hydroacoustic models could be easily implemented when they become available.

The following two sections describe the functionality of each software module in detail. Section 4 gives an example of calculated flow rates from several acoustic flares, showing the capabilities of the software. In Section 5 we compare results obtained with the software with those obtained with direct/visual methods.

5.2. FlareHunter

FlareHunter is an interactive software for processing splitbeam echosounder data (EK60) recorded in the .raw format of Kongsberg (Simrad, 2012) The GUI can be called at the MATLAB interface using the *FlareHunter.m* file giving access to a set of functions. The flowchart in Fig. 5.1 summarizes the features of FlareHunter, the different inputs and outputs as well as the link to the FlareFlowModule.

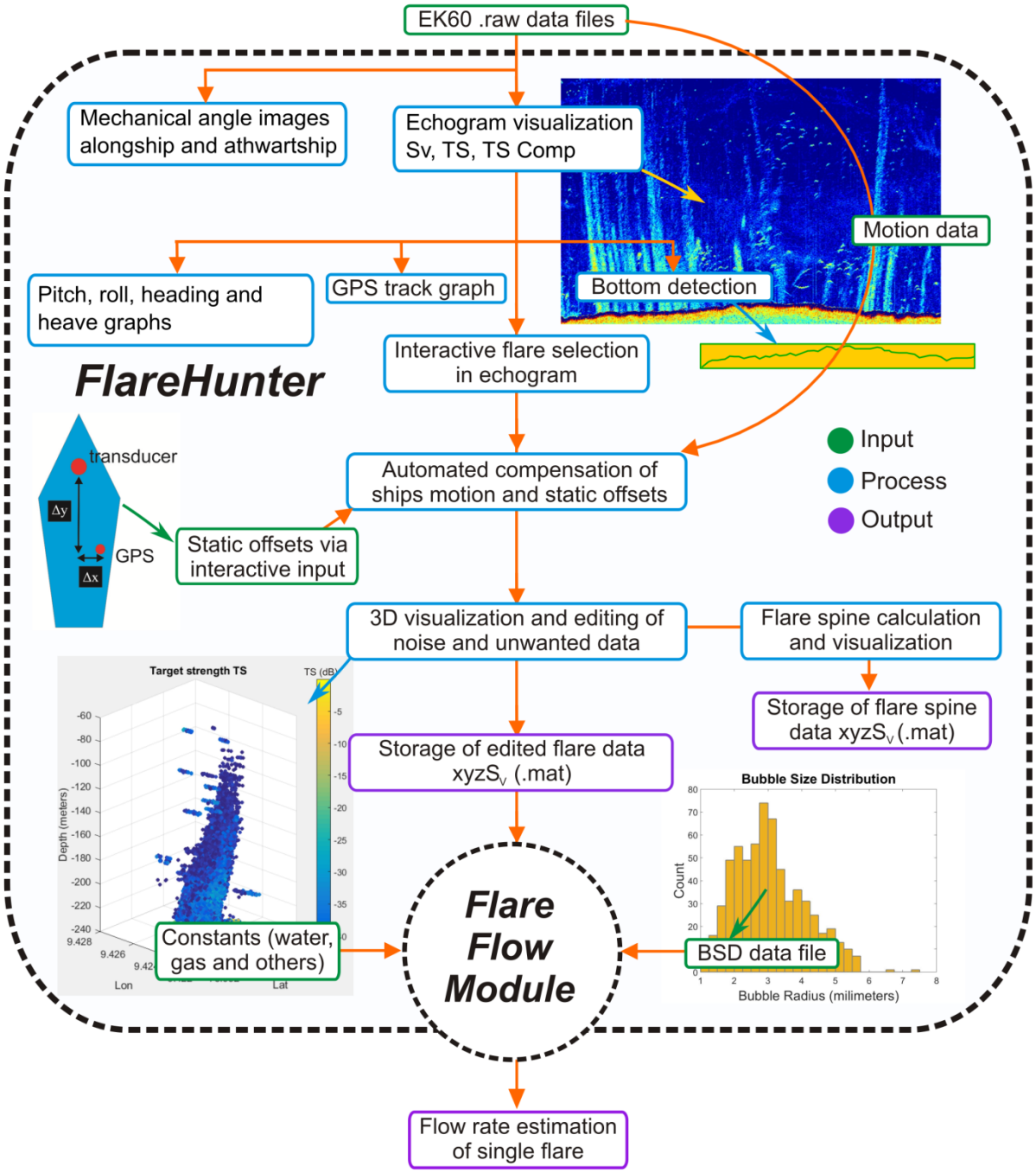

Figure 5.1. Work flow of FlareHunter and the link to the FlareFlowModule.

Input datagrams incorporated in the .raw file format (Simrad, 2012) should include position information (latitude, longitude), vessel orientation (heading in degrees) and motion (heave in meter, role and pitch in degrees). In case the recorded position information does not represent the location of the echosounder transducer but the GPS antenna, the actual transponder position is calculated by FlareHunter if correct offset values are given. Offset correction for motion data is currently not done in FlareHunter.

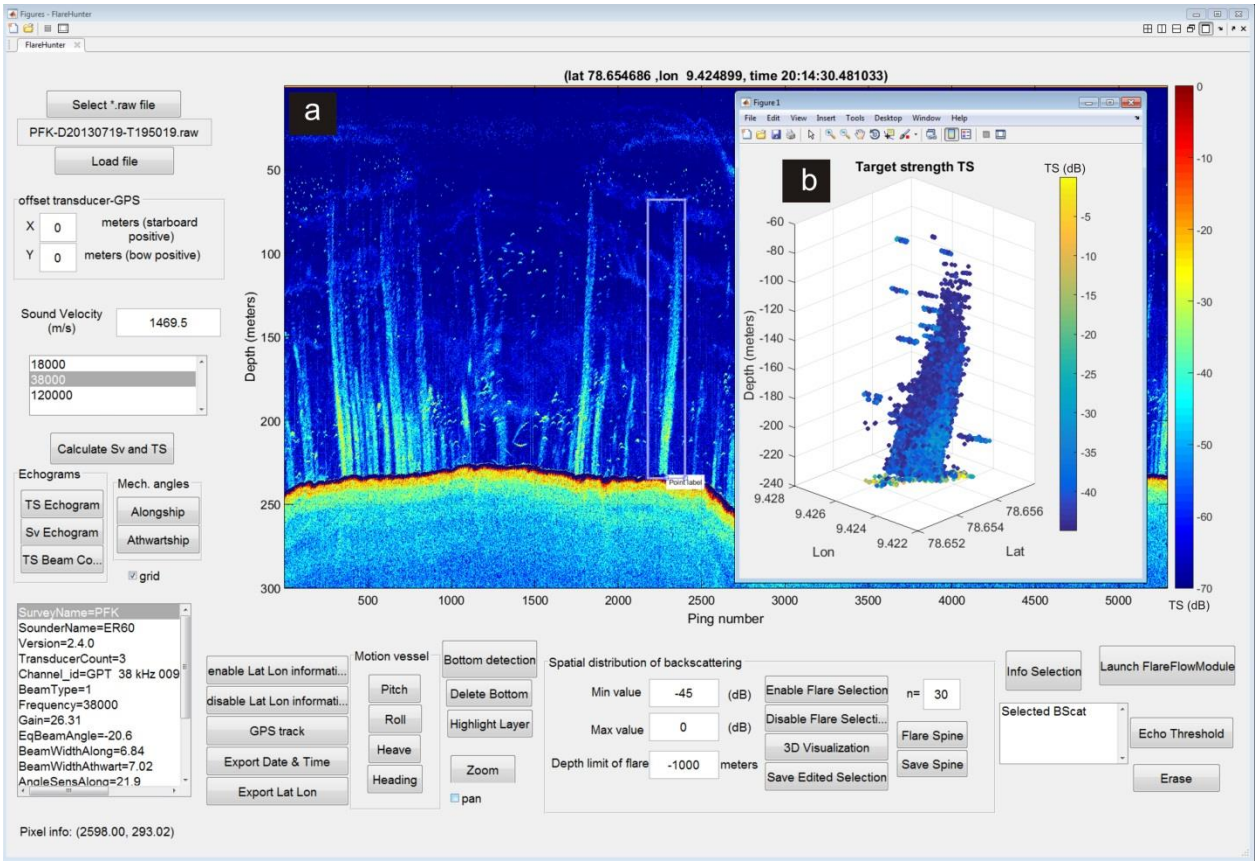

Figure 5.2. FlareHunter GUI (a) with an additional graph showing a 3D view of the selected flare (h). The screenshot shows a 38 kHz target strength echogram ('PFK-D20130719-T195019.raw'), collected with an EK60 echosounder system on a survey at Prins Karl Forland (PKF), offshore Svalbard (~78 N) the 19th of July 2013 on board the RV Helmer Hanssen. The same echogram was used as an example (Fig. 10) in Veloso et al., (2015; chapter 4) describing the acoustic flare detection and flow rate estimation processing.

The FlareHunter GUI displays single target strength (*TS*) and volume backscattering strength (S_V) echograms (Fig. 5.2.a) of which the color palette can be adjusted by the user. Additionally, the GUI displays an echogram with compensated *TS* values according to the position of the target inside the beam using the method by Simrad (Appendix 1). The same method is also used and described by Echoview software (Echoview webpage: http://www.echoview.com/; see compensated target strength at user manual, section 7.5, supplementary material). EK60 echosounders are capable of running different frequencies simultaneously; the frequency to display and process can be selected. Input data as vessel heading, heave, roll, pitch and the ships track can be displayed separately to check for irregularities or data gaps (Fig. 5.3.a-e). FlareHunter performs its own bottom detection (Fig. 5.3.f) by finding the strongest return signal in each transmitted ping.

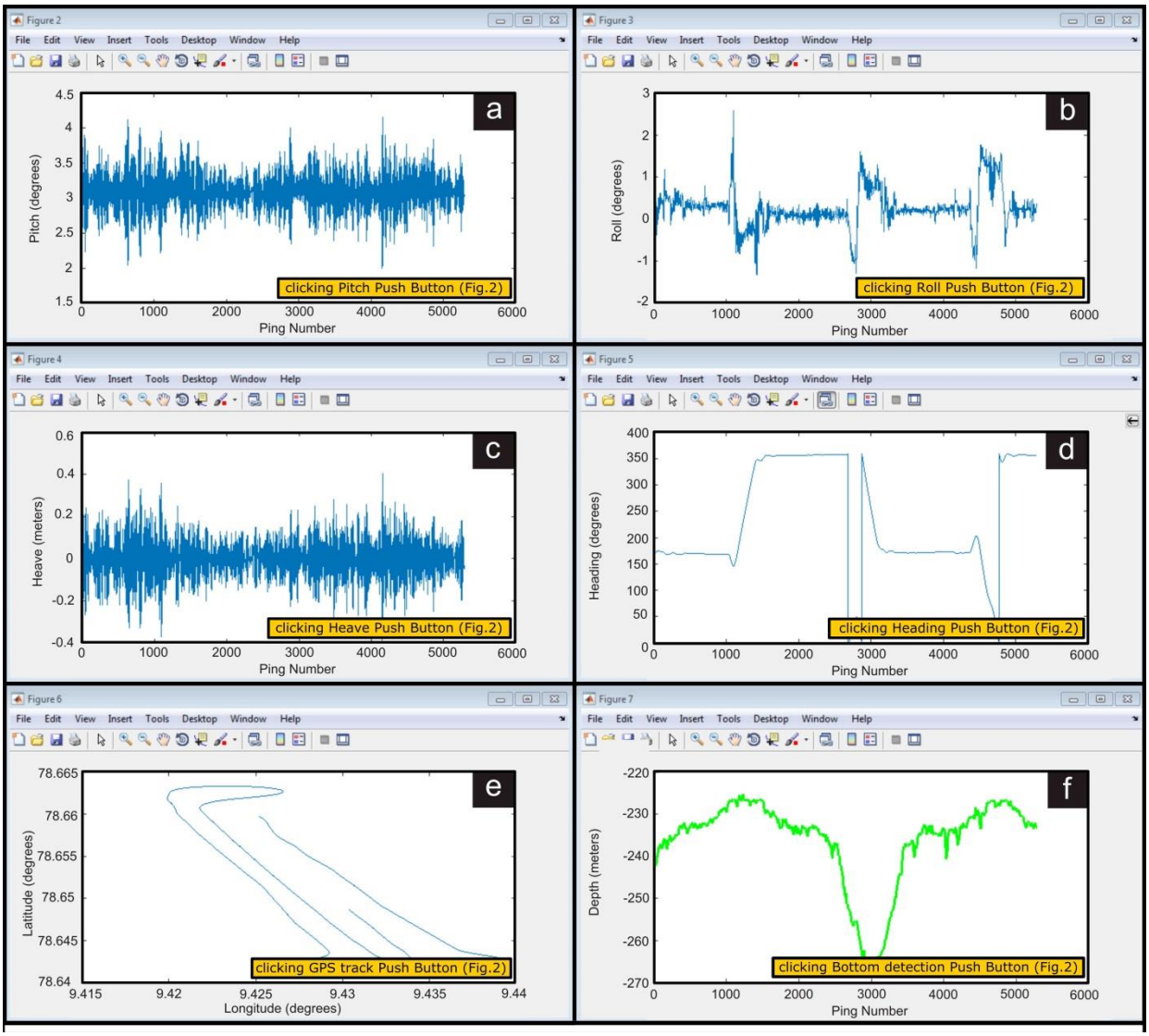

Figure 5.3. Corresponding information of *TS* echogram from Fig. 2 obtained with FlareHunter GUI. The images show vessel motion parameters (a to d), navigation data (e) and the detected water depth (f).

The user can select a flare by drawing a rectangular area on the echogram (Fig. 5.2.a) and then plot the location and strength of the signals inside selected area as 3D point cloud using the alongship and athwartship angle information of the split-beam system (Fig. 5.2.b). Athwartship and alongship angles for each depth sample can also be displayed in the main echogram window. The 3D representation includes motion compensation (pitch, roll, heading/yaw and heave information) and considers the user given static offsets. Minimum and maximum thresholds can be set before the 3D visualization to use only backscatter values within a given backscattering strength range; this acts as a simple threshold filtering for the selected flare to eliminate unwanted noise and reverberation.

Using the figure tools available in MATLAB, the user can delete backscatter signals coming from other sources of noise and reverberation, e.g. fish, bottom multiples, noise from other hydroacoustic systems. The resulting 'pure' information of individual acoustic flares can be obtained and saved as MATLAB data file for later processing. A more accurate localization of the actual bubble releasing spot at the seafloor

can be derived by geometrically averaging the cleaned flare signals using a moving window of a user definable size. This is best applied in case the footprint (insonified area by the echosounder at the seafloor) covers a single bubble stream. The result, the 'flare spine', shows the spatial tendency of the bubble distribution in the water column, indicating water current directions. Results can also be used for more accurate positioning of the release spot/active area at the seafloor. The flare-spine data can be saved as well as MATLAB data files.

5.3. FlareFlowModule (FFM)

The FlareFlowModule GUI (FFM, Fig. 5.4) can be launched from FlareHunter. The module calculates the gas flow rate of the processed (selected and cleaned) flare data using the inverse method published by Veloso et al. (2015; chapter 4). The method is based on calculating the flow rate of free gas based on the received compensated average target strength *TS* (Appendix 1) from bubbles when they are insonified with a wave front of certain frequency. The inverse method by Veloso et al., (2015; chapter 4) uses the acoustical scattering cross-section model of Thuraisingham (1997) for single bubbles. This model is valid for all *kr* values, where *k* is the wave number and *r* represents the bubble radius. At the moment, the inverse method included in FFM only considers bubbles without a hydrate skin. Therefore the user has to be aware that the final absolute flow rate might not be correct in case acoustic signals are used from within the gas hydrate stability zone (below a certain depth; e.g. Kvenvolden, 2003).

The FFM uses the following mathematical expression to estimate the volume flow rate of free gas release coming from an acoustic flare.

$$\emptyset_{\mathrm{V}} = (6 \times 10^{7}) 10^{\frac{\overline{TS}}{10}} \Psi \tag{5.1}$$

where,

$$\Psi = \frac{8\pi}{3 c_{\mathrm{w}} \tau} \frac{\int_{r_1}^{r_2} r^3 f(r) U(r) dr}{\int_{r_1}^{r_2} f(r) \sigma_{\mathrm{bs}}(r, f_{\mathrm{echo}}) dr} \tag{5.2}$$

and,

$\emptyset_{\mathrm{V}}$	:	Volume flow rate (mL/minute)
ρ_{G}	:	Gas density of the bubble at the respective water depth (kg/m^3)
$\overline{TS}$	:	Average target strength of selected backscattering (dB)
τ	:	Sample interval (s)
c_{w}	:	Speed of sound in the seawater (m/s)
$f(r)$	:	Probability density function of the bubble size distribution (1/m)
$U(r)$	:	BRS in function of the bubble radius (m/s)
$\sigma_{\mathrm{bs}}(r)$	:	Acoustical backscattering cross-section of a single bubble (m^2)
f_{echo}	:	Echosounder frequency (Hz)
r	:	Bubble radius (m)
r_1, r_2	:	Lower and upper limit of the bubble size distribution (m)

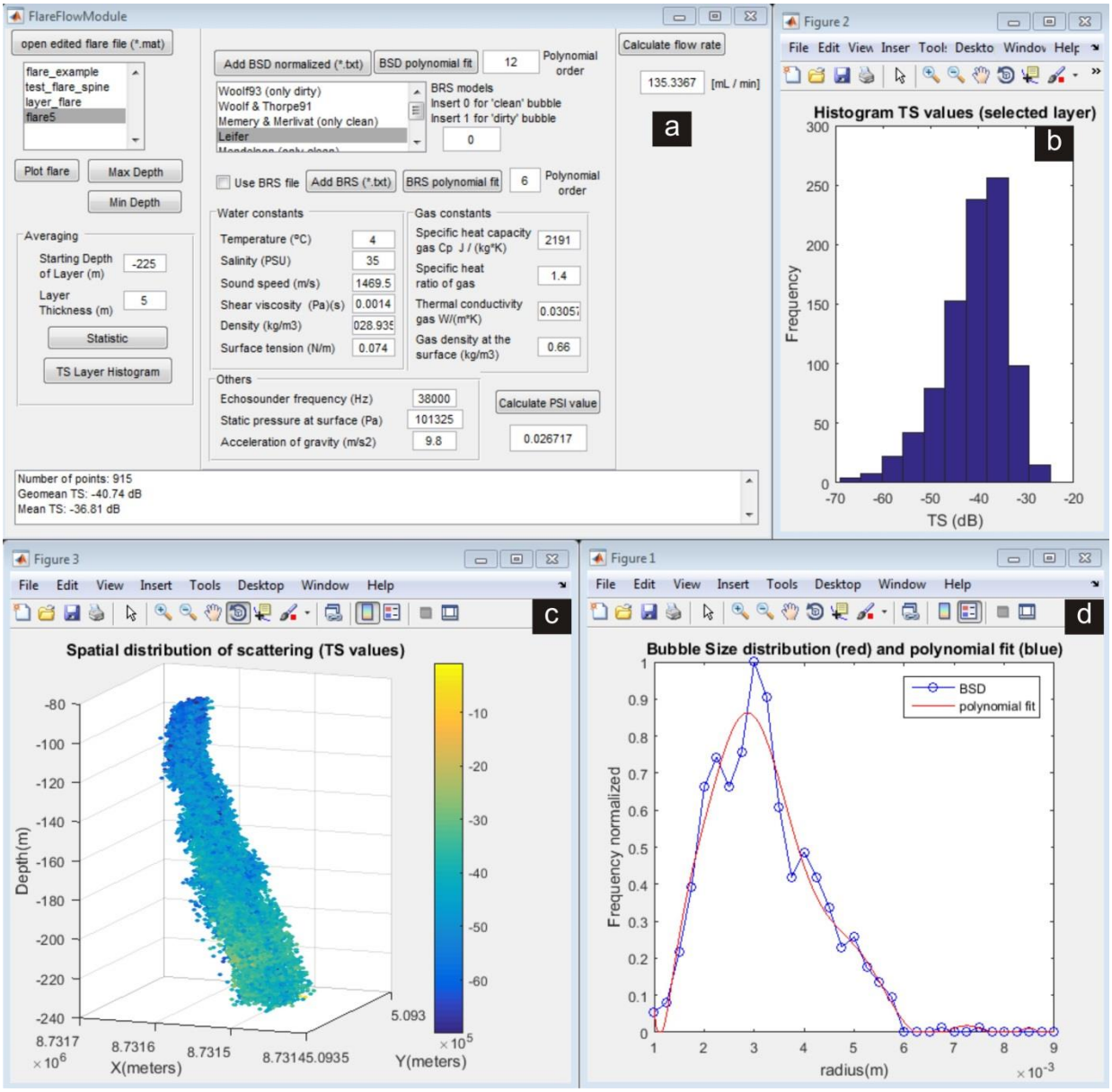

Figure 5.4. a) FlareFlowModule GUI. b) Histogram of *TS* values of the selected layer. c) Three dimensional representation of flare selected for flow rate estimation (done by FlareHunter). The selected flare is the same flare shown at Fig. 5.2 after being manually cleaned. The 3D representation is done in UTM coordinates (Zone 33X).The color palette of image (c) represents target strength in decibels. d) BSD and polynomial fit.

As shown by the equation [5.1], the flow rate can be evaluated using the average target strength value $\overline{TS}$ of a selected area of the flare that was edited and saved with FlareHunter. The FFM reads the respective data file and lists the existing flares in a list field from which each flare can be selected and displayed in 3D.

To obtain the average target strength value $\overline{TS}$ of the flare at a specific water depth, FFM allows defining a depth layer by specifying its upper and lower limit. The Ψ value as defined in Veloso et al. (2015; chapter 4) is calculated automatically using environmental and transducer specific input values from the respective text fields for temperature, salinity, sound speed, shear viscosity, water density,

surface tension, static pressure, acceleration, and echosounder frequency. Furthermore for calculating Ψ the bubble size distribution (BSD) needs to be known as well as the bubble size specific rising speed.

The BSD can be given as ASCII file containing a normalized BSD (maximum value = 1). Once the BSD file is loaded, a polynomial fit of the BSD is created based on a user-definable order. This polynomial fit is used as input for the inverse hydroacoustic modeling. The result of the polynomial fit as well as the original input data can be displayed (Fig. 5.3.e). The bubble size dependent BRSs can either be calculated based on several literature models for 'clean' and 'dirty' bubbles (Leifer et al., 2000; Leifer and Patro, 2002; Mendelson, 1967; Woolf, 1993; Woolf and Thorpe, 1991) or it can be given by an ASCII input file. A set of MATLAB scripts including the BRS models are embedded in the FFM GUI. These scripts have been kindly provided by Ira Leifer (Bubbleology Research International).The user needs to define the BRS model in order to obtain correct flow rate estimates. It has been shown that the presence of surfactants on the bubble surface influences the BRS (e.g. Leifer and Patro, 2002) and therefore the flow rates.

Once all the needed data are loaded or entered, the flow rate of the currently selected flare and depth layer is calculated and displayed. The described procedure allows flow estimates on a flare by flare base. Veloso et al. (2015; chapter 4) also describe how the flow rate and flux can be calculated over larger areas and for different depth layers above the seafloor.

5.4. Performance of the software (flow rate calculation examples)

In order to describe the performance of the software, a data file containing several acoustic flares collected at PKF during a cruise in 2013 on board RV Helmer Hanssen was selected. The volumetric flow rates just above the seafloor (5 m thick, ranging from 5 to 10 m above the bottom) of 10 acoustic flares were estimated using different BRS models. The echogram in Fig. 5 shows the 38 kHz data collected with the EK60 echosounder system; the flow rates (Table 5.1) were calculated for both 38 kHz and 120 kHz backscattered signal using the described inverse method (equation 1).

Flow rate values were calculated using the bubble size distribution given in McGovern (2012) from the study area and the available BRSM in the FFM GUI (Leifer et al., 2000; Leifer and Patro, 2002; Mendelson, 1967; Woolf, 1993; Woolf and Thorpe, 1991). Although it is assumed that there are no surfactants on the bubble surfaces in the study area, flow rates calculated with 'dirty' BRS models are presented as well to illustrate the FFM GUI performance. Flow rate results are shown in Table 5.1; water, gas and environmental constants are displayed in Table 5.2. A comparison between data from the 38 kHz and 120 kHz frequency are presented in Table 5.3.

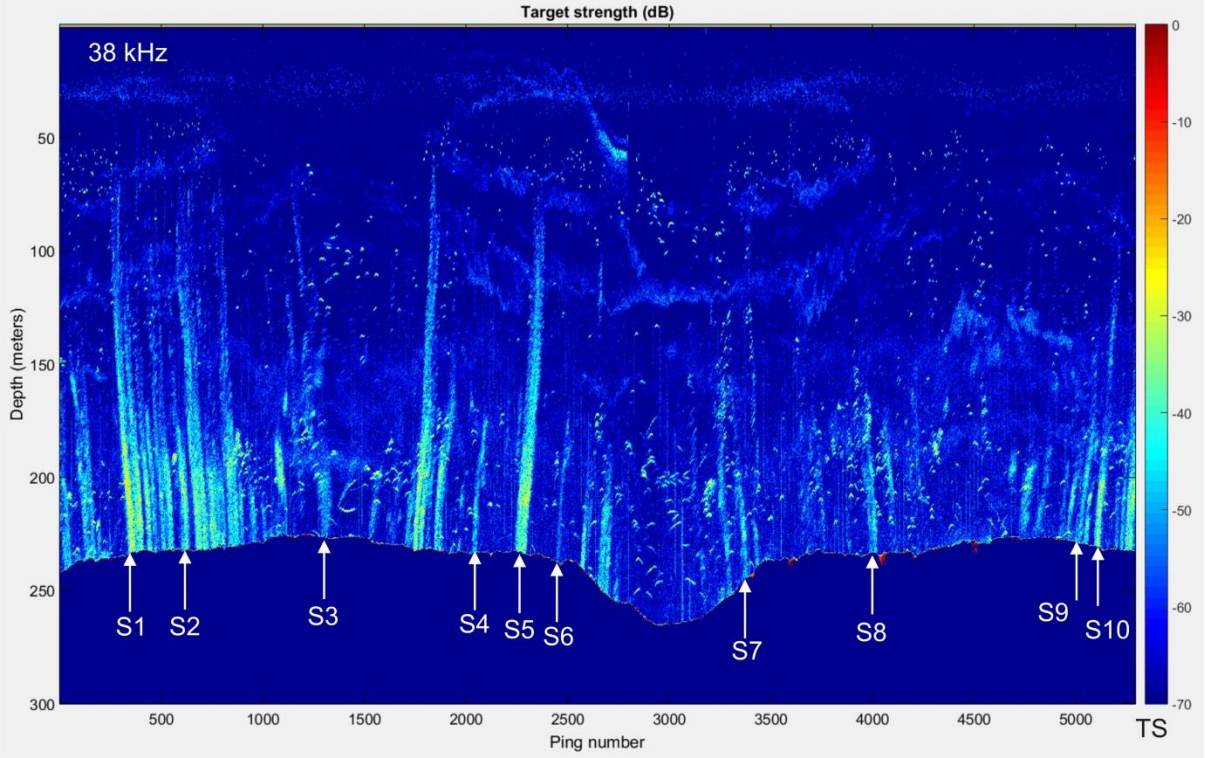

Figure 5.5. Target strength echogram (38 kHz) example for volume flow rate evaluation ('PFK-D20130719- T195019.raw'), collected on a survey at PKF, offshore Svalbard (~78 N) in July 2013 on board the RV Helmer Hanssen. The image shows 10 acoustic flares chosen to calculate their volume flow rate above the seafloor. The color palette specifies the *TS* values in dB. Seafloor was detected and deleted. Upper and lower thresholds, 0 dB and -70 dB respectively, were applied to the image.

Table 5.1. Volume flow rates estimates of 10 acoustic flares the using inverse hydroacoustic method from Veloso et al., 2015 (chapter 4).

							Clean bubble			Dirty bubble		
Flare	**Lat**	**Lon**	**Time**	**Bottom depth (m bsl)**	***TS* geometrical mean (dB)**		**BRS Model**	**Flow rate (mL /minute)**		**BRS Model**	**Flow rate (mL /minute)**	
	N	E			**38 kHz**	**120 kHz**		**38 kHz**	**120 kHz**		**38 kHz**	**120 kHz**
S1	78.654490	9.428517	19:54:14	232	-35.78	-44.31	Leifer	423	468	Leifer	349	386
							Leifer & Patro	536	593	Leifer & Patro	435	481
							Mendelson	543	600	Woolf93	543	601
										Woolf & Thorpe91	467	517
S2	78.650238	9.431529	19:57:09	231	-44.48	-52.44	Leifer	56	72	Leifer	47	59
							Leifer & Patro	72	91	Leifer & Patro	59	74
							Mendelson	73	92	Woolf93	73	92
										Woolf & Thorpe91	63	79
S3	78.641884	9.435525	20:04:28	225	-52.94	-61.04	Leifer	8	10	Leifer	7	8
							Leifer & Patro	10	13	Leifer & Patro	8	10
							Mendelson	10	13	Woolf93	10	13

										Woolf & Thorpe91	9	11
S4	78.651100	9.426933	20:12:08	233	-50.83	-59.95	Leifer	13	13	Leifer	11	11
							Leifer & Patro	18	16	Leifer & Patro	14	13
							Mendelson	17	16	Woolf93	17	16
										Woolf & Thorpe91	15	14
S5	78.654724	9.424883	20:14:32	232	-41.00	-48.35	Leifer	127	184	Leifer	104	152
							Leifer & Patro	161	233	Leifer & Patro	130	190
							Mendelson	163	236	Woolf93	163	237
										Woolf & Thorpe91	140	203
S6	78.657623	9.423307	20:16:27	238	-54.44	-61.79	Leifer	5	8	Leifer	5	7
							Leifer & Patro	7	11	Leifer & Patro	6	9
							Mendelson	7	11	Woolf93	7	11
										Woolf & Thorpe91	6	9
S7	78.659180	9.420930	20:26:57	245	-52.07	-58.87	Leifer	10	16	Leifer	8	13
							Leifer & Patro	13	21	Leifer & Patro	10	17
							Mendelson	13	21	Woolf93	13	21
										Woolf & Thorpe91	11	18
S8	78.649734	9.426115	20:33:45	233	-51.77	-57.66	Leifer	11	22	Leifer	9	18
							Leifer & Patro	13	27	Leifer & Patro	11	22
							Mendelson	14	28	Woolf93	14	28
										Woolf & Thorpe91	12	24
S9	78.644531	9.432934	20:44:37	229	-51.84	-58.10	Leifer	11	20	Leifer	9	16
							Leifer & Patro	13	25	Leifer & Patro	11	20
							Mendelson	14	25	Woolf93	14	25
										Woolf & Thorpe91	12	22
S10	78.645874	9.432114	20:45:37	231	-44.25	-50.71	Leifer	60	107	Leifer	50	88
							Leifer & Patro	76	136	Leifer & Patro	62	110
							Mendelson	77	137	Woolf93	77	138
										Woolf & Thorpe91	66	118

Table 5.2. Water, gas and environmental constants values used as inputs in FFM GUI to estimate the flow rate of the acoustic flares.

Constant	**Unit**	**Value**
Average temperature water	C°	4
Static pressure at surface	Pa	101325
Water salinity	psu	35

Water density (Millero et al., 1980)	kg/m^3	1028,935
Average sound speed in the water	m/s	1468
Water shear viscosity	Pa·s	0.0014
Water surface tension	N/m	0.074
Gas density at the surface (CH_4)	kg/m^3	0.66
Static pressure at surface	Pa	101325
Acceleration of gravity	m/s^2	9.8
Specific heat capacity gas	$J/(kg \cdot m^3)$	2191
Specific ratio of gas	dimensionless	1.4

Table 5.3. Summary of estimated average flow rate of each acoustic flare. Averaging was done for the corresponding 'clean' flow rate estimations derived from the BRS models. Average was done for each frequency. Standard deviation (SD) and relative error are also shown.

	38 kHz			**120 kHz**		
Flare	**Flow rate mean (mL /minute)**	**SD (mL /minute)**	**Relative error (%)**	**Flow rate mean (mL /minute)**	**SD (mL /minute)**	**Relative error (%)**
S1	501	67	16	554	74	15
S2	67	10	16	85	11	15
S3	9	1	14	12	2	17
S4	16	3	19	15	2	13
S5	150	20	16	218	29	15
S6	6	1	21	10	2	20
S7	12	2	17	19	3	17
S8	13	2	14	26	3	14
S9	13	2	14	23	3	14
S10	71	10	16	127	17	16

A comparison among the mass flow rates derived from 38 kHz and 120 kHz echosounder data using the inverse hydroacoustic method was done. This comparison uses the BRS model of Leifer for clean bubbles (Fig. 5.6). The very good agreement between the results of the two frequencies is shown in Fig. 6, with a linear correlation coefficient $R^2$of ~ 0.9917.

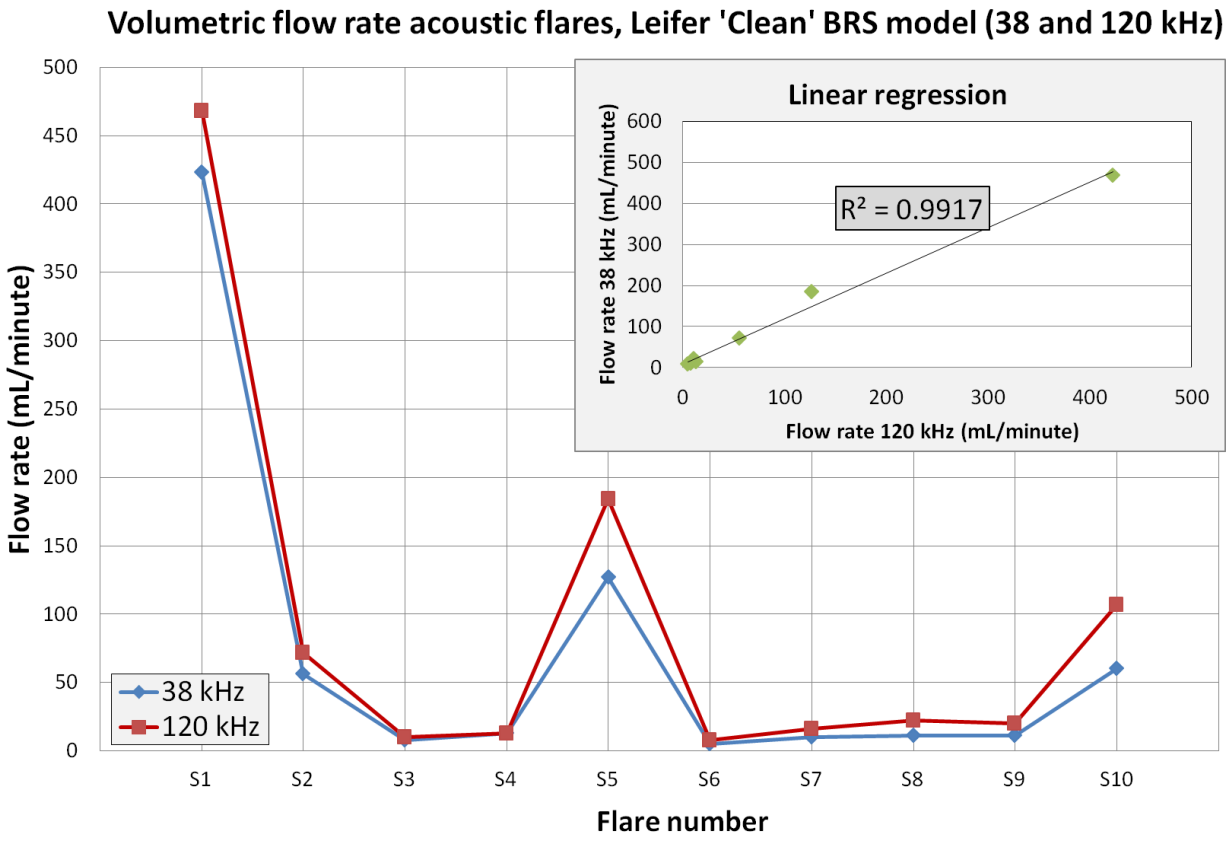

Figure 5.6. Comparison between flow rate results estimated with different frequencies (38 and 120 kHz). Image displays the comparison for estimations carry out with Leifer 'clean' bubble BRS model.

5.5. Discussion

The presented software tools FlareHunter and FlareFlowModule are the only software package that currently allows direct flow and flux calculation from singlebeam echosounder data. With MatLab as executing environment it is embedded in a powerful software that allows advances in processing and usability by adding new features as well as changing/adapting critical parts as the relation of bubble backscatter response and bubble size. We are aware of the fact that using the relation by Thuraisingham (1997) might not be valid for massive release of bubbles and that independent bubble size and rising speed measurements are crucial. Unfortunately, we do not have the optimum validation data set in hand. Such a data set would need an artificial bubble source, able to release different bubble size spectra with varying flow rates. The bubble release itself would need to be visually monitored and the same set of gas flow experiments would need to be performed in different water depth. However, this work does not aim to validate the methodology but to present the software tool to do so. Nevertheless the presented data as well as those presented in Veloso et al. (2015; chapter 4) can be compared to other bubble flow quantifying studies (Table 5.4). Sahling et al., (2014) worked in the same area as our example data set was recorded. Despite not all data are exactly from the same area, the comparison provides an idea about the order of magnitude of flow rates that single or multiple bubble streams can produce (Table 5.4).

Table 5.4. Summary of flow rate measurements of single bubble streams and bubble stream clusters using the invert funnel technique and visual observations at different study areas. The range of our flow rate estimates is also specified.

	Study Area	**Water Depth (m bsl)**	**Flow Rate (mL/minute)**		
			Bubble stream cluster	**Single bubble stream**	
			Visual	**Visual**	**Bubble catcher**
Sauter et al., (2006)	Håkon Mosby MV Norwegian-Barents-Spitzbergen Continental Margin	1250-1270	~1800	80-360	
Sahling et al., (2009)	Black Sea, Vodyanitskii MV	2070		32-120	
Greinert et al., (2010)	Black Sea	70-112		320-850	
Römer et al., (2012)	Makran Continental Margin	575-2870	9-831		
Schneider von Deimling et al., [35]	North Sea	~72		~23.2	~12.5
Sahling et al., (2011)	PKF (Svalbard)	240-396		5.2-26.5	3-41
			Hydroacoustics (single bubble stream or bubble stream cluster)		
Our example	PKF (Svalbard)	~230	6-501		

Table 5.4 shows that flow rates of single bubble streams measured with visual/direct techniques can largely fluctuate (3 to 850 mL/minute) depending on the strength of the gas release. It is clear that flow rates from individual vents can also be comparable to several bubble streams, bubble stream clusters. To better appreciate the very good correlation with real-world flow rates, it should be highlighted that an acoustic flare in an echogram can be the result of one or several bubble streams within the insonified volume of water. Here we define a bubble stream as a more or less continuous chain of bubbles rising towards the surface. Because the footprint covered area increases with depth, it can easily insonify several bubble streams at the same time (e.g. with 7° of beam width, the footprint diameter is ~30 m at ~240 m bsl; e.g. Römer et al., 2012). The amount of bubble streams producing a flare cannot be quantified using hydroacoustic single beam echosounder data. It can be assumed that our volume lower flow rates are representative for single bubble stream and those with higher flows might represent clusters as they have been observed by McGovern (2012). Then, we are confident to say that our results are within a realistic range of flow rates.

FlareHunter and the FlareFlowModule were designed from a user perspective to allow an easy access to flare data also for people who are not as deeply into hydroacoustic and to speed up repetitive tasks. This led to a wide set of functions which grew over time with a focus on processing data and not on software

architectural aspects. Thus FlareHunter and FlareFlowModule can still be considered prototypes, which need to be modularized and improved in the future. Because the software package has been evolved according to the needs of our research, it is believed that the use by others will lead to new functionalities performance improvements. We are aware that the tool still needs improvements such as algorithm optimization and implementation of tools associated with the digital image processing. One future task is the automated removal of artificial noise and reverberation without losing signal information. This is in general an important aspect in hydroacoustic data interpretation related to submarine gas release. This aspect has been highlighted by Veloso et al. (2015; chapter 4) as noisy data will increase the uncertainty and error margin of flow calculations.

5.6 Conclusions

FlareHunter and the FFM are tools allowing easy interaction with hydroacoustic data of gas release in the water column that have been recorded in the EK60 splitbeam echosounder specific format. Specialized tools for flare processing and interactive editing are implemented in FlareHunter, whereas the FFM allows for an easy evaluation of gas flow rates at different depth layers. Estimated Flow rates give realistic results compared with direct measurements (Greinert et al., 2010; Römer et al., 2012; Sahling et al., 2014, 2009; Sauter et al., 2006; Schneider von Deimling et al., 2011).

We think that both software tools could be of great value to 1) standardize gas flow rate estimates based on singlebeam echosounder data and 2) give the increasing number of research groups involved in such measurements a functional software to quickly determine gas flow rates and investigate temporal changes.

References

Artemov, Y.G., 2006. Software support for investigation of natural methane seeps by hydroacoustic method. Morskyji ehkologichnyji zhurnal (Marine Ecological Journal) 5, 57–71.

Artemov, Y.G., Egorov, V.N., Polikarpov, G.G., Gulin, S.B., 2007. Methane emission to the hydro- and atmosphere by gas bubble streams in the Dnieper paleo-delta, the Black Sea. Morskyji ehkologichnyji zhurnal (Marine Ecological Journal) 6, 5–26.

Bergès, B.J.P., Leighton, T.G., White, P.R., 2015. Passive acoustic quantification of gas fluxes during controlled gas release experiments. Int. J. Greenh. Gas Control 38, 64–79. doi:10.1016/j.ijggc.2015.02.008

Clark, J.F., Washburn, L., Schwager Emery, K., 2010. Variability of gas composition and flux intensity in natural marine hydrocarbon seeps. Geo-Mar. Lett. 30, 379–388. doi:10.1007/s00367-009-0167-1

DelSontro, T., Kunz, M.J., Kempter, T., Wüest, A., Wehrli, B., Senn, D.B., 2011. Spatial Heterogeneity of Methane Ebullition in a Large Tropical Reservoir. Environ. Sci. Technol. 45, 9866–9873. doi:10.1021/es2005545

Greinert, J., McGinnis, D.F., Naudts, L., Linke, P., De Batist, M., 2010. Atmospheric methane flux from bubbling seeps: Spatially extrapolated quantification from a Black Sea shelf area. J. Geophys. Res. 115. doi:10.1029/2009JC005381

Kvenvolden, K.A., 1993. Gas hydrates—geological perspective and global change. Rev. Geophys. 31, 173–187.

Leifer, I., 2005. Turbine tent measurements of marine hydrocarbon seeps on subhourly timescales. J. Geophys. Res. 110. doi:10.1029/2003JC002207

Leifer, I., Patro, R.K., 2002. The bubble mechanism for methane transport from the shallow sea bed to the surface: A review and sensitivity study. Cont. Shelf Res. 22, 2409–2428. doi:10.1016/S0278-4343(02)00065-1

Leifer, I., Patro, R.K., Bowyer, P., 2000. A Study on the Temperature Variation of Rise Velocity for Large Clean Bubbles. J. Atmospheric Ocean. Technol. 17, 1392–1402. doi:10.1175/1520-0426(2000)017<1392:ASOTTV>2.0.CO;2

Leighton, T.G., White, P.R., 2012. Quantification of undersea gas leaks from carbon capture and storage facilities, from pipelines and from methane seeps, by their acoustic emissions. Proc. R. Soc. Math. Phys. Eng. Sci. 468, 485–510. doi:10.1098/rspa.2011.0221

Malakhova, L.V., Egorov, V.N., Malakhova, T.V., Gulin, S.B., Artemov, Y.G., 2010. Methane in the Sevastopol coastal area, Black Sea. Geo-Mar. Lett. 30, 391–398. doi:10.1007/s00367-010-0198-7

Marshall, M., Strahan, D., 2012. Total foresaw the North Sea gas leak. New Sci. 214, 6–7. doi:10.1016/S0262-4079(12)60870-7

MATLAB and Image Processing Toolbox, 2015. . The MathWorks, Inc., Natick, Massachusetts, United States.

Mau, S., Valentine, D.L., Clark, J.F., Reed, J., Camilli, R., Washburn, L., 2007. Dissolved methane distributions and air-sea flux in the plume of a massive seep field, Coal Oil Point, California. Geophys. Res. Lett. 34. doi:10.1029/2007GL031344

McGovern, C., 2012. Video-based quantification of gas bubble fluxes from the seafloor offshore western Svalbard (Msc. thesis). Univ. of Bremen.

Mendelson, H.D., 1967. The prediction of bubble terminal velocities from wave theory. AIChE J. 13, 250–253. doi:10.1002/aic.690130213

Millero, F.J., Chen, C.-T., Bradshaw, A., Schleicher, K., 1980. A new high pressure equation of state for seawater. Deep Sea Res. Part Oceanogr. Res. Pap. 27, 255–264. doi:10.1016/0198-0149(80)90016-3

Murvay, P.-S., Silea, I., 2012. A survey on gas leak detection and localization techniques. J. Loss Prev. Process Ind. 25, 966–973. doi:10.1016/j.jlp.2012.05.010

Muyakshin, S.I., Sauter, E., 2010. The hydroacoustic method for the quantification of the gas flux from a submersed bubble plume. Oceanology 50, 995–1001. doi:10.1134/S0001437010060202

Nikolovska, A., Sahling, H., Bohrmann, G., 2008. Hydroacoustic methodology for detection, localization, and quantification of gas bubbles rising from the seafloor at gas seeps from the eastern Black Sea: HYDROACOUSTIC GAS QUANTIFICATION. Geochem. Geophys. Geosystems 9, n/a–n/a. doi:10.1029/2008GC002118

Ostrovsky, I., McGinnis, D.F., Lapidus, L., Eckert, W., 2008. Quantifying gas ebullition with echosounder: the role of methane transport by bubbles in a medium-sized lake. Limnol. Oceanogr. Methods 6, 105–118. doi:10.4319/lom.2008.6.105

Römer, M., Sahling, H., Pape, T., Bohrmann, G., Spieß, V., 2012. Quantification of gas bubble emissions from submarine hydrocarbon seeps at the Makran continental margin (offshore Pakistan). J. Geophys. Res. 117. doi:10.1029/2011JC007424

Sahling, H., Bohrmann, G., Artemov, Y.G., Bahr, A., Brüning, M., Klapp, S.A., Klaucke, I., Kozlova, E., Nikolovska, A., Pape, T., Reitz, A., Wallmann, K., 2009. Vodyanitskii mud volcano, Sorokin trough, Black Sea: Geological characterization and quantification of gas bubble streams. Mar. Pet. Geol. 26, 1799–1811. doi:10.1016/j.marpetgeo.2009.01.010

Sahling, H., Römer, M., Pape, T., Bergès, B., dos Santos Fereirra, C., Boelmann, J., Geprägs, P., Tomczyk, M., Nowald, N., Dimmler, W., Schroedter, L., Glockzin, M., Bohrmann, G., 2014. Gas emissions at

the continental margin west off Svalbard: mapping, sampling, and quantification. Biogeosciences Discuss. 11, 7189–7234. doi:10.5194/bgd-11-7189-2014

Sauter, E.J., Muyakshin, S.I., Charlou, J.-L., Schlüter, M., Boetius, A., Jerosch, K., Damm, E., Foucher, J.-P., Klages, M., 2006. Methane discharge from a deep-sea submarine mud volcano into the upper water column by gas hydrate-coated methane bubbles. Earth Planet. Sci. Lett. 243, 354–365. doi:10.1016/j.epsl.2006.01.041

Schneider von Deimling, J., Rehder, G., Greinert, J., McGinnnis, D.F., Boetius, A., Linke, P., 2011. Quantification of seep-related methane gas emissions at Tommeliten, North Sea. Cont. Shelf Res. 31, 867–878. doi:10.1016/j.csr.2011.02.012

Simrad, 2012. Simrad EK60 Reference Manual Release 2.4.X, Rev. D. Kongsberg Maritime AS, Strand promenaden 50, 3190 Horten, Norway.

Solomon, E.A., Kastner, M., MacDonald, I.R., Leifer, I., 2009. Considerable methane fluxes to the atmosphere from hydrocarbon seeps in the Gulf of Mexico. Nat. Geosci. 2, 561–565. doi:10.1038/ngeo574

Thuraisingham, R.A., 1997. New expressions of acoustic cross-sections of a single bubble in the monopole bubble theory. Ultrasonics 35, 407–409. doi:10.1016/S0041-624X(97)00021-8

Towler, R., 2010. readEKRaw EK/ES60 ME/MS70 MATLAB toolkit.

Veloso, M., Greinert, J., Mienert, J., De Batist, M., 2015. A new methodology for quantifying bubble flow rates in deep water using splitbeam echosounders: Examples from the Arctic offshore NW-Svalbard: Quantifying bubble flow rates in deep water. Limnol. Oceanogr. Methods 13, 267–287. doi:10.1002/lom3.10024

Weber, T.C., Mayer, L., Jerram, K., Beaudoin, J., Rzhanov, Y., Lovalvo, D., 2014. Acoustic estimates of methane gas flux from the seabed in a 6000 km 2 region in the Northern Gulf of Mexico. Geochem. Geophys. Geosystems 15, 1911–1925. doi:10.1002/2014GC005271

Woolf, D.K., 1993. Bubbles and the air-sea transfer velocity of gases. Atmosphere-Ocean 31, 517–540. doi:10.1080/07055900.1993.9649484

Woolf, D.K., Thorpe, S.A., 1991. Bubbles and the air-sea exchange of gases in near-saturation conditions. J. Mar. Res. 49, 435–466. doi:10.1357/002224091784995765

6. Spatial and temporal variability of free gas emission inferred from repeated hydroacoustic surveys offshore Svalbard

Mario E. Veloso-Alarcón, P. Jansson, M. De Batist, T. A. Minshull, G. Westbrook, H. Pälike, S. Bünz, J. Greinert

(To be submitted to Nature Geosciences in a highly modified version)

Abstract

The Svalbard continental margin is located in the main gateway of Atlantic waters flowing northward into the Arctic Ocean, the Fram Strait. As such, changes in global temperature can strongly affect this region. Furthermore, the seabed sediments of this area are considered to store large reservoirs of gas hydrates that could be potentially destabilized in response to global warming. A seepage area offshore Prins Karl Forland (PKF) has received particular attention because vent sites are distributed in the proximity of the landward limit of the GHSZ. The latter makes this seepage area an ideal natural laboratory for studying an eventual hydrate degradation scenario triggered by Arctic warming. As hydrate dissociation is thought to increase the gas emissions from the seabed and 'turn on' new seep sites, the spatiotemporal analysis of gas seepage seems to be a good tool to monitor the stability of gas hydrates. Particularly offshore PKF, hydroacoustic surveys have been carried out since the first acoustic flares were recorded in 2008. Hydroacoustic data collected here have been used mainly to estimate the amount of gas released and the spatial distribution of seeps, but no attempt of spatiotemporal analysis of the seepage has been done mainly due to the lack of information. The present work aims to elucidate the possible fluctuations of seafloor bubble emissions. Hydroacoustic data were collected using an EK60 SBES during eleven surveys on board R/V Helmer Hanssen (The Arctic University of Norway, Tromsø) and R/V James Clark Ross (National Oceanography Centre, Southampton) between 2008 and 2014. We used an inverse hydroacoustic method to derive flow rates from acoustic flares. From 2000 echosounder data files analyzed, a total of 3145 flares were detected. We applied three different comparison approaches and conclude that, for assessing variability, a common area comparison (CAC) is the method that best fits our dataset. The dataset itself, although extensive, is temporally and spatially sparse and some uncertainty is associated with the remote sensing method. Firm and final, conclusions can therefore not be drawn. Nevertheless, results show that the inverse method uncertainty is small compared to the observed flow rate variability, thus we believe that our method is adequate for a temporal and spatial comparison. Our analysis shows that the free gas flow fluctuates but it does not show a trend towards increasing flow rates with time. This implies that accelerating gas hydrate dissociation is not happening within the period of the undertaken surveys over seven years. We assume that gas release is governed by bottom water temperature but our time series is too short to show a clear trend towards increased gas emissions or the migration of the gas seepage areas downslope that can be linked to ocean warming.

Contributions: The manuscript was written by MV and PJ and revised by JG and MDB. Fieldwork was conducted by MV, JG, PJ, TM, GW, HP and SB during different surveys. Discussion of results and interpretation were done by MV, PJ and JG. Data processing was carried out by MV and PJ.

6.1. Introduction

Methane venting from the seafloor as free gas phase has been observed at many locations in the ocean; it is often detected as "flares" in echograms of single- or multibeam echosounder systems. These locations include the Black Sea (e.g. Artemov et al., 2007; Greinert et al., 2006; Naudts et al., 2006; Nikolovska et al., 2008), the southeastern United States Atlantic margin (Brothers et al., 2013), Hydrate Ridge, west of Oregon (e.g. Heeschen et al., 2005; Kannberg et al., 2013), the Gulf of Mexico (Weber et al.,2014), the Hikurangi Margin off New Zealand (Greinert et al., 2010), the North Sea (Schneider v. Deimling et al., 2007, 2011), the seas around Norway (Sauter et al., 2006; Sahling et al., 2014), the Laptev Sea (Shakova et al., 2014), and on the shelf and margin west of Svalbard (e.g. Fisher et al., 2011; Westbrook et al., 2009). It is speculated that, in some of these locations, the gas seepage is a result of gas hydrates dissociating as the GHSZ migrates further offshore as bottom water temperature increases due to global warming (Biastoch et al., 2011; Ferré et al., 2012). Since methane is by far the most abundant species in gas hydrates worldwide and its presence in the atmosphere is an important contributor to Earths greenhouse effect; methane release from the seafloor triggered by increasing bottom water temperature can represent a positive feedback mechanism on global warming.

The amount of methane stored in sub-seafloor hydrate reservoirs globally is comparable to the sum of all fossil fuels (Milkov, 2004, Wallmann et al., 2012), therefore, scientists have speculated that an accelerating destabilization of hydrates has the potential to alter the atmospheric gas composition and trigger abrupt climate warming (Shakhova et al., 2010). Such a global methane hydrate dissociation event is recorded in sediments as a negative carbon isotope ratio excursion in foraminifera during the Pate-Paleocene thermal maximum (LPTM), 55 million years ago, when the global temperature was 4-8 °C warmer than present (Dickens 2003).

Regardless of the gas origin from dissociating hydrates or other sources, methane bubbles dissolve as they rise through the water column and dissolved methane becomes available to microbial oxidation. Thus, originally free gas released from the seafloor also represents sources for dissolved methane in the water column which can be oxidized by microbes. Methanotrophic microbes use dissolved methane as an energy source and convert it to carbon dioxide altering the seawater carbonate system. In other words, methane seeping from the seafloor, both in gas- and aqueous phase, has the potential to affect the oceanic carbonate system, lowering the pH, as well as fueling pelagic and benthic ecosystems.

In order to understand the implications for the environment and climate it is important to monitor the spatial and temporal variability of these greenhouse gas emissions from the seafloor. Investigations of temporal variability of acoustically inferred gas venting shows that some bubbling seep areas are persistently and others more intermittently active (Greinert, 2008; Jerram et al., 2015; Kannberg et al., 2013; Römer et al., 2012a; Schneider von Deimling et al., 2011). However, long-term monitoring of methane seeps over larger areas has not been conducted to date.

West of Prins Karls Forland (PKF; study area described in section 1.6) a significant number of methane seeps at the shallow shelf area (70-150 m; Area 3 from Fig, 1.10), along the shelf (Area 1 from Fig, 1.10) and along the shelf break at 450 and at 350 m water depth (Area 2 from Fig, 1.10) have been surveyed with single beam echo sounders since 2008 (e.g. see Rajan et al., 2012; Veloso et al., 2015, chapter 4; Westbrook et al., 2009; Wright and et al, 2012). The aim of the presented work is to characterize the spatiotemporal fluctuations of gas emissions at the seep site offshore PKF in order to elucidate a possible connection with ocean warming. We present a synthesis of 11 surveys (2008-2014) in order to evaluate spatio/temporal variability of bubble flow rates. To our knowledge, this is the first attempt to compare emission data between surveys that have been recorded by different groups and different research vessels over such a long period of time. A Simrad EK60 echosounder was used for acoustic data acquisition during all research cruises included in this study (Table 6.1). Calibration of instruments has been maintained, allowing for impartial comparison. We use a method for gas quantification developed by Veloso et al. (2015; chapter 4) to map and quantify rates and variability of free gas flow between the eleven surveys, focusing on flare hot spots on the shelf and margin west of PKF. Our acoustic records of gas release cover depths between 90 to 400 m bsl. In section 6.2 we present the underlying datasets and the methodology used for flow rate and flux calculations. Section 6.3 presents two different comparison approaches between surveys. A summary and discussion is given in section 6.4.

6.2 Material and methods

6.2.1. Surveys

This study is based on 11 surveys carried out on the shelf and margin west of PKF, Svalbard on board of RV Helmer Hanssen and RV James Clark Ross. Studies were part of national and international research groups such as CAGE (Center for Arctic Gas Hydrates, Environment and Climate), ESONET (European Seafloor Observatory Network of Excellence) project that contributed to finance the AOEM demo mission (Arctic Ocean Esonet Mission), Pergamon (Permafrost and gas hydrate related methane release in the Arctic and impact on climate change: European cooperation for long-term monitoring), as well as student courses of the University of Tromsø.

The 11 surveys are detailed in Table 6.1. For an easy comparison, a sequential survey number has been assigned to each survey. In the following, each survey will be referred with this survey number (S1 – 11).

Table 6.1. **List of hydracoustic surveys considered in this study**

Survey number	Survey name	Month-year	Vessel
S1	JR211	August-2008	RV James Clark Ross
S2	AOEM	July-2009	RV Helmer Hanssen
S3	AOEM	October-2010	RV Helmer Hanssen
S4	JR253	July-2011	RV James Clark Ross
S5	JR269A	August-2011	RV James Clark Ross
S6	JR269B	July-2012	RV James Clark Ross
S7	Geo3144_2012	July-2012	RV Helmer Hanssen
S8	HH_13-7	July-2013	RV Helmer Hanssen

Table 6.1. (continued)

S9	HH_13-10	October-2013	RV Helmer Hanssen
S10	CAGE_14-1	June-2014	RV Helmer Hanssen
S11	CAGE 14_5	October-2014	RV Helmer Hanssen

A SeaBird911plus CTD was used for oceanographic measurements during all the surveys. Data were processed with the Seabird software to obtain temperature, water density, salinity and sound speed profiles (Appendix 3).

6.2.2. Visual observations

During S2 and S3 an underwater video camera (built at the Netherlands Institute of Sea Research, NIOZ) was used for observing and recording bubble release at the seafloor. The system was self-powered and used DSL modem technology for data connection from the camera via the winch cable to a computer on the ship, showing real-time video footage. The video was recorded directly on a hard drive in the pressure housing so that it could be replayed and recorded to DVD after the dive. Data were used to obtain an average bubble size distribution in the study area at the 240 m site (McGovern, 2012).

6.2.3. Hydroacoustic systems

The hydroacoustic water column backscattering was acquired with a Kongsberg EK60 scientific echosounder during all 11 surveys. Gas release in the water column can be easily detected with this system because of the strong acoustic impedance change between the liquid to gas medium. The system has the capability to detect the position of single targets inside the beam using the split-beam technique. The EK60 system at RV Helmer Hanssen had three different operating frequencies, 18, 38 and 120 kHz; while on board at RV James Clark the available frequencies were 38, 120 and 200 kHz. Data were recorded with the ER60 software and stored as *.raw files.

6.2.4. Data processing

Water column data were visualized with FMMidwater from the Fledermaus Software Suite (QPS, now member of SAAB Group) in order to select data files with acoustic flares. Final data processing was done using the Matlab-based Graphical User Interface FlareHunter (Chapter 5). FlareHunter was used to obtain target strength values (TS) coming from the source of the detected acoustic flares. The processed information was stored in *.mat files containing specific information of the selected backscattering.

Flow rate estimates were processed using the FlareFlowModule GUI (Chapter 5) which applies the inverse hydroacoustic method by Veloso et al. (2015; chapter 4). Essential inputs to use the GUI are hydroacoustic information of the acoustic flares (*.raw files processed with FlareHunter); normalized bubble size distribution (BSD as a *.txt file); BRS (as a *.txt files or produced with the BRSMs included in the GUI); as well as gas, water, ambient property values (defined as a text input in the GUI). A modified version of the FlareFlowModule GUI able to calculate flow rates from a set of files in a folder was used.

Maps showing bathymetry, flare positions, footprint covered area, flare clusters, acoustic maps were produced using the Generic Mapping Tools (GMT; Wessel et al., 2013).

6.3. Results

6.3.1. Acoustic flare detection, processing and mapping

EK60 *.raw data were visualized with FMMidwater (Fig.6.1) in order to detect files containing flares. From a total of 2101 examined *.raw files, 436 files showed flares in the echogram. Using FlareHunter 3145 acoustic flares were detected (Fig.6.2) concentrated in 3 main areas highlighted in Fig.6.2. These areas are located on the shelf, on the shelf-edge and on the slope at 90, 200 m and between 350 and 400 m water depth, respectively.

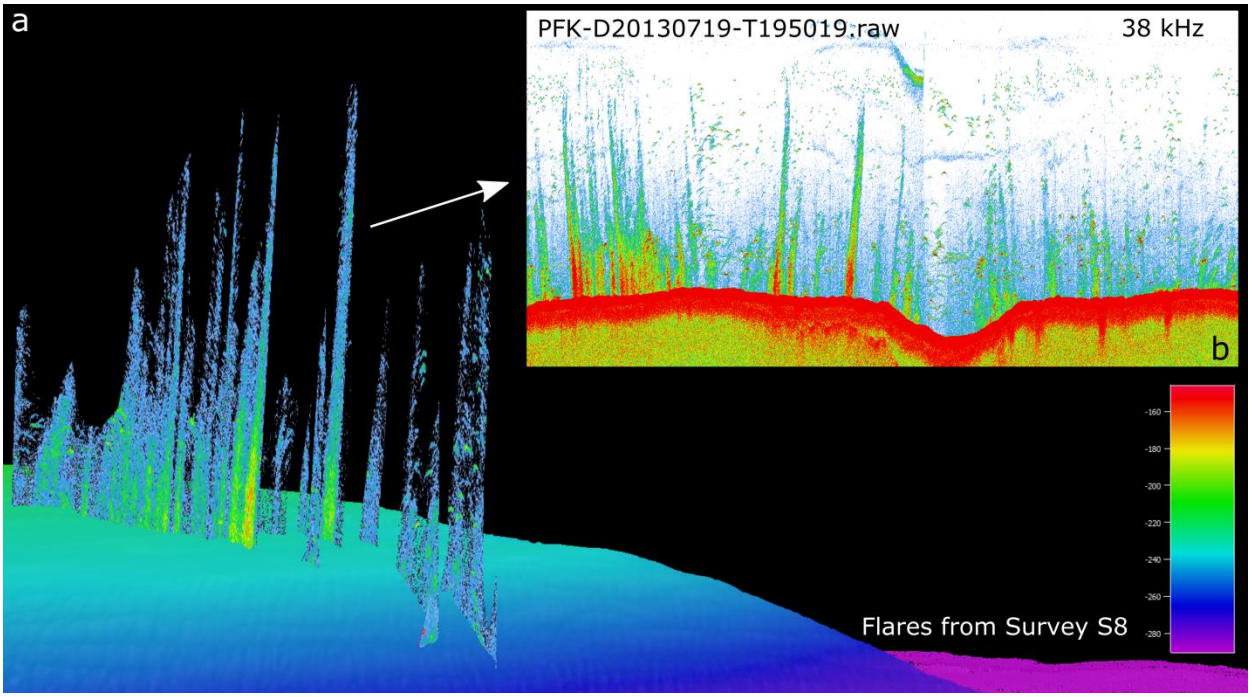

Figure 6.1. Acoustic flares at PKF displayed in Fledermaus and FMmidwater. a) 3-dimensional image with sonar curtain of flares extracted from echogram (b) and bathymetry of the study area. Flares are located at ~200 m bsl (Area 1). b) 38 kHz echogram with acoustic flares visualized with FMMidwater.

Fig.6.2 also shows the total covered area during all surveys (insonified seafloor based on the approximated beam footprint, blue lines). The footprint radius (assuming a circular footprint at the seabed) was obtained using the bottom detection tool implemented in the FlareHunter GUI. With noisy data, the automatic bottom detection sometimes gave wrong depth values, resulting in wrong values of footprint radius at the seafloor (see Fig. 6.2b). However, automatic bottom detection was used only to generate and visualize the ship track of all the surveys considered in this study and does not have any consequence in our flow rate calculations. For raw files containing flares, bottom detection was done manually.

EK60 data contain hydroacoustic information of the water column backscattering at different frequencies. Because 38 kHz data show less artificial noise, and unwanted reverberation, and strong backscattering of the bubbles than 120 kHz data they were used as the common data set for all cruises.

Since the focus is on the release of methane at the seafloor, a 5 m thick layer in the water column ranging from 5 to 10 m above the seafloor was selected to extract TS for each acoustic flare (Fig. 6.3). TS values were compensated using the angle information of the split beam technique in the same way as described for the software package Echoview (http://support.echoview.com). As a result, *.mat files of the information of the processed data are created.

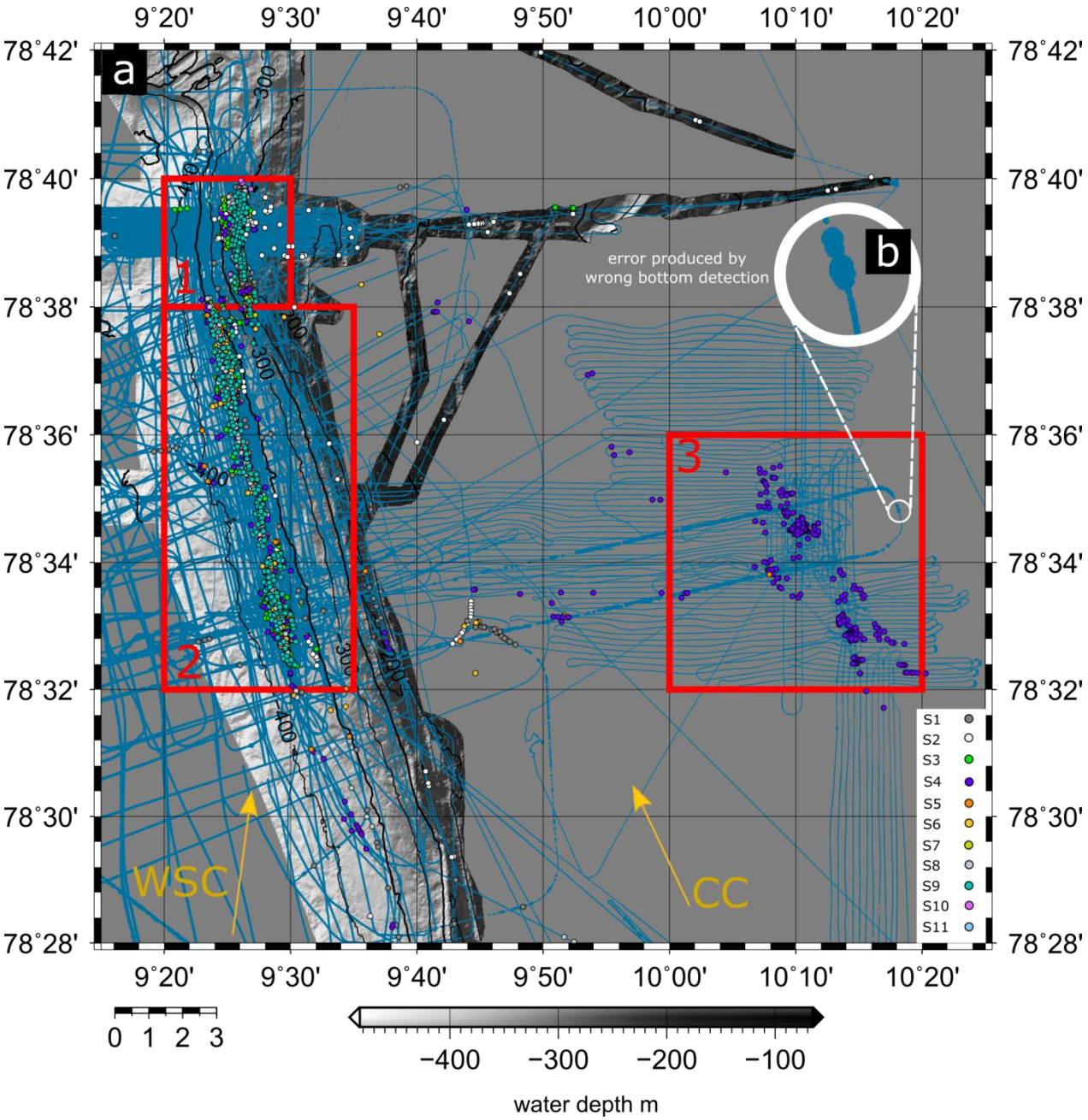

Figure 6.2. Descriptive map of the total study area. The image shows the bathymetric data, real coverage of the echosounder at the seafloor and all the detected acoustic flares coming from the available data surveys. In the map are defined three important areas (Area 1, Area 2 and Area 3) where acoustic flares are concentrated. The map also shows the influence of the West Spitsbergen Current (WSC) and the Coastal Current (CC). In addition, image (b) shows the footprint errors produced due to wrong automatic bottom detection at the echograms.

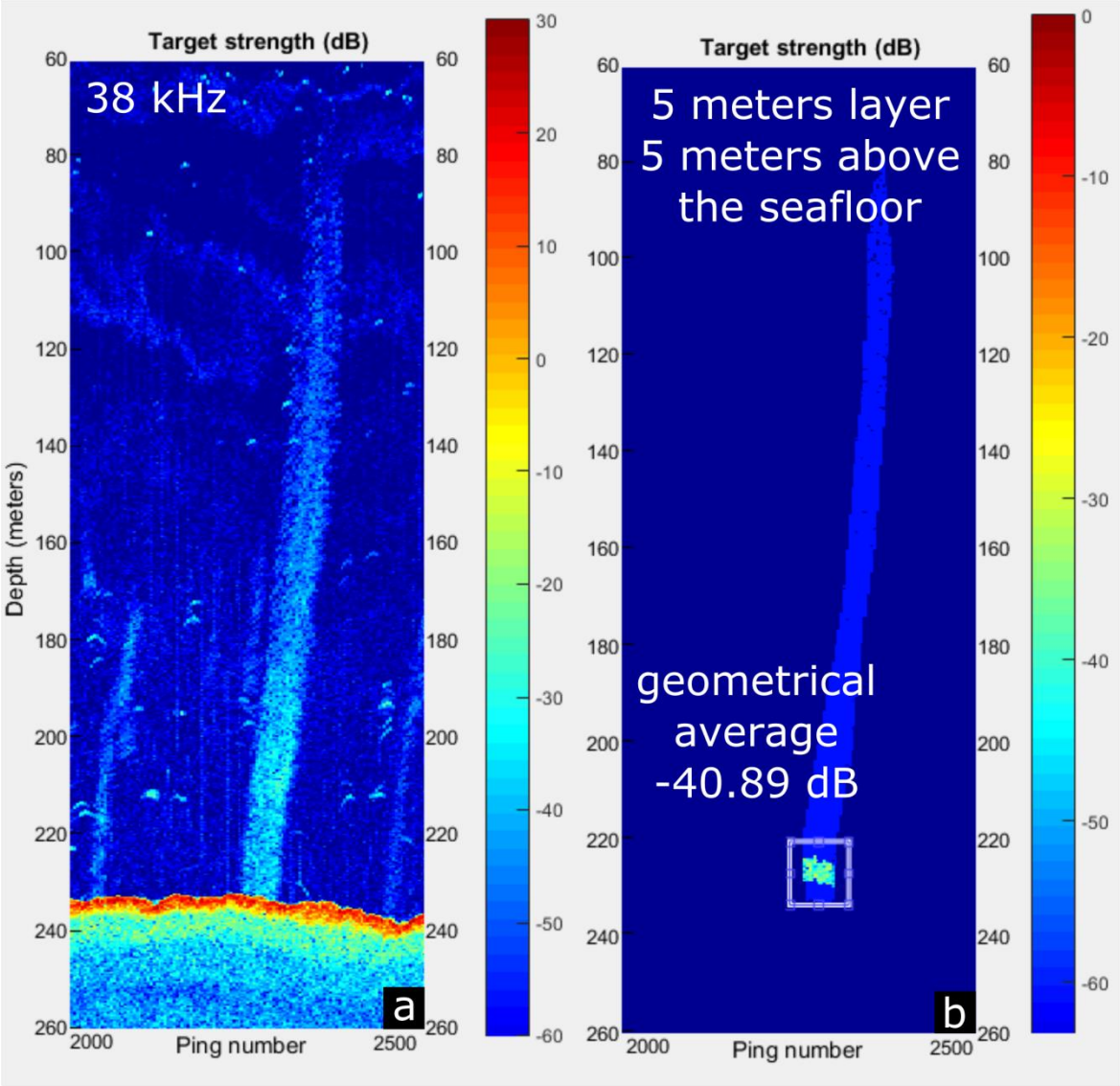

Figure 6.3. Acoustic flare detection and processing. a) Acoustic flare in target strength echogram above defined threshold (-70 dB). b) Edited acoustic flare showing the selected 5 m layer, starting 5 m above the seafloor. Image shows a geometrical average of the selection (-40.89 dB) which will be used to derive the flow rate using the inverse hydroacoustic method.

6.3.2. Spatial flow rate calculations

Flow rates of each acoustic flare were analyzed using the inverse hydroacoustic method described by Veloso et al. (2015; chapter 4). The essential information required are TS mean values obtained from the processed EK60 data, BSD obtained from visual observations (Fig. 4.11 and 6.4; McGovern, 2012) and BRS models (BRSMs). The inverse method is implemented in the FlareFlowModule GUI and flow calculations for each flare of the 11 surveys were done using this tool and the provided seven different BRSMs (Mendelson (1967), Woolf and Thorpe (1991), Woolf (1993), Leifer et al. (2000) and Leifer and Patro (2002)). Water, gas and environmental constants are detailed in Table 6.2.

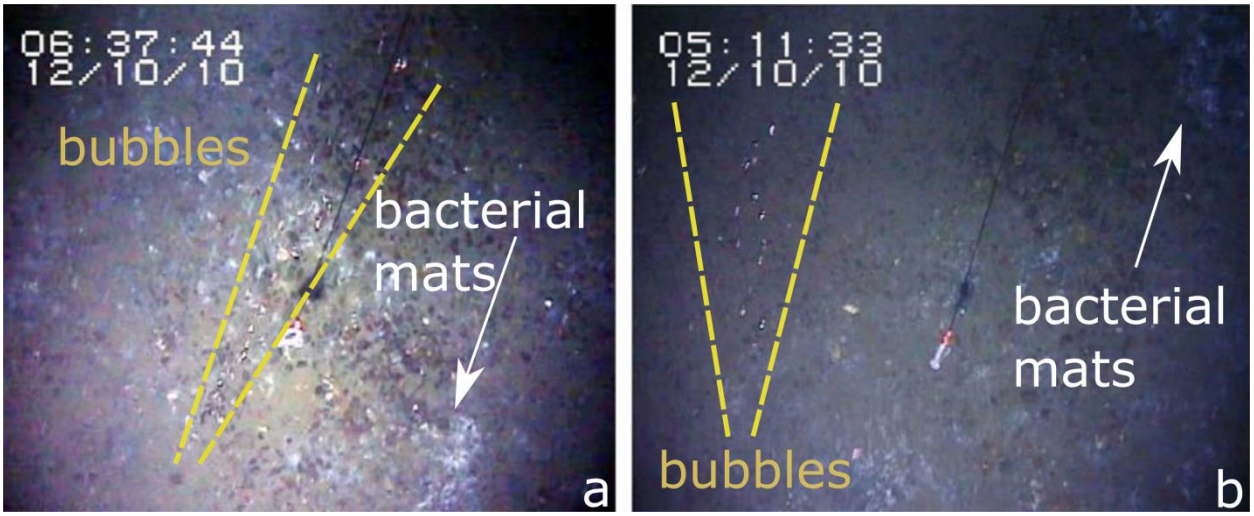

Figure 6.4. Video footage examples from two bubble streams. These images have been used to define our BSD (Fig. 4.11; McGovern, 2012). The image shows the path of the bubbles when they rise. Additionally, the image indicates the presence of bacterial mats, which are organisms related to the methane seeps existence.

Table 6.2. Water, gas and ambient constants used to evaluate flow rates of acoustic flares using the inverse hydroacoustic method.

Constant Average	**Unit**	**Value**
Temperature water	C°	From CTD profiles (Appendix 3)
Static pressure at surface	Pa	101325
Water salinity	PSU	From CTD profiles (Appendix 3)
Water density	kg/m^3	From CTD profiles (Appendix 3)
Average sound speed in the water	m/s	From CTD profiles (Appendix 3; DelGrosso eq.)
Water shear viscosity	Pa·s	0.0014
Water surface tension	N/m	0.074
Gas density at the surface (CH_4)	kg/m^3	0.66
Acceleration of gravity	m/s^2	9.8
Specific heat capacity, CH_4	$J/(kg \cdot m^3)$	2191
Ratio of specific heat of gas	dimensionless	1.4

6.3.3. Temporal flow rate comparison

As every survey has a unique combination of navigation, heave, pitch and roll data, each survey produces a unique insonified area at the seafloor. Even when navigation plans (waypoints) are identical, the surveyed/insonified part of the seafloor is slightly different from one survey to the other. Therefore, flow rates produced during one survey cannot be directly compared to flow rates of another survey. To derive spatio/temporal variations the question is how to interpolate data and assign flux values to a

certain area at the seafloor while avoiding over-estimation. Three different comparison methodologies are presented below focusing on Area 1 ~200 m bsl (78°38', 78°40', 9°20' 9°30'; Figs. 1.10 and 6.2) and Area 2 ~370 m bsl (78°32', 78°38', 9°20' 9°35'; Figs. 1.10 and 6.2). Area 3 was not considered for this comparison as it was only insonified during survey S4.

6.3.4. Gas release variability, Total Average Flux Method (TAF Method)

For each survey in Areas 1 and 2 the acoustic flares with overlapping footprint at the seabed were clustered and a flow rate was assigned to each cluster (for more detail of the clustering see Veloso et al., 2015; chapter 4). To evaluate the spatio/temporal variability of the seafloor gas emission, a mean flux was calculated for each area. The mean flux was calculated by normalizing the summation of the cluster (or isolated flares) flow rates with the insonified area at the seafloor associated to the detected flares (Equation [6.1]). This calculation was done for Area1 and Area 2 separately.

$$Q_C = \frac{\sum_i \emptyset_{M,V}^{C,i}}{A_H} \qquad [6.1]$$

$\emptyset_{M,V}^{C,i}$: Flow rate (volumetric or in mass) of i-cluster or i-isolated flare
A_H : Area related to the hydroacoustic data with flares within the analyzed area
Q_C : Mean flux (volumetric or in mass)

Results are shown in Tables 6.3-4 and 6.5-6 as well as in Figs.6.5 and 6.6. Flow rates and flux values have been calculated for the different BRSM included in the FlareFlowModule GUI.

Table 6.3. Flow rates and flux values of Area 1 for surveys S1, S2, S3, S4, S7, S8, S9, S10 and S11 using different BRSM (M1C: "Leifer" clean; M2C: "Mendelson" clean; M3C: "Leifer & Patro" clean; M1D:"Leifer" clean; M2D: "Leifer & Patro" dirty; M3D: "Woolf93"; M4D: "Thorpe 91" dirty).

		BRSM							
	Units	**clean bubble**			**dirty bubble**				
Survey S1									
		M1C	**M2C**	**M3C**	**M1D**	**M2D**	**M3D**	**M4D**	**total area (m^2)**
flow rate (vol)	L/min	16.99	21.99	21.73	14.00	17.63	22.00	18.94	152286
flow rate annual (mass)	T/yr	141.32	182.88	180.76	116.45	146.61	182.99	157.50	
flux area (vol)	mL/(min·m^2)	0.11	0.14	0.14	0.09	0.12	0.14	0.12	
flux annual (mass)	kg/(yr·m^2)	0.93	1.20	1.19	0.76	0.96	1.20	1.03	
Survey S2									
flow rate (vol)	L/min	51.67	66.55	65.77	42.58	53.36	66.60	57.32	206603

Table 6.3 (continued)

flow rate annual (mass)	T/yr	425.33	547.84	541.42	350.48	439.23	548.22	471.83	
flux (vol)	mL/(min·m^2)	0.25	0.32	0.32	0.21	0.26	0.32	0.28	
Flux annual (mass)	kg/(yr·m^2)	2.06	2.65	2.62	1.70	2.13	2.65	2.28	
Survey S3									
flow rate (vol)	L/min	17.64	22.69	22.42	14.53	18.19	22.70	19.54	125661
flow rate annual (mass)	T/yr	145.89	187.66	185.46	120.22	150.46	187.80	161.64	
flux (vol)	mL/(min·m^2)	0.14	0.18	0.18	0.12	0.14	0.18	0.16	
flux annual (mass)	kg/(yr·m^2)	1.16	1.49	1.48	0.96	1.20	1.49	1.29	
Survey S4									
flow rate (vol)	L/min	17.87	23.11	22.84	14.73	18.53	23.13	19.90	151935
flow rate annual (mass)	T/yr	150.40	194.52	192.26	123.93	155.94	194.64	167.52	
flux (vol)	mL/(min·m^2)	0.12	0.15	0.15	0.10	0.12	0.15	0.13	
flux annual (mass)	kg/(yr·m^2)	0.99	1.28	1.27	0.82	1.03	1.28	1.10	
Survey S7									
flow rate (vol)	L/min	44.71	57.80	57.13	36.84	46.34	57.84	49.78	237936
flow rate annual (mass)	T/yr	394.79	510.42	504.48	325.32	409.20	510.74	439.58	
flux (vol)	mL/(min·m^2)	0.19	0.24	0.24	0.15	0.19	0.24	0.21	
flux annual (mass)	kg/(yr·m^2)	1.66	2.15	2.12	1.37	1.72	2.15	1.85	
Survey S8									
flow rate (vol)	L/min	29.47	38.19	37.74	24.29	30.61	38.21	32.89	180101
flow rate annual (mass)	T/yr	277.37	359.57	355.41	228.56	288.25	359.78	309.67	
flux (vol)	mL/(min·m^2)	0.16	0.21	0.21	0.13	0.17	0.21	0.18	
flux annual (mass)	kg/(yr·m^2)	1.54	2.00	1.97	1.27	1.60	2.00	1.72	
Survey S9									
flow rate (vol)	L/min	29.52	37.68	37.23	24.33	30.22	37.71	32.46	177399
flow rate annual (mass)	T/yr	276.78	354.13	349.93	228.07	283.96	354.42	305.06	
flux (vol)	mL/(min·m^2)	0.17	0.21	0.21	0.14	0.17	0.21	0.18	
flux annual (mass)	kg/(yr·m^2)	1.56	2.00	1.97	1.29	1.60	2.00	1.72	
Survey S10									
flow rate (vol)	L/min	25.32	32.66	32.28	20.87	26.18	32.68	28.13	112258
flow rate annual (mass)	T/yr	210.53	271.51	268.35	173.48	217.68	271.70	233.87	

Table 6.3 (continued)

flux (vol)	mL/(min·m^2)	0.23	0.29	0.29	0.19	0.23	0.29	0.25	
flux annual (mass)	kg/(yr·m^2)	1.88	2.42	2.39	1.55	1.94	2.42	2.08	
Survey S11									
flow rate (vol)	L/min	15.32	19.58	19.35	12.63	15.70	19.60	16.87	67981
flow rate annual (mass)	T/yr	127.85	163.36	161.42	105.35	130.99	163.50	140.73	
flux (vol)	mL/(min·m^2)	0.23	0.29	0.28	0.19	0.23	0.29	0.25	
flux annual (mass)	kg/(yr·m^2)	1.88	2.40	2.37	1.55	1.93	2.41	2.07	

Table 6.4. Mean values, standard deviation and relative error of all nine surveys, separately averaged for clean and dirty BRSs for Area 1 (Table 6.3).

					Clean bubble models				
Surveys	**S1**	**S2**	**S3**	**S4**	**S7**	**S8**	**S9**	**S10**	**S11**
Mean flux[kg/(yr·m^2)]	1.105	2.444	1.377	1.179	1.975	1.837	1.843	2.228	2.219
Stdev	0.154	0.334	0.187	0.164	0.274	0.257	0.245	0.306	0.294
Average relative error ; BRSM					~ ±10 %				
					Dirty bubble models				
Mean flux[kg/(yr·m^2)]	0.991	2.190	1.234	1.056	1.770	1.647	1.651	1.997	1.988
Stdev	0.181	0.396	0.223	0.193	0.323	0.302	0.295	0.362	0.354
Average relative error ; BRSM					~ ±12 %				

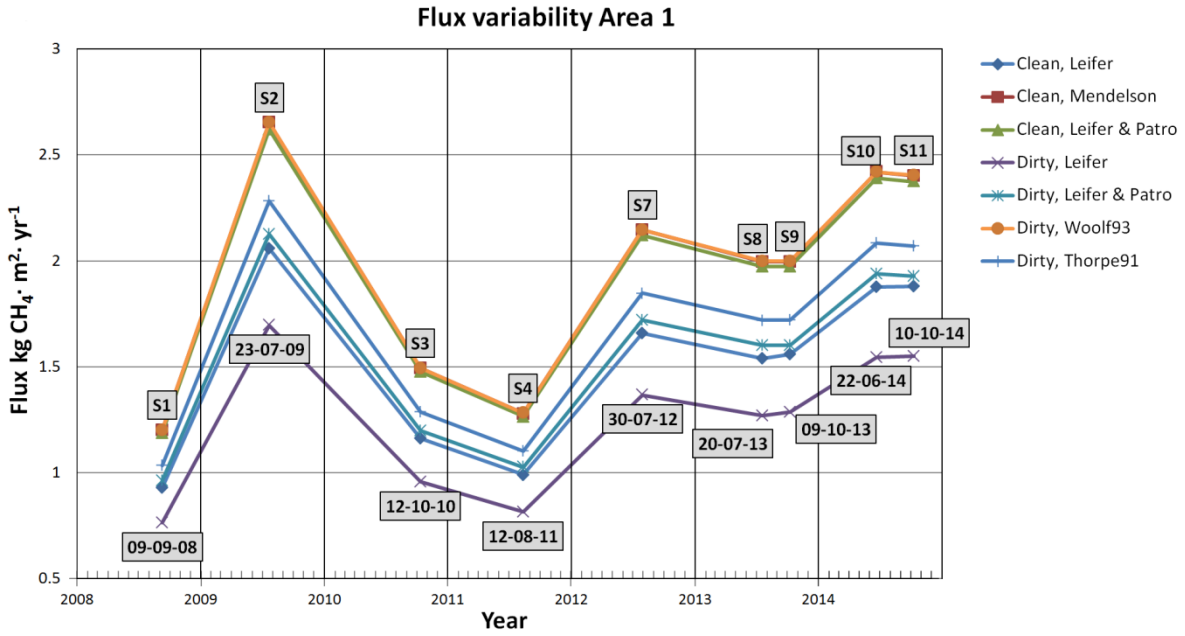

Figure 6.5. Flux changes for Area 1 during nine surveys (surveys S5 and S6 did not investigate this area).

Fig.6.5 shows how the flux changed between 2008 (S1) and 2014 (S11). Flux values derived from different rising speed models vary in the same range as the temporal fluctuations themselves (about 1 kg CH_4 $m^{-2}yr^{-1}$). Flux values ranging from 0.75 to 2.6 kg CH_4 $m^{-2}yr^{-1}$ point towards a moderate variability.

Tables 6.5 and 6.6 show the flux variability in Area 2 at the slope of PKF. Fig. 6.6 depicts the change over time of the mean fluxes at Area 2 with similar fluxes as in Area 1. In contrast, the flux peaks between October 2013 and August 2014 with higher values as the maximum flux in Area 1.

Table 6.5. Estimated flow rates and fluxes of Area 2 for surveys S1, S2, S3, S4, S5, S6, S7, S8 and S9 using different BRSM (M1C: "Leifer" clean; M2C: "Mendelson" clean; M3C: "Leifer & Patro" clean; M1D:"Leifer" clean; M2D: "Leifer & Patro" dirty; M3D: "Woolf93"; M4D: "Thorpe 91" dirty).

		BRSM							
Survey S1	**Units**	**Clean bubble**			**Dirty bubble**				
		M1C	**M2C**	**M3C**	**M1D**	**M2D**	**M3D**	**M4D**	**Total area (m^2)**
flow rate (vol)	L/min	24.27	31.39	31.03	20.003	25.17	31.4173	27.03	202163
flow rate annual (mass)	T/yr	229.39	297.21	293.77	189.00	238.26	297.38	255.94	
flux (vol)	mL/(min·m^2)	0.12	0.15	0.15	0.09	0.12	0.15	0.13	
Flux annual (mass)	kg/(yr·m^2)	1.13	1.47	1.45	0.93	1.17	1.47	1.26	
Survey S2									
flow rate (vol):	L/min	21.74	28.07	27.74	17.91	22.50	28.09	24.18	233105
flow rate annual (mass)	T/yr	217.67	280.95	277.67	179.36	225.24	281.14	241.97	
flux (vol)	mL/(min·m^2)	0.09	0.12	0.11	0.076	0.09	0.12	0.10	
flux annual (mass)	kg/(yr·m^2)	0.93	1.20	1.19	0.76	0.96	1.20	1.03	
Survey S3									
flow rate (vol)	L/min	26.17	33.97	33.58	21.56	27.23	33.99	29.26	423938
flow rate annual (mass)	T/yr	338.06	438.87	433.81	278.57	351.81	439.11	377.96	
flux area (vol)	mL/(min·m^2)	0.06	0.08	0.07	0.05	0.06	0.08	0.06	
flux annual (mass)	kg/(yr·m^2)	0.79	1.03	1.02	0.65	0.82	1.03	0.89	
Survey S4									
flow rate (vol)	L/min	52.40	68.18	67.40	43.18	54.65	68.21	58.71	342149
flow rate annual (mass)	T/yr	687.54	894.74	884.45	566.55	717.20	895.17	770.45	
flux area (vol)	mL/(min·m^2)	0.15	0.19	0.19	0.12	0.15	0.19	0.17	
flux annual (mass)	kg/(yr·m^2)	2.00	2.61	2.58	1.65	2.09	2.61	2.25	

Table 6.5 (continued)

Survey S5									
flow rate (vol)	L/min	59.43	77.36	76.48	48.97	62.01	77.40	66.62	337486
flow rate annual (mass)	T/yr	784.89	1021.91	1010.17	646.77	819.138	1022.4	879.96	
flux (vol)	mL/(min·m^2)	0.17	0.22	0.22	0.14	0.18	0.22	0.19	
flux annual (mass)	kg/(yr·m^2)	2.32	3.0	2.99	1.91	2.42	3.02	2.60	
Survey S6									
flow rate (vol)	L/min	59.03	76.82	75.94	48.64	61.58	76.86	66.15	326863
flow rate annual (mass)	T/yr	775.72	1009.72	998.12	639.21	809.37	1010.21	869.46	
flux (vol)	mL/(min·m^2)	0.18	0.23	0.23	0.14	0.18	0.23	0.20	
flux annual (mass)	kg/(yr·m^2)	2.37	3.08	3.05	1.95	2.47	3.09	2.66	
Survey S7									
flow rate (vol)	L/min	34.36	44.26	43.74	28.31	35.48	44.29	38.12	214762
flow rate annual (mass)	T/yr	362.14	465.96	460.49	298.41	373.5941	466.29	401.35	
flux (vol)	mL/(min·m^2)	0.16	0.20	0.20	0.13	0.16	0.20	0.17	
flux annual (mass)	kg/(yr·m^2)	1.68	2.16	2.14	1.38	1.73	2.17	1.86	
Survey S8									
flow rate (vol)	L/min	40.08	52.14	51.54	33.02	41.79	52.17	44.90	307272
flow rate annual (mass)	T/yr	503.43	655.08	647.55	414.83	525.10	655.40	564.11	
flux (vol)	mL/(min·m^2)	0.13	0.16	0.16	0.10	0.13	0.16	0.14	
flux annual (mass)	kg/(yr·m^2)	1.63	2.13	2.10	1.35	1.70	2.13	1.83	
Survey S9									
flow rate (vol)	L/min	23.26	29.78	29.43	19.16	23.88	29.80	25.65	345878
flow rate annual (mass)	T/yr	295.41	378.17	373.70	243.42	303.24	378.49	325.76	
flux (vol)	mL/(min·m^2)	0.06	0.08	0.08	0.05	0.06	0.08	0.07	
flux annual (mass)	kg/(yr·m^2)	0.85	1.09	1.08	0.70	0.876	1.09	0.94	

Table 6.6. Mean values, standard deviation and relative error of all nine surveys, separately averaged for clean and dirty BRSs for Area 2 (Table 6.5).

				Clean bubble models					
Surveys	**S1**	**S2**	**S3**	**S4**	**S5**	**S6**	**S7**	**S8**	**S9**
Mean flux[kg/(yr·m^2)]	1.353	1.110	0.952	2.403	2.782	2.839	2.000	1.959	1.009

Table 6.6(continued)

Stdev	0.189	0.153	0.134	0.341	0.396	0.403	0.272	0.278	0.135
Average relative error; BRSM					~ ±10 %				
					Dirty bubble models				
Mean flux[kg/(yr·m^2)]	1.213	0.995	0.854	2.155	2.495	2.546	1.792	1.757	0.904
Stdev	0.222	0.181	0.157	0.398	0.461	0.470	0.324	0.324	0.162
Average relative error; BRSM					~ ±12 %				

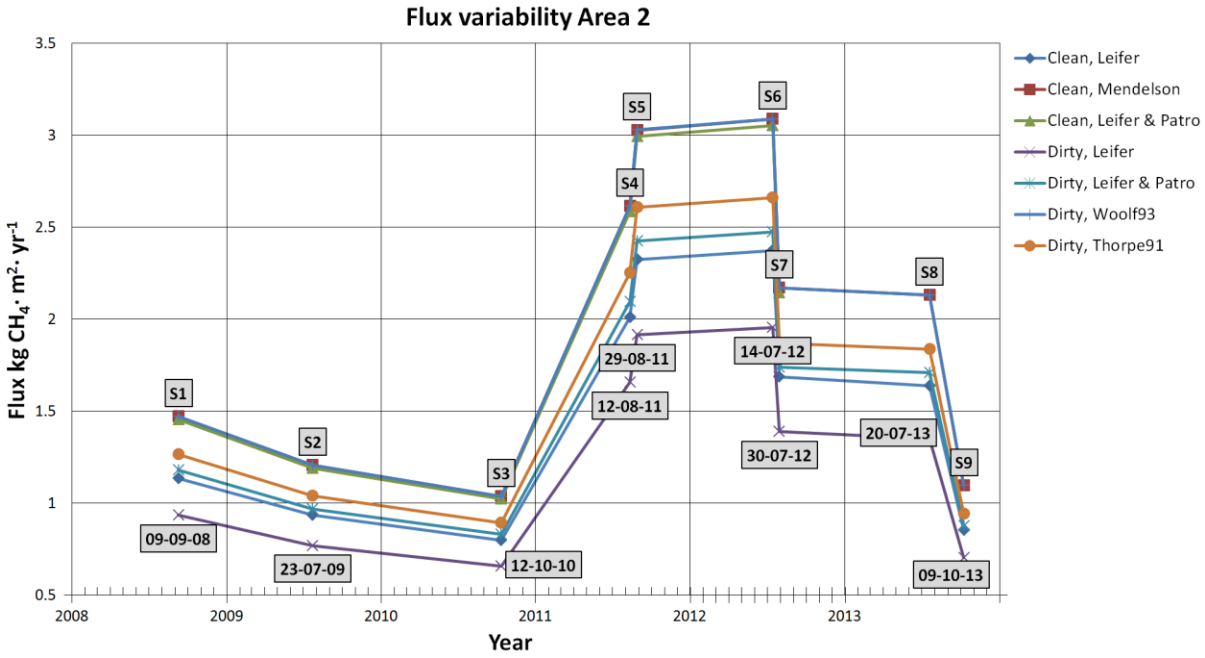

Figure 6.6. Average flux values versus survey date (Area 2) obtained with first comparison method using different BRSM (surveys S10 and S11 did not investigate this area).

6.3.5. Gas release variability, Common Area Comparison Method (CAC method)

The second approach used to evaluate gas release changes over time was comparing common areas that have been mapped during different surveys (Figs. 6.7 and 6.8). This was done by clustering the processed flares within a survey in the same way as described for the TAF method in chapter 4 (section 4.4.3.2) Subsequently, positions of all the clusters were gridded in Matlab using a cell size of 1x1 m and a flux value was assigned to each cell. This value was the mean flux of the cluster (mean value of fluxes from flares that belong to a cluster; equation 4.18) of which the specific cell is part of. The so generated data sets were exported as ASCII files (x, y, flux value) and used for the following comparison.

Common areas between surveys were derived by generating binary matrices with GMT, using the xyz coordinates of the ASCII files and gridding them using the *blockmean* and *nearneighbor* commands of GMT (cell size= 1 m, search radius = 50 m; fixed z values of 0 and 1 with 1 = cells with a flux value). A second matrix of the same area and grid size is created holding median flux values per cell (cell size 1m,

z=flux) again using the *blockmedian* and *nearneighbor* commands of GMT. This process was done for all the surveys. For defining the common areas between N surveys, the binary matrices were multiplied (GMT command *gridmath* operator MUL) resulting in a new binary matrix with cell values of one only where all surveys showed gas release. Following, the gridded flux matrices of each survey are multiplied with the binary matrix resulting in a comparison binary flux matrix of the common areas. The representative flux (Q_{RF}) and the flow rate ($\emptyset_{RF}$) of all common areas are calculated with equation 6.2 and 6.3 respectively.

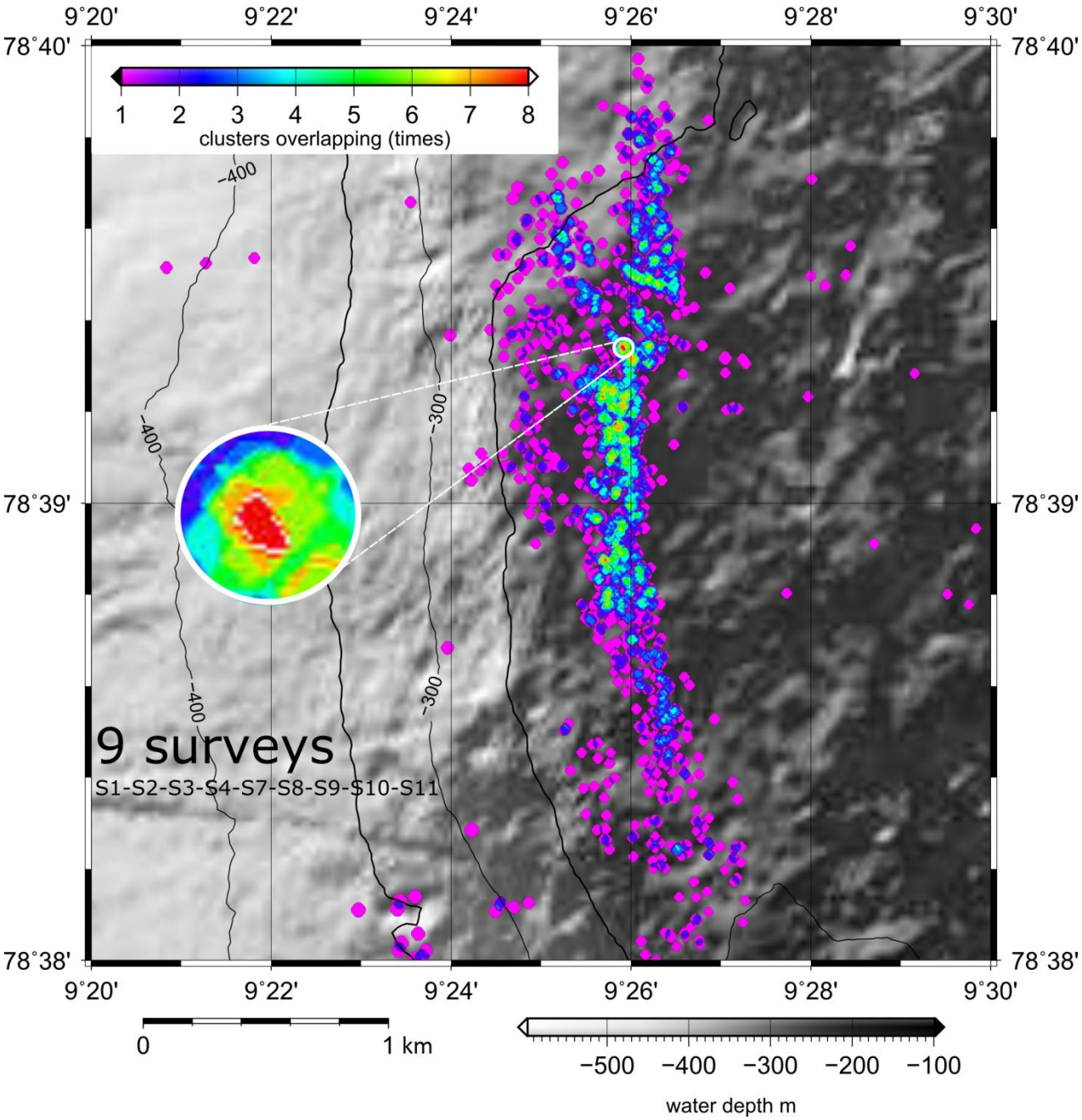

Figure 6.7. Maps of flare clusters at Area 1. The colors of the map shows how many times flare clusters from different surveys overlap. From 9 surveys (S1, S2, S3, S4, S7, S8, S9, S10, S11) the maximum overlap obtained was 8 times.

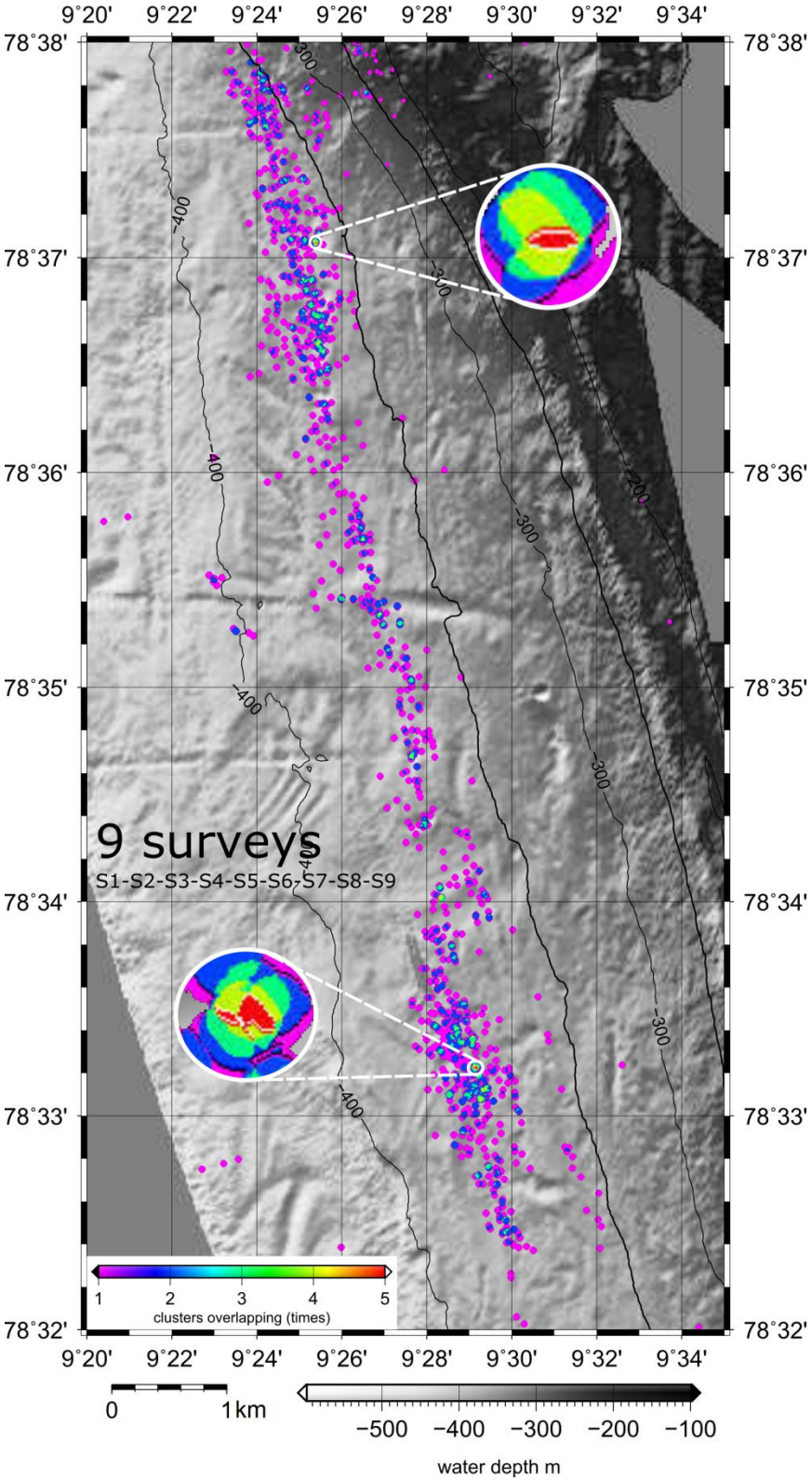

Figure 6.8. Maps of flare clusters at Area 2. The colors of the map shows how many times flare clusters from different surveys overlap. From 9 surveys (S1, S2, S3, S4, S5, S6, S7, S8, S9) the maximum overlap obtained was 5 times.

$$Q_{RF} = \frac{\sum_j^m \sum_i^n q_{i,j}}{Ne} \quad [6.2]$$

$$\emptyset_{RF} = \Delta x \Delta y \sum_j^m \sum_i^n q_{i,j} \quad [6.3]$$

Where,

$q_{i,j}$: Flux at the i, j grid
Ne : Number of cells with flux values
Δx : Horizontal cell size
Δy : Vertical cell size
Q_{RF} : Approximated representative flux (mean flux) of common area
$\emptyset_{RF}$: Representative flow rate of common area

Results of these comparisons are detailed in Tables 6.7 and 6.8, and illustrated in Figs. 6.9 and 6.10, respectively. For Area 1 we found 29 common areas which have been mapped by up to 6 surveys; for Area 2 a total of 35 common areas could be identified again with up to 6 surveys covering the same area.

Table 6.7. Results using the second comparison method for Area 1. Fluxes are detailed for different surveys involved in the common area combination. Here, a total of 29 combinations are shown. At the end of the table average flux values, standard deviation and relative errors per each survey are detailed.

	S1	S2	S3	S4	S7	S8	S9	S10	S11	Common area (m^2)
Flux [Kg/(yr·m^2)]		7.16	1.67		2.96		7.61	2.89		5284
		9.39	3.80					6.19	2.41	9156
	1.15	8.02	3.33	4.06				6.80	4.05	8
		7.11			3.23					140924
		7.30			3.47	2.84	7.20			19512
					5.31	6.04	8.45	4.99	2.91	4916
		7.50				2.54	7.05			28708
		7.88						3.76		82248
		4.06						3.59	1.64	59612
		7.42		1.97	2.85					6708
					3.21	2.22	6.82			31588
						1.92	6.59			48960
								3.59	1.64	59612

Table 6.7. (continued)

Flux [Kg/(yr·m^2)]										
	1.83	8.78	3.11				6.84	3.15		2868
	1.65	8.26	3.20		3.08	3.81				68
	1.34	10.09	3.57		5.48	3.59		6.34		1740
	2.34	8.97	3.81		4.62	3.41	6.10		6.10	1684
	1.40	8.45	3.35		3.97		7.36	3.37		2640
	1.22		3.72		5.35		7.74		1.83	1328
	2.88	7.98	3.67		3.62			4.52		5412
	2.85	8.25	3.91					4.94	1.93	2956
	1.76	7.16			2.96		7.61	2.89		5284
	2.32	7.47						3.48	1.91	9096
	1.28		3.12		3.78		7.25	3.49		3152
	2.19							3.24	1.66	15260
				1.49	2.61					15816
				2.35	2.76	3.22				3564
				2.07		2.16				7056
				2.05			7.68			5912
	1.86	7.84	3.35	2.33	3.70	3.17	7.25	4.20	2.60	
	0.60	1.25	0.60	0.88	0.97	1.19	0.59	1.28	1.44	
	26.99	10.75	11.67	24.90	21.22	24.92	6.30	25.48	40.21	

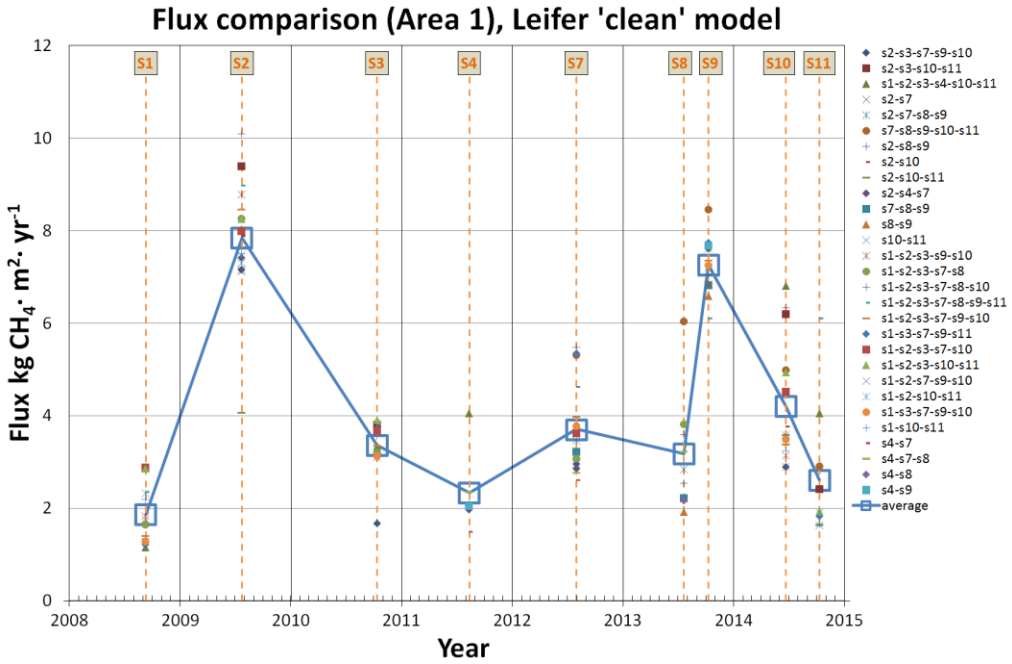

Figure 6.9. Results of common areas fluxes from Area 1 calculated with 'Leifer', clean bubble 'BRSM at different surveys. The results are shown for the multiple combinations between surveys carried out to obtain different common areas.

Table 6.8. Results using the second comparison method for Area 2. Fluxes are detailed for different surveys involved in the common area combination. Here, a total of 35 combinations are shown. At the end of the table average flux values, standard deviation and relative errors per each survey are detailed.

	S1	S2	S3	S4	S5	S6	S7	S8	S9	Common area (m^2)
Flux Kg/(yr·m^2)			0.57	1.45	1.27	0.23		0.46	3.32	20
		0.39	0.53							6724
		0.39							2.70	15052
			0.63				1.86			16828
			0.86				0.83	5.23	1.51	148
			0.58					1.01	3.02	10568
			0.53						1.54	138064
			0.57	4.03						86816
			0.63	5.94				1.36		7744
			0.57	1.54				0.76	2.74	1608
			0.52	2.98					2.08	21992
			0.59	5.14	2.37					8628
			0.62	1.26	1.44			1.56		772
			0.57	1.45	1.27	0.23		0.46		216
			0.57	1.45	1.27	0.23			3.32	684
			0.57	1.45		0.23		0.46		216
			0.59		1.59					34656
			0.57		1.27	0.23		0.46		228
								1.54	3.23	54400
	1.16		0.58							6396
	0.84		0.59						3.74	1684
	1.18		0.58	10.70						1776
	0.85		0.59	17.63					3.74	1032
				6.34				1.91	3.63	11580
				13.09	1.39	0.64		0.51		1760
				1.44	1.35	0.35			3.42	992
		0.31					0.44			16
							0.89	0.51	0.59	21148
				9.70			5.17			18248
				10.68			2.13	1.79		6824
				5.01			0.53	1.59	3.89	1488
				6.79			0.75		3.85	4484
				3.16	2.02		0.29			412
					1.20		1.33			4444
						0.77	2.55			4264
Mean	1.00	0.35	0.59	5.77	1.50	0.36	1.52	1.30	2.86	
Stdev	0.18	0.04	0.06	4.63	0.37	0.21	1.41	1.21	0.97	
Relative error (%); mean	15.92	27.95	6.20	136.56	18.51	47.44	66.87	59.28	27.39	

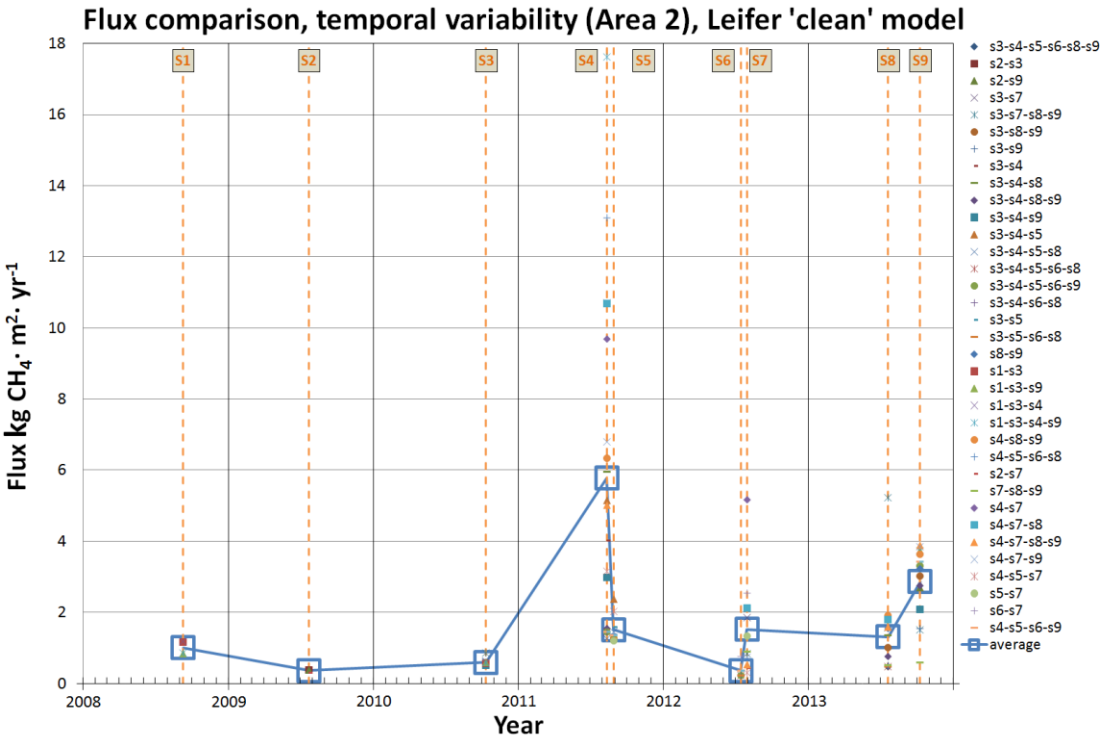

Figure 6.10. Results of common areas fluxes from Area 2 calculated with 'Leifer, clean bubble' BRSM at different surveys. The results are shown for the multiple combinations between surveys carried out to obtain different common areas.

6.3.7. Gas release variability, Cell by Cell Comparison Method (CCC method)

An alternative method proposed to evaluate the spatio/temporal changes is the direct comparison of each grid cell for the common area fluxes between different surveys. The CCC method uses the interpolated flux values of the common areas obtained for the CAC method (cell size of 1x1 m). Unlike the other methods, this comparison allows to observe temporal changes in the spatial distribution of the gas seepage intensity (or flux strength). The method is applied for survey combinations that present spatial overlapping among the hydroacoustic data of flares. Here, the CCC method is applied to two survey combinations and the flux results (using the Leifer "clean" BRSM) from the common areas are graphically presented in Figs. 6.11 and 6.12. The first example (Fig. 6.11) shows the temporal flux variability at Area 1 for 717 cells that belong to a common area of 5 surveys (S1, S2, S3, S9 and S10). The second example (Fig.6.12) shows the gas release changes of 372 common-area cells at Area 2 including 4 surveys (S4, S7, S8 and S9). As shown the common areas can be subdivided in clusters of neighboring cells. In both examples cell clusters are illustrated in different colors. The sizes of these clusters are generally comparable to the sizes of the echosounder footprint. Additionally, both figures display the results coming from the TAF and CAC method for the respective surveys involved. Here, the CCC method is only applied to some examples of common areas to only illustrate how the flux-strength and spatial distribution is temporally changing. Not all common areas and possible comparisons are shown.

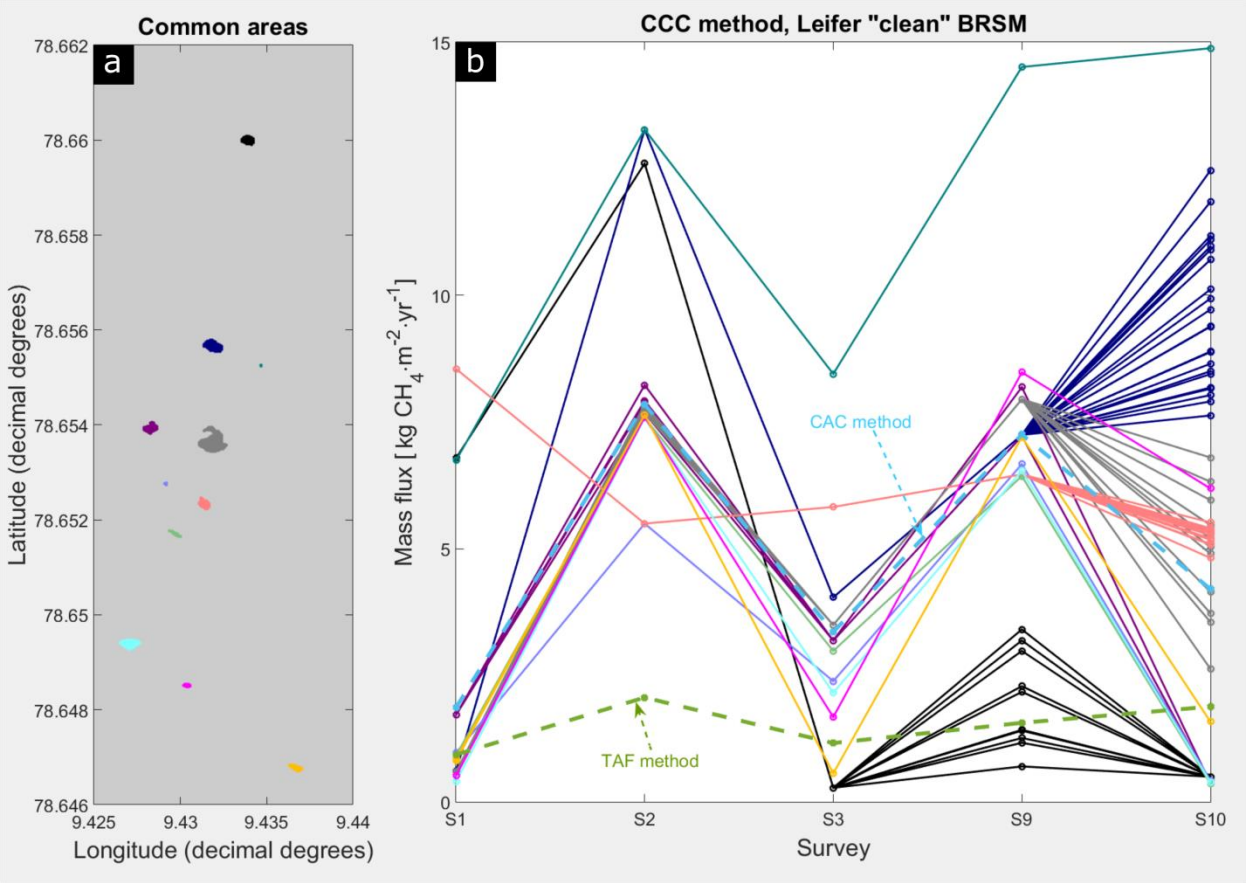

Figure 6.11. Flux results obtained by using CCC method in common area resulting from the combination of S1, S2, S3, S9 and S10. The image represents the flux variability of 717 cells (1x1 m size) in time a) Map of total common area. Sub-areas are grouped according their position and displayed in different colors. b) Flux values of cells at different survey time. Curve colors are associated to the location of the sub-groups indicated in (a). Additionally, flux results from TAF and CAC method are illustrated for comparison.

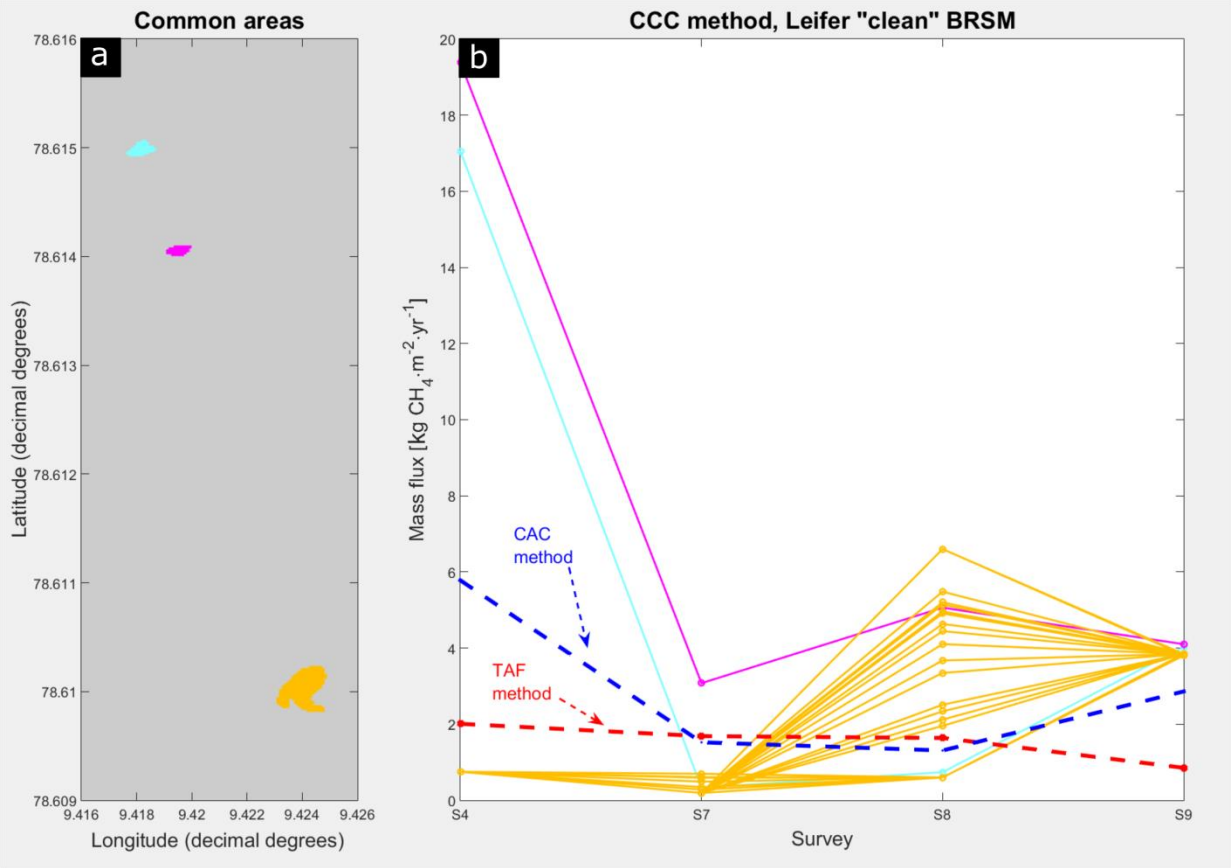

Figure 6.12. Flux results obtained by using GGC method in common area resulting from the combination of S4, S7, S8 and S9. The image represents the flux variability of 372 cells (1x1 m size) in time. a) Map of total common area. Sub-areas are grouped according their position and displayed in different colors. b) Flux values of cells at different survey time. Curve colors are associated to the location of the sub-groups indicated in (a). Additionally, flux results from TAF and CAC method are illustrated for comparison.

6.3.8. Total flow rate and flux

A total flow rate was calculated by merging the hydroacoustic information of the entire set of flares detected during the 11 surveys. Flares located within a certain area (area Fig.6.2) were clustered when their footprints overlapped. Cluster flow rates were derived using the same procedure explained in section 4.4.3.2. Finally, total flow rates were calculated by the summation of the clusters (or isolated flares) flow rate. Results are detailed for the different BRSMs in Table 6.9. Additionally, flow rates and fluxes were calculated separately for Area 1, Area 2 and Area 3 (Fig. 6.2).

Table 6.9. Total volumetric flux and flow rate of methane calculated using merged hydroacoustic information of area from Fig.6.2 (78°28' N, 78°42 N; 9° 15' E, 10° 20' E) using different BRSM (M1C: "Leifer" clean; M2C: "Mendelson" clean; M3C: "Leifer & Patro" clean; M1D:"Leifer" clean; M2D: "Leifer & Patro" dirty; M3D: "Woolf93"; M4D: "Thorpe 91" dirty).

	Clean bubble models				Dirty bubble models		
Total area (Fig. 6.2)	**M1C**	**M2C**	**M3C**	**M1D**	**M2D**	**M3D**	**M4D**
Flow rate vol (L/min)	305.65	395.06	390.47	251.86	316.72	395.31	340.24
Flow rate mass (T/yr)	3141.03	4063.72	4016.52	2588.28	3257.80	4066.20	3499.78
Flux vol (L/min*m^2)	0.13	0.17	0.17	0.11	0.14	0.17	0.15
Flux vol (T/yr*m^2)	1.40	1.81	1.79	1.15	1.45	1.81	1.56
Area with acoustic data [m^2]				2241772			
Mean annual flow rate [T/yr]		3740.42				3499.78	
Standard deviation Flow rate BRSM [T/yr]		519.62				612.11	
Mean relative error Flow rate BRSM [%]		± ~ 10				± ~ 12	
Area 1	**M1C**	**M2C**	**M3C**	**M1D**	**M2D**	**M3D**	**M4D**
Flow rate vol (L/min)	122.96	158.28	156.43	101.32	126.91	158.40	136.33
Flow rate mass (T/yr)	1032.03	1328.57	1313.00	850.41	1065.19	1329.51	1144.31
Flux vol (L/min*m^2)	0.19	0.24	0.24	0.16	0.20	0.25	0.21
Flux vol (T/yr*m^2)	1.60	2.06	2.03	1.32	1.65	2.06	1.77
Area with acoustic data [m^2]				646234			
Mean annual flow rate [T/yr]		1224.53				1097.35	
Standard deviation Flow rate BRSM [T/yr]		166.89				198.42	
Mean relative error Flow rate BRSM [%]		± ~ 10				± ~ 12	
Area 2	**M1C**	**M2C**	**M3C**	**M1D**	**M2D**	**M3D**	**M4D**
Flow rate vol (L/min)	150.49	195.18	192.92	124.01	156.46	195.28	168.08
Flow rate mass (T/yr)	1949.25	2528.28	2499.05	1606.23	2026.77	2529.69	2177.31
Flux vol (L/min*m^2)	0.10	0.13	0.13	0.08	0.11	0.13	0.11
Flux vol (T/yr*m^2)	1.33	1.72	1.70	1.10	1.38	1.72	1.48
Area with acoustic data [m^2]				1466867			
Mean annual flow rate [T/yr]		2325.53				2085.00	
Standard deviation Flow rate BRSM [T/yr]		326.19				382.48	
Mean relative error Flow rate BRSM [%]		± ~ 10				± ~ 12	
Area 3	**M1C**	**M2C**	**M3C**	**M1D**	**M2D**	**M3D**	**M4D**
Flow rate vol (L/min)	60.80	78.53	77.62	50.10	62.96	78.58	67.64
Flow rate mass (T/yr)	555.96	718.50	710.14	458.12	576.02	718.95	618.82
Flux vol (L/min*m^2)	0.12	0.15	0.15	0.10	0.12	0.15	0.13
Flux vol (T/yr*m^2)	1.10	1.42	1.40	0.90	1.14	1.42	1.22
Area with acoustic data [m^2]				507447			
Mean annual flow rate [T/yr]		661.53				592.98	
Standard deviation Flow rate BRSM [T/yr]		126.21				108.03	
Mean relative error Flow rate BRSM [%]		± ~ 10				± ~ 12	

6.4. Discussion

6.4.1. Data analyses

6.4.1.1. Temporal variability

Our analysis cover results obtained from the TAF and CAC method (Fig. 6.13). Results from the CCC method are not considered in this method comparison because they do not cover all surveys. Results obtained with both, the TAF and CAC method from Area 1 seem to be moderately correlated (linear correlation; r^2 = 0.59). The comparison of both methods shows different flux magnitudes for all the surveys at Area 1 with the CAC method giving higher values. For Area 2, results obtained with the two methods do not correlate (r^2 = 0.19). On the other hand, flux magnitudes obtained with the two methods show very similar values for some surveys (S1, S3, S7 and S8).

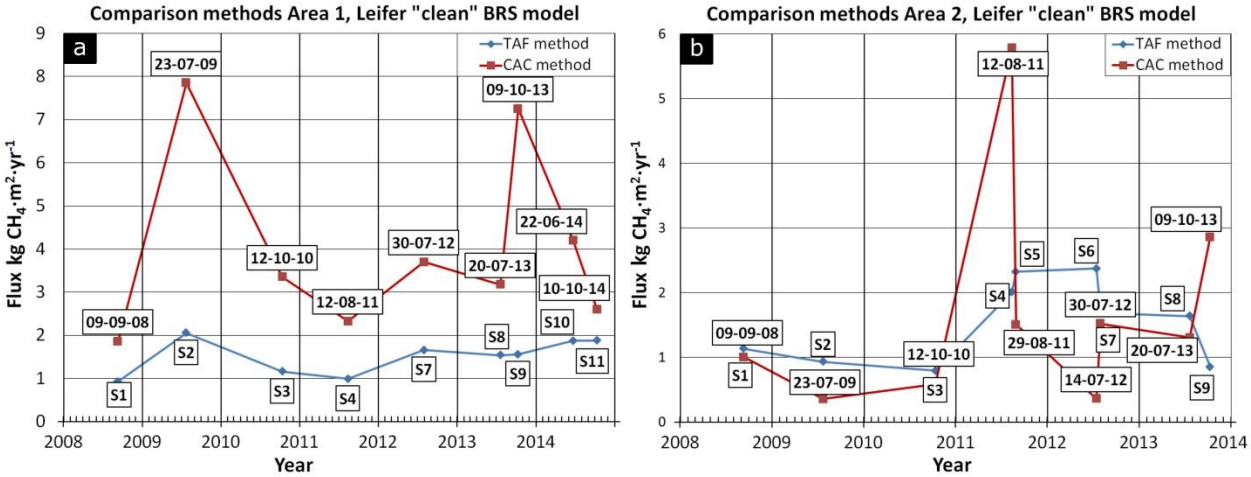

Figure 6.13. Graphical comparison of mass flux results obtained from with TAF and CAC method for Area 1 (a) and Area 2 (b). Results correspond to the fluxes obtained with the Leifer "clean" BRSM. The comparison is done for surveys containing flare-hydroacoustic data at the respective areas. Flux results that represent the CAC method are the respective average Q_{RF} values at each survey (see also Figs. 6.9 and 6.10).

It is clear that flux results obtained with the two different methods show a mismatch (Fig.6.13) and logically, raising the question which one of the two methods better represents the gas release in the study area? According to the possible errors that each method can produce, the conclusion is that the TAF method could introduce a larger error. The reason is that hydroacoustic data of flares from different surveys do not come always from the same insonified area at the seafloor. One specific survey could cover a larger amount of hot spots (seep sites with higher flow rates) than other surveys; therefore comparing total mean fluxes from both of them would be not appropriate. It has been shown that seepage intensity (or strength) spatially changes over the study area (see acoustic map Fig. 4.14) and therefore the TAF method is not able to represent the gas flux realistically by using a mean flux value (Q_C). Nevertheless, the TAF method seems to be an acceptable tool to visualize substantial changes in gas emission over time. On the other hand, the CAC method provides a localized comparison using common areas where flare information associated to the same area of each survey exist. Thus, results obtained from the CAC method (Q_{RF}) are more reliable in terms of flux comparison. In contrast, Q_{RF} values do not represent the gas emission of the entire area because these fluxes are associated to the much smaller common area. An argument that supports the use of a Q_{RF} value is that most survey-

related fluxes obtained from different overlapping hydroacoustic data (different survey combinations) show a tendency to be grouped around the mean Q_{RF} value (see Figs. 6.9 and 6.10; see standard deviation Figs. 6.14 and 6.15). From this it could be concluded wrongly that the area is homogeneously seeping gas; other acoustic maps show that this is not the case (Fig. 4.14). Therefore the tendency of flux values around the mean Q_{RF} value is interpreted as a result of the similarities in fluxes from common areas that are relatively close to each other or even overlap.

Results from Area 1 (Fig. 6.14) show that the mean flux from the common area method varies between 2 and 8 kg CH_4 yr^{-1} m^{-2}; the standard deviation is relatively moderate (0.6 to 1.4 kg CH_4 yr^{-1} m^{-2}). The variations illustrate that flux values fluctuate around a mean value of ~3 kg CH_4 yr^{-1} m^{-2} except for surveys S2 and S9 that show higher values. A moderate correlation between the average bottom water temperatures and fluxes has been observed (r^2: 0.55).

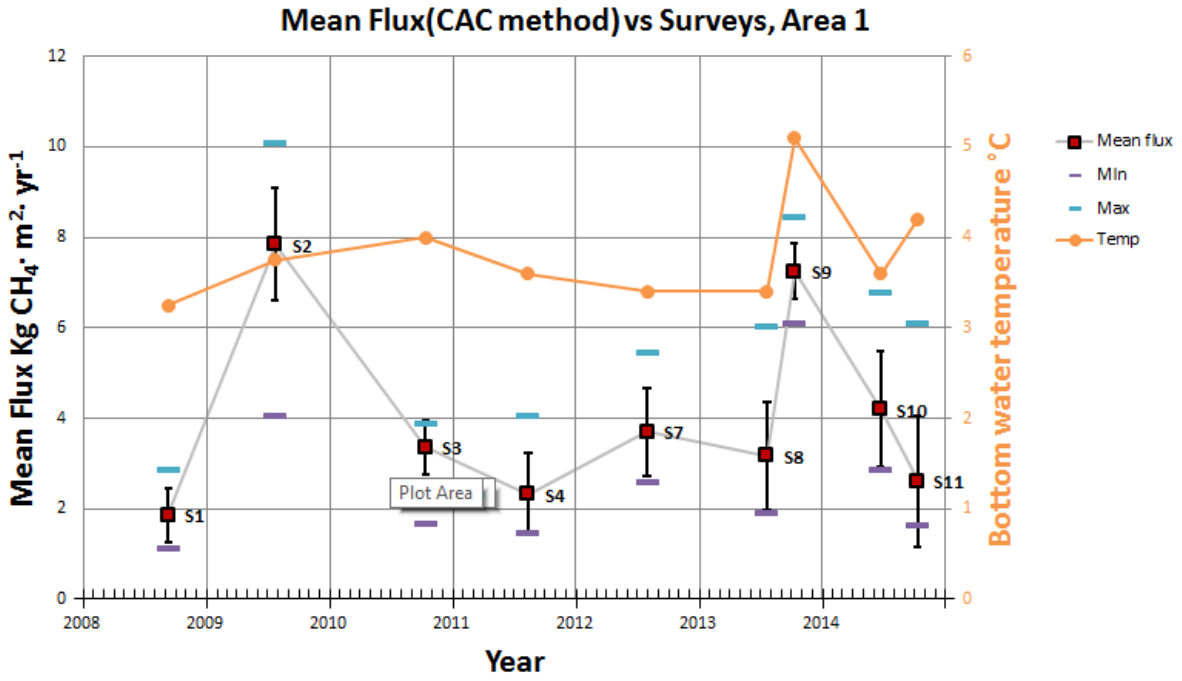

Figure 6.14. Temporal variability of the average Q_{RF} value (CAC method; Leifer "clean" BRSM) and water associated average water bottom temperature at Area 1. Additionally, the figure illustrates minimum, maximum and standard deviation size.

Mean flux results from Area 2 (Fig. 6.15) show values between 0.35 and 5.7 kg CH_4 yr^{-1} m^{-2} with a mean value of 1.7 kg CH_4 yr^{-1} m^{-2}. A peak in flux magnitude is observed for survey S4 accompanied with a higher standard deviation for Q_{RF} values obtained from common areas resulting from different survey combinations. The high standard deviation as a consequence of very different fluxes indicates that the common areas of survey S4 could be spatially separated from each other.

Unlike the calculated fluxes for S4, all other Q_{RF} values show a moderate standard deviation. Because of that, the correlation between temperature and fluxes was done without the S4 data and results show a moderate correlation of r^2 0.679.

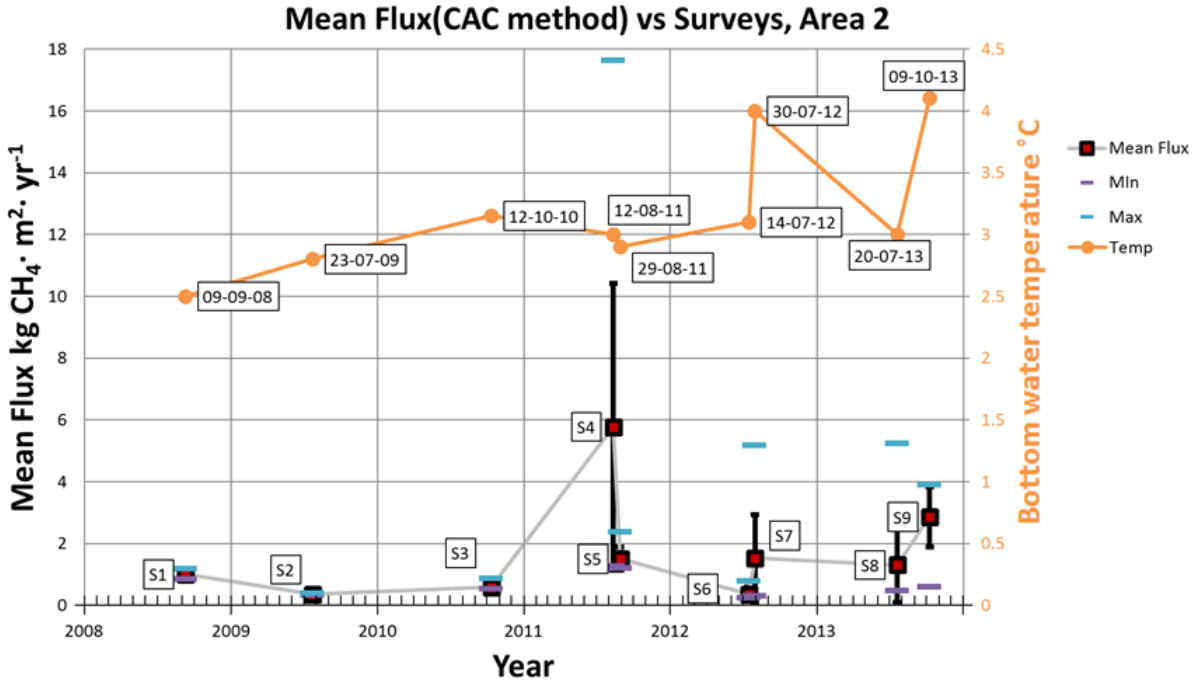

Figure 6.15. Temporal variability of the average Q_{RF} value (CAC method; Leifer "clean" BRSM) and water associated average water bottom temperature at Area 2. The figure includes minimum, maximum and a representative length of standard deviation.

For interpreting the results it is necessary to have a clear understanding about why methane release could change in time. We grouped the possible reasons according to the time scales on which they most likely occur.

- In general, gas release from seep site could be affected by changes of the hydrostatic pressure over the bubble outlet (the water depth). On short time scales gas release could thus be affected by pressure changes originated by e.g. tidal cycles or changing bottom currents. The influence of tidal cycles and currents over gas vents fluxes has been reported e.g. Boles et al. (2001), Joyce and Jewell, (2003) or Schneider von Deimling et al. (2010). Because our results are just 'snapshots' of gas release, it cannot be discarded that hydroacoustic flare data were acquired at times when the observed gas vents were under the influence of different static pressure. As such, the observed flux differences could be just a response of short term variability of ambient conditions and not originate from long term process such as gas hydrate destabilization induced by anthropogenic warming. It has been reported that the area is strongly affected by currents (Graves et al., 2015; Steinle et al., 2015) but it is unknown how strong their influence is on the gas bubble release. An influence of tidal cycles and currents in our results cannot be discarded. In order to visualize such influences on hour to week time scales it is necessary that observatories constantly monitor the gas release at the seafloor e. g. hydroacoustically (e.g. Greinert, 2008) or visually(e.g. Römer et al.,

2012b; Sauter et al., 2006)and that environmental conditions (static pressure, direction and magnitude of currents) are recorded as well.

- Results published by Berndt et al. (2014) indicate that seasonal temperature changes could have an influence in the methane released from Area 2 because of a seasonal migration of the TGHZ. At the same time flow rates at Area 1 could be influenced if both areas are sedimentologically connected allowing the migration of gas from Area 2 into Area 1. At Area 2, changes in gas flow rates would be expected to be associated to the seasonal formation and dissociation of shallow gas hydrates in the upper part of the sediment where the TGHZ seasonally migrates. The rate of already dissociating hydrates could be accelerated by the seasonal increase of temperature and therefore increase gas flow rates. Results show a moderate correlation between fluxes and temperature at Area 2 (Fig. 6.15). For both, Area 1 and Area 2, this moderate correlation does not allow to argue for a clear link between methane bubble release and seasonal changes in temperature. Again, a continuous observation e.g. carried out with a sideward-looking hydroacoustic observatory like GasQuant (Greinert 2008) would be appropriate to give more conclusive answers. To evaluate if there is any sub-seafloor connection between Area 1 and Area 2, mean Q_{RF} values from both areas need to be compared (Fig. 16). It becomes clear that Area 1 shows a higher release intensity (or flux) than Area 2 for the common areas. This should not be misinterpreted with the fact that Area 2 releases more gas than Area 1 because of its higher abundance of seeps (Table 6.9). A second observation is that increasing fluxes in Area 1 are accompanied by decreasing fluxes in Area 2 for surveys S1, S2, S3, S4 and S7. This highlights the possibility that both areas share the same gas source that either releases gas in Area 1 or Area 2. A probable explanation of the gas release alternation would be the existence of migration pathways that are blocked and opened maybe together with changes of the TGHZ. Migration pathways could become temporally permeable allowing gas to escape “earlier” in Area 2 closer to the TGHZ.

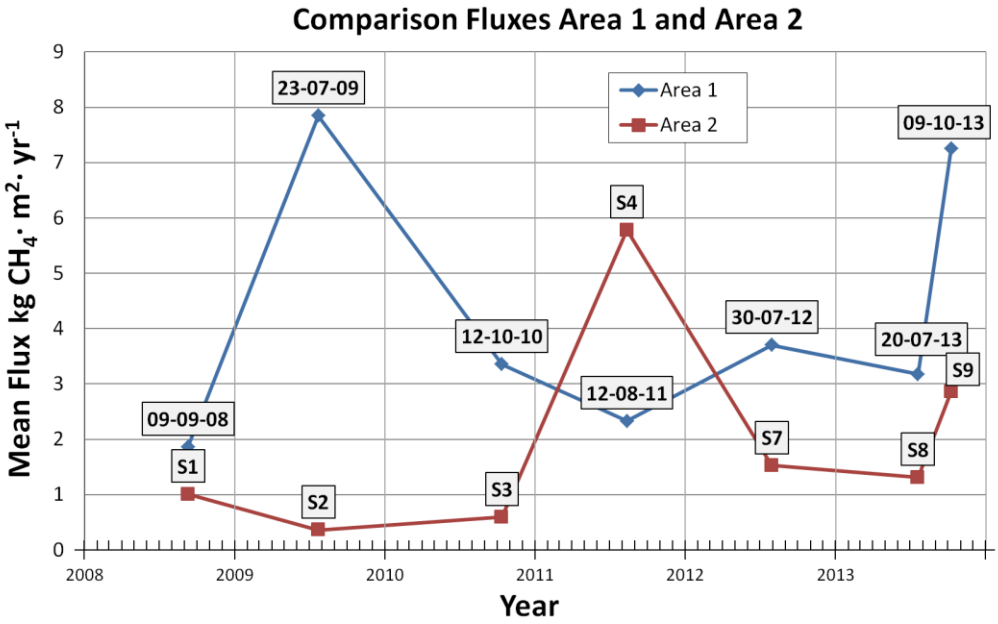

Figure 6.16. Graphical comparison of average Q_{RF} values between Area 1 and Area 2 for surveys containing flare-hydroacoustic information from both areas.

- For both Areas no increase or decrease trend in fluxes is visible over the 6 years of observation. It can be assumed that some of the processes that control the gas release (e.g. TGHZ long-term migration, average annual temperatures, tectonic changes processes) probably did change during the years of the surveys but not significantly. In addition it can be concluded that the source(s) of the seeping gas are not being depleted. Because shallow hydrates are sensitive to bottom water temperature changes, a much longer record (decades) is needed to see if and how increasing global temperature changes the bottom water around Svalbard and how this really influences the gas release at the TGHZ. At the same time, a long term observation could also reveal how increasing global temperatures could affect the methanogenesis in the deep and surface sediments.

CCC method results

The results of the CCC method (Figs. 6.11 and 6.12) are useful to illustrate how gas seepage intensity changes across the study area. This method is highly recommended for future spatio/temporal analysis of gas release when larger common areas with flare-related hydroacoustic information exist. Unfortunately this is not the case for our data set. The results also show that in most grid cells used for the comparison, independently of the absolute magnitude, fluxes follow a common increase/decrease pattern which correlates very well with CAC results. From this observation it can be deduced that the flux-strength spatial distribution does not change considerably through time. Some of the cells that belong to the spatial domain of the flare common areas show different flux variations and cannot be represented with an average pattern. A possible explanation is that some gas vents are intermittently active as a consequence of the formation/dissociation of shallow gas hydrates. This scenario has already been postulated for the PKF seep site area (Berndt et al., 2014). In order to proof the link between spatially different distribution fluxes and gas hydrate formation/dissociation again, a continuous hydroacoustic monitoring is required utilizing the capabilities of a permanent hydroacoustic observatory.

6.4.1.2. Spatial variability

No clear sign of bubble source displacements has been observed in the entire region. At Area 1, this observation supports the hypothesis that methane (free and dissolved gas) is coming from deep sources and migrates along a defined permeable pathway beneath an impermeable glacigenic debris flow (Rajan et al., 2012; Sarkar et al., 2012). At Area 2, no clear downward migration of the gas seepage associated with changes of the TGHZ could be found. However, the used data set is not sufficient enough to detect a gradual migration of the seepage locations over long-term because of the not complete hydroacoustic coverage of the seep site area and the lack of precision to visualize small spatial changes. Westbrook et al. (2009) hypothesized that a downward migration of the TGHZ was triggered by a 1°C increase of the bottom water temperature over ~30 years. Sarkar et al., (2012) modeled the migration of the TGHZ in response to the 1°C temperature variation and obtained a displacement from 370 to 410 m bsl. Our data cover only 7 years (2008-2014) which is considered a short period to detect a possible gradual migration of seepage linked to the gas hydrate destabilization. To prove or disprove a possible downward displacement again long term monitoring is recommended, in order to obtain comparable information;

acoustic surveys should be done during the same season and the areas insonified during each survey should be the same. To advance such an approach it is recommended to also use MBES information to have a complete coverage of the gassing seep sites in the mapped area. Additionally, MBESs give better resolution because of the smaller beam width (usually < 2°) when compared to common SBESs (normally ~7°). Annual complete mapping of the area with a multibeam system would allow a much better identification of potential seep migration at the seafloor. With parallel running SBES for flow rate quantifications and their link to the backscatter data of MBES systems, spatial changes could be rather exactly detected and quantified. Then, a new challenge could be the calibration of MBES using SBES.

Influences of seasonal temperature in the spatial migration of the TGHZ also need to be considered; an area that was not seeping at a certain time of the year could release gas in a warmer period due to seasonal formation and dissociation of shallow gas hydrates. In this respect, the evaluation of long term changes of gas release in a specific area using the comparison of annual fluxes should be carried out with hydroacoustic information acquired during the same season (ideally the late same months when bottom water and increased bottom water temperatures could migrate into the seabed. During the acquisition of the hydroacoustic surveys described in this thesis, this point could not be considered as data where acquired on cruises of opportunity.

6.4.1.3. Total flow rate

Comprehensive hydroacoustic information can reveal how much gas is being released into the water column. In the presented work the total flow rates range from ca. 2500 to ca. 4000 T CH_4 yr^{-1} for the entire region (region Fig. 6.2), assuming a continuous release of bubbles of 100% methane. For Area 1, Area 2, and Area 3 separately calculated flow rates are between 850 - 1300 T CH_4 yr^{-1}, 1600 - 2500 T CH_4 $yr^{-1}$and 450 - 700 T CH_4 yr^{-1}, respectively.

The results can be compared with results obtained in other studies of similar/the same seep areas (Table 6.10). A first comparison can be done with results published by Veloso et al. (2015; chapter 4) using the same hydroacoustic inverse method for calculating fluxes for a sub-area of Area 1. Differences in flow rates (~400-600 T CH_4 yr^{-1}; see Table 6.10) are attributed to the different area sizes and the higher number of hydroacoustic data sets (9 merged surveys) compared to only two surveys used by Veloso et al. (2015). A larger hydroacoustic dataset most likely has a wider coverage at the seafloor and seeps that were not mapped before can be included in the estimate. Therefore it can be expected that results given by this comprehensive data set better represent the amount of methane released at the study area than the previous calculations by Veloso et al. (2015). It is necessary to highlight that large errors can be introduced in flow rate estimations if the accuracy in acoustic flare positioning is low. A wrong positioning of acoustic flares could lead to flow rate overestimation as the same seep site could be multiple times considered in the flow rate calculation if its detected locations do not overlap. An additional error in our calculations is the possible transient formation of bubble vents e.g. due to changes of static pressure over the gas outlets. This temporal variability of gas bubble emissions on short time scale is neglected when the hydroacoustic information from different surveys is combined.

Flow rate values presented here can also be compared with results by Sahling et al. (2014) for the same study area; they used a combination of optical and acoustical observations to estimate flow rates

(Sahling et al. 2014 call flow rates flux in their paper). Their results are given for Area 2 and Area 3, which are regions comparable to Area 1 and Area 2 in this study. The here presented flow rates (~1075 T CH_4 yr^{-1} for Area 1 and ~2050 T CH_4 yr^{-1} for Area 2) are higher than the mean values of 433 T CH_4 yr^{-1} and 417 T CH_4 yr^{-1} obtained by Sahling et al. (2014). Despite that the mean flow rate in Area 1 is different to the obtained by Sahling et al. (2014), the value is still inside their uncertainty range. Differences can be attributed to the amount of hydroacoustic information related to gas release used to derive flow rates in both studies. While detected flares by Sahling et al., (2014) were acquired with a MBES, which has higher resolution than SBES, their data collection represents the release of just one survey. Methane seeps that are intermittent in time could not be considered in their quantification approach. Differences can also be a consequence of the extrapolation of flow rates from localized observations to the entire area. Total flow rates given by Sahling et al. (2014) are based on the extrapolation of localized bubble flow rates obtained from direct and visual techniques. As a result, extrapolated flow rates could be wrong in case hot spots with higher seepage intensity were not observed. In contrast, flow rate results presented here consider the total variability in seepage intensity of the seep area and despite the inverse methodology is less precise than direct/visual techniques the overall flow rate might be closer to reality,

Following, a set of bubble flow rate calculations at different study areas is presented to be compared with our calculations (Table 6.10). A general conclusion is that the calculated flow rates are within the same order of magnitude for similar places in the world where bubble seepage has been reported (Table 6.10).

Table 6.10. Flow rate results (considering a CH_4 molecular weight of =16.04 g/mol) for several seep sites located in the world for comparison

Annual Flow rate (T CH_4/yr)	**Water depth (mbsl)**	**Study area**	**Reference**
3250 (2500-4000)	67-410	PKF Total area (Fig.6.2)	This study
1075 (850 -1300)	193-352	PKF Area 1	This study
2050 (1600 -2500)	194-410	PKF Area 2	This study
575 (450 - 700)	67-117	PKF Area 3	This study
440 -675	~240	PKF 78°38'30''-78°40'N; 9°23'-9°28' E	Veloso et al., 2015
433 (80-1090)	240-245	PKF Area 2 (comparable to Area 1 in this article)	Sahling et al., 2014
417 (64-802)	380-390	PKF Area 3 (comparable to Area 2 in this article)	Sahling et al., 2014
304	1250–1270	Håkon Mosby Mud Volcano–all three emission sites	Sauter et al., 2006
32-1395	890	Kerch Flare, Black Sea	Römer et al., 2012a
21.9	600–700	Northern summit of Hydrate Ridge, offshore Oregon	Torres et al., 2002
24	65–75	Tommeliten field, North Sea	Schneider von Deimling et al., 2011
641.6 (±513.28)	575–2870	Makran continental margin (50 km broad segment)	Römer et al., 2012b
3.6892 to 36.892	1690	Carbonate slab, Nile Deep Sea Fan	Römer et al., 2014

6.4.2. Sources of error

6.4.2.1. Inverse method, data quality and processing

Applying the inverse method of Veloso et al. (2015) a prominent error in the flow rate estimate can be introduced by a wrong bubble size distribution (BSD). Our video observations correspond to only two surveys (S2 and S3) and the collected footage contains only partial information of the total amount of gas vents in the study area. We realize that assuming a unique BSD increase the uncertainty in our results. A relative error of ~± 60 % in flow rate estimates was reported by Veloso et al., (2015; chapter 4), which shows that the inverse method is highly sensitive to the BSD. This can be explained by the strong backscattering-bubble size dependence of the acoustical cross-section model for single bubbles (Thuraisingham, 1997) embedded in the inverse method. It is recommended to collect high quality visual information of bubble sizes in order to decrease the error in flow rate estimates.

Noise and reverberation are additional error sources due to the overlap with the backscattering of bubbles, resulting in inaccurate target strength (TS) values. Veloso et al. (2015; chapter 4) reported a relative error of ~± 26 % in the flow rate when the average TS of an acoustic flare source has an uncertainty of ± 1 dB. The presence of fish in the study area has been confirmed visually and acoustically. It is therefore highly probable that there is a degree of overlap between backscattering caused by fish and by bubbles (Fig. 4.1). In addition, noise coming from the vessel (periodical) has been clearly observed in echograms, in many cases overlapping with acoustic flares. In light of these problems it should be pointed out that data acquired in the future should be of very high quality meaning that artificial noise should be avoided as much as possible (diminish vessel noise by steaming slowly, shut off additional hydroacoustic and seismic systems). Better techniques for data cleaning and filtering still have to be developed to diminish the influence of noise and reverberation (e.g. removing backscattering from fish).

Multiple scattering effects (e.g. Foldy 1945; Carey and Roy 1993; Prosperetti et al. 1993) have not been included in the inverse hydroacoustic method but should be considered as a possible error source. However this can only be evaluated in a future experimental validation of the inverse method by artificially create a bubble stream of which the BSD and flow rates can be adjusted under controlled conditions and SBES surveys are undertaken with great care.

According to the BSD and the classification of Amaya-Bower and Lee (2010), bubbles in the study area are in the ellipsoidal regime when they are rising. Because of this the used model of a single spherical bubble by Thuraisingham (1997) could be considered an additional error source. It is possible to correct for this error by modifying the current inverse method by incorporating backscattering predictions from ellipsoidal bubbles (Strasberg, 1953; Stanton, 1989; Feuillade and Werby, 1994; Leblond et al., 2014). An additional error related to the bubble backscattering model is that it is designed for bubbles in free-field and not for bubbles close to a boundary, here the seafloor. Some researchers concluded that boundaries have a direct influence in the scattering cross-section of the bubble (e.g. Gaunaurd, 1995; Maksimov et al., 2014).

It is further important to highlight that the bubble model does not consider bubbles that are hydrate-coated. At many other study areas bubbles rise through the GHSZ, allowing the formation of a hydrate

skin around the bubble (e.g. Greinert et al., 2006; Rehder et al., 2002 and 2009; Römer et al., 2012b; Smith et al., 2014). It is known that a hydrate skin has a direct influence on the bubble stiffness and therefore the acoustical backscattering of a hydrate-coated bubble is expected to be different than that of one without a hydrate skin (Church, 1995; Maksimov and Sosedko, 2005). In the present work, all flow rate calculations assumed that the bubbles where outside the GHSZ regime. For Area 2 this could be an extra source of error.

Finally, an additional source of error included in our estimates is related to the content of methane in the bubble. Our assumption of bubbles completely full of methane (100 %) has been based on few observations (Sahling et al., 2014); our estimates of the total carbon content might not be correct in case the content of the bubble differs from site to site.

6.4.2.2. Flare Clustering

Clustering was carried out considering acoustic flares with overlapped footprints (see clustering method chapter 4). This was done in order to obtain representative information of the same seep site when insonified multiple times (at least two times). Here, we define as a seep site, an area with multiple bubble streams where streams are close to each other. The bubble streams themselves do not need to have the same or even similar flow rates. An additional error is thus introduced when it is assumed that the entire cluster can be represented with one mean flux value.

6.4.2.3. Method Comparison

Generally errors can be introduced by the instrumentation used to observe the phenomena of interest. With respect to remote (ship-based) hydroacoustic bubble mapping the greatest problem is that the resolution of the system (echosounder footprint) is not sufficient (small enough) to observe individual bubble vents/streams in a large bubble releasing area. SBES cannot distinguish if the derived flow rate from an acoustic flare is produced by one or multiple bubble streams. Moreover, under those conditions of multiple release spots echosounders are not able to define an accurate position of the bubble stream outlets. Under these conditions, a temporal variability evaluation of bubble flow rate would be possible only if the insonified area at the seafloor is 'strictly' the same. This is very difficult to accomplish at open sea when a vessel is under the influence of wind and waves (motion during data acquisition) and when only limited time is available to complete a hydroacoustic survey. Experience shows that even planning the same ship track, the hydroacoustically covered areas on the seafloor are most of the time different. Data presented were collected by several scientific groups and surveys were planned and conducted in different ways. As a consequence the data collection shows different hydroacoustic coverage between years which makes it not possible to compare flow rates among surveys. On the other hand, different hydroacoustic coverage at the seafloor possibly allows for a better flow rate estimate of the entire region when data are merged for the final calculation.

To overcome the problems when comparing different survey results , the first attempt using the TAF method was based on the temporal analysis of the average 'fluxes' per year, with the average fluxes represented by the total annual flow rate divided by the total area containing hydroacoustic flare information (eq. [1]). This comparison becomes 'logical' in case the flux does not change considerably in space, being a mean flux a representative value of the complete analyzed area (e.g. Area 1 or Area 2)

even when the comparison involves surveys with different hydroacoustic coverage. It becomes clear that the TAF comparison only gives correct results if the area releases gas homogeneously or in other words, if bubble streams are uniformly distributed in space and have similar bubble release intensities. Unfortunately the hydroacoustic evidence does not support a homogeneous emission of bubbles for Area 1 and Area 2. From acoustics maps of Area1 (Figs. 4.13c and 4.13d), it is easy to understand that hot spots exist where the bubble release intensity is higher than in other places. Using the CAC method it is also possible to visualize differences in Q_{RF} values from the same survey (Fig. 6.10; strong standard deviation at S4, Fig. 6.15) associated to the spatial variability of bubble flux intensities. The latter is also supported by the CCC method (Figs. 6.10 and 6.11) that shows different flux values in different locations of a common area obtained from different surveys. Based on this it can be concluded that the TAF method is useful to visualize 'significant' changes in fluxes over time and large areas but it is not the appropriate method to evaluate the temporal variability of fluxes in the study area.

It was not possible to find a larger and continuous area with identical hydroacoustic coverage between several or even two surveys. However, common areas that have been insonified up to 6 times during different years exist. The CAC method was based on the analysis of these common areas with the smallest area with hydroacoustic flare information (SBES resolution) represented by the footprint at the seafloor where a flare was detected. This emphasizes that the real position of the bubble stream(s) generating the flare is/are unknown; it is only known that the bubbles are released from within the delimited area, the footprint coverage. However, a common area could be smaller than a footprint at the seafloor as the common area forms if at least two footprints with flare information partially overlap (Fig. 6.17). As described in section 6.4 the temporal variability analysis of gas emissions using common areas was done by calculating the Q_{RF} value.

A general error is that it is not possible to assign a flux to a process that is not homogeneously distributed. A flux represents the transport of a quantity (here methane) per time over an area when the entire area is carrying out this transport. A bubble stream is coming from a discrete outlet (the vent) at the seafloor and therefore it is not appropriate to assign its flow rate to an area to derive a flux. Unfortunately there is no other choice to temporally compare the hydroacoustic information presented in this study which is the reason why a flux value was introduced. This value was an approximated flux (volumetric or in mass) calculated by normalizing the flow rate of an acoustic flare with the footprint area at the depth the flare was detected. Then, a 'false' but useful assumption is that each piece of the footprint contributes with a certain amount of gas to the total flow rate can be made. This approximation does not correctly represent the bubble release phenomena and evidently is a source of error. Despite that, the approximation can be used to detect 'considerable' variability in gas emissions over time in the common areas. To illustrate the error introduced by this approximation one could think about two acoustics flares captured during different surveys with their footprints partially overlapping. Such an example is shown in Fig. 6.17 where the common area has different fluxes from each survey. In this example the common area fluxes of the two surveys are assumed to be different, which could be a wrong conclusion in case bubble streams did not change in time (same flow rate and position). The reason for assuming different fluxes is that because the footprint during the second survey covers a

higher number of bubble streams than the footprint during the first survey. This source of error inevitably is introduced in all three comparison methods presented in this study.

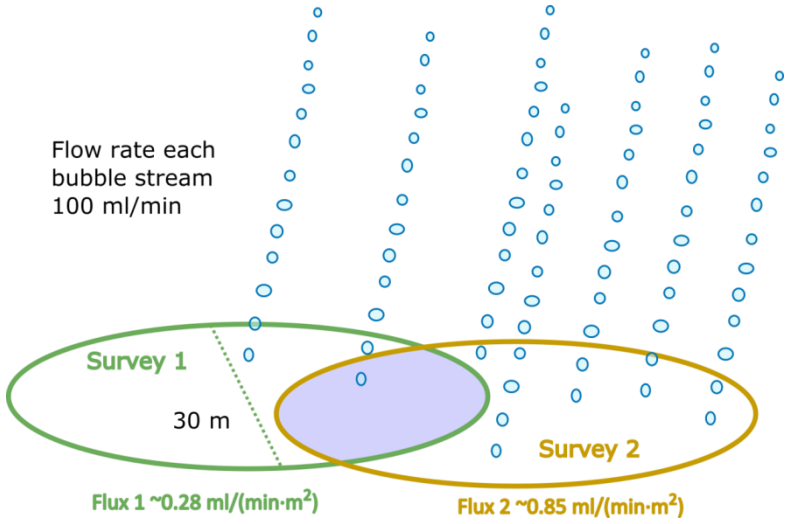

Figure 6.17. Example to illustrate error induced by normalizing flow rates to an area (flux) and using CAC method

6.4.2.4. Continuous vs. seasonal gas release

An additional uncertainty is that flow rates are considered stable over short time (e.g. hours, days, months). As mentioned before, bubble release from seep sites can strongly depend on environmental conditions as tides, wave height, currents, etc. (e.g. Boles et al., 2001; Joyce and Jewell, 2003; Schneider von Deimling et al., 2010). Different flux results were obtained for surveys carried out during the same year and one explanation for this would be that gas emissions change seasonally e.g. if they are linked to the water temperature changes. Under such conditions it is necessary to highlight that an annual flux value is just an approximation of the real amount of gas released from the area.

6.4.3. Future hydroacoustics survey planning (recommendations summary)

It is clear that using SBES for flare monitoring is challenging when the gas release is distributed over a large area because of the SBES coverage capabilities are limited and thus the time required to carry out a complete hydroacoustic survey is high. As a consequence, just partial information of the total area related to gas release can usually be acquired. Because of this it is highly recommended to follow the same survey plan repeatable in time in order to obtain comparable information. This plan should be optimized to be time efficient (covering the most intense area not necessarily resulting in full coverage), and it should include measures to acquire high quality data. Based on the gained experience during this work, we propose some recommendations for future hydroacoustic surveys related to submarine gas release.

- Incorporation of MBESs for water column scanning in the hydroacoustic survey. MBESs have high resolution and are able to cover large areas in a short period of time allowing then a complete overview of the seeps distributed over the area.

- Use of calibrated SBES for gas flow rate quantification through inverse methods.
- Repetition of tracks surveyed in order to obtain comparable hydroacoustic information (same insonified area).
- Hydroacoustic cross-track recording over seep sites (e.g. at hot spots) to diminish the instrumental error in flow rate estimates.
- Definition of vessel speed limits to morphologically differentiate gas release from other scatterers in SBES echograms. Speeds should be defined according to the seabed depth and the beam width of the echosounder.
- Execution of hydroacoustic surveys under similar environmental conditions (e.g. tidal cycles, seasonal temperature and currents) for flux comparison in case gas release is strongly controlled by these environmental parameters.
- Acquisition of hydroacoustic information from different seasons within a year to understand how i dynamic gas release is under the influence of seasonal changes of ambient parameters (e.g. temperature
- Motion compensation and static offsets corrections of hydroacoustic data for accurate positioning of acoustic flares.
- Reduction of artificial noise to improve the quality of the collected data.
- Optical observations of seep sites for physical characterization of the bubble release (e.g. BSD, BRS, bubble shapes, bubble composition).
- Use of observatories with horizontally looking hydroacoustic systems (e.g. Greinert, 2008) for a continuous observation of gas release.

6.5. Conclusions

Due to the lack of hydroacoustic data recorded at exactly the same area, a direct and unbiased flow rate comparison over time was not possible to achieve. As a consequence, three methods have been elaborated to overcome this shortcoming, which is a general problem for all so far undertaken temporal analysis of submarine gas release. The three comparison methods introduce the term ‘flux’ by associating the calculated flow rate to an area in three different ways; this is to find a value that has been derived in a certain way over time for a specific area and thus can be compared. According to the presented data set the CAC method seems to be the best method to carry out the temporal analysis.

The two investigated areas show fluctuations in fluxes between the time periods when surveys were carried out, but no clear trend towards increased seepage is observed. Because of the limited length of time, it is not possible to discard or prove that anthropogenic influence of global warming could lead to an accelerated dissociation of gas hydrates in the future. As hydroacoustic information is only a ‘snapshot’ in time, it is concluded that observed flux changes can be in general attributed to a) short time variations of ambient conditions as pressure changes over the gas vents due to currents and tidal cycles, b) blocking and opening of gas conduits due to seasonal formation and dissociation of shallow gas hydrates (linked to seasonal changes in bottom water temperature), c) dissociation of shallow hydrates related to water temperature changes induced by anthropogenic global warming, d) variability

in geological migration pathways of gas driven by unknown sub-seabed structural changes. From our results it can also be concluded that the gas supplying reservoir is not depleting to a measurable extent.

No evidence of displacements of the gas/bubbles sources has been detected in the region. At Area 1, this supports the hypothesis that methane is coming from deep sources and migrates along defined permeable pathways (Rajan et al., 2012; Sarkar et al., 2012). At Area 2, a pronounced downward migration of the TGHZ has not been observed. Small TGHZ displacements are not detectable due to limitations of our data resolution and different coverage between surveys.

Results derived from the CCC method clearly show that the seepage intensity changes in space meaning that large areas are not represented by a 'unique' mean flux value. From the same results it is also concluded that the spatial distribution of the seepage intensity follows a similar rising/decreasing pattern of gas fluxes over time. This observation is only valid for the common areas involved in the comparison.

By merging hydroacoustic information from different surveys it was possible to estimate the total flow rates of the seep areas considered. Derived flow rates are higher than gas estimates carried out using direct/visual techniques in the same study area. Assuming no errors in our calculations, flow rate differences could be attributed to: a) a more complete hydroacoustic data set than the one survey used by Sahling et al. (2014); b) observations that are missing hot spots with higher flow rates in the extrapolations carried out by Sahling et al. (2014). It is shown that our flow rates are comparable to estimates from similar seep site areas located in other parts of the world.

We conclude that the use of SBES for studying the spatio/temporal analysis of submarine gas release can be a powerful tool in case it is used properly. The challenge in this study was to make flare-hydroacoustic data comparable from one survey to the other due to partial and different hydroacoustic coverage between surveys. It is recommended to keep an optimized-repeatable plan for future surveys in order to improve the data comparability (hydroacoustic data coming from the same insonified area). Additionally, complementary systems such as MBES should be included in future surveys to overcome the SBES limitations associated to the hydroacoustic coverage, time consumption and seafloor resolution. Nevertheless, SBES are the tool of choice when it comes to gas flux quantification.

References

Amaya-Bower, L., Lee, T., 2010. Single bubble rising dynamics for moderate Reynolds number using Lattice Boltzmann Method. Comput. Fluids 39, 1191–1207. doi:10.1016/j.compfluid.2010.03.003

Artemov, Y.G., Egorov, V.N., Polikarpov, G.G., Gulin, S.B., 2007. Methane emission to the hydro-and atmosphere by gas bubble streams in the Dnieper paleo-delta, the Black Sea. Morskyji ehkologichnyji zhurnal (Marine Ecological Journal) 6, 5–26.

Berndt, C., Feseker, T., Treude, T., Krastel, S., Liebetrau, V., Niemann, H., Bertics, V.J., Dumke, I., Dünnbier, K., Ferré, B., Graves, C., Gross, F., Hissmann, K., Hühnerbach, V., Krause, S., Lieser, K., Schauer, J., Steinle, L., 2014. Temporal Constraints on Hydrate-Controlled Methane Seepage off Svalbard. Science 343, 284–287. doi:10.1126/science.1246298

Biastoch, A., Treude, T., Rüpke, L.H., Riebesell, U., Roth, C., Burwicz, E.B., Park, W., Latif, M., Böning, C.W., Madec, G., Wallmann, K., 2011. Rising Arctic Ocean temperatures cause gas hydrate

destabilization and ocean acidification. Geophys. Res. Lett. 38, L08602. doi:10.1029/2011GL047222

Boles, J.R., Clark, J.F., Leifer, I., Washburn, L., 2001. Temporal variation in natural methane seep rate due to tides, Coal Oil Point area, California. J. Geophys. Res. Oceans 106, 27077–27086. doi:10.1029/2000JC000774

Brothers, L.L., Dover, C.L.V., German, C.R., Kaiser, C.L., Yoerger, D.R., Ruppel, C.D., Lobecker, E., Skarke, A.D., Wagner, J.K.S., 2013. Evidence for extensive methane venting on the southeastern U.S. Atlantic margin. Geology 41, 807–810. doi:10.1130/G34217.1

Carey, W.M., Roy, R.A., 1993. Sound Scattering from Microbubble Distributions Near the Sea Surface, in: Ellis, D.D., Preston, J.R., Urban, H.G. (Eds.), Ocean Reverberation. Springer Netherlands, pp. 25–43.

Church, C.C., 1995. The effects of an elastic solid surface layer on the radial pulsations of gas bubbles. J. Acoust. Soc. Am. 97, 1510–1521. doi:10.1121/1.412091

Ferré, B., Mienert, J., Feseker, T., 2012. Ocean temperature variability for the past 60 years on the Norwegian-Svalbard margin influences gas hydrate stability on human time scales. J. Geophys. Res. Oceans 117, C10017. doi:10.1029/2012JC008300

Feuillade, C., Werby, M.F., 1994. Resonances of deformed gas bubbles in liquids. J. Acoust. Soc. Am. 96, 3684–3692. doi:10.1121/1.410558

Foldy, L.L., 1945. The Multiple Scattering of Waves. I. General Theory of Isotropic Scattering by Randomly Distributed Scatterers. Phys. Rev. 67, 107–119. doi:10.1103/PhysRev.67.107

Gaunaurd, G.C., 1995. Acoustic scattering by an air-bubble near the sea surface. IEEE J. Ocean. Eng. 20, 285–292. doi:10.1109/48.468243

Graves, C.A., Steinle, L., Rehder, G., Niemann, H., Connelly, D.P., Lowry, D., Fisher, R.E., Stott, A.W., Sahling, H., James, R.H., 2015. Fluxes and fate of dissolved methane released at the seafloor at the landward limit of the gas hydrate stability zone offshore western Svalbard. J. Geophys. Res. Oceans 120, 6185–6201. doi:10.1002/2015JC011084

Greinert, J., 2008. Monitoring temporal variability of bubble release at seeps: The hydroacoustic swath system GasQuant. J. Geophys. Res. Oceans 113, C07048. doi:10.1029/2007JC004704

Greinert, J., Artemov, Y., Egorov, V., De Batist, M., McGinnis, D., 2006. 1300-m-high rising bubbles from mud volcanoes at 2080 m in the Black Sea: Hydroacoustic characteristics and temporal variability. Earth Planet. Sci. Lett. 244, 1–15. doi:10.1016/j.epsl.2006.02.011

Greinert, J., Lewis, K.B., Bialas, J., Pecher, I.A., Rowden, A., Bowden, D.A., De Batist, M., Linke, P., 2010. Methane seepage along the Hikurangi Margin, New Zealand: Overview of studies in 2006 and 2007 and new evidence from visual, bathymetric and hydroacoustic investigations. Mar. Geol. 272, 6–25. doi:10.1016/j.margeo.2010.01.017

Heeschen, K.U., Collier, R.W., de Angelis, M.A., Suess, E., Rehder, G., Linke, P., Klinkhammer, G.P., 2005. Methane sources, distributions, and fluxes from cold vent sites at Hydrate Ridge, Cascadia Margin. Glob. Biogeochem. Cycles 19, GB2016. doi:10.1029/2004GB002266

Jerram, K., Weber, T.C., Beaudoin, J., 2015. Split-beam echo sounder observations of natural methane seep variability in the northern Gulf of Mexico. Geochem. Geophys. Geosystems 16, 736–750. doi:10.1002/2014GC005429

Joyce, J., Jewell, P.W., 2003. Physical Controls on Methane Ebullition from Reservoirs and Lakes. Environ. Eng. Geosci. 9, 167–178. doi:10.2113/9.2.167

Kannberg, P.K., Tréhu, A.M., Pierce, S.D., Paull, C.K., Caress, D.W., 2013. Temporal variation of methane flares in the ocean above Hydrate Ridge, Oregon. Earth Planet. Sci. Lett. 368, 33–42. doi:10.1016/j.epsl.2013.02.030

Kvenvolden, K.A., 1988. Origins of Methane in the Earth Methane hydrate — A major reservoir of carbon in the shallow geosphere? Chem. Geol. 71, 41–51. doi:10.1016/0009-2541(88)90104-0

Leblond, I., Scalabrin, C., Berger, L., 2014. Acoustic monitoring of gas emissions from the seafloor. Part I: quantifying the volumetric flow of bubbles. Mar. Geophys. Res. 35, 191–210. doi:10.1007/s11001-014-9223-y

Leifer, I., Patro, R.K., 2002. The bubble mechanism for methane transport from the shallow sea bed to the surface: A review and sensitivity study. Cont. Shelf Res. 22, 2409–2428. doi:10.1016/S0278-4343(02)00065-1

Leifer, I., Patro, R.K., Bowyer, P., 2000. A Study on the Temperature Variation of Rise Velocity for Large Clean Bubbles. J. Atmospheric Ocean. Technol. 17, 1392–1402. doi:10.1175/1520-0426(2000)017<1392:ASOTTV>2.0.CO;2

Maksimov, A.O., Burov, B.A., Salomatin, A.S., Chernykh, D.V., 2014. Sounds of marine seeps: A study of bubble activity near a rigid boundary. J. Acoust. Soc. Am. 136, 1065–1076. doi:10.1121/1.4892753

Maksimov, A.O., Sosedko, E.V., 2005. Dynamics of sea bubbles covered by a hydrate skin. Presented at the XVI Session of the Russian Acoustical Society, Moscow.

McGovern, C., 2012. Video-based quantification of gas bubble fluxes from the seafloor offshore western Svalbard (Msc. thesis). Univ. of Bremen.

Mendelson, H.D., 1967. The prediction of bubble terminal velocities from wave theory. AIChE J. 13, 250–253. doi:10.1002/aic.690130213

Milkov, A.V., 2004. Global estimates of hydrate-bound gas in marine sediments: how much is really out there? Earth-Sci. Rev. 66, 183–197. doi:10.1016/j.earscirev.2003.11.002

Naudts, L., Greinert, J., Artemov, Y., Staelens, P., Poort, J., Van Rensbergen, P., De Batist, M., 2006. Geological and morphological setting of 2778 methane seeps in the Dnepr paleo-delta, northwestern Black Sea. Mar. Geol. 227, 177–199. doi:10.1016/j.margeo.2005.10.005

Nikolovska, A., Sahling, H., Bohrmann, G., 2008. Hydroacoustic methodology for detection, localization, and quantification of gas bubbles rising from the seafloor at gas seeps from the eastern Black Sea: HYDROACOUSTIC GAS QUANTIFICATION. Geochem. Geophys. Geosystems 9, n/a–n/a. doi:10.1029/2008GC002118

Ostrovsky, I., 2009. Hydroacoustic assessment of fish abundance in the presence of gas bubbles. Limnol. Oceanogr. Methods 7, 309–318. doi:10.4319/lom.2009.7.309.

Prosperetti, A., 1977. Thermal effects and damping mechanisms in the forced radial oscillations of gas bubbles in liquids. J. Acoust. Soc. Am. 61, 17–27. doi:10.1121/1.381252

Rajan, A., Mienert, J., Bünz, S., 2012. Acoustic evidence for a gas migration and release system in Arctic glaciated continental margins offshore NW-Svalbard. Mar. Pet. Geol. 32, 36–49. doi:10.1016/j.marpetgeo.2011.12.008

Rehder, G., Brewer, P.W., Peltzer, E.T., Friederich, G., 2002. Enhanced lifetime of methane bubble streams within the deep ocean. Geophys. Res. Lett. 29, 21–1. doi:10.1029/2001GL013966

Rehder, G., I. Leifer, P. G. Brewer, G. Friederich, and E. T. Peltzer. 2009. Controls on methane bubble dissolution inside and outside the hydrate stability field from open ocean field experiments and numerical modeling. Mar. Chem. 114:19-30, [doi:10.1016/j.marchem.2009.03.004]

Römer, M., Sahling, H., Pape, T., Bahr, A., Feseker, T., Wintersteller, P., Bohrmann, G., 2012a. Geological control and magnitude of methane ebullition from a high-flux seep area in the Black Sea—the Kerch seep area. Mar. Geol. 319–322, 57–74. doi:10.1016/j.margeo.2012.07.005

Römer, M., Sahling, H., Pape, T., Bohrmann, G., Spieß, V., 2012b. Quantification of gas bubble emissions from submarine hydrocarbon seeps at the Makran continental margin (offshore Pakistan). J. Geophys. Res. Oceans 117, C10015. doi:10.1029/2011JC007424

Römer, M., Sahling, H., Pape, T., dos Santos Ferreira, C., Wenzhöfer, F., Boetius, A., Bohrmann, G., 2014. Methane fluxes and carbonate deposits at a cold seep area of the Central Nile Deep Sea Fan, Eastern Mediterranean Sea. Mar. Geol. 347, 27–42. doi:10.1016/j.margeo.2013.10.011

Sahling, H., Römer, M., Pape, T., Bergès, B., dos Santos Fereirra, C., Boelmann, J., Geprägs, P., Tomczyk, M., Nowald, N., Dimmler, W., Schroedter, L., Glockzin, M., Bohrmann, G., 2014. Gas emissions at the continental margin west off Svalbard: mapping, sampling, and quantification. Biogeosciences Discuss. 11, 7189–7234. doi:10.5194/bgd-11-7189-2014

Sarkar, S., Berndt, C., Minshull, T.A., Westbrook, G.K., Klaeschen, D., Masson, D.G., Chabert, A., Thatcher, K.E., 2012. Seismic evidence for shallow gas-escape features associated with a retreating gas hydrate zone offshore west Svalbard. J. Geophys. Res. Solid Earth 117, B09102. doi:10.1029/2011JB009126

Sauter, E.J., Muyakshin, S.I., Charlou, J.-L., Schlüter, M., Boetius, A., Jerosch, K., Damm, E., Foucher, J.-P., Klages, M., 2006. Methane discharge from a deep-sea submarine mud volcano into the upper water column by gas hydrate-coated methane bubbles. Earth Planet. Sci. Lett. 243, 354–365. doi:10.1016/j.epsl.2006.01.041

Schneider von Deimling, J., Brockhoff, J., Greinert, J., 2007. Flare imaging with multibeam systems: Data processing for bubble detection at seeps. Geochem. Geophys. Geosystems 8, Q06004. doi:10.1029/2007GC001577

Schneider von Deimling, J., Greinert, J., Chapman, N.R., Rabbel, W., Linke, P., 2010. Acoustic imaging of natural gas seepage in the North Sea: Sensing bubbles controlled by variable currents. Limnol. Oceanogr. Methods 8, 155–171. doi:10.4319/lom.2010.8.155

Schneider von Deimling, J., Rehder, G., Greinert, J., McGinnnis, D.F., Boetius, A., Linke, P., 2011. Quantification of seep-related methane gas emissions at Tommeliten, North Sea. Cont. Shelf Res. 31, 867–878. doi:10.1016/j.csr.2011.02.012

Shakhova, N., Semiletov, I., Leifer, I., Sergienko, V., Salyuk, A., Kosmach, D., Chernykh, D., Stubbs, C., Nicolsky, D., Tumskoy, V., Gustafsson, Ö., 2014. Ebullition and storm-induced methane release from the East Siberian Arctic Shelf. Nat. Geosci. 7, 64–70. doi:10.1038/ngeo2007

Shakhova, N., Semiletov, I., Salyuk, A., Yusupov, V., Kosmach, D., Gustafsson, Ö., 2010. Extensive Methane Venting to the Atmosphere from Sediments of the East Siberian Arctic Shelf. Science 327, 1246–1250. doi:10.1126/science.1182221

Smith, A.J., Mienert, J., Bünz, S., Greinert, J., 2014. Thermogenic methane injection via bubble transport into the upper Arctic Ocean from the hydrate-charged Vestnesa Ridge, Svalbard. Geochem. Geophys. Geosystems 15, 1945–1959. doi:10.1002/2013GC005179

Stanton, T.K., 1989. Simple approximate formulas for backscattering of sound by spherical and elongated objects. J. Acoust. Soc. Am. 86, 1499–1510. doi:10.1121/1.398711

Steinle, L., Graves, C.A., Treude, T., Ferré, B., Biastoch, A., Bussmann, I., Berndt, C., Krastel, S., James, R.H., Behrens, E., Böning, C.W., Greinert, J., Sapart, C.-J., Scheinert, M., Sommer, S., Lehmann, M.F., Niemann, H., 2015. Water column methanotrophy controlled by a rapid oceanographic switch. Nat. Geosci. 8, 378–382. doi:10.1038/ngeo2420

Strasberg, M., 1953. The Pulsation Frequency of Nonspherical Gas Bubbles in Liquids. J. Acoust. Soc. Am. 25, 536–537. doi:10.1121/1.1907076

Thuraisingham, R.A., 1997. New expressions of acoustic cross-sections of a single bubble in the monopole bubble theory. Ultrasonics 35, 407–409. doi:10.1016/S0041-624X(97)00021-8

Torres, M.E., McManus, J., Hammond, D.E., de Angelis, M.A., Heeschen, K.U., Colbert, S.L., Tryon, M.D., Brown, K.M., Suess, E., 2002. Fluid and chemical fluxes in and out of sediments hosting methane hydrate deposits on Hydrate Ridge, OR, I: Hydrological provinces. Earth Planet. Sci. Lett. 201, 525–540. doi:10.1016/S0012-821X(02)00733-1

Veloso, M., Greinert, J., Mienert, J., De Batist, M., 2015. A new methodology for quantifying bubble flow rates in deep water using splitbeam echosounders: Examples from the Arctic offshore NW-Svalbard: Quantifying bubble flow rates in deep water. Limnol. Oceanogr. Methods 13, 267–287. doi:10.1002/lom3.10024

Wallmann, K., Pinero, E., Burwicz, E., Haeckel, M., Hensen, C., Dale, A., Ruepke, L., 2012. The Global Inventory of Methane Hydrate in Marine Sediments: A Theoretical Approach. Energies 5, 2449–2498. doi:10.3390/en5072449

Weber, T.C., Mayer, L., Jerram, K., Beaudoin, J., Rzhanov, Y., Lovalvo, D., 2014. Acoustic estimates of methane gas flux from the seabed in a 6000 km 2 region in the Northern Gulf of Mexico. Geochem. Geophys. Geosystems 15, 1911–1925. doi:10.1002/2014GC005271

Wessel, P., Smith, W.H.F., Scharroo, R., Luis, J., Wobbe, F., 2013. Generic Mapping Tools: Improved Version Released. Eos Trans. Am. Geophys. Union 94, 409–410. doi:10.1002/2013EO450001

Westbrook, G.K., Thatcher, K.E., Rohling, E.J., Piotrowski, A.M., Pälike, H., Osborne, A.H., Nisbet, E.G., Minshull, T.A., Lanoisellé, M., James, R.H., Hühnerbach, V., Green, D., Fisher, R.E., Crocker, A.J., Chabert, A., Bolton, C., Beszczynska-Möller, A., Berndt, C., Aquilina, A., 2009. Escape of methane gas from the seabed along the West Spitsbergen continental margin. Geophys. Res. Lett. 36, L15608. doi:10.1029/2009GL039191

Woolf, D.K., 1993. Bubbles and the air-sea transfer velocity of gases. Atmosphere-Ocean 31, 517–540. doi:10.1080/07055900.1993.9649484

Woolf, D.K., Thorpe, S.A., 1991. Bubbles and the air-sea exchange of gases in near-saturation conditions. J. Mar. Res. 49, 435–466. doi:10.1357/002224091784995765

Wright, I.C., et al, 2012. RRS James Clark Ross Cruise 253, 26 Jul -25 Aug 2011. Arctic methane hydrates [WWW Document]. URL http://nora.nerc.ac.uk/439241/ (accessed 2.25.16).

7. Conclusions

7.1. Scientific achievements

Several groups of scientists around the world have been trying to evaluate the contribution of submarine methane sources to the atmospheric methane budget and therefore another facet of the impact of the ocean on climate change (e.g. Etiope, 2009; Etiope and Milkov, 2004; Hornafius et al., 1999; Hovland and Judd, 1988; Judd, 2004; Judd and Hovland, 2009; Kvenvolden et al., 2001). The research associated to methane emissions from submarine sources consists of several sub-topics that together can answer how influential submarine methane sources are in the context of climate change. Some of these subtopics are 1) the assessment of the amount of methane stored in sediments and its vulnerability to be released, 2) the quantification of methane that is released from the seafloor, 3) the mechanisms that trigger the release, 4) the methane dynamics in the water column (bubble dissolution, oxidation, and distribution) and 5) the net methane flux from the surface water to the atmosphere.

Contribution

The presented thesis has been focused on the development of a hydroacoustic method for quantifying free gas/bubble released from the seabed and the application of this method in a seepage area in the Arctic. The main contribution of this work can be summarized as follows:

- A new hydroacoustic inverse method for quantifying free gas flow rates and fluxes is now available (chapter 4). The method inverts the total backscattering produced by a group of spherical bubbles when they are insonified by a monochromatic plane wave. The method has shown flow rate results comparable to direct/visual estimates in the same area, although it has not been completely validated by open ocean experiments. In addition, a methodology for clustering and cluster-flow rates averaging has been proposed and used to calculate the total flow rate of large seep areas.
- A new software package, FlareHunter and FlareFlowModule GUIs, has been created and is made available to the scientific community (chapter 5). The software design and its capabilities is driven by the need to have an organized way to analyze, post-process and finally estimate flow rates of acoustic information extracted from echograms. FlareHunter includes a set of specialized tools for flare processing and interactive editing, whereas the FlareFlowModule allows an easy and fast evaluation of gas flow rates of acoustic flares in different depth layers.
- The first spatio/temporal variability evaluation of the gas released in a large seep site area using hydroacoustic information is presented in this thesis (chapter 6). This study is the result of a long term monitoring program offshore PKF (Svalbard) and it is an important contribution for understanding the degassing dynamics of an area prone to hydrate destabilization.

Conclusions

From the hydroacoustic observations and the different analysis carried out during this work, the main conclusions can be summarized as follows:

- Observed changes in fluxes are associated to changes on static pressure, formation and dissociation of hydrates linked to seasonal changes of bottom water temperature, temperature changes related to anthropogenic warming and unknown changes of geological pathways that control gas migration.
- Additionally, the constant seeping of gas at the study area suggests that gas sources are not being depleted.
- From the temporal variability analysis of the gas emissions at the study area (chapter 6), it is suggested that two different areas are connected and share the same gas source. The latter is deduced due to the observed alternation in gas flux magnitudes between two separated areas, which can be explained by the opening and blocking of gas conduits produced by seasonal migration of the TGHZ.
- From gas/flare spatial analysis, a pronounced displacement of the TGHZ in response to annual average temperature changes is still unclear. Migration of the TGHZ has been just attributed to seasonal changes of temperature (Berndt et al., 2014) but in our study no evidence of this migration has been observed. Visualization of the TGHZ migration has not been possible because of the lack of information produced by the partial insonification of the seafloor at different surveys and the echosounder resolution limitation.
- Spatial analysis of methane fluxes (CCC method) at PKF indicate that the spatial distribution of the seepage intensity does not change in time, at least for the common areas considered in the analysis.
- The total gas flow rate of the three main seep site areas was calculated. Here, total flow rate values range approximately from 2500 to 4000 T CH_4 yr^{-1}, for the entire region.

7.2. Limitations and challenges

A clear understanding of the limitations and the current challenges is the key to address the direction of the continuity of this work. In the following section, a set of limitations and challenges found during the evolution of this research are listed.

7.2.1. SBES data

The first recognized limitation during this work is related to the data resolution. Echosounder data resolution is low compared to the size of the phenomena observed (gas released as bubble streams). Then, the amount of bubble streams that is represented by the flow rate derived from an acoustic flare is unknown.

Another limitation is associated to the time required to carry out a “flare hunting” survey over a large seep site area. SBES footprint sizes compared to a large area are considered small and are time consuming during data acquisition considering that the vessel speed has to be moderately slow to obtain good quality echograms.

An identified problem is the difficulty to hydroacoustically map the same area at different surveys. This has a direct implication in the spatio/temporal analysis of gas emissions because flow rates can only be compared in case they were derived strictly from the same insonified area.

Sources of noise and reverberation are considered a problem that has direct consequences in the flow rate calculations. Acoustic flares are commonly overlapped by unwanted targets and noise (natural or artificial) which could cause wrong calculations of flow rates using the inverse method.

7.2.2. Inverse method

The first challenge associated to the inverse method is its validation, which is required to increase the reliability in the derived flow rates. For validation, artificial bubble sources able of releasing different flow rates accompanied with visual monitoring when bubble sources are insonified are needed. Unfortunately an experimental setup to carry out this validation is still not available.

A second challenge has to do directly with the physical considerations that the bubble model, embedded in the inverse method, needs to have. At the moment a simplistic backscattering model of single unbounded spherical bubble insonified by a monochromatic plane wave is considered (Thuraisingham, 1997). As mentioned in chapter 4, future improvements of the model should consider additional aspects such as multiple scattering effects (e.g. Kafesaki et al., 2000; Prosperetti et al., 1993), bubble deformation (e.g. Strasberg, 1953; Feuillade and Werby, 1994) and changes in the total backscattering cross-section when bubbles are located near to a boundary (e.g. Gaunaurd, 1995; Maksimov, 2015). In addition to that, it is necessary to highlight that the inverse method is restricted to bubbles without hydrate coating and in the future this aspect should be considered. As it is expected, the hydrate coating could change the physical properties of the bubble such as e.g. stiffness influencing the character of acoustical scattering (Church, 1995; Maksimov and Sosedko, 2005).

7.2.3. Data quality and tools for post-processing

As already described, Flarehunter and FFM GUI present different tools for post-processing and evaluation of flare flow rates, however there are still some problems that have to be solved. A first challenge, proper to the software as a prototype, is the scripts optimization in order to improve the software performance. A second challenge is the capability of this tool to remove or clean noise and reverberation from unwanted targets. It is known that the signal overlapping can have a strong implication in the derived gas flow rates and therefore it is essential that noise/reverberation sources are removed in order to obtain realistic results. So far, tools for manually removing of noise/reverberation are implemented in the GUI. Possible techniques to remove noise that have been developed by other researchers could be implemented in a future version (Korneliussen, 2000; Robertis and Higginbottom, 2007). Together with that, the future work should be addressed to create new techniques for removing and deleting noise/reverberation.

7.3. Future work

According to the findings, limitations and problems found during the evolution of this thesis, the following points can be suggested as a future work.

- A validation of the inverse hydroacoustic method is still needed to provide reliable flow rate estimates. The validation should consider an experimental setup where the total flow rate coming from artificial bubble streams is determined through mechanical/visual methods. At the same time, bubble streams should be insonified with the echosounder. Bubble stream sources should be strictly

located within the area defined by echosounder footprint. It is suggested that the experimental setup includes a mechanism able to control the flow rate strength, the bubble stream numbers and bubble sizes, in order to test how the method responds to different total flow rates. The insonified water section should be free of unwanted scatterers for validation. Additional measurements including unwanted scatterers (e.g. fish) are also recommended in order to evaluate the errors in flow rate estimates produced by overlapping of the backscattered signals.

- Improvements of the inverse method should include multiple scattering effects, scattering of deformed bubbles, bubble scattering effects near boundaries and scattering of hydrate-coated bubbles. An experimental setup could be useful to evaluate the sensitivity of the flow rate estimates to these improvements.
- New techniques of removing noise and reverberation from the echograms have to be implemented in order to decrease the error in flow rate estimates induced by the overlapping of the backscattered signal coming from these sources.
- Because flarehunting surveys over large seepage areas using SBES is a highly time-consuming process, future work should be addressed in the creation of techniques for gas flow rate quantification combining SBES (calibrated system) and MBES (a non-calibrated system). The combination should be based in finding a relationship between the backscattering received with both systems when they insonify the same seep site. Then, flow rates derived from the calibrated system (SBES) could be associated to the backscattered amplitude obtained with the uncalibrated system (MBES). A relationship (If there is one), could be useful to derive flow rates from a large seep site area using the backscattering information obtained with the MBES.
- Passive acoustic techniques to determine BSD and bubble flow rates have been implemented by others (Bergès et al., 2015; Leifer and Tang, 2007; Leighton and White, 2012). As BSD is one of the important inputs in the presented inverse hydroacoustic method, these techniques should be considered in future fieldwork.
- At the study area, optical observations should be carried out in order to derive BRS associated to bubble sizes. These measurements will decrease the uncertainties in flow rate estimates produced by using BRSM.
- At the study area, an increase in methane release from submarine sources triggered by climate effects still cannot be discarded. Because clear manifestations of an increment in methane emissions due to accelerated hydrate dissociation could be expected to be a long term process, it is recommendable to continue the data acquisition at the study area. Surveys have to be efficiently planned in order that acquired hydroacoustic data come from a same insonified area at different times. The latter will allow having a better evaluation of the spatio/temporal changes in gas release.
- At the study area, a hydroacoustic observatory (side-looking sonar) is suggested to be located within the area where the TGHZ seasonally oscillates (between 360 to 410 m bsl). According to Berndt et al. (2014), seasonal fluctuations in the bottom-water temperature originates gas hydrates formation and dissociation. The existence of a hydroacoustic observatory will ideally allow visualization and evaluation of changes in methane emissions associated to increasing bottom-water temperature. Additionally, the same hydroacoustic observations will be useful to evaluate the influence of static pressure changes (produced by e.g. tidal cycles or currents near the seabed) over the gas release.

References

Bergès, B.J.P., Leighton, T.G., White, P.R., 2015. Passive acoustic quantification of gas fluxes during controlled gas release experiments. Int. J. Greenh. Gas Control 38, 64–79. doi:10.1016/j.ijggc.2015.02.008

Berndt, C., Feseker, T., Treude, T., Krastel, S., Liebetrau, V., Niemann, H., Bertics, V.J., Dumke, I., Dünnbier, K., Ferré, B., Graves, C., Gross, F., Hissmann, K., Hühnerbach, V., Krause, S., Lieser, K., Schauer, J., Steinle, L., 2014. Temporal Constraints on Hydrate-Controlled Methane Seepage off Svalbard. Science 343, 284–287. doi:10.1126/science.1246298

Church, C.C., 1995. The effects of an elastic solid surface layer on the radial pulsations of gas bubbles. J. Acoust. Soc. Am. 97, 1510–1521. doi:10.1121/1.412091

Etiope, G., 2009. Natural emissions of methane from geological seepage in Europe. Atmos. Environ., Natural and Biogenic Emissions of Environmentally Relevant Atmospheric Trace Constituents in Europe 43, 1430–1443. doi:10.1016/j.atmosenv.2008.03.014

Etiope, G., Milkov, A.V., 2004. A new estimate of global methane flux from onshore and shallow submarine mud volcanoes to the atmosphere. Environ. Geol. 46, 997–1002. doi:10.1007/s00254-004-1085-1

Feuillade, C., Werby, M.F., 1994. Resonances of deformed gas bubbles in liquids. J. Acoust. Soc. Am. 96, 3684–3692. doi:10.1121/1.410558

Gaunaurd, G.C., 1995. Acoustic scattering by an air-bubble near the sea surface.IEEE J. Ocean. Eng. 20, 285–292. doi:10.1109/48.468243

Hornafius, J.S., Quigley, D., Luyendyk, B.P., 1999. The world's most spectacular marine hydrocarbon seeps (Coal Oil Point, Santa Barbara Channel, California): Quantification of emissions. J. Geophys. Res. Oceans 104, 20703–20711. doi:10.1029/1999JC900148

Hovland, M., Judd, A., 1988. Seabed pockmarks and seepages: impact on geology, biology, and the marine environment. Springer

Judd, A.G., 2004. Natural seabed gas seeps as sources of atmospheric methane. Environ. Geol. 46, 988–996. doi:10.1007/s00254-004-1083-3

Judd, A.G., Hovland, M., 2009. Seabed fluid flow: the impact of geology, biology and the marine environment, Digitally print. version. ed. Cambridge Univ. Press, New York, NYKafesaki, M., Penciu, R.S., Economou, E.N., 2000. Air Bubbles in Water: A Strongly Multiple Scattering Medium for Acoustic Waves. Phys. Rev. Lett. 84, 6050–6053. doi:10.1103/PhysRevLett.84.6050

Korneliussen, R.J., 2000. Measurement and removal of echo integration noise. ICES J. Mar. Sci. J. Cons. 57, 1204–1217. doi:10.1006/jmsc.2000.0806

Kvenvolden, K.A., Lorenson, T.D., Reeburgh, W.S., 2001. Attention turns to naturally occurring methane seepage. Eos Trans. Am. Geophys. Union 82, 457–457. doi:10.1029/01EO00275

Leifer, I., Tang, D., 2007. The acoustic signature of marine seep bubbles. J. Acoust. Soc. Am. 121, EL35–EL40. doi:10.1121/1.2401227

Leighton, T.G., White, P.R., 2012. Quantification of undersea gas leaks from carbon capture and storage facilities, from pipelines and from methane seeps, by their acoustic emissions. Proc. R. Soc. Math. Phys. Eng. Sci. 468, 485–510. doi:10.1098/rspa.2011.0221

Maksimov, A., 2015. Nonlinear activity of acoustically driven gas bubble near a rigid boundary, in: AIP Conference Proceedings. Presented at the RECENT DEVELOPMENTS IN NONLINEAR ACOUSTICS: 20th International Symposium on Nonlinear Acoustics including the 2nd International Sonic Boom Forum, AIP Publishing, p. 050006. doi:10.1063/1.4934422

Maksimov, A.O., Sosedko, E.V., 2005. Dynamics of sea bubbles covered by a hydrate skin.Presented at the XVI Session of the Russian Acoustical Society, Moscow.

Prosperetti, A., Lu, N.Q., Kim, H.S., 1993. Active and passive acoustic behavior of bubble clouds at the ocean's surface. J. Acoust. Soc. Am. 93, 3117–3127. doi:10.1121/1.405696

Robertis, A.D., Higginbottom, I., 2007. A post-processing technique to estimate the signal-to-noise ratio and remove echosounder background noise. ICES J. Mar. Sci. J. Cons. 64, 1282–1291. doi:10.1093/icesjms/fsm112

Strasberg, M., 1953.The Pulsation Frequency of Nonspherical Gas Bubbles in Liquids. J. Acoust. Soc. Am. 25, 536–537. doi:10.1121/1.1907076

Thuraisingham, R.A., 1997. New expressions of acoustic cross-sections of a single bubble in the monopole bubble theory. Ultrasonics 35, 407–409. doi:10.1016/S0041-624X(97)00021-8

Westbrook, G.K., Thatcher, K.E., Rohling, E.J., Piotrowski, A.M., Pälike, H., Osborne, A.H., Nisbet, E.G., Minshull, T.A., Lanoisellé, M., James, R.H., Hühnerbach, V., Green, D., Fisher, R.E., Crocker, A.J., Chabert, A., Bolton, C., Beszczynska-Möller, A., Berndt, C., Aquilina, A., 2009. Escape of methane gas from the seabed along the West Spitsbergen continental margin. Geophys. Res. Lett. 36, L15608.doi:10.1029/2009GL039191

Appendices

Appendix.1

S_V, *TS* and TS_{COMP} calculation

The received backscattered signal can be displayed as *TS*, TS_{COMP} and S_V values after calculation. *TS* and S_V values are obtained using the following equations (Echoview formulas verified by SIMRAD derived from the online support of Echoview):

$$TS = P_r + 40logR + 2\alpha R - 10log\left(\frac{P_t G_0^2 \lambda^2}{16\pi^2}\right) \quad \text{(A.4.1)}$$

$$S_V = P_r + 20logR + 2\alpha R - 10log\left(\frac{P_t G_0^2 \lambda^2 c\tau\psi}{32\pi^2}\right) - 2S_a \quad \text{(A.4.2)}$$

where:

R : corrected range (m) =*r – sT*
r : uncorrected range (m) = *nc(τ/2)*
s : TVG range correction offset value
T : sample thickness (m) = *c(τ/2)*
n : sample number
P_r : received power (dB re 1 W)
P_t : transmitted power (W)
α : absorption coefficient (dB/m)
G_0 : transducer peak gain (non-dimensional)
λ : wavelength (m) = *c/f*
f : frequency (Hz)
c : sound speed (m/s)
τ : transmit pulse duration (s) - also known as the pulse length
ψ : Equivalent Two-way beam angle (Steradians)
S_a : Simrad correction factor (dB re $1m^{-1}$) determined during calibration of theEK60

TS_{COMP} is calculated using the following equation:

$$TS_{COMP} = TS + COMP \quad \text{[A.4.33]}$$

where:

$$COMP = 6.0206(x^2 + y^2 - 0.18x^2y^2)$$
$$x = \alpha_{\mathrm{M}}/BW\alpha \qquad (-1 \leq x \leq 1)$$
$$y = \beta_{\mathrm{M}}/BW\beta \qquad (-1 \leq y \leq 1)$$

and:

α_{M} : Alongship mechanical angle (degrees)
β_{M} : Athwarpship mechanical angle (degrees)
$BW\alpha$: Beam width alongship (degrees)
$BW\beta$: Beam width athwarpship (degrees)

Appendix.2

Work flow diagram of the data processing

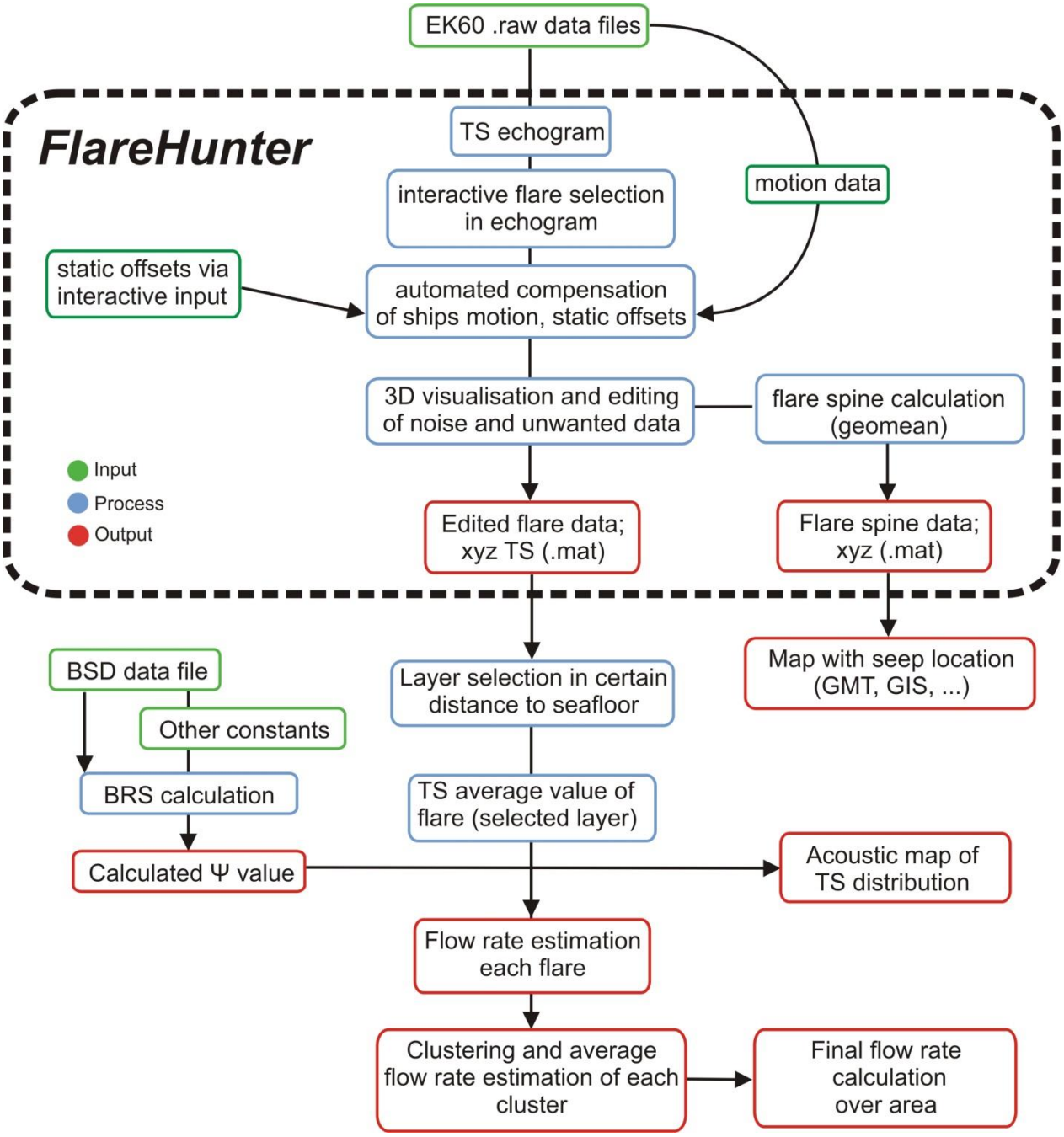

Appendix.3

Salinity, temperature, density and sound velocity profiles for the 11 surveys considered in this study.

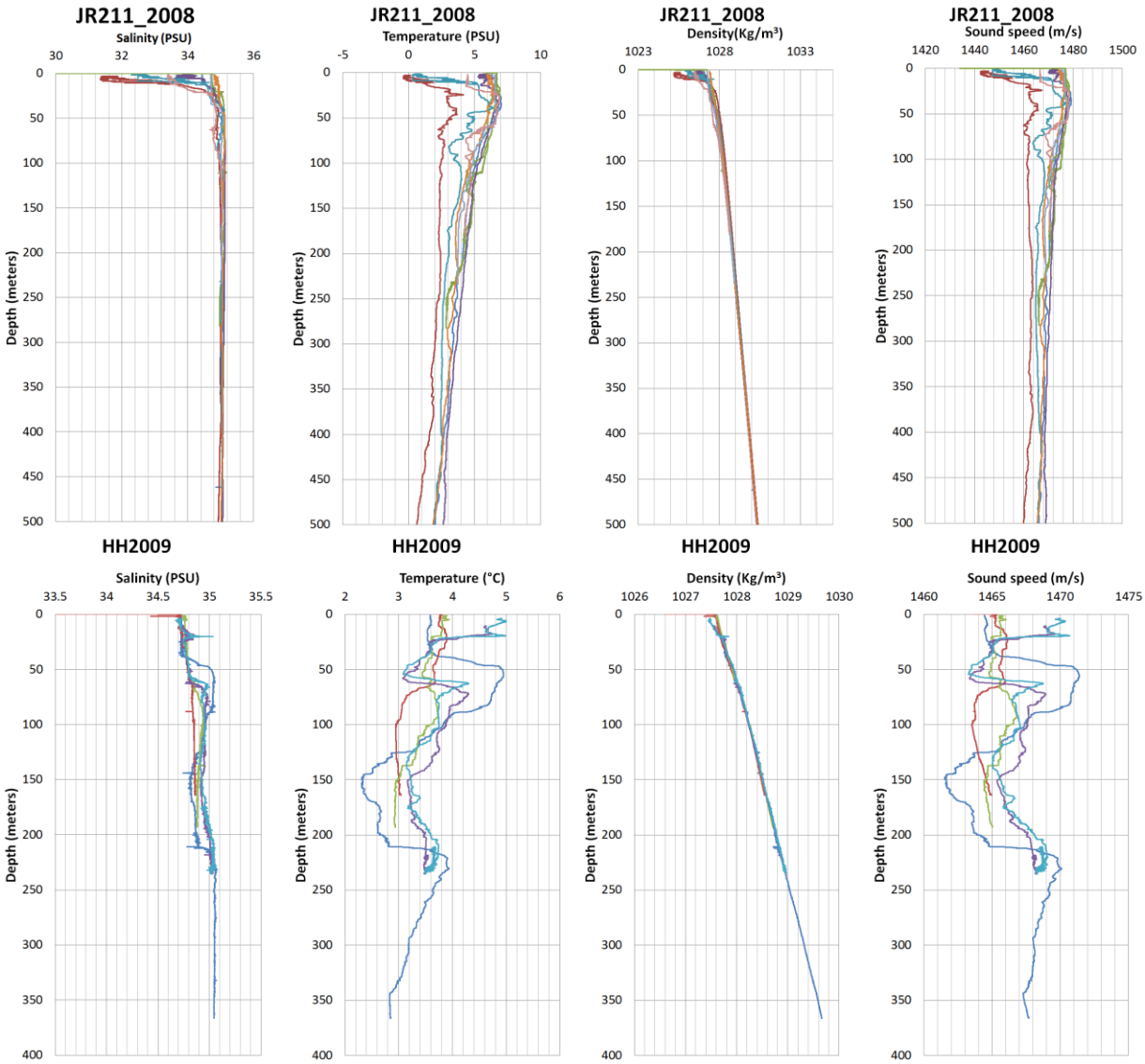

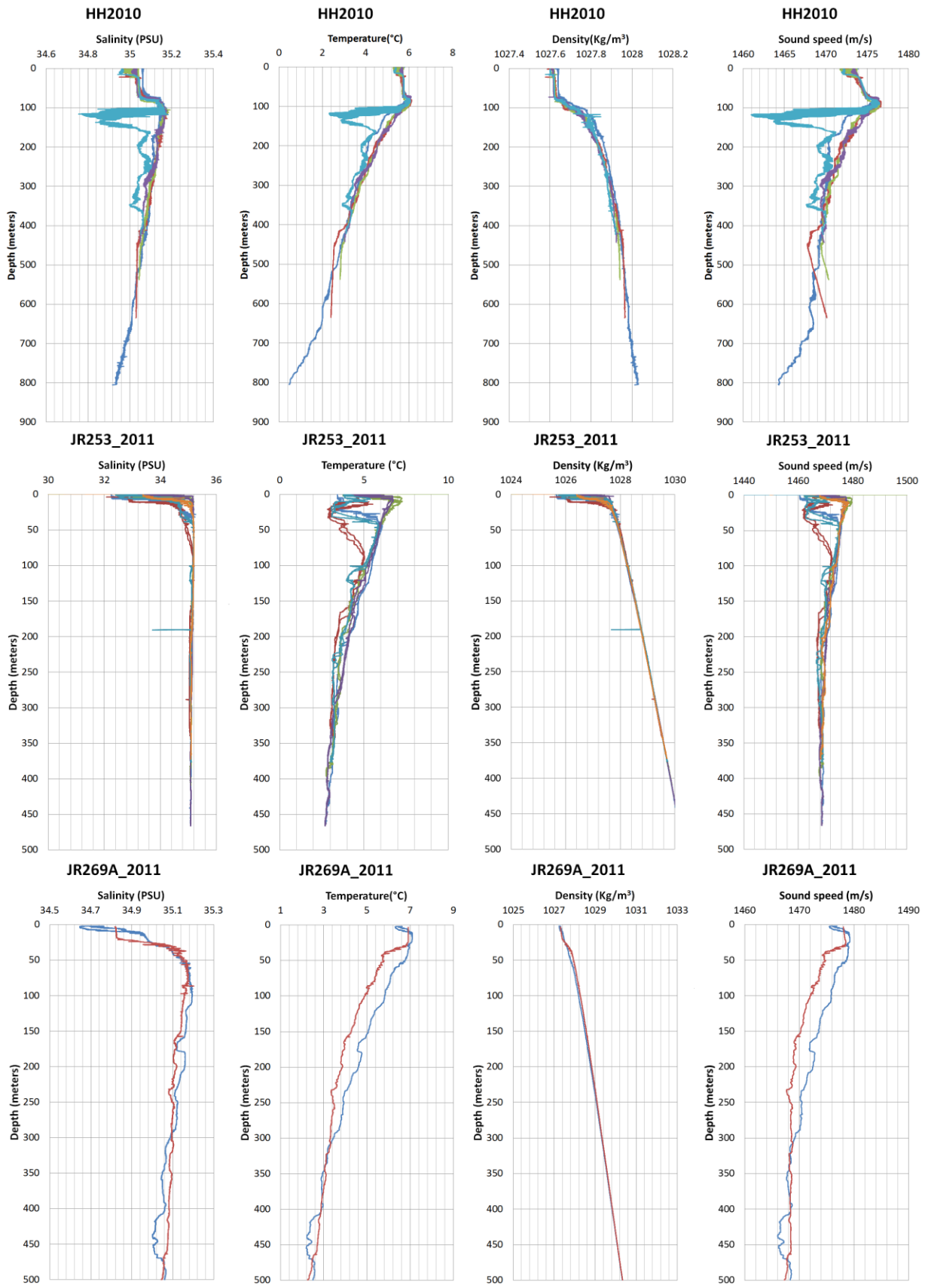
HH2010
Salinity (PSU)
34.6 34.8 35 35.2 35.4
Depth (meters)
0 100 200 300 400 500 600 700 800 900
HH2010
Temperature(°C)
0 2 4 6 8
Depth (meters)
0 100 200 300 400 500 600 700 800 900
HH2010
Density(Kg/m³)
1027.4 1027.6 1027.8 1028 1028.2
Depth (meters)
0 100 200 300 400 500 600 700 800 900
HH2010
Sound speed (m/s)
1460 1465 1470 1475 1480
Depth (meters)
0 100 200 300 400 500 600 700 800 900
JR253_2011
Salinity (PSU)
30 32 34 36
Depth (meters)
0 50 100 150 200 250 300 350 400 450 500
JR253_2011
Temperature (°C)
0 5 10
Depth (meters)
0 50 100 150 200 250 300 350 400 450 500
JR253_2011
Density (Kg/m³)
1024 1026 1028 1030
Depth (meters)
0 50 100 150 200 250 300 350 400 450 500
JR253_2011
Sound speed (m/s)
1440 1460 1480 1500
Depth (meters)
0 50 100 150 200 250 300 350 400 450 500
JR269A_2011
Salinity (PSU)
34.5 34.7 34.9 35.1 35.3
Depth (meters)
0 50 100 150 200 250 300 350 400 450 500
JR269A_2011
Temperature(°C)
1 3 5 7 9
Depth (meters)
0 50 100 150 200 250 300 350 400 450 500
JR269A_2011
Density (Kg/m³)
1025 1027 1029 1031 1033
Depth (meters)
0 50 100 150 200 250 300 350 400 450 500
JR269A_2011
Sound speed (m/s)
1460 1470 1480 1490
Depth (meters)
0 50 100 150 200 250 300 350 400 450 500

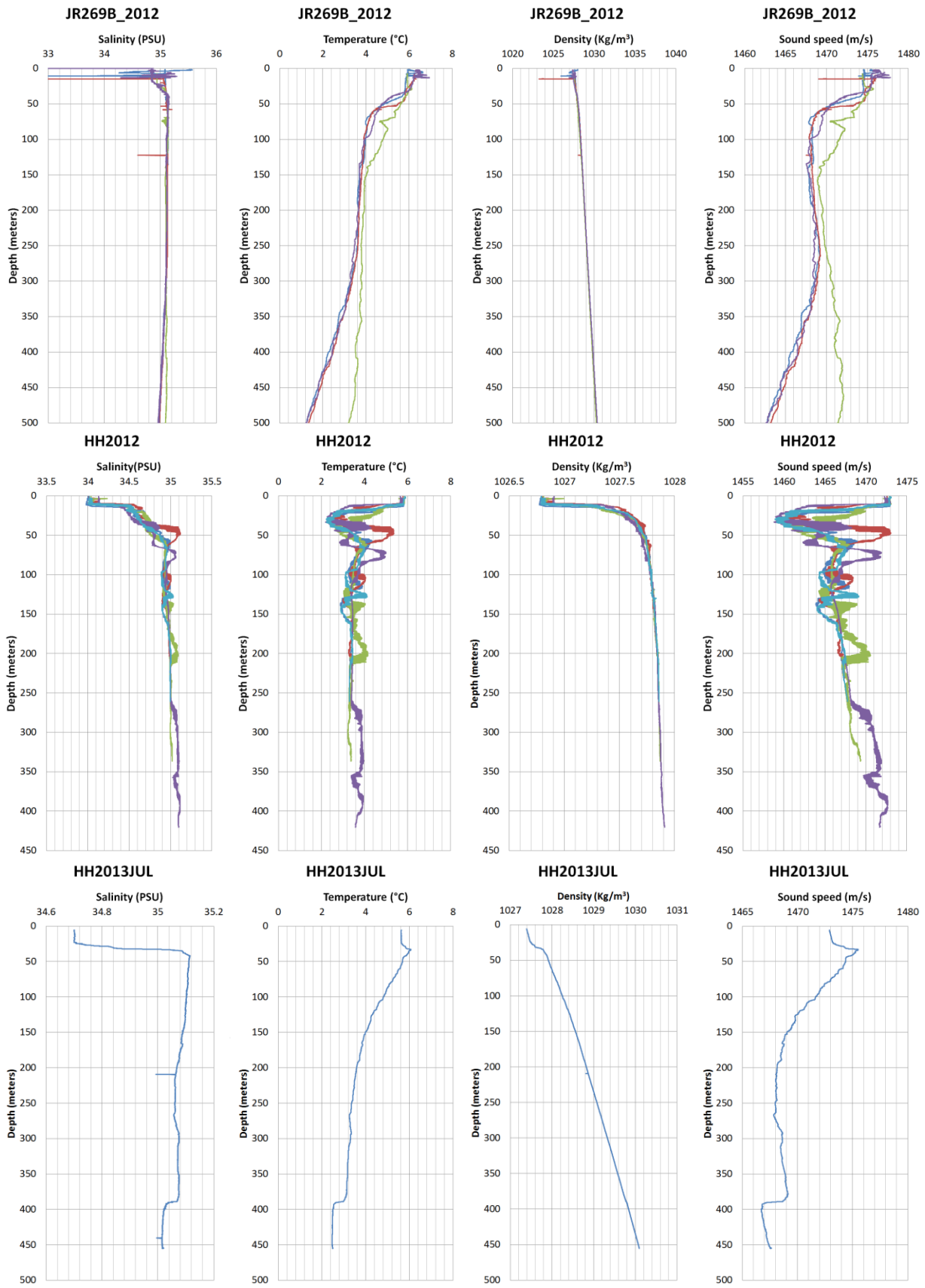
JR269B_2012
Salinity (PSU)
33 34 35 36
Temperature (°C)
0 2 4 6 8
Density (Kg/m³)
1020 1025 1030 1035 1040
Sound speed (m/s)
1460 1465 1470 1475 1480
Depth (meters)
0 50 100 150 200 250 300 350 400 450 500
HH2012
Salinity(PSU)
33.5 34 34.5 35 35.5
Temperature (°C)
0 2 4 6 8
Density (Kg/m³)
1026.5 1027 1027.5 1028
Sound speed (m/s)
1455 1460 1465 1470 1475
Depth (meters)
0 50 100 150 200 250 300 350 400 450
HH2013JUL
Salinity (PSU)
34.6 34.8 35 35.2
Temperature (°C)
0 2 4 6 8
Density (Kg/m³)
1027 1028 1029 1030 1031
Sound speed (m/s)
1465 1470 1475 1480
Depth (meters)
0 50 100 150 200 250 300 350 400 450 500

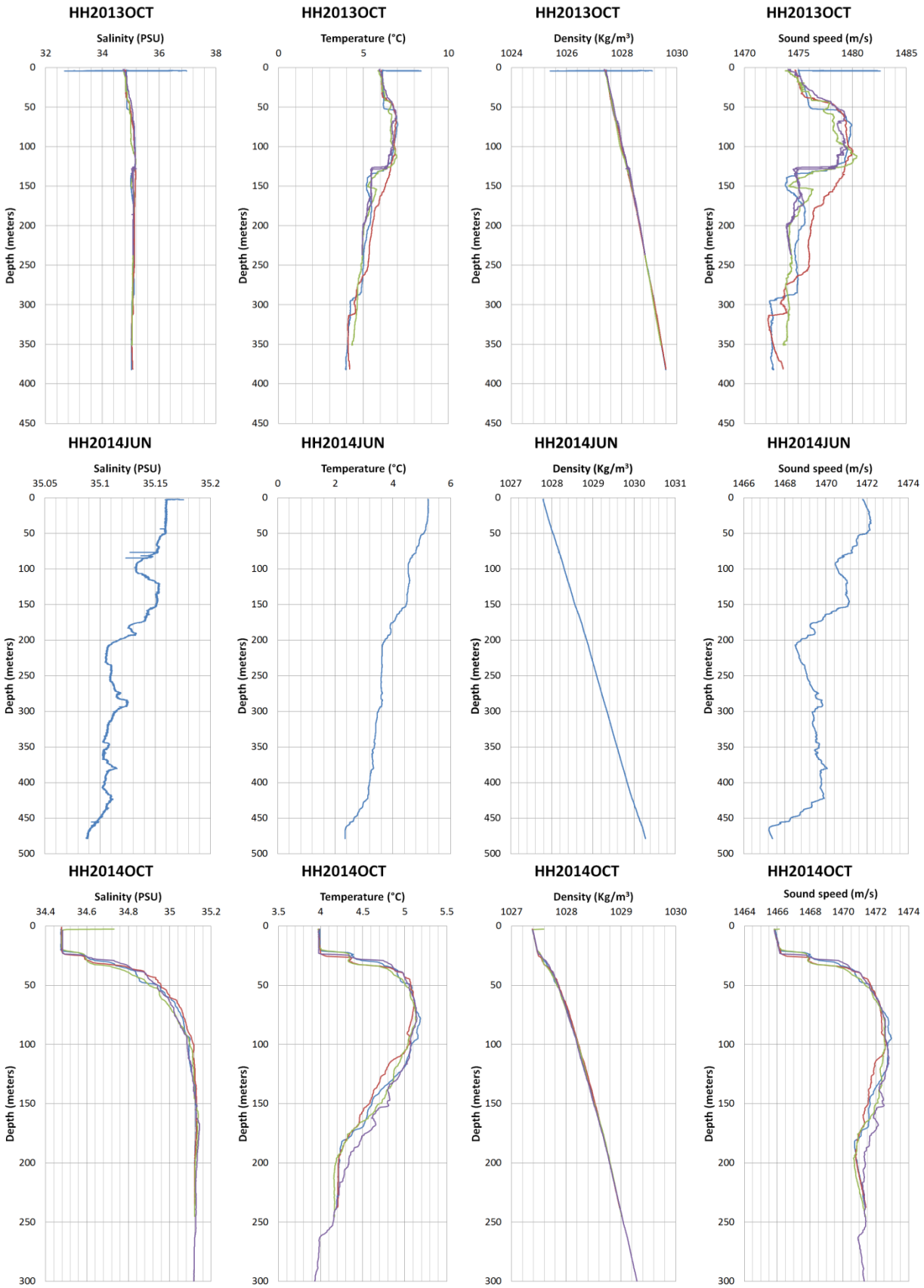
HH2013OCT
Salinity (PSU)
32 34 36 38
Temperature (°C)
0 5 10
Density (Kg/m³)
1024 1026 1028 1030
Sound speed (m/s)
1470 1475 1480 1485
Depth (meters)
0 50 100 150 200 250 300 350 400 450
HH2014JUN
Salinity (PSU)
35.05 35.1 35.15 35.2
Temperature (°C)
0 2 4 6
Density (Kg/m³)
1027 1028 1029 1030 1031
Sound speed (m/s)
1466 1468 1470 1472 1474
Depth (meters)
0 50 100 150 200 250 300 350 400 450 500
HH2014OCT
Salinity (PSU)
34.4 34.6 34.8 35 35.2
Temperature (°C)
3.5 4 4.5 5 5.5
Density (Kg/m³)
1027 1028 1029 1030
Sound speed (m/s)
1464 1466 1468 1470 1472 1474
Depth (meters)
0 50 100 150 200 250 300

Appendix.4

Damping as function of bubble radius calculated according to equations [4.5] and [4.6] for 38 kHz and 220 m water depth.